The Diffraction of Monsters from Complex Apertures

Towards an Electromagnetic Approach

By

HOLLY ALICE JESS MIDDLETON-SPENCER

Joule Physics Laboratory
UNIVERSITY OF SALFORD

A dissertation submitted to the University of Salford in accordance with the requirements of the degree of MASTER OF SCIENCE in the School of Computing, Science and Engineering.

AUGUST 2018

ABSTRACT

The research presented in this MSc thesis is concerned with understanding the way incoming electromagnetic waves are diffracted by various different types of scattering screens. These classes of problem are fundamental in the laser optics community, and within the arena of wave physics more generally. They are also of potential interest to applied mathematics researchers, particularly those concerned with describing scattering through boundary integral equations.

Analysis begins with revisiting Lamb's ingenious solution to the classic knife-edge problem, known for over a century. Maxwell's equations are solved for an incoming plane wave (subject to appropriate boundary conditions on a perfectly-conducting semi-infinite screen of negligible thickness) and this building-block calculation is then generalized to allow for incident and scattered waveforms that have multiscale characters. A candidate model used throughout is the Weierstrass function. In its original form, this function is well known to be *continuous everywhere but differentiable nowhere* and it was dubbed a 'monster' by Charles Hermite. Two distinct families of solution are derived which, for the first time, provide a fairly rigorous description of pre-fractal electromagnetic waves scattering from a single knife-edge.

Subsequent investigations consider plane waves scattering from conducting screens that can have a multi-scale character, such as a pre-fractal Cantor set (that is, a diffraction grating modelled on any finite iteration of the Cantor set). Previous related studies have been concerned predominantly with regimes wherein the outgoing waves are observed in the far field (that is, at large distances from the screen), and where recourse has typically been made to the scalar approximation. Here, a more general formulation is developed that is based on Rayleigh-Sommerfeld diffraction integrals, and the scattered waves are connected more directly to Maxwell's equations in terms of calculating the corresponding magnetic-field components.

Finally, the first steps are taken toward modelling a physical scenario where an incident pre-fractal wave scatters from a pre-fractal Cantor set. Research into this regime is still ongoing, largely due to the computationally-expensive nature of the required calculations.

DEDICATION AND ACKNOWLEDGEMENTS

I'd firstly like to thank my friends who have not only kept me relatively sane during the production of this work but have made the last four years at Salford University both utterly bizarre and extremely enjoyable. Secondly, I'd like to express thanks to my secondary supervisor Dr. Edmund Chadwick for his assistance in understanding the mathematical subtleties underlying derivations in this thesis. Finally, special thanks go to my supervisor Dr. James Christian. The freedom he has given me during this project alongside his constant support has ensured that I have been working to the best of my abilities. He provided me with the skills to become a well-rounded academic researcher. It was his persuasion that led me to take a research MSc instead of the taught MPhys - I cannot express in words how good a decision that was.

This last year of research has been the best year of my life. I cannot wait to see what the next three hold.

TABLE OF CONTENTS

List of Tables

Table **Page**

List of Figures

Figure **Page**

CHAPTER 1

INTRODUCTION

1.1 Research context

The research in this thesis is concerned with investigating how electromagnetic waves, particularly those with a pre-fractal character (known colloquially as *monsters*), can scatter from obstacles that may be either simple (as in the case of a single knife edge) or complex. In this sense, the *complex domain* of the thesis title pertains to a scattering obstacle that can possess structure over potentially many decimal orders of spatial scale. The candidate complex domain used throughout this thesis is based on the famous Cantor set, but other equally well-known examples might be the von Koch snowflake or the Sierpinski triangle, for instance. From the outset, it is noted that some substantial early (and still unpublished) work has already been undertaken in this general area, beginning in around 2013 [3–5]. All the preceding analysis has been based upon the assumption that the paraxial approximation holds true and that the framework of scalar wave optics is sufficient to describe the multi-scale scattering phenomena under consideration. Adoption of the simpler paraxial-based model is desirable for a number of reasons, most obviously that the governing partial differential equations (PDEs) are vastly reduced in complexity (going from the elliptic Helmholtz equation to the parabolic paraxial diffraction equation), boundary conditions play only a marginal role in the ensuing diffraction-integral formulation, and exact continuous-wave (cw) solutions can be immediately written down in the form of Fresnel integrals. Finally, through deployment of Hastings's rational approximations, the paraxial description of diffraction patterns can be readily interpreted in the context of Young's edge waves – clearly a major advantage when grappling with such complicated systems. It is also helpful that all those paraxial patterns can be parametrized quite conveniently by a single dimensionless constant, namely the aperture Fresnel number.

Here, the research programme is effectively 'reset' and the diffraction problem is attacked from an altogether different direction. Starting from scratch, the assumptions underlying previous work will be re-examined and any mathematical approximations kept to a minimum. The motivation for such a re-consideration comes from several gradual realizations. Firstly, there is a dawning that the paraxial approximation is not necessarily a feasible starting point for describing high-frequency regimes defined by the inequality $\frac{|k_\perp|}{k} \approx \mathcal{O}(1)$, where $k_\perp$ is the magnitude of the transverse projection of the wavevector and $k = \frac{2\pi}{\lambda}$ is the wavenumber—we return to this point shortly. The Fresnel approximation tends to be valid in low-frequency regimes only, where $\frac{|k_\perp|}{k} \ll \mathcal{O}(1)$. It works best under conditions of normal incidence, scalar diffraction, and for describing waves travelling in the forward longitudinal sense only [6]. It cannot be expected to provide quantitatively reliable results whenever deviating from these constraints. There is also an acceptance that paraxial theory inherently is unlikely to provide a satisfactory prediction for the high-frequency cut-offs which are such a crucial part of physically realistic pre-fractal structures. The reason is that the cut-off condition is based on geometrical considerations involving propagation angles close to 90° and that are hence in violation of the small-angle (i.e., low-frequency) assumption.

The remainder of Chapter 1 provides a summary of some key concepts used throughout the rest of the thesis. These concepts fall broadly into two categories: mathematical and physical. The mathematical background introduces the reader to the concept of fractals, particularly the Cantor set and dust, and the notion of dimension with particular focus on the Hausdorff dimension. The Weierstrass function is reviewed and a brief description of four mainstream fractal-dimension estimation measures for real (finite) data sets is provided (variogram, power spectrum, roughness-length, and rescaled-range). There is also a discussion on how the standard Weierstrass function must be truncated if it is to represent a physically-meaningful electromagnetic field. The physical background provides an overview of the free-space Maxwell equations and details how the subsequent electric and magnetic components of a wave may be derived for cw solutions. The chapter concludes with an asymptotic analysis to show how earlier (paraxial) work must emerge as a special case.

In Chapter 2, attention is paid to Sommerfeld's classic knife-edge problem where an incoming wave impinges on a semi-infinite, perfectly-conducting screen of negligible thickness and where electromagnetic energy is scattered into the far field. Lamb's solution is considered, derived in detail, and subsequently generalized to allow for incoming waves that are pre-fractal in nature and where a truncated form of the Weierstrass function is used as a model for multiscaledness. The results of that analysis are the fundamental Weierstrass-Lamb waves: exact vector solutions to Maxwell's equations (in both transverse-electric, TE, and transverse-magnetic, TM, families) that describe the linearly-polarized cw electromagnetic field at all points in space and time and that fully respect the boundary conditions on the screen. These novel solutions are still naturally described in terms of Fresnel integrals because of some interesting properties of the underlying

Helmholtz equation. As a consequence, one of the Weierstrass-Lamb waves captures as a limit the known paraxial Weierstrass-type wave for a knife edge. That is, a paraxial solution emerges when the assumptions of paraxial theory are satisfied (as should be the case): one requires small angles relative to the reference axis (i.e., at large longitudinal and small transverse distances), observation to be in the forward half-plane only, and when the incoming electric field is polarized parallel to the screen's edge. A preliminary attempt has been made to quantify the fractal dimension of the Weierstrass-Lamb solution by deploying the BENOIT software package, but limited available computational resources have, to some extent, hindered that analysis (and also at other points throughout the research).

Chapter 3 begins the formal investigation of how normally-incident electromagnetic plane waves are diffracted by complex apertures, and where the scattering obstacle is modelled as iterations of the Cantor set. The motivation for this work, and the particular choice of a Cantor-set grating, arises from recent developments in the Applied Mathematics community [7, 8] (waves interacting with complex domains is becoming a research area with increasing momentum) and where some attention is focused on fractal-type generalizations of classic sound transmission problems in acoustics. Here, the thesis prescribes a similar scattering problem (though in electromagnetics and for TE waves only) by applying a Rayleigh-Sommerfeld (RS) diffraction-integral approach that is essentially exact in the case of a single transverse dimension. Some very encouraging agreement has been found with the more computationally rigorous boundary-element method developed by other researchers. Preliminary results for the RS scattering of plane waves from the Cantor dust (a variation of the Cantor set but with two transverse dimensions) are given in Appendix E, but the strong time constraints on the 12-month MSc programme and a high number of computationally-expensive calculations have not yet permitted a fuller development of that research strand.

Chapter 4 continues with the RS diffraction-integral approach by considering a single slit aperture (in essence, the zero-order iteration of a Cantor-set initiator-generator algorithm) illuminated by a truncated Weierstrass-type input wave. An advantage here is that the results are unconstrained by the paraxial limitations of earlier analyses, numerical solutions are computed that are formally valid in essentially all of the forward half-plane, and they are free from the sub-wavelength features that typically plague paraxial predictions for the diffracted electric field. Further dimension estimations are carried out using BENOIT for a variety of parameter regimes, and fast Fourier transforms uncover some surprising results for both the intensity (typically the object of principle concern in scalar wave optics due to its ease of observation in the laboratory) and also the electric field (which tends to be of more fundamental interest to the Applied Mathematics community, as solutions to a set of PDEs with boundary conditions).

Chapter 5 begins to extend the analysis of Chapter 4 through the generator hierarchy, applying truncated Weierstrass-type input waveforms to increasing iterations of the Cantor set. Of particular interest here is that two different constructions are used. Considered first is the classic Cantor

set from fractal geometry, where each application $n = 1,2,3\ldots$ of the generator algorithm reduces the initial slit width by a factor of 3^n (so that as $n \to \infty$, the slits tend toward zero width) and all the slits remain within a fixed region of space. A second construction is also considered, wherein for $n = 1,2,3\ldots$ the slits have constant width (i.e., are independent of n) but are increasingly separated in space (this is the configuration typically favoured in the early optics experiments). Analysis in BENOIT looks for trends in the datasets when estimating the fractal dimension. Conclusions about the research undertaken here are drawn in Chapter 6, and some suggestions are given for future avenues of investigation.

1.2 Fractals

One of the first things we learn during childhood is the concept of dimension. The world is inherently three-dimensional (3D), the paper you see this thesis written on is two-dimensional (2D) and a line is one-dimensional (1D). This is very simple to comprehend; the problem is when dimension becomes non-integer. These entities with a non-integer dimension are commonly referred to as fractals. Anyone can appreciate their underlying beauty through pictures however the mathematics behind such structures is abstruse. Mandelbrot, in his seminal essay "The Fractal Geometry of Nature" [9], defined a fractal as such:

> *"A fractal is by definition a set for which the [Hausdorff] dimension strictly exceeds the topological dimension."*

The Hausdorff dimension mentioned here is *the* go-to dimension of an object. It is by no means the only dimension but it is useful since it can be defined for every set [10]. In this thesis, two different fractals are considered in detail: the Cantor set and the Weierstrass function.

1.2.1 Cantor set

The Cantor set is a fractal that is easily recognisable and although it may not look as exciting as others such as the von Koch curve or the Mandelbrot set [10], it remains extremely important to the field. The traditional Cantor set is constructed through an iterative process. To begin, one takes a unit length (this is the zeroth iteration, or initiator, $n = 0$) and then removes the middle third of this length (the generator). One then takes the middle third out of the remaining two lengths, $n = 1$. As $n \to \infty$, what is left is an infinite uncountable set (see Fig 1.1). The Cantor set is self similar; it can be regarding as being made of scaled versions of itself. One can hence use the Hausdorff scaling property to state that a given Cantor set, F, can be split into two parts – F_L and F_R, where $F_L \subset F[0, \frac{1}{3}]$ and $F_R \subset F[\frac{2}{3}, 1]$. If D_0 denotes the dimension and $\mathscr{H}^{D_0}(F)$ is the D_0-dimensional Hausdorff measure of F (where one assumes that $0 < \mathscr{H}^{D_0}(F) < \infty$) [10] then

$$\mathscr{H}^{D_0}(F) = \mathscr{H}^{D_0}(F_L) + \mathscr{H}^{D_0}(F_R) = 2\left(\frac{1}{3}\right)^{D_0} \mathscr{H}^{D_0}(F). \tag{1.1}$$

Dividing by $\mathscr{H}^{D_0}$ gives $1 = 2\left(\frac{1}{3}\right)^{D_0}$, which then yields the Hausdorff dimension of the traditional (middle third) Cantor set as $D_0 = \frac{\log 2}{\log 3} \approx 0.6309$.

Figure 1.1: The first four iterations of the pre-fractal Cantor set.

1.2.2 Cantor dust

The 2D analogue of the Cantor set is Cantor dust. Similar to the aforementioned Cantor set, one takes the generator square and replaces it by four versions of itself – each scaled down to a ninth of its original size. This process is repeated *ad infinitum*.

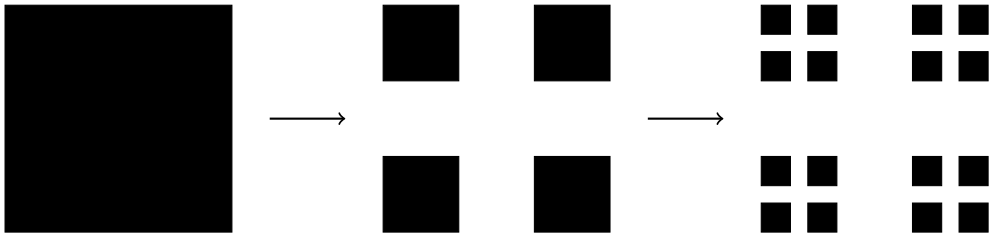

Figure 1.2: The first three iterations of the Cantor dust.

1.2.3 Weierstrass functions

In 1886 Karl Weierstrass presented a function that was different from all others – it was *everywhere continuous but nowhere differentiable* [11],

$$W(t) = \sum_{\nu=0}^{\infty} \lambda^{-(2-D_0)\nu} \sin(\lambda^\nu t), \tag{1.2}$$

where $1 < D_0 \leq 2$ and is shown graphically in Fig. 1.3. Essentially, it is a weighted superposition of periodic patterns with a scale-length of $\frac{2\pi}{\lambda^\nu}$. It is now known that there is a whole family of functions that holds these properties,

$$W(t) = \sum_{\nu=0}^{\infty} \lambda^{-(2-D_0)\nu} g(\lambda^\nu t), \tag{1.3}$$

if g is a suitable periodic function (such as a sine or cosine). As D_0 increases, the graph gets more

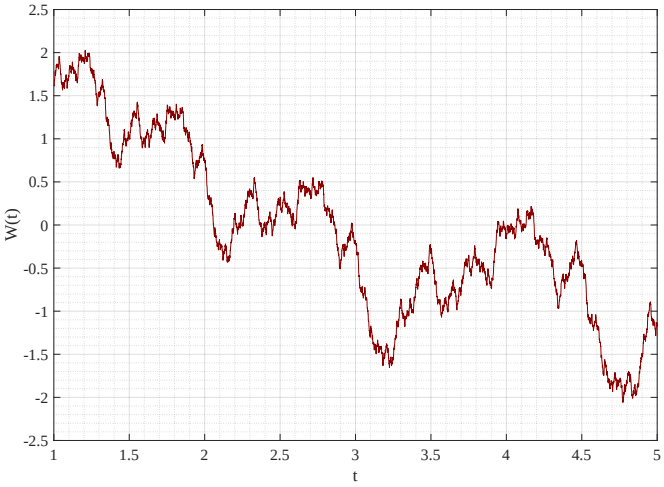

Figure 1.3: A plot of the Weierstrass function given by Eq. (1.2), for $D_0 = 1.37$ and $\gamma = 1.5$.

erratic – more *space filling*. Weierstrass functions can be represented in a multitudes of ways, for example a formulation used in the literature [12, 13] is

$$W(t) = \sum_{\nu=0}^{\infty} \frac{1}{\gamma^{(2-D_0)\nu}} \cos\left(\frac{2\pi}{\Lambda}\gamma^{\nu} t + \phi_{\nu}\right), \tag{1.4}$$

where the parameter $\gamma > 1$ is chosen so that the values of γ^{ν} determine the Weierstrass spectrum of frequencies, $\Lambda > 0$ fixes the largest scalelength and ϕ_{ν} is a phase that may be 0, chosen deterministically or be random. Equation (1.4) is shown graphically in Fig. 1.4. The parameter D_0 has been proven to be the capacity dimension [14] as well as the packing dimension [15]. Hunt [13] has proven that the Hausdorff dimension of $W(t)$ is D_0 for "almost every sequence $\Theta = \{\theta_0, \theta_1, ...\}$" as long as the parameter g from Eq. (1.3) is Lipschitz and periodic.

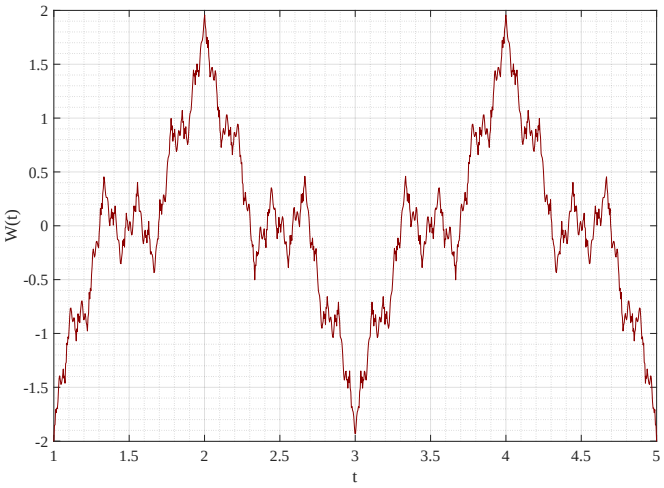

Figure 1.4: The Weierstrass function, from Eq. (1.4), for $D_0 = 1.37$, $\gamma = 3$ and $\Lambda = 2$.

1.2.4 Dimension analysis

An important aspect of the work undergone in this thesis requires an estimation of fractal dimension. The software package BENOIT [16, 17] can analyse self-affine fractals by the use of multiple methods: the variogram method, power spectrum, roughness-length and finally rescale-range. All are designed to work well on various self-affine fractals and each have their own strengths and weaknesses.

1.2.4.1 Variogram background

The variogram is the mean-squared increment of the points in the series [18, 19],

$$\gamma(\Delta t) = \frac{1}{2N}\sum_{i=0}^{N}[Y(t) - Y(t+\Delta t)]^2, \tag{1.5}$$

where $Y(t)$ is the sampled data at a given t value, where t is the independent variable. Δt is the "lag distance" – the increment along t and N is the number of points in $Y(t)$ measured for the given Δt value. The Hurst exponent, H, can be obtained from the proportionality $\gamma(\Delta t) \propto (\Delta t)^H$, [19] i.e.,

$$H = \frac{1}{2}\frac{\ln\gamma(\Delta t)}{\ln \Delta t}, \tag{1.6}$$

where the dimension, D, can be simply calculated via $D = 2 - H$.

1.2.4.2 Power spectrum method

If $p(k)$ is defined as the discrete Fourier transform [20] of the time series Y,

$$p(k) = \sum_{j=0}^{N-1} Y(j)\exp\Big(-\frac{2\pi i}{N}kj\Big), \tag{1.7}$$

then the parameter β is [21]

$$\beta = \frac{\ln[|p(k)|]}{\ln(k)}. \tag{1.8}$$

The dimension of the self-affine series can then be obtained for a topologically 1D sequence from [22]

$$D = \frac{5-\beta}{2}. \tag{1.9}$$

The power spectrum method is widely used in the Physics community due to its simplicity, ease of use and interpretation.

1.2.4.3 Roughness-length method

The roughness-length estimation works on the principle of (as the name suggests) calculating the roughness of self-affine series [1]. The "roughness" here is defined as the root mean squared (RMS) of the residues (z_j) [23], so that

$$RMS(w) = \frac{1}{n_w} \sum_{i=1}^{n_w} \sqrt{\frac{1}{m_i - 2} \sum_{j \in w_i} (z_j - \bar{z})^2}, \tag{1.10}$$

where n_w is the total number of windows (of length w), m_i is the number of points in the window, z_j is the particular residual of the window, and $\bar{z}$ is the mean residual of the window.
The window lengths vary in size from being at least 10 points wide to around 20% of the total length of the total series. Results in [24] suggest the method is reliable when there are roughly between 5 and 50 data points per unit length and is best when the estimated D is between 1.3 and 1.7. The Hurst exponent, H, can be determined from the gradient of the logorithmic plot of the $RMS(w)$ and w, i.e.

$$H = \frac{\ln[RMS(w)]}{\ln(w)}, \tag{1.11}$$

and, as with the variogram method, $D = 2 - H$.

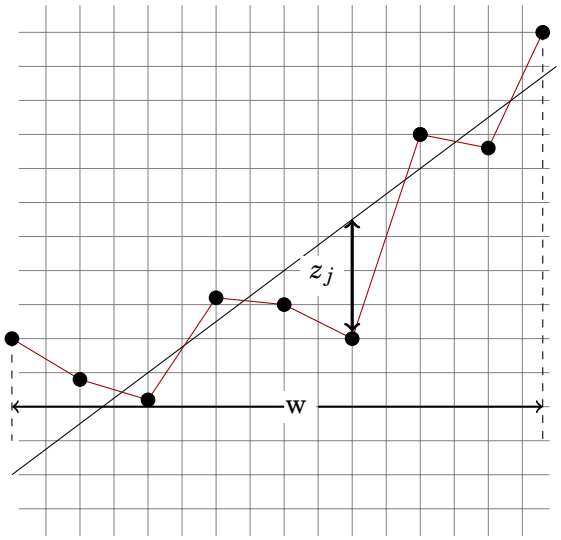

Figure 1.5: Adapted from Fig. 2 in [1].

1.2.4.4 Rescaled-range method

The rescaled-range method was originally developed by Hurst [25] to calculate how large reservoirs in Egypt needed to be in order to store an adequate amount of water. Since then, it has found many uses in engineering and finance. The R/S (rescale-range) method for a discrete time

series X_t is defined as [26]

$$R/S(\tau) = \frac{R(\tau)}{S(\tau)}, \tag{1.12}$$

where $R(\tau)$ is a measure of average deviation,

$$R(\tau) = \max_{0\le t\le \tau-1} Y(t,\tau) - \min_{0\le t\le \tau-1} Y(t,\tau). \tag{1.13}$$

Here, τ is the range and $Y(t,\tau)$ is defined such that

$$Y(t,\tau) = \sum_{i=0}^{t-1} \left| X_i - \langle X \rangle_\tau \right|, \tag{1.14}$$

where $\langle X \rangle_\tau$ is the mean of the time series, while $S(\tau)$ is the time averaged standard deviation,

$$S(\tau) = \sqrt{\left(\frac{1}{\tau} \sum_{t=0}^{\tau-1} (X_t - \langle X \rangle_\tau)^2 \right)}. \tag{1.15}$$

It follows that

$$\frac{R}{S} \propto \tau^H \tag{1.16}$$

and hence the Hurst exponent $H = \frac{\ln\left(\frac{R}{S}\right)}{\ln(\tau)}$ and the estimated D can be determined once again from $D = 2 - H$.

1.2.5 Truncation of the Weierstrass function

The formal Weierstrass function involves a summation over an infinite number of terms, but this object naturally cannot be calculated computationally. Therefore one must instead look for a summation over a large, but finite, number of terms N. An important task is hence to calculate exactly how large N is allowed to be. In order to do this, one must use a method of estimating the dimension of a given data-set, such as the the aforementioned truncated-Weierstrass function,

$$W(t) \equiv \lim_{N\to\infty} w_N(t), \tag{1.17}$$

where

$$w_N(t) = \sum_{\nu=0}^{N} \frac{1}{\gamma^{(2-D_0)\nu}} \cos\left(\frac{2\pi}{\Lambda} \gamma^\nu t + \phi_\nu \right). \tag{1.18}$$

What, too, must be considered is the growth of computation time with N. It is therefore necessary to find a compromise between the two. Another important aspect is to decide on which estimation method to use (as shown in Section 1.2.4) – all have pros and cons. After experimenting with different N values, it was found that $N = 7$ provided a reasonably faithful representation of $W(t)$ for moderate D_0 values (i.e., D_0 not close to 2). For $\gamma = 3$, selecting $N = 7$ is equivalent to retaining

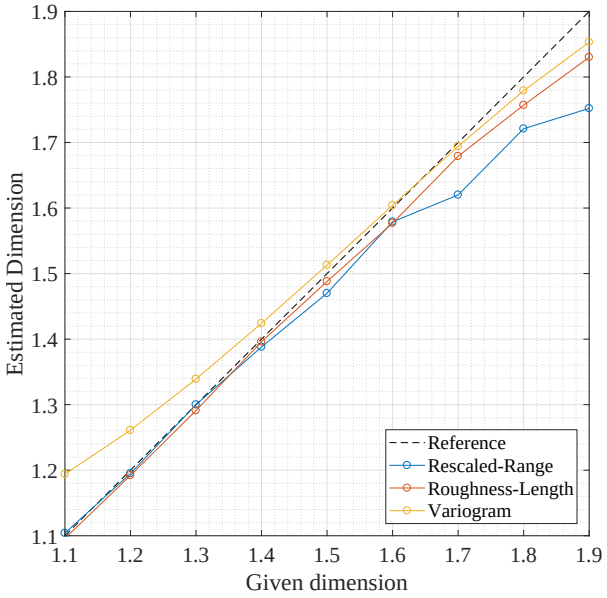

Figure 1.6: Estimated D_0 values for given dimensions of $D_0 = 1.1$ to 1.9 for multiple dimension estimation methods.

just over two decimal orders of scale in $W(t)$. For $D_0 \to 2$, one requires much larger N values to reproduce $W(t)$ with any degree of reliability. However, a numerical grid with $\Delta x = \frac{\lambda}{32}$ (i.e., spatial resolution sufficiently sampling the smallest scale-length $\Lambda_{min} \equiv \frac{\Lambda}{\gamma^N}$) requires extensibility large array sizes to capture $W(t)$ even just across the range $\frac{\Lambda}{2} \leq x \leq \frac{\Lambda}{2}$. As shown in Fig. 1.6 both the rescaled-range and roughness-length methods tend to give good approximations for lower D_0 values but which start to falter at $D_0 = 1.6$ where all three methods begin to underestimate the given dimension. That is expected – if they were exact they would not be estimation methods! The variogram does give a better evaluation for higher D_0 values, however this is paired with the fact that it overestimates the dimension for lower D_0 values. The limitations of the power-spectrum method will be discussed within the context of the diffractive-optics problem at hand in Section 3.4. Hence, roughness-length is the method of choice for all the data analysed in this thesis. An important point is that the numerical data considered during this testing phase of the different methods are more complex than the wave-scattering data that will be analysed later on (which has no sub-wavelength structure) and therefore it is likely that all methods would give better estimations of the diffracted waveforms.

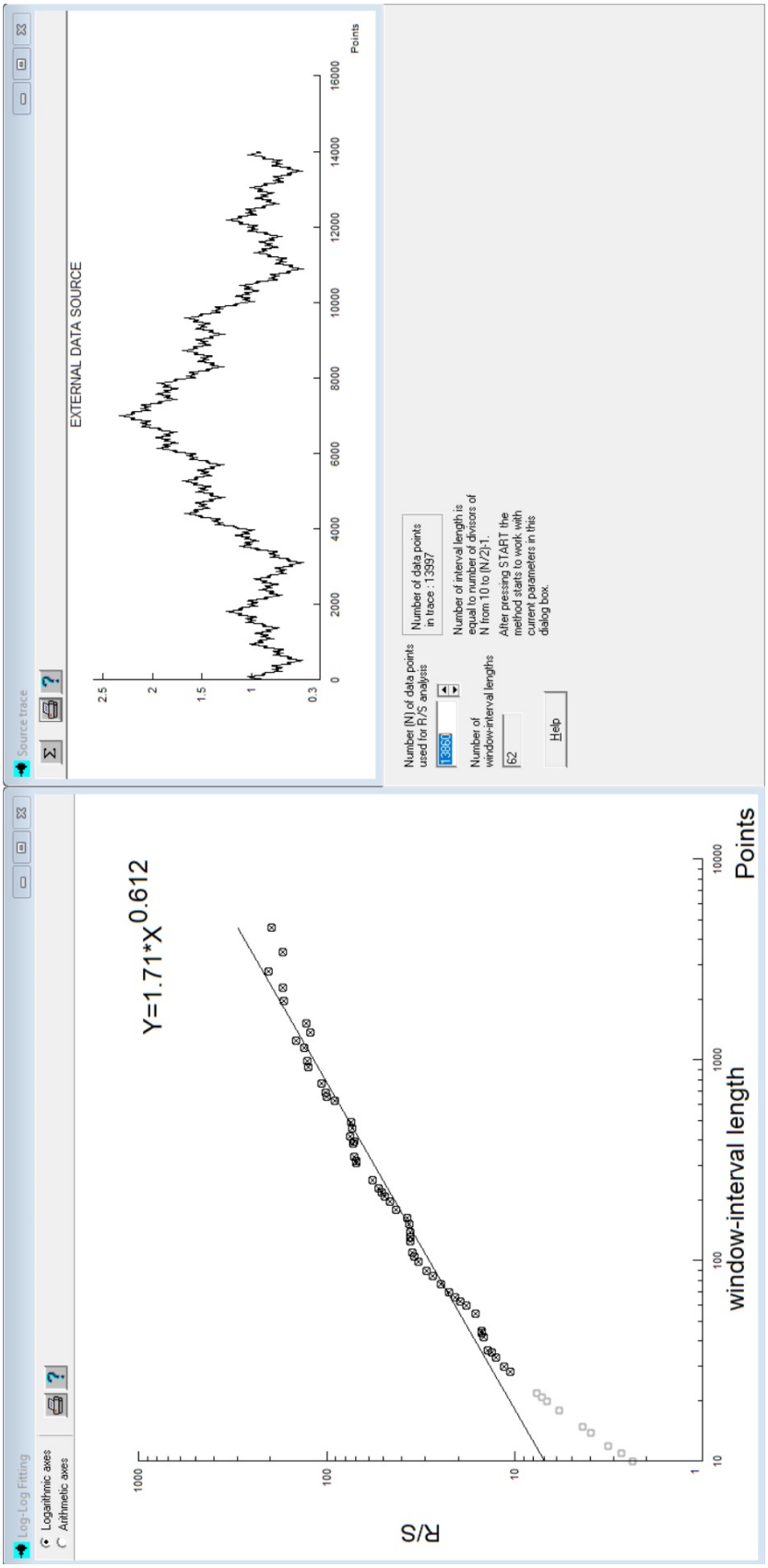

Figure 1.7: An example of the dimension estimation via the Rescaled-range method for a Weierstrass function truncated to $N = 7$ with $D_0 = 1.5$. The data is manually cut-off to exclude all data with a window-length lower than the spatial resolution ($\Delta x = \frac{\Lambda_{min}}{32}$ where $\Lambda_{min} = \frac{\Lambda}{\gamma^N}$)

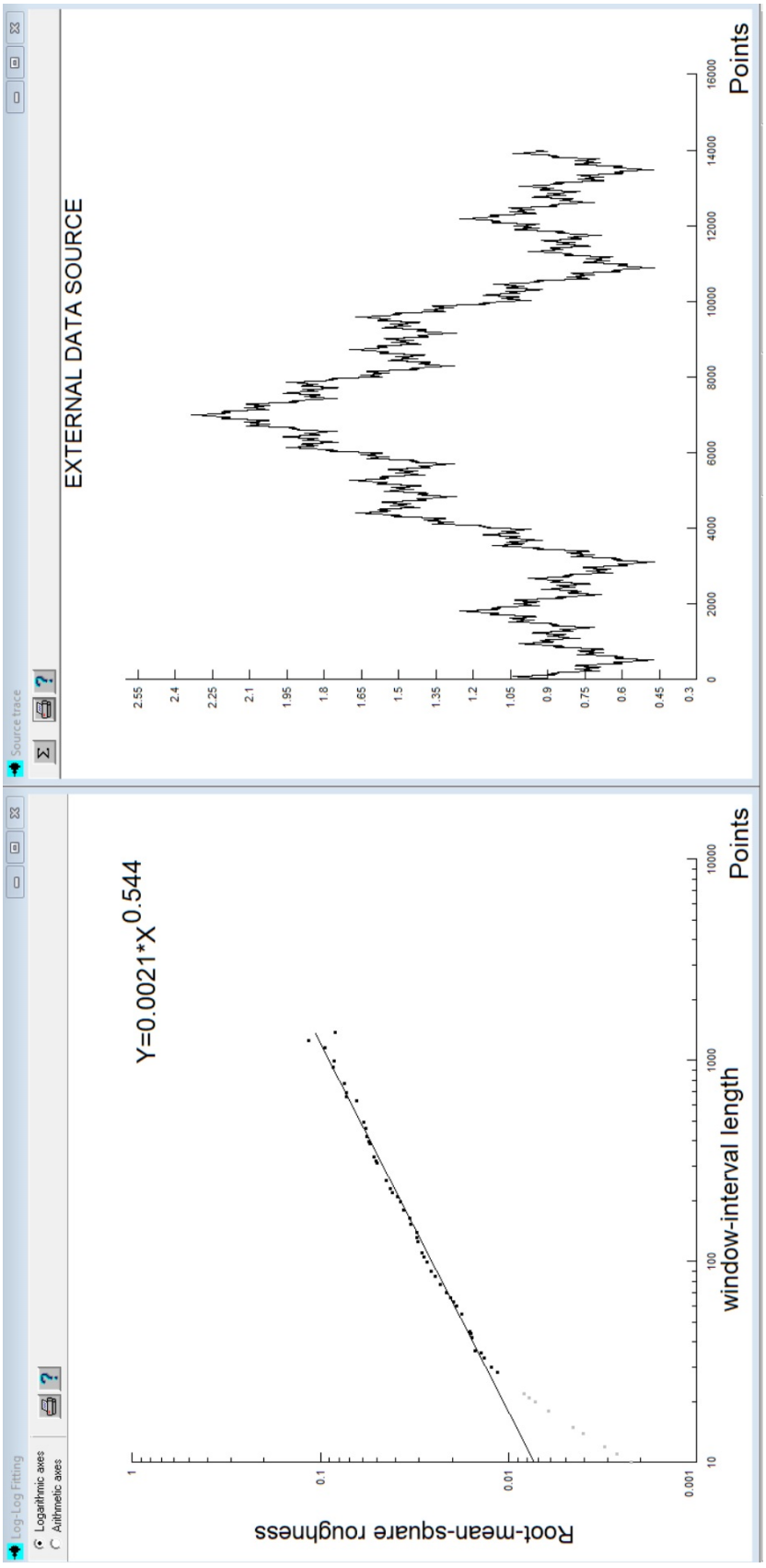

Figure 1.8: An example of the dimension estimation via the Roughness-length method for a Weierstrass function truncated to $N = 7$ with $D_0 = 1.5$. The data is manually cut-off to exclude all data with a window-length lower than the spatial resolution ($\Delta x = \frac{\Lambda_{min}}{32}$ where $\Lambda_{min} = \frac{\Lambda}{\gamma^N}$)

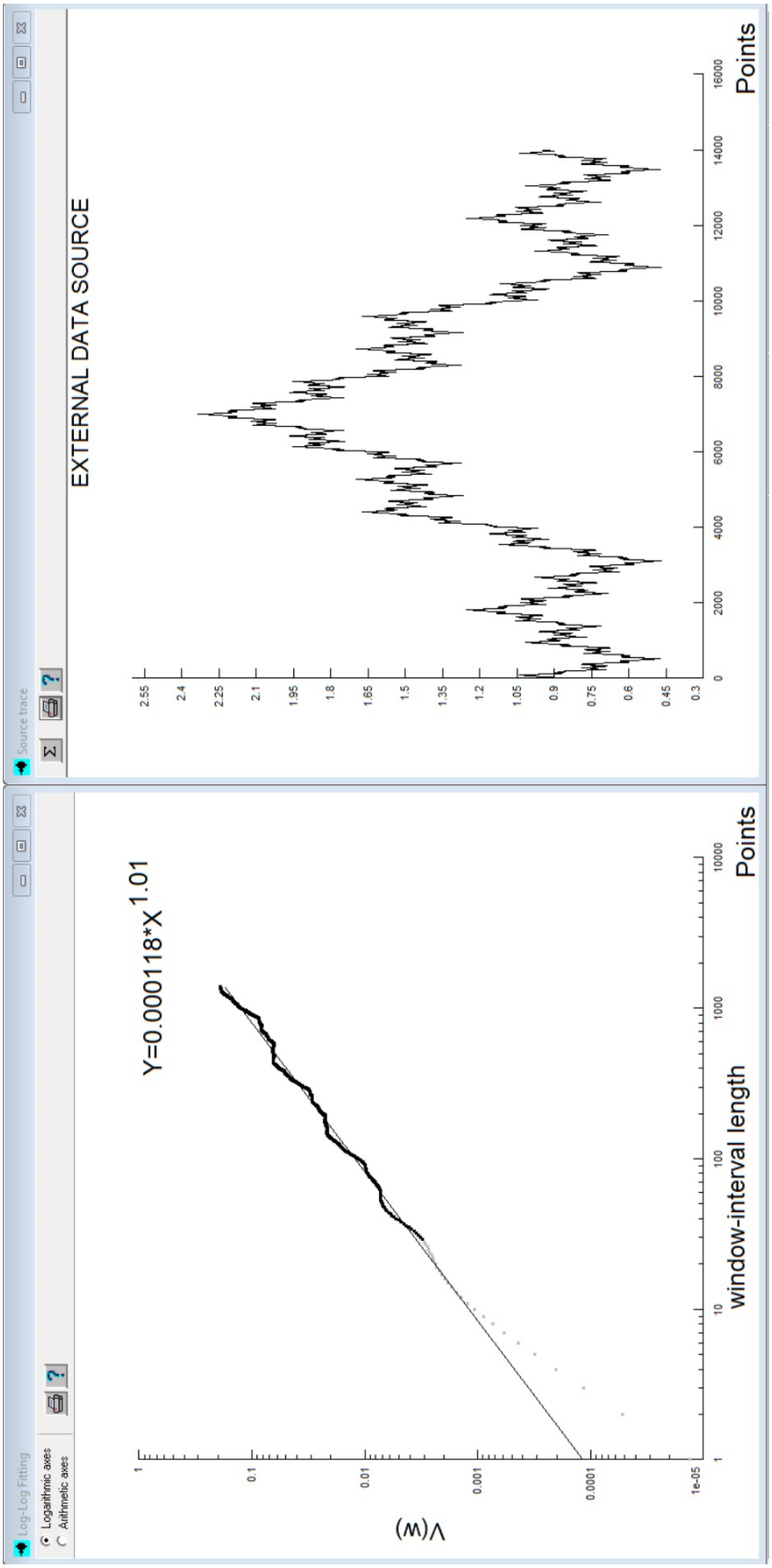

Figure 1.9: An example of the dimension estimation via the Variogram method for a Weierstrass function truncated to $N = 7$ with $D_0 = 1.5$. The data is manually cut-off to exclude all data with a window-length lower than the spatial resolution ($\Delta x = \frac{\Lambda_{min}}{32}$ where $\Lambda_{min} = \frac{\Lambda}{\gamma^N}$)

1.3 Electromagnetics background

Electromagnetism is governed by Maxwell's equations [27]. In free space, Maxwell's equations are as follows, firstly with Faraday's law,

$$\nabla \times \mathscr{E} = -\frac{\partial \mathscr{B}}{\partial t}, \tag{1.19}$$

the Maxwell-Ampére equation,

$$\nabla \times \mathscr{B} = \mu_0 \epsilon_0 \frac{\partial \mathscr{E}}{\partial t}, \tag{1.20}$$

Gauss's law,

$$\nabla \cdot \mathscr{E} = 0, \tag{1.21}$$

and Gauss's magnetic law,

$$\nabla \cdot \mathscr{B} = 0, \tag{1.22}$$

where $\mathscr{E}$ and $\mathscr{B}$ are the electric field and magnetic flux density, respectively, ϵ_0 is the permittivity of free space and μ_0 is the permeability of free space. The constitutive relations are

$$\mathscr{D} = \epsilon_0 \mathscr{E}, \tag{1.23}$$

and

$$\mathscr{B} = \mu_0 \mathscr{H}, \tag{1.24}$$

where $\mathscr{D}$ is the displacement electric field and $\mathscr{H}$ is the magnetic field. Each quantity can be broken down into continuous-wave (cw) structure such as

$$\mathscr{E}(\mathbf{x}, t) = \mathbf{E}(\mathbf{x}) \exp(-i\omega t) + \mathbf{E}^*(\mathbf{x}) \exp(i\omega t), \tag{1.25}$$

where $\mathbf{x}$ denotes space, $*$ is the complex conjugate, t the time, and ω the temporal frequency. Combining Eqs. (1.20) and (1.25) one arrives at

$$\mathbf{B}(\mathbf{x}) = \frac{1}{i\omega} \nabla \times \mathbf{E}(\mathbf{x}), \tag{1.26}$$

where components in Cartesian coordinates are

$$\mathbf{B}(\mathbf{x}) = \frac{1}{i\omega} \left\{ \left(\frac{\partial}{\partial y} E_z - \frac{\partial}{\partial z} E_y \right) \hat{\mathbf{e}}_x + \left(\frac{\partial}{\partial z} E_x - \frac{\partial}{\partial x} E_z \right) \hat{\mathbf{e}}_y + \left(\frac{\partial}{\partial x} E_y - \frac{\partial}{\partial y} E_x \right) \hat{\mathbf{e}}_z \right\}, \tag{1.27}$$

and for cylindrical polar coordinates,

$$\mathbf{B}(\mathbf{x}) = \frac{1}{i\omega} \left\{ \left(\frac{1}{r} \frac{\partial}{\partial \phi} E_z - \frac{\partial}{\partial z} E_\phi \right) \hat{\mathbf{e}}_r + \left(\frac{\partial}{\partial z} E_r - \frac{\partial}{\partial r} E_z \right) \hat{\mathbf{e}}_\phi + \frac{1}{r} \left(\frac{\partial}{\partial r} (r E_\phi) - \frac{\partial}{\partial \phi} E_r \right) \hat{\mathbf{e}}_z \right\}. \tag{1.28}$$

On the other hand, $\mathbf{B}(\mathbf{x})$ is given by

$$\mathbf{E}(\mathbf{x}) = \frac{c^2}{i\omega}\nabla \times \mathbf{B}(\mathbf{x}) \tag{1.29}$$

so that the individual components of $\mathbf{E}$ in Cartesian coordinates are,

$$\mathbf{E}(\mathbf{x}) = \frac{c^2}{i\omega}\left\{\left(\frac{\partial}{\partial y}B_z - \frac{\partial}{\partial z}B_y\right)\hat{\mathbf{e}}_x + \left(\frac{\partial}{\partial z}B_x - \frac{\partial}{\partial x}B_z\right)\hat{\mathbf{e}}_y + \left(\frac{\partial}{\partial x}B_y - \frac{\partial}{\partial y}B_x\right)\hat{\mathbf{e}}_z\right\}, \tag{1.30}$$

and in cylindrical polar coordinates,

$$\mathbf{E}(\mathbf{x}) = \frac{c^2}{i\omega}\left\{\left(\frac{1}{r}\frac{\partial}{\partial \phi}B_z - \frac{\partial}{\partial z}B_\phi\right)\hat{\mathbf{e}}_r + \left(\frac{\partial}{\partial z}B_r - \frac{\partial}{\partial r}B_z\right)\hat{\mathbf{e}}_\phi + \left(\frac{\partial}{\partial r}(rB_\phi) - \frac{\partial}{\partial \phi}B_r\right)\hat{\mathbf{e}}_z\right\}. \tag{1.31}$$

The Poynting vector, $\mathscr{S}(\mathbf{x},t)$, is defined as [28]

$$\mathscr{S}(\mathbf{x},t) = c^2\epsilon_0\mathscr{E}(\mathbf{x},t)\times\mathscr{B}(\mathbf{x},t), \tag{1.32}$$

so that for a configuration where the electric field is linearly-polarized along the z direction, (i.e. the TE solution),

$$\mathscr{S}(\mathbf{x},t) = c^2\epsilon_0\big[-\hat{\mathbf{e}}_x\mathscr{E}_z(\mathbf{x},t)\mathscr{B}_y(\mathbf{x},t) + \hat{\mathbf{e}}_y\mathscr{E}_z(\mathbf{x},t)\mathscr{B}_x(\mathbf{x},t)\big]. \tag{1.33}$$

The intensity of the diffracted field can be obtained from the time-average of the Poynting vector. A large part of this thesis is considering how light diffracting from a simple 1D aperture (e.g., see Fig 1.10) can be calculated via the the 1D Rayleigh-Sommerfeld (RS) integral [28],

$$E_z(x,y) = i\frac{ky}{2}\int_{-\infty}^{\infty} dx' E_z(x',0)\frac{H_1^{(1)}(kR)}{R}, \tag{1.34}$$

where $R \equiv \sqrt{(x-x')^2+y^2}$ and $E_z(x',0)$ is the known field across the aperture. The axes x and y are aligned in the manner given in Fig. 1.10, so that x and y are coordinates transverse and longitudinal to the aperture, respectively, and $H_1^{(1)}(kR)$ is the Hankel function of the first kind [29]. The RS formation is only valid in the forward half-plane (i.e. $y > 0$). A full derivation of Eq. (1.34) can be found in Appendix A.

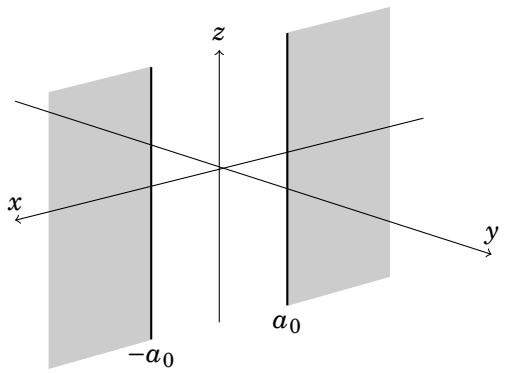

Figure 1.10: The typical set-up for a single slit experiment, where the slit is at $y = 0$ and $x = -a_0 \to a_0$ and extends from $-\infty \to \infty$ in z.

A 2D analogue of Eq. (1.34) is the 2DRS equation, which is used to calculate the approximate field diffracted from a closed aperture in the (x,z) plane,

$$E_z(x,y,z) = \frac{-1}{2\pi}\int_{-\infty}^{\infty}\int_{-\infty}^{\infty} dx'dz' E_z(x,'z',0)\frac{\partial}{\partial y}\frac{\exp(ikR)}{R}, \tag{1.35}$$

where $R \equiv \sqrt{(x-x')^2+(z-z')^2+y^2}$.

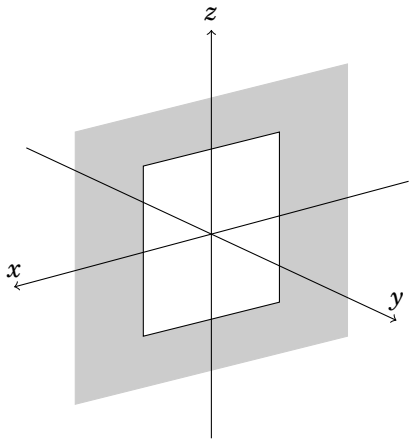

Figure 1.11: A 2D aperture at $y = 0$.

1.3.1 The paraxial limit of the Rayleigh-Sommerfeld integral

Paraxial methods are ubiquitous in physics. Assuming that the argument of the Hankel function, $kR \gg \mathcal{O}(1)$, the $H_1^{(1)}(kR)$ can be approximated by [30]

$$H_1^{(1)}(kR) \approx \sqrt{\frac{2}{\pi kr}}\left[P(1,kR)+iQ(1,kR)\right]\exp(i\chi), \tag{1.36}$$

where $\chi = kR - \frac{3\pi}{4}$. Then, assuming the small angle approximation [i.e. that $\frac{|x-x'|}{y} \ll \mathcal{O}(1)$] one can then consider how R behaves:

$$R \approx y\left[1+\frac{1}{2}\frac{(x-x')^2}{y^2}-\frac{1}{8}\frac{(x-x')^4}{y^4}\right]. \tag{1.37}$$

Substituting Eq. (1.37) back into Eq. (1.34),

$$\begin{aligned} E_z(x,y) = \exp\left(\frac{-i\pi}{4}\right)\exp(iky)\frac{y}{2}\sqrt{\frac{2k}{\pi}}\int_{-\infty}^{\infty} dx' E_z(x',0)\frac{1}{R^{\frac{3}{2}}}\left[P(1,kR)+iQ(1,kR)\right] \\ \exp\left[\frac{ik}{2}\frac{(x-x')^2}{y}-\frac{ik}{8}\frac{(x-x')^4}{y^3}\right]. \end{aligned} \tag{1.38}$$

Assuming that the contribution in Eq. (1.38) from $\frac{k}{8}\frac{(x-x')^4}{y^3}$ is much less than the contribution from $\frac{k}{2}\frac{(x-x')^2}{y}$, it can be determined that the distance y downstream from the aperture plane must satisfy $y \gg L_{char}$, where

$$L_{char} \equiv \left(\frac{kb^4}{8}\right)^{\frac{1}{3}} \tag{1.39}$$

and b is the largest length-scale associated with the aperture (i.e. the width). Returning back to Eq. (1.38) one can rearrange so that

(1.40)
$$E_z(x,y) \approx \exp\Big(\frac{-i\pi}{4}\Big)\frac{ky}{2}\sqrt{\frac{2}{\pi}}\frac{\exp(iky)}{k^{\frac{1}{2}}}\int_{-\infty}^{\infty} dx' E_z(x',0)\frac{1}{R^{\frac{3}{2}}}\Big[P(1,kR)+iQ(1,kR)\Big]\exp\Big[i\frac{k(x-x')^2}{2y}\Big]$$

where the $\exp\Big[\frac{ik(x-x')^2}{2y}\Big]$ is the Fresnel factor for a 1D aperture. The $R^{-\frac{3}{2}}$ factor is approximated by

$$\frac{1}{R^{\frac{3}{2}}} \approx \frac{1}{y^{\frac{3}{2}}}\Big[1-\frac{3}{4}\frac{(x-x')^2}{y^2}\Big]. \tag{1.41}$$

The $\frac{3}{4}\frac{(x-x')^2}{y^2}$ component is assumed to be negligible and hence

$$E_z \approx \frac{1+i}{2i}\sqrt{\frac{k}{\pi y}}\exp(iky)\int_{-\infty}^{\infty} dx' E_z(x',0)[P(1,kR)+iQ(1,kR)]\exp\Big[i\frac{k(x-x')^2}{2y}\Big]. \tag{1.42}$$

Hankel's asymptotic expansions, $P(1,kR)$ and $Q(1,kR)$, are

$$P(1,kR) = \sum_{j=0}^{\infty}(-)^j\frac{(1,2j)}{(2kR)^{2j}} = 1+\frac{15}{2!(8kR)^2}-\frac{14175}{4!(8kR)^4}-\cdots, \tag{1.43}$$

and

$$Q(1,kR) = \sum_{j=0}^{\infty}(-)^j\frac{(1,2j+1)}{(2kR)^{2j+1}} = \frac{3}{8kR}-\frac{315}{3!(8kR)^3}+\cdots, \tag{1.44}$$

respectively [30]. For our assumption of $kR \gg \mathcal{O}(1)$, $P(1,kR) \approx 1+\mathcal{O}(kR)^{-2}$ and $Q(1,kR) \approx \mathcal{O}(kR)^{-1}$. Substituting these back into Eq. (1.42) one ends up with,

$$E_z(x,y) \approx \frac{1+i}{2i}\sqrt{\frac{k}{\pi y}}\exp(iky)\int_{-\infty}^{\infty} dx' E_z(x',0)\exp\Big[\frac{ik(x-x')^2}{2y}\Big]. \tag{1.45}$$

Referring to the Helmholtz equation [Eq. (B.1) from the full 1DRS derivation in App. B], then using a substitution of $E_z(x,y) = u(x,y)\exp(iky)$, one finds an equation for u:

$$\frac{\partial^2 u}{\partial y^2}+i2k\frac{\partial u}{\partial y}+\frac{\partial^2 u}{\partial x^2} = 0. \tag{1.46}$$

Assuming the slowly-varying envelope approximation (SVEA),

$$\Big|\frac{\partial^2 u}{\partial y^2}\Big| \ll \Big|2k\frac{\partial u}{\partial y}\Big|, \tag{1.47}$$

Eq. (1.46) then becomes the paraxial diffraction equation,

$$2ik\frac{\partial u}{\partial y}+\frac{\partial^2 u}{\partial x^2} = 0. \tag{1.48}$$

The Fresnel integral is an exact solution to Eq. (1.48) for one transverse dimension,

$$u(x,y) \equiv \frac{1+i}{2i}\sqrt{\frac{k}{\pi y}}\int_{-\infty}^{\infty} dx' E_z(x',0)\exp\Big[\frac{ik(x-x')^2}{2y}\Big]. \tag{1.49}$$

Paraxial methods are valid, assuming normal incidence, small angle approximation, scalar approximation and diffraction in the forward half-plane only. Equation (1.49) is widely used in the optics community for a broad range of areas including diffraction of plane waves by fractal objects. Examples of this include Berry's paper on the Talbot effect [31], and the study of plane wave diffraction from fractal phase screens [32]. A measure of the relative error between the RS and Fresnel diffraction patterns can be seen in Fig. 1.12. While the amplitude of each pattern tends to zero as $y \to \infty$, their difference becomes negligible since the Fresnel result must always emerge asymptotically from the RS prediction.

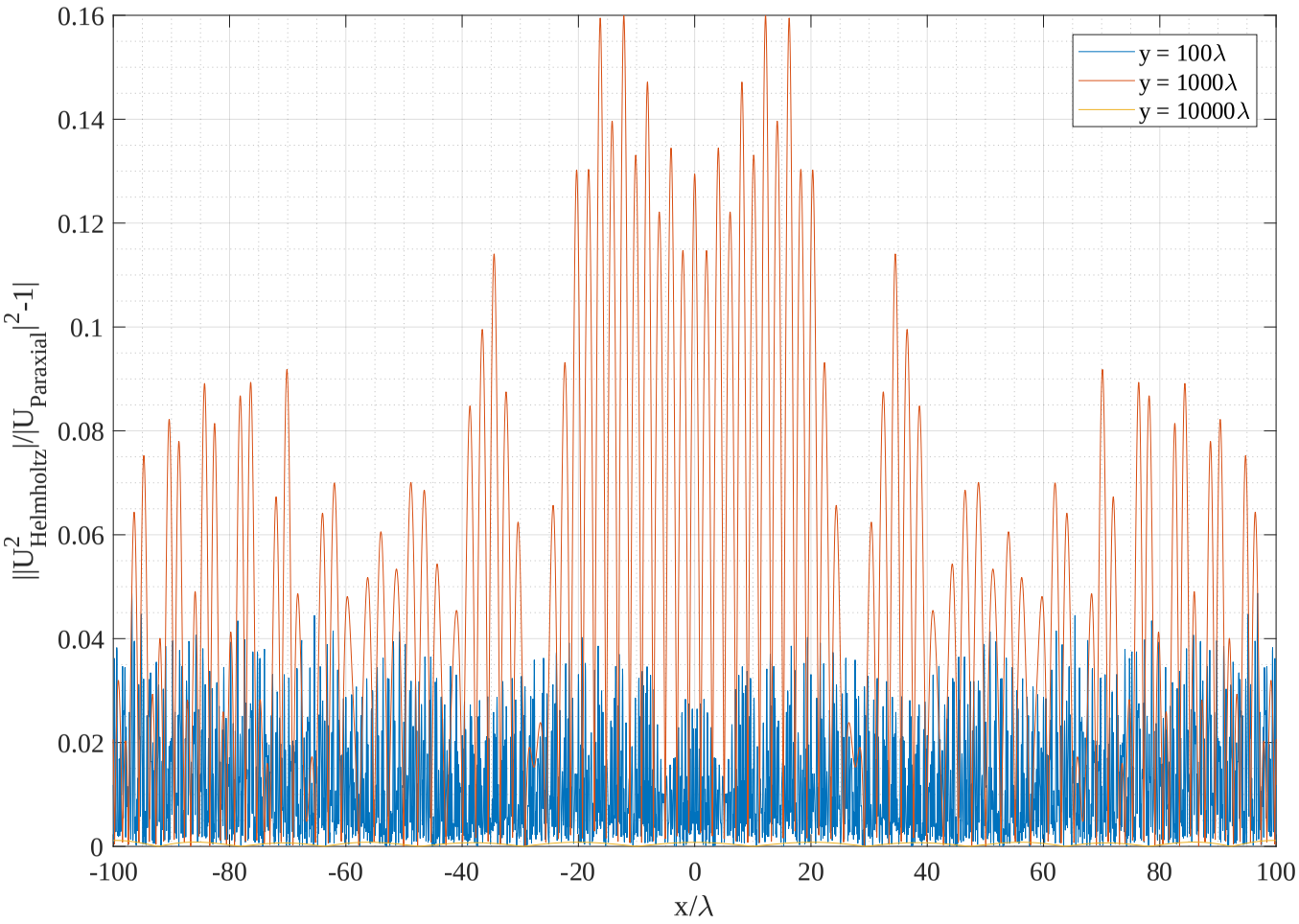

Figure 1.12: A comparison of the difference between the intensity, $\left|\frac{E_z}{E_0}\right|^2$ calculated by the RS and paraxial equations for $y = 100\lambda, 1000\lambda$ and 10000λ for plane wave diffraction at a single slit. The slit half-width is 250λ and $L_{char} = 1079\lambda$. One can see as y gets larger, the difference between the two gets smaller. Indeed, for $y = 10000\lambda$ the difference is negligible (and almost indiscernible on the graph).

CHAPTER 2

THE SOMMERFELD PROBLEM

The Sommerfeld problem is one that has been around for many years. Its premise is simple to understand – calculate the electromagnetic field diffracted from an infinitely-thin, perfectly-conducting screen. It is named as such due to the first full mathematical derivation by Sommerfeld in 1896 [33]. Numerous techniques have been used to derive the results when the electric field is linearly-polarized in an orientation parallel to the edge of the screen (the TE solution) or when the magnetic field is linearly-polarized parallel to the edge of the screen (the TM solution) [34]. In the TE solution $\mathbf{E} = (0, 0, E_z)$ and $\mathbf{B} = (B_x, B_y, 0)$, where B_x is the dominant component in $\mathbf{B}$ whereas in the TM solution $\mathbf{B} = (0, 0, B_z)$ and $\mathbf{E} = (E_x, E_y, 0)$, where E_x is the dominant component in $\mathbf{E}$. A full derivation of the TE result is given in Appendix B.

2.1 Half-plane diffraction of a plane wave

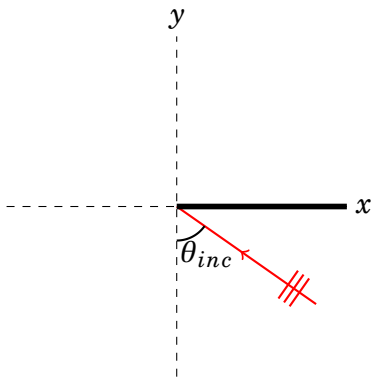

Figure 2.1: A single plane-wave, at an incidence angle of θ_{inc}, diffracting from a semi-infinite screen.

In the TE solution, the total transverse electric field, E_z, is a linear superposition of the input wave, $E_0 \exp(i\mathbf{k_{inc}}\cdot\mathbf{x})$, and the scattered field, Ψ_{TE}, i.e.,

$$\frac{E_z}{E_0} = \exp(i\mathbf{k_{inc}}\cdot\mathbf{x}) + \frac{\Psi_{TE}}{E_0}, \tag{2.1}$$

where,

$$\begin{aligned}\Psi_{TE} = &-E_0\frac{1+i}{2i}\Big[\exp(i\mathbf{k_{inc}}\cdot\mathbf{x})F(\chi_-) - \exp i(\mathbf{k_{ref}}\cdot\mathbf{x})F(\chi_+)\Big]\\ &-\frac{E_0}{2}\Big[\exp(i\mathbf{k_{inc}}\cdot\mathbf{x}) + \exp(i\mathbf{k_{ref}}\cdot\mathbf{x})\Big],\end{aligned} \tag{2.2}$$

and $F(\alpha) = \int_0^\alpha ds \exp\left(i\frac{\pi}{2}s^2\right)$, $\chi_\pm = \left(\frac{2kr}{\pi}\right)^{\frac{1}{2}}\left[\cos\left(\frac{\phi\pm\theta_{inc}}{2}\right) \pm \sin\left(\frac{\phi\pm\theta_{inc}}{2}\right)\right]$, $\mathbf{k_{inc}}\cdot\mathbf{x} = -\frac{2\pi}{\lambda}[\sin(\theta_{inc})x - \cos(\theta_{inc})y]$, and $\mathbf{k_{ref}}\cdot\mathbf{x} = -\frac{2\pi}{\lambda}[\sin(\theta_{inc})x + \cos(\theta_{inc})y]$. Equation (2.1) is physically equivalent to that given by Durgin [35]. The two solutions are connected by complex conjugation and where the angle of incidence has been redefined (compare Fig. 2.1 to Fig. 1 in [35]). The Fresnel integral has also been rescaled (to bring it in-line with the more traditional representation [30]) and its limits manipulated to remove the infinite domain of integration. The polar components of the magnetic flux density are then [see Eq. (1.28)],

$$\begin{aligned}\frac{B_r}{B_0} = &\cos(\phi-\theta_{inc})\exp(i\mathbf{k_{inc}}\cdot\mathbf{x}) - \frac{1+i}{\sqrt{\pi kr}}\exp(ikr)\cos\left(\frac{\phi}{2}\right)\cos\left(\frac{\theta_{inc}}{2}+\frac{\pi}{4}\right)\\ &-\frac{1+i}{2i}\Big[\cos(\phi-\theta_{inc})\exp(i\mathbf{k_{inc}}\cdot\mathbf{x})F(\chi_-) + \cos(\phi+\theta_{inc})\exp(i\mathbf{k_{ref}}\cdot\mathbf{x})F(\chi_+)\Big]\\ &-\frac{1}{2}\Big[\cos(\phi-\theta_{inc})\exp(i\mathbf{k_{inc}}\cdot\mathbf{x}) - \cos(\phi+\theta_{inc})\exp(i\mathbf{k_{ref}}\cdot\mathbf{x})\Big],\end{aligned} \tag{2.3}$$

and

$$\begin{aligned}\frac{B_\phi}{B_0} = &-\sin(\phi-\theta_{inc})\exp(i\mathbf{k_{inc}}\cdot\mathbf{x}) + \frac{1+i}{\sqrt{\pi kr}}\exp(ikr)\sin\left(\frac{\phi}{2}\right)\cos\left(\frac{\theta_{inc}}{2}+\frac{\pi}{4}\right)\\ &+\frac{1+i}{2i}\Big[\sin(\phi-\theta_{inc})\exp(i\mathbf{k_{inc}}\cdot\mathbf{x})F(\chi_-) + \sin(\phi+\theta_{inc})\exp(i\mathbf{k_{ref}}\cdot\mathbf{x})F(\chi_+)\Big]\\ &+\frac{1}{2}\Big[\sin(\phi-\theta_{inc})\exp(i\mathbf{k_{inc}}\cdot\mathbf{x}) - \sin(\phi+\theta_{inc})\exp(i\mathbf{k_{ref}}\cdot\mathbf{x})\Big].\end{aligned} \tag{2.4}$$

In the TM solution, the total transverse magnetic field, B_z, is (akin to its TE counterpart) a linear superposition of the input wave, $B_0\exp(i\mathbf{k_{inc}}\cdot\mathbf{x})$, and the scattered field, Ψ_{TM},

$$\frac{B_z}{B_0} = \exp(i\mathbf{k_{inc}}\cdot\mathbf{x}) + \frac{\Psi_{TM}}{B_0}, \tag{2.5}$$

where

$$\begin{aligned}\Psi_{TM} = &-B_0\frac{1+i}{2i}\Big[\exp(i\mathbf{k_{inc}}\cdot\mathbf{x})F(\chi_-) + \exp(i\mathbf{k_{ref}}\cdot\mathbf{x})F(\chi_+)\Big]\\ &-\frac{B_0}{2}\Big[\exp(i\mathbf{k_{inc}}\cdot\mathbf{x}) - \exp(i\mathbf{k_{ref}}\cdot\mathbf{x})\Big],\end{aligned} \tag{2.6}$$

and the polar components are [Eq. (1.31)],

$$\begin{aligned}\frac{E_r}{E_0} = & -\cos(\phi-\theta_{inc})\exp(i\mathbf{k_{inc}}\cdot\mathbf{x}) + \frac{1+i}{\sqrt{\pi kr}}\exp(ikr)\sin\Big(\frac{\phi}{2}\Big)\cos\Big(\frac{\theta_{inc}}{2}-\frac{\pi}{4}\Big) \\ & + \frac{1+i}{2i}\Big[\cos(\phi-\theta_{inc})\exp(i\mathbf{k_{inc}}\cdot\mathbf{x})F(\chi_-) - \cos(\phi+\theta_{inc})\exp(i\mathbf{k_{ref}}\cdot\mathbf{x})F(\chi_+)\Big] \\ & + \frac{1}{2}\Big[\cos(\phi-\theta_{inc})\exp(i\mathbf{k_{inc}}\cdot\mathbf{x}) + \cos(\phi+\theta_{inc})\exp(i\mathbf{k_{ref}}\cdot\mathbf{x})\Big],\end{aligned} \tag{2.7}$$

and

$$\begin{aligned}\frac{E_\phi}{E_0} = & \sin(\phi-\theta_{inc})\exp(i\mathbf{k_{inc}}\cdot\mathbf{x}) - \frac{1+i}{2i}\exp(ikr)\cos\Big(\frac{\phi}{2}\Big)\cos\Big(\frac{\theta_{inc}}{2}-\frac{\pi}{4}\Big) \\ & - \frac{1+i}{2i}\Big[\sin(\phi-\theta_{inc})\exp(i\mathbf{k_{inc}}\cdot\mathbf{x})F(\chi_-) - \sin(\phi+\theta_{inc})\exp(i\mathbf{k_{ref}}\cdot\mathbf{x})F(\chi_+)\Big] \\ & - \frac{1}{2}\Big[\sin(\phi-\theta_{inc})\exp(i\mathbf{k_{inc}}\cdot\mathbf{x}) + \sin(\phi+\theta_{inc})\exp(i\mathbf{k_{ref}}\cdot\mathbf{x})\Big].\end{aligned} \tag{2.8}$$

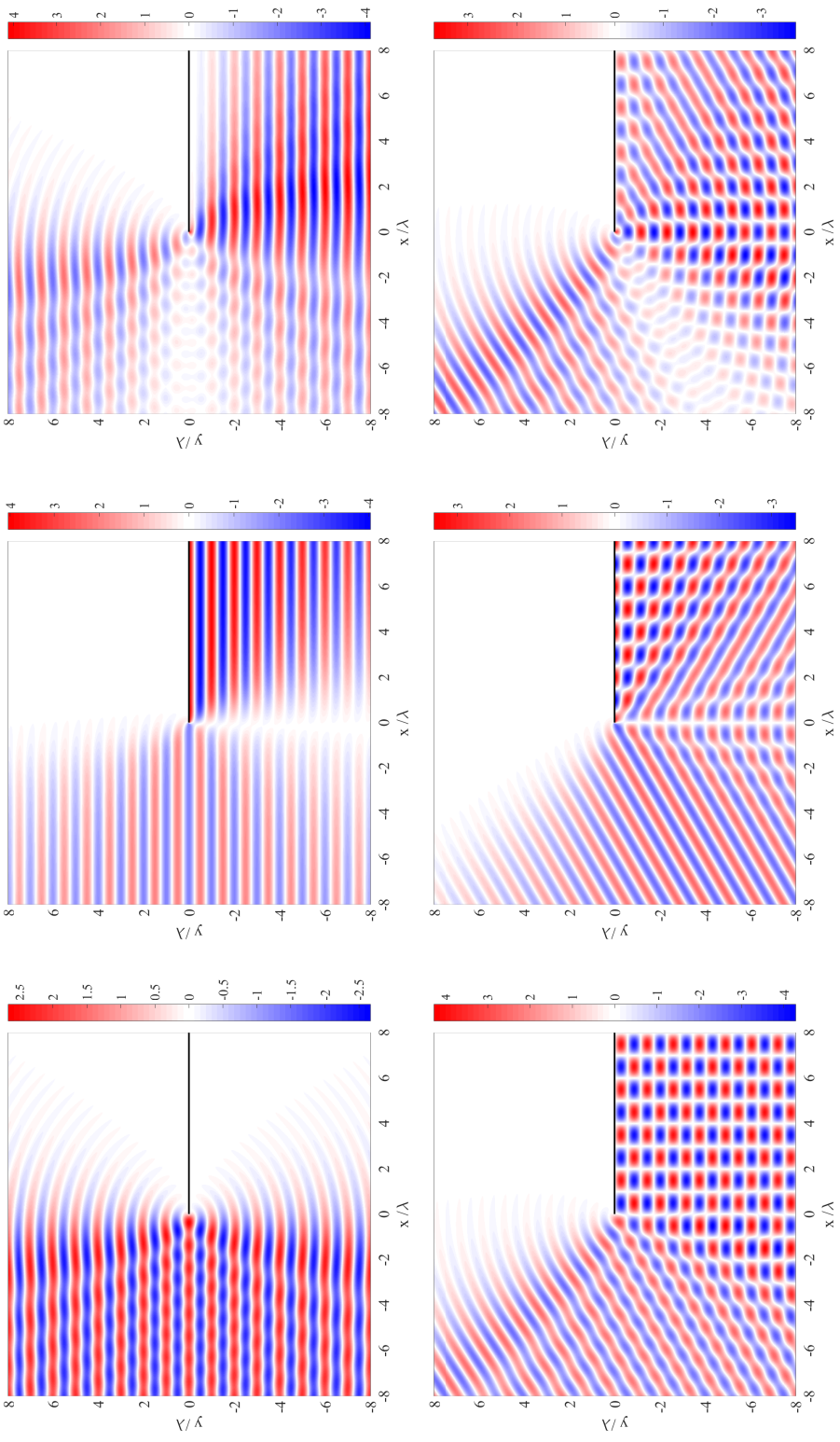

Figure 2.2: Plane-wave TE solution for $2\Re e\left(\frac{E_z}{E_0}\right)$ (left column), $2\Re e\left(\frac{B_r}{B_0}\right)$ (middle column) and $2\Re e\left(\frac{B_\phi}{B_0}\right)$ (right column). The top and bottom rows show the diffraction of a normally-incidence plane wave and a plane wave originating from 30°, respectively.

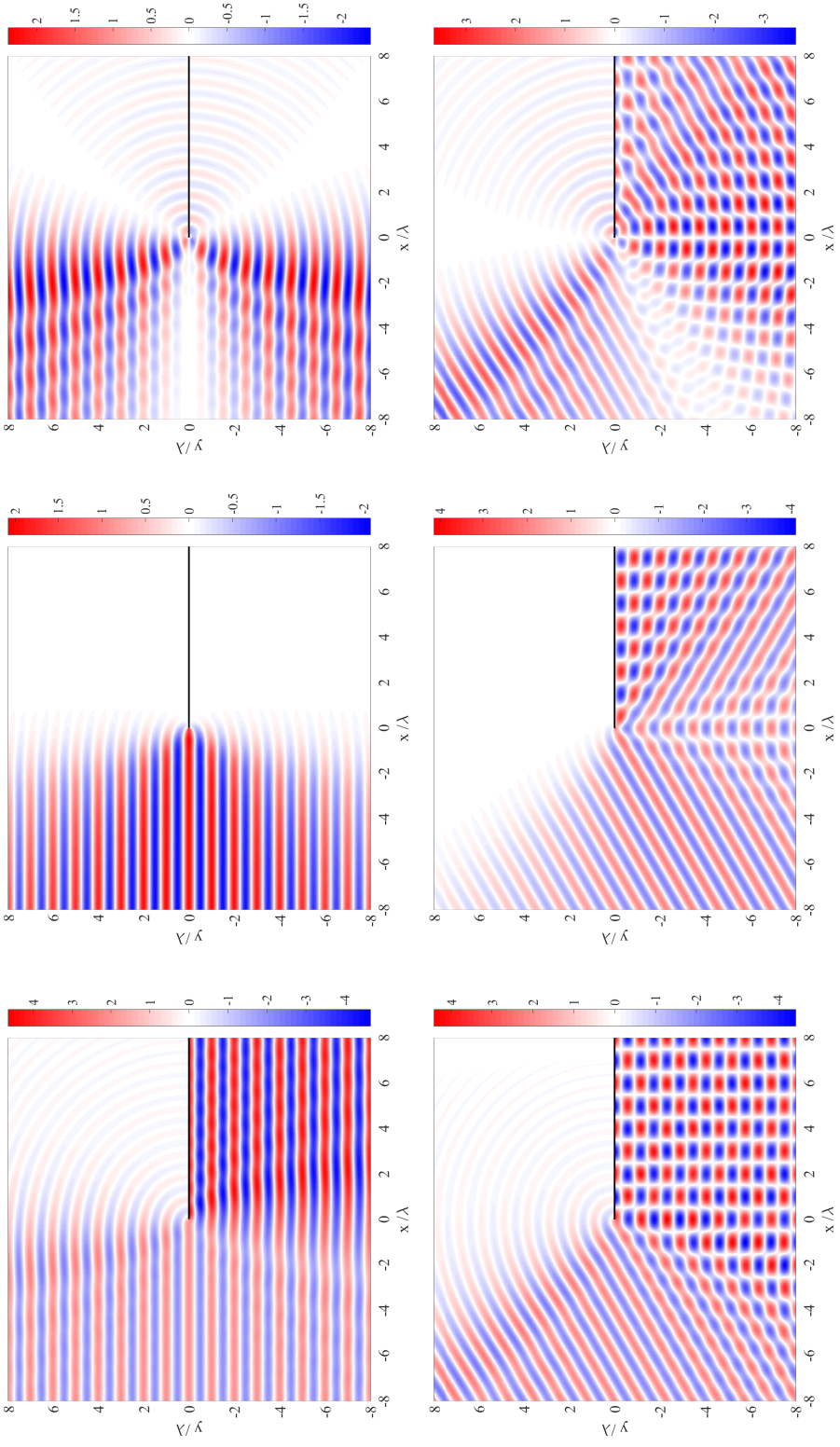

Figure 2.3: Plane-wave TM solution for $2\Re e\left(\frac{B_z}{B_0}\right)$ (left column), $2\Re e\left(\frac{E_r}{E_0}\right)$ (middle column) and $2\Re e\left(\frac{E_\phi}{E_0}\right)$ (right column). The top and bottom rows show the diffraction of a normally-incidence plane wave and a plane wave originating from 30°, respectively.

2.2 The Weierstrass-Lamb solutions

The Weierstrass function from Eq. (1.4) can be interpreted physically as the summation of a normal-incidence plane wave and pairs of plane waves at specific incident angles, $\pm\theta_\nu$, obtained from

$$\theta_\nu = \sin^{-1}\left(\frac{\lambda\gamma^\nu}{\Lambda}\right), \tag{2.9}$$

where $\nu = 0, 1, ...N$ and $N = \left\lfloor \frac{\log\left(\frac{\Lambda}{\lambda}\right)}{\log(\gamma)} \right\rfloor$ (i.e., the N that gives the largest possible non-complex angle, θ_N), and the angle for the complementary plane-wave is $-\theta_\nu$. The total input field is now taken to be

$$\frac{E_z}{E_0} = \exp(iky) + \frac{\epsilon}{2}\sum_{\nu=0}^{N}\frac{1}{\gamma^{(2-D_0)\nu}}\left\{\exp[i\mathbf{k}_{\mathbf{inc}}^{(\nu+)}\cdot\mathbf{x}] + \exp[i\mathbf{k}_{\mathbf{inc}}^{(\nu-)}\cdot\mathbf{x}]\right\}, \tag{2.10}$$

where $\mathbf{k}_{\mathbf{inc}}^{(\nu+)} = k[-\hat{\mathbf{e}}_x\sin(\theta_\nu) + \hat{\mathbf{e}}_y\cos(\theta_\nu)]$, $\mathbf{k}_{\mathbf{inc}}^{(\nu-)} = k[\hat{\mathbf{e}}_x\sin(\theta_\nu) + \hat{\mathbf{e}}_y\cos(\theta_\nu)]$ and ϵ determines the strength of the pre-fractal modulation. Values of Λ and γ can be determined so that $N = 7$, as previously mentioned in Subsection 1.2.5. Evaluating Eq. (2.10) at $y = 0$ (the plane of the edge) gives

$$\frac{E_{inc}}{E_0} = 1 + \epsilon\sum_{\nu=0}^{N}\frac{1}{\gamma^{(2-D_0)\nu}}\cos(K_\nu x), \tag{2.11}$$

where $K_\nu = k\sin\theta_\nu = \frac{2\pi}{\Lambda}\gamma^\nu$. In this way the incident wave at $y = 0$ can be mapped onto a bandwidth-limited Weierstrass function (c.f. Eq. (1.4)) [36]. Moreover, when $\gamma > 0$ is an integer, the incident wave itself is periodic in x (at all y) with period Λ.

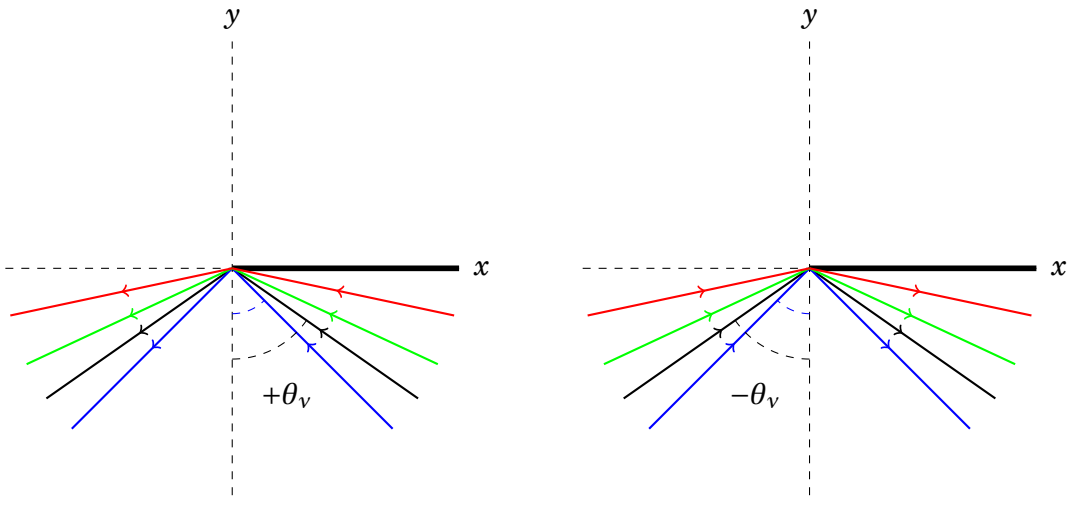

Figure 2.4: The linear superposition of pairs of plane-waves, each at the angles $\pm\theta_\nu$.

Firstly for the TE solution for the diffraction of a truncated-Weierstrass waveform (i.e., the

addition of a normally-incident plane wave plus the summation of oblique plane waves),

(2.12)
$$\begin{aligned}\frac{E_z}{E_0} &= \exp\left(i\frac{2\pi}{\lambda}y\right) - \cos\left(\frac{2\pi}{\lambda}y\right) - \frac{1+i}{2i}\left[\exp\left(i\frac{2\pi}{\lambda}y\right)F(\chi_-) - \exp\left(-i\frac{2\pi}{\lambda}y\right)F(\chi_+)\right] \\ &+ \frac{\epsilon}{2}\sum_{\nu=0}^{N}\frac{1}{\gamma^{(2-D_0)\nu}}\left\{\exp(i\mathbf{k}_{\mathbf{inc}}^{(\nu+)}\cdot\mathbf{x}) - \frac{1+i}{2i}\left[\exp(i\mathbf{k}_{\mathbf{inc}}^{(\nu+)}\cdot\mathbf{x})F(\chi_-^{(\nu+)}) - \exp(i\mathbf{k}_{\mathbf{ref}}^{(\nu+)}\cdot\mathbf{x})F(\chi_+^{(\nu+)})\right]\right. \\ &- \frac{1}{2}\left[\exp(i\mathbf{k}_{\mathbf{inc}}^{(\nu+)}\cdot\mathbf{x}) + \exp(i\mathbf{k}_{\mathbf{ref}}^{(\nu+)}\cdot\mathbf{x}) + \exp(i\mathbf{k}_{\mathbf{inc}}^{(\nu-)}\cdot\mathbf{x}) + \exp(i\mathbf{k}_{\mathbf{ref}}^{(\nu-)}\cdot\mathbf{x})\right] \\ &\left.+ \exp(i\mathbf{k}_{\mathbf{inc}}^{(\nu-)}\cdot\mathbf{x}) - \frac{1+i}{2i}\left[\exp(i\mathbf{k}_{\mathbf{inc}}^{(\nu-)}\cdot\mathbf{x})F(\chi_-^{(\nu-)}) - \exp(i\mathbf{k}_{\mathbf{ref}}^{(\nu-)}\cdot\mathbf{x})F(\chi_+^{(\nu-)})\right]\right\},\end{aligned}$$

where $\chi_\pm^{(\nu+)} = \left(\frac{2kr}{\pi}\right)^{\frac{1}{2}}\left[\cos\left(\frac{\phi\pm\theta_\nu}{2}\right) \pm \sin\left(\frac{\phi\pm\theta_\nu}{2}\right)\right]$, $\chi_\pm^{(\nu-)} = \left(\frac{2kr}{\pi}\right)^{\frac{1}{2}}\left[\cos\left(\frac{\phi\mp\theta_\nu}{2}\right) \pm \sin\left(\frac{\phi\mp\theta_\nu}{2}\right)\right]$, $\mathbf{k}_{\mathbf{inc}}^{(\nu\pm)}\cdot\mathbf{x} = -\frac{2\pi}{\lambda}[\sin(\pm\theta_\nu)x - \cos(\theta_\nu)y]$, $\mathbf{k}_{\mathbf{ref}}^{(\nu\pm)}\cdot\mathbf{x} = -\frac{2\pi}{\lambda}[\sin(\pm\theta_\nu)x + \cos(\theta_\nu)y]$ and $\epsilon = 1$. The magnetic components are

(2.13)
$$\begin{aligned}\frac{B_r}{B_0} &= \cos\phi\exp\left(i\frac{2\pi}{\lambda}y\right) - \frac{1+i}{\sqrt{2\pi kr}}\exp(ikr)\cos\left(\frac{\phi}{2}\right) - \frac{1}{2}\left[\cos\phi\exp\left(i\frac{2\pi}{\lambda}y\right) - \cos\phi\exp\left(-i\frac{2\pi}{\lambda}y\right)\right] \\ &- \frac{1+i}{2i}\left[\cos\phi\exp\left(i\frac{2\pi}{\lambda}y\right)F(\chi_-) + \cos\phi\exp\left(-i\frac{2\pi}{\lambda}y\right)F(\chi_+)\right] \\ &+ \frac{\epsilon}{2}\sum_{\nu=0}^{N}\frac{1}{\gamma^{(2-D_0)\nu}}\left\{\cos(\phi-\theta_\nu) - \frac{1+i}{\sqrt{\pi kr}}\exp(ikr)\cos\left(\frac{\phi}{2}\right)\cos\left(\frac{\theta_\nu}{2}+\frac{\pi}{4}\right)\right. \\ &- \frac{1+i}{2i}\left[\cos(\phi-\theta_\nu)\exp(i\mathbf{k}_{\mathbf{inc}}^{(\nu+)}\cdot\mathbf{x})F(\chi_-^{(\nu+)}) + \cos(\phi+\theta_\nu)\exp(i\mathbf{k}_{\mathbf{ref}}^{(\nu+)}\cdot\mathbf{x})F(\chi_+^{(\nu+)})\right] \\ &- \frac{1}{2}\left[\cos(\phi-\theta_\nu)\exp(i\mathbf{k}_{\mathbf{inc}}^{(\nu+)}\cdot\mathbf{x}) - \cos(\phi+\theta_\nu)\exp(i\mathbf{k}_{\mathbf{ref}}^{(\nu+)}\cdot\mathbf{x})\right] \\ &+ \cos(\phi+\theta_\nu) - \frac{1+i}{\sqrt{\pi kr}}\exp(ikr)\cos\left(\frac{\phi}{2}\right)\cos\left(-\frac{\theta_\nu}{2}+\frac{\pi}{4}\right) \\ &- \frac{1+i}{2i}\left[\cos(\phi+\theta_\nu)\exp(i\mathbf{k}_{\mathbf{inc}}^{(\nu-)}\cdot\mathbf{x})F(\chi_-^{(\nu-)}) + \cos(\phi-\theta_\nu)\exp(i\mathbf{k}_{\mathbf{ref}}^{(\nu-)}\cdot\mathbf{x})F(\chi_+^{(\nu-)})\right] \\ &\left.- \frac{1}{2}\left[\cos(\phi+\theta_\nu)\exp(i\mathbf{k}_{\mathbf{inc}}^{(\nu-)}\cdot\mathbf{x}) - \cos(\phi-\theta_\nu)\exp(i\mathbf{k}_{\mathbf{ref}}^{(\nu-)}\cdot\mathbf{x})\right]\right\},\end{aligned}$$

and

(2.14)
$$\begin{aligned}
\frac{B_\phi}{B_0} = &-\sin\phi\exp\Big(i\frac{2\pi}{\lambda}y\Big)+\frac{1+i}{\sqrt{2\pi kr}}\exp(ikr)\sin\Big(\frac{\phi}{2}\Big)+\frac{1}{2}\Big[\sin\phi\exp\Big(i\frac{2\pi}{\lambda}y\Big)-\sin\phi\exp\Big(-i\frac{2\pi}{\lambda}y\Big)\Big]\\
&+\frac{1+i}{2i}\Big[\sin\phi\exp\Big(i\frac{2\pi}{\lambda}y\Big)F(\chi_-)+\sin\phi\exp\Big(-i\frac{2\pi}{\lambda}y\Big)F(\chi_+)\Big]\\
&+\frac{\epsilon}{2}\sum_{\nu=0}^{N}\frac{1}{\gamma^{(2-D_0)\nu}}\Big\{-\sin(\phi-\theta_\nu)\exp(i\mathbf{k}_{\mathbf{inc}}^{(\nu+)}\cdot\mathbf{x})+\frac{1+i}{\sqrt{\pi kr}}\exp(ikr)\sin\Big(\frac{\phi}{2}\Big)\cos\Big(\frac{\theta_\nu}{2}+\frac{\pi}{4}\Big)\\
&+\frac{1+i}{2i}\Big[\sin(\phi-\theta_\nu)\exp(i\mathbf{k}_{\mathbf{inc}}^{(\nu+)}\cdot\mathbf{x})F(\chi_-^{(\nu+)})+\sin(\phi+\theta_\nu)\exp(i\mathbf{k}_{\mathbf{ref}}^{(\nu+)}\cdot\mathbf{x})F(\chi_+^{(\nu+)})\Big]\\
&+\frac{1}{2}\Big[\sin(\phi-\theta_\nu)\exp(i\mathbf{k}_{\mathbf{inc}}^{(\nu+)}\cdot\mathbf{x})-\sin(\phi+\theta_\nu)\exp(i\mathbf{k}_{\mathbf{ref}}^{(\nu+)}\cdot\mathbf{x})\Big]\\
&-\sin(\phi+\theta_\nu)\exp(i\mathbf{k}_{\mathbf{inc}}^{(\nu-)}\cdot\mathbf{x})+\frac{1+i}{\sqrt{\pi kr}}\exp(ikr)\sin\Big(\frac{\phi}{2}\Big)\cos\Big(-\frac{\theta_\nu}{2}+\frac{\pi}{4}\Big)\\
&+\frac{1+i}{2i}\Big[\sin(\phi+\theta_\nu)\exp(i\mathbf{k}_{\mathbf{inc}}^{(\nu-)}\cdot\mathbf{x})F(\chi_-^{(\nu-)})+\sin(\phi-\theta_\nu)\exp(i\mathbf{k}_{\mathbf{ref}}^{(\nu-)}\cdot\mathbf{x})F(\chi_+^{(\nu-)})\Big]\\
&+\frac{1}{2}\Big[\sin(\phi+\theta_\nu)\exp(i\mathbf{k}_{\mathbf{inc}}^{(\nu-)}\cdot\mathbf{x})-\sin(\phi-\theta_\nu)\exp(i\mathbf{k}_{\mathbf{ref}}^{(\nu-)}\cdot\mathbf{x})\Big]\Big\}.
\end{aligned}$$

For the TM solution,

(2.15)
$$\begin{aligned}
\frac{B_z}{B_0} = &\exp\Big(i\frac{2\pi}{\lambda}y\Big)-\frac{1+i}{2i}\Big[\exp\Big(i\frac{2\pi}{\lambda}y\Big)F(\chi_-)+\exp\Big(-i\frac{2\pi}{\lambda}y\Big)F(\chi_+)\Big]-i\sin\Big(\frac{2\pi}{\lambda}y\Big)\\
&+\frac{\epsilon}{2}\sum_{\nu=0}^{N}\frac{1}{\gamma^{(2-D_0)\nu}}\Big\{\exp(i\mathbf{k}_{\mathbf{inc}}^{(\nu+)}\cdot\mathbf{x})-\frac{1+i}{2i}\Big[\exp(i\mathbf{k}_{\mathbf{inc}}^{(\nu+)}\cdot\mathbf{x})F(\chi_-^{(\nu+)})+\exp(i\mathbf{k}_{\mathbf{ref}}^{(\nu+)}\cdot\mathbf{x})F(\chi_+^{(\nu+)})\Big]\\
&-\frac{1}{2}\Big[\exp(i\mathbf{k}_{\mathbf{inc}}^{(\nu+)}\cdot\mathbf{x})-\exp(i\mathbf{k}_{\mathbf{ref}}^{(\nu+)}\cdot\mathbf{x})+\exp(i\mathbf{k}_{\mathbf{inc}}^{(\nu-)}\cdot\mathbf{x})-\exp(i\mathbf{k}_{\mathbf{ref}}^{(\nu-)}\cdot\mathbf{x})\Big]\\
&+\exp(i\mathbf{k}_{\mathbf{inc}}^{(\nu-)}\cdot\mathbf{x})-\frac{1+i}{2i}\Big[\exp(i\mathbf{k}_{\mathbf{inc}}^{(\nu-)}\cdot\mathbf{x})F(\chi_-^{(\nu-)})+\exp(i\mathbf{k}_{\mathbf{ref}}^{(\nu-)}\cdot\mathbf{x})F(\chi_+^{(\nu-)})\Big]\Big\},
\end{aligned}$$

(2.16)
$$\begin{aligned}
\frac{E_r}{E_0} = &-\exp\Big(i\frac{2\pi}{\lambda}y\Big)\cos\phi+\frac{1+i}{\sqrt{2\pi kr}}\exp(ikr)\sin\Big(\frac{\phi}{2}\Big)+\cos\phi\cos\Big(\frac{2\pi}{\lambda}y\Big)\\
&+\frac{1+i}{2i}\Big[\cos\phi\exp\Big(i\frac{2\pi}{\lambda}y\Big)F(\chi_-)-\cos\phi\exp\Big(-i\frac{2\pi}{\lambda}y\Big)F(\chi_+)\Big]\\
&-\frac{\epsilon}{2}\sum_{\nu=0}^{N}\frac{1}{\gamma^{(2-D_0)\nu}}\Big\{-\cos(\phi-\theta_\nu)\exp(i\mathbf{k}_{\mathbf{inc}}^{(\nu+)}\cdot\mathbf{x})+\frac{1+i}{\sqrt{\pi kr}}\exp(ikr)\sin\Big(\frac{\phi}{2}\Big)\cos\Big(\frac{\theta_\nu}{2}-\frac{\pi}{4}\Big)\\
&+\frac{1+i}{2i}\Big[\cos(\phi-\theta_\nu)\exp(i\mathbf{k}_{\mathbf{inc}}^{(\nu+)}\cdot\mathbf{x})F(\chi_-^{(\nu+)})-\cos(\phi+\theta_\nu)\exp(i\mathbf{k}_{\mathbf{ref}}^{(\nu+)}\cdot\mathbf{x})F(\chi_+^{(\nu+)})\Big]\\
&+\frac{1}{2}\Big[\cos(\phi-\theta_\nu)\exp(i\mathbf{k}_{\mathbf{inc}}^{(\nu+)}\cdot\mathbf{x})+\cos(\phi+\theta_\nu)\exp(i\mathbf{k}_{\mathbf{ref}}^{(\nu+)}\cdot\mathbf{x})\Big]\\
&-\cos(\phi+\theta_\nu)\exp(i\mathbf{k}_{\mathbf{inc}}^{(\nu-)}\cdot\mathbf{x})+\frac{1+i}{\sqrt{\pi kr}}\exp(ikr)\sin\Big(\frac{\phi}{2}\Big)\cos\Big(\frac{-\theta_\nu}{2}-\frac{\pi}{4}\Big)\\
&+\frac{1+i}{2i}\Big[\cos(\phi+\theta_\nu)\exp(i\mathbf{k}_{\mathbf{inc}}^{(\nu-)}\cdot\mathbf{x})F(\chi_-^{(\nu-)})-\cos(\phi-\theta_\nu)\exp(i\mathbf{k}_{\mathbf{ref}}\cdot\mathbf{x})F(\chi_+^{(\nu-)})\Big]\\
&+\frac{1}{2}\Big[\cos(\phi+\theta_\nu)\exp(i\mathbf{k}_{\mathbf{inc}}^{(\nu-)}\cdot\mathbf{x})+\cos(\phi-\theta_\nu)\exp(i\mathbf{k}_{\mathbf{ref}}^{(\nu-)}\cdot\mathbf{x})\Big]\Big\},
\end{aligned}$$

and finally

$$
\begin{aligned}
\frac{E_\phi}{E_0} &= \sin\phi \exp\Big(i\frac{2\pi}{\lambda}y\Big) - \frac{1+i}{\sqrt{2\pi kr}}\exp(ikr)\cos\Big(\frac{\phi}{2}\Big) - \sin\phi\cos\Big(\frac{2\pi}{\lambda}y\Big) \\
&\quad - \frac{1+i}{2i}\Big[\sin\phi\exp\Big(i\frac{2\pi}{\lambda}y\Big)F(\chi_-) - \sin\phi\exp\Big(-i\frac{2\pi}{\lambda}y\Big)F(\chi_+)\Big] \\
&\quad + \frac{\epsilon}{2}\sum_{\nu=0}^{N}\frac{1}{\gamma^{(2-D_0)\nu}}\Big\{\sin(\phi-\theta_\nu)\exp(i\mathbf{k}_{\mathbf{inc}}^{(\nu+)}\cdot\mathbf{x}) - \frac{1+i}{2i}\exp(ikr)\cos\Big(\frac{\phi}{2}\Big)\cos\Big(\frac{\theta_\nu}{2}-\frac{\pi}{4}\Big) \\
&\quad - \frac{1+i}{2i}\Big[\sin(\phi-\theta_\nu)\exp(i\mathbf{k}_{\mathbf{inc}}^{(\nu+)}\cdot\mathbf{x})F(\chi_-^{(\nu+)}) - \sin(\phi+\theta_\nu)\exp(i\mathbf{k}_{\mathbf{ref}}^{(\nu+)}\cdot\mathbf{x})F(\chi_+^{(\nu+)})\Big] \\
&\quad - \frac{1}{2}\Big[\sin(\phi-\theta_\nu)\exp(i\mathbf{k}_{\mathbf{inc}}^{(\nu+)}\cdot\mathbf{x}) + \sin(\phi+\theta_\nu)\exp(i\mathbf{k}_{\mathbf{ref}}^{(\nu+)}\cdot\mathbf{x})\Big] \\
&\quad + \sin(\phi+\theta_\nu)\exp(i\mathbf{k}_{\mathbf{inc}}^{(\nu-)}\cdot\mathbf{x}) - \frac{1+i}{2i}\exp(ikr)\cos\Big(\frac{\phi}{2}\Big)\cos\Big(-\frac{\theta_\nu}{2}-\frac{\pi}{4}\Big) \\
&\quad - \frac{1+i}{2i}\Big[\sin(\phi+\theta_\nu)\exp(i\mathbf{k}_{\mathbf{inc}}^{(\nu-)}\cdot\mathbf{x})F(\chi_-^{(\nu-)}) - \sin(\phi-\theta_\nu)\exp(i\mathbf{k}_{\mathbf{ref}}^{(\nu-)}\cdot\mathbf{x})F(\chi_+^{(\nu-)})\Big] \\
&\quad - \frac{1}{2}\Big[\sin(\phi+\theta_\nu)\exp(i\mathbf{k}_{\mathbf{inc}}^{(\nu-)}\cdot\mathbf{x}) + \sin(\phi-\theta_\nu)\exp(i\mathbf{k}_{\mathbf{ref}}^{(\nu-)}\cdot\mathbf{x})\Big]\Big\}.
\end{aligned}
\tag{2.17}
$$

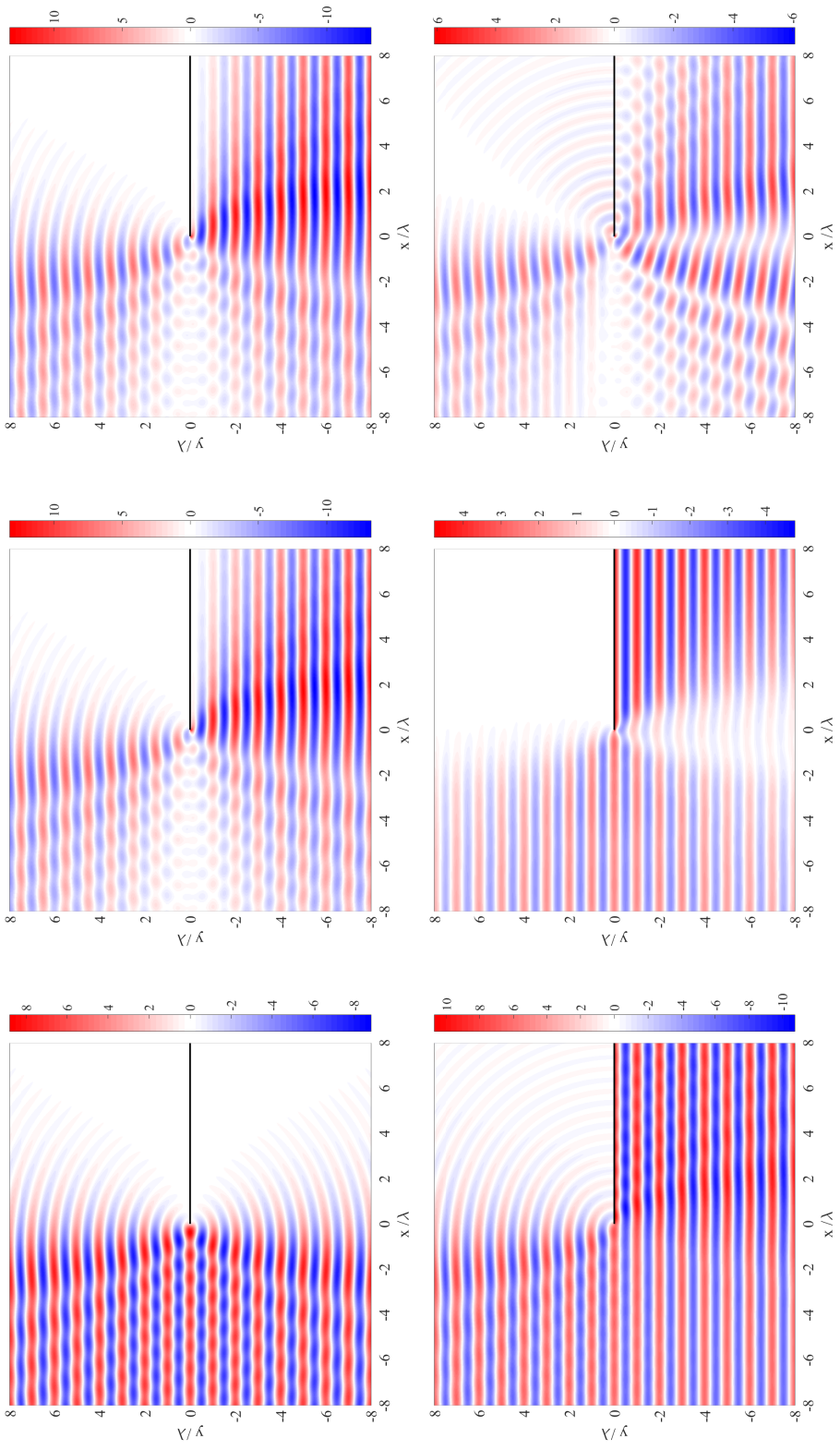

Figure 2.5: TE solution for the truncated-Weierstrass wave at a screen, $2\Re e\left(\frac{E_z}{E_0}\right)$ (top left), $2\Re e\left(\frac{B_r}{B_0}\right)$ (top middle) and $2\Re e\left(\frac{B_\phi}{B_0}\right)$ (top right). TM solution on bottom row with $2\Re e\left(\frac{B_z}{B_0}\right)$ (bottom left), $2\Re e\left(\frac{E_r}{E_0}\right)$ (bottom middle) and $2\Re e\left(\frac{E_\phi}{B_0}\right)$ (bottom right). Parameters are $\Lambda = 2500\lambda$, $\gamma = 3$ and $D_0 = 1.5$.

2.3 Intensity

Here, the intensity of a field is defined as the electromagnetic energy delivered per unit area per unit time (power density) crossing the (x,z) plane. In order to find the intensity of the TE solution, one must first employ the use of the Poynting vector,

$$\mathscr{S}(\mathbf{x},t) = c^2\epsilon_0\mathscr{E}(\mathbf{x},t)\times\mathscr{B}(\mathbf{x},t). \tag{2.18}$$

The projection of the Poynting vector in the y direction for the TE solution is hence

$$\mathscr{S}_y(\mathbf{x},t) = c^2\epsilon_0\mathscr{E}_z(\mathbf{x},t)\mathscr{B}_x(\mathbf{x},t). \tag{2.19}$$

The intensity is defined as the time-average of the Poynting vector,

$$I \equiv \lim_{T\to\infty}\frac{1}{T}\int_{t-\frac{T}{2}}^{t+\frac{T}{2}} dt'\,\mathscr{S}_y(x,y,t'), \tag{2.20}$$

where the sampling time T is much larger than the period of oscillation, $\frac{2\pi}{\omega}$. Substituting Eq. (2.19) into Eq. (2.20) one gets

$$I = c^2\epsilon_0\lim_{T\to\infty}\frac{1}{T}\int_{t-\frac{T}{2}}^{t+\frac{T}{2}} dt'\left[\mathscr{E}_z(x,y,t')\mathscr{B}_x^*(x,y,t') + \mathscr{E}_z^*(x,y,t')\mathscr{B}_x(x,y,t')\right]. \tag{2.21}$$

From Ambramowitz and Stegun [30]

$$\lim_{T\to\infty}\frac{1}{T}\int_{t-\frac{T}{2}}^{t+\frac{T}{2}} dt'\exp(\pm i2\omega t') = 0, \tag{2.22}$$

and therefore

$$I(x,y) = c^2\epsilon_0[E_z(x,y)B_x^*(x,y) + E_z^*(x,y)B_x(x,y)]. \tag{2.23}$$

The intensity of the TE field diffracted from a screen is hence

$$I(x,y) = c^2\epsilon_0 2\Re e[E_z(x,y)B_x^*(x,y)]. \tag{2.24}$$

Comparison of the plane-wave and truncated-Weierstrass surface intensity plot (Fig. 2.6) may lead one to conclude that there is little to no difference (other than in magnitude) between the two diffraction patterns. This, however, on closer inspection is not the case when one compares 1D cross-sections through each pattern. By doing this, one finds that there is a profound quantitative difference, as shown in Figs. 2.7 and 2.8.

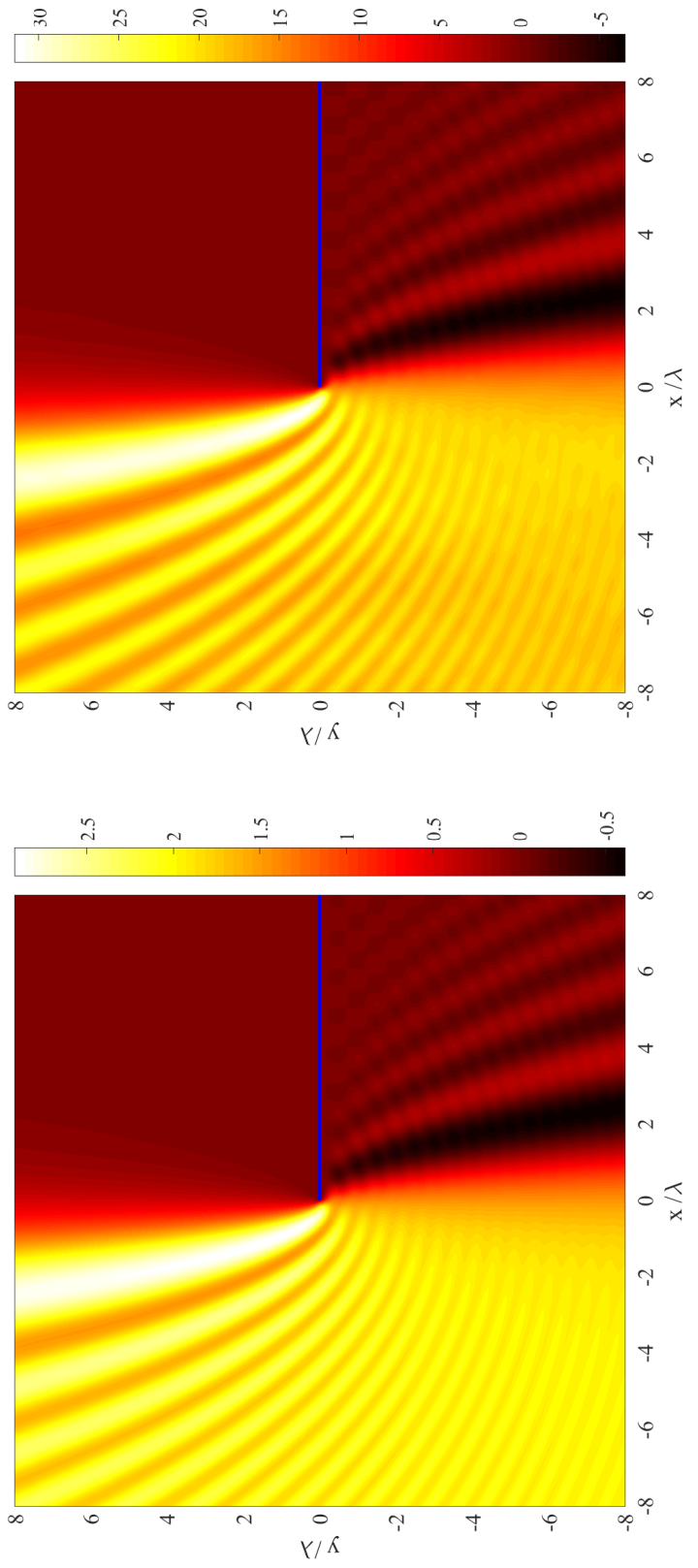

Figure 2.6: The intensity, $\frac{I}{c^2\epsilon_0 E_0 B_0}$, of the diffracted normally-incident plane-wave (*left*) and the TE Weierstrass-Lamb solution with $D_0 = 1.5$, $\Lambda = 2500\lambda$, $\epsilon = 1$ and $\gamma = 3$ (*right*).

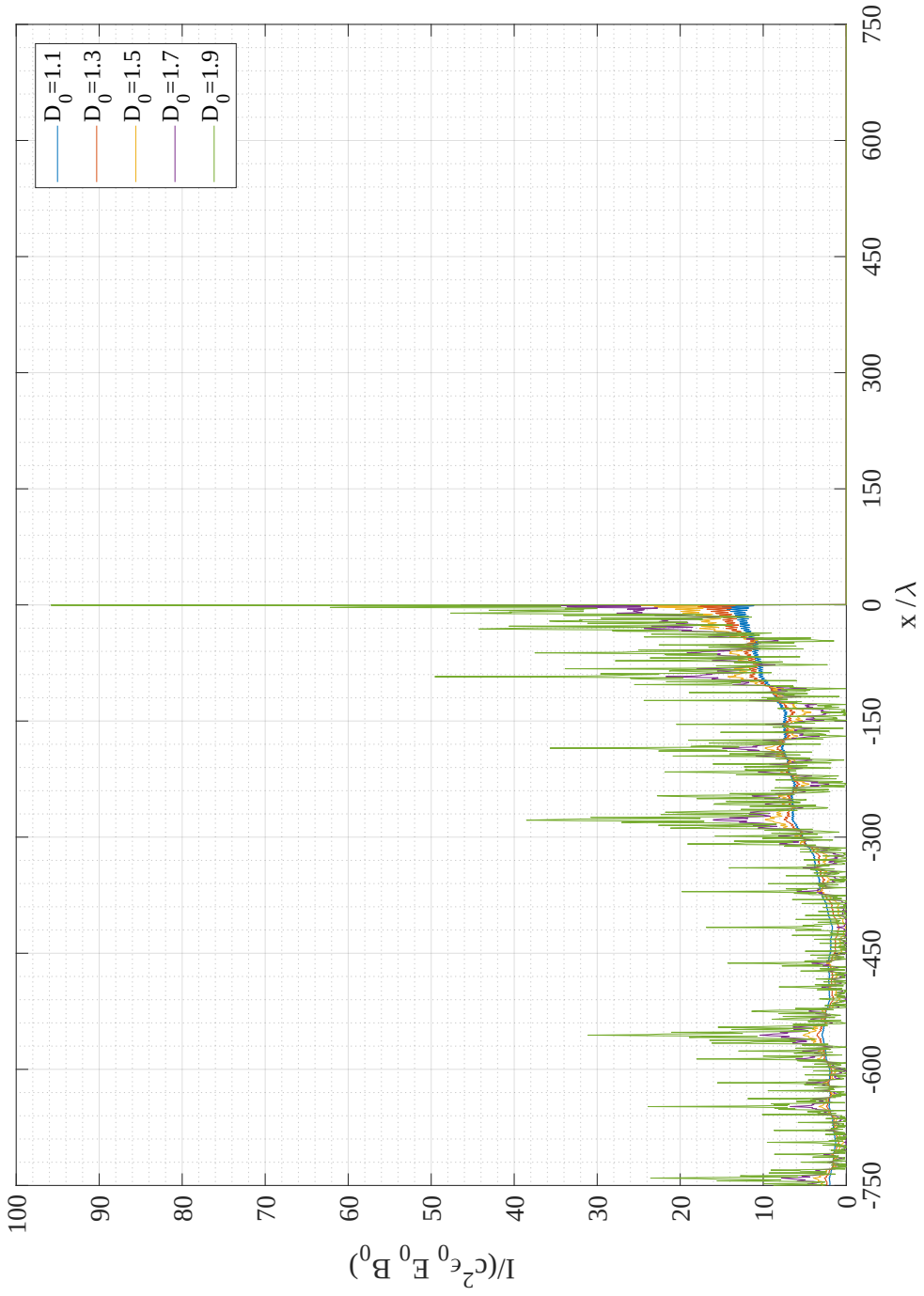

Figure 2.7: The intensity, $\frac{I}{c^2\epsilon_0 E_0 B_0}$, of the TE field diffracted by a knife-edge, [cf. Eq. (2.24)]. A variety of D_0 values is considered with $\gamma = 3$, $\Lambda = 2500\lambda$ and $y = 10^{-1}\lambda$.

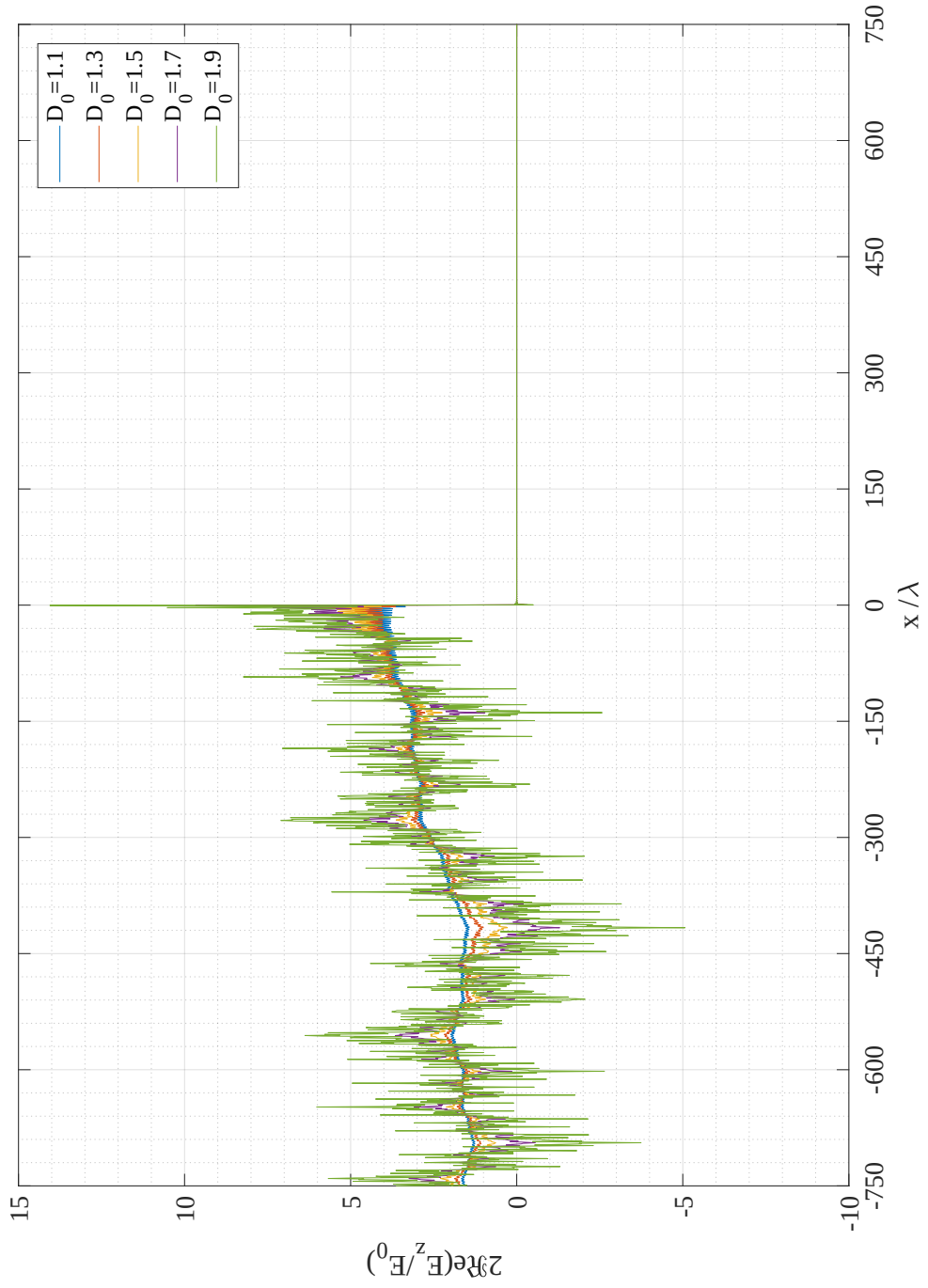

Figure 2.8: The electric field of the TE solution. A variety of D_0 values is considered with $\gamma = 3$, $\Lambda = 2500\lambda$ and $y = 10^{-1}\lambda$.

2.4 Dimension analysis of the Weierstrass-Lamb solution

In this subsection, attention is paid to estimating the dimension of the TE Weierstrass-Lamb solution at various longitudinal positions downstream from the screen (distances from $10^{-1}\lambda$ to $10^{3}\lambda$ in the forward half-plane, linearly spaced on the logarithmic scale). The parameters of the truncated-Weierstrass function are set to $\Lambda = 2500\lambda$ and $\gamma = 3$ – these are the same values used in subsequent chapters and ensures that N is sufficiently large that the input field may be considered to be pre-fractal.

One of the first findings here is that the estimated dimension of the electric field can change substantially during a single cycle in the time period, $\frac{2\pi}{\omega} = T_0$ (see Fig. 2.9). It is desirable to estimate the dimension of a quantity that remains stationary in time (i.e., is not subject to temporal fluctuations) and hence attention will focus on intensity I (related to the time-averaged Poynting vector), as defined in Eq. (2.24). For cw solutions, the intensity is time-independent (it is also the physical quantity most easily measured in a laboratory) so one may associate I with a single estimated dimension at any longitudinal position y.

In scalar wave optics, one usually assumes that $|B_y| \ll |B_x|$ so that the electromagnetic field is approximately transverse [i.e. an $(\mathbf{E},\mathbf{B},\mathbf{k})$ triad]. In that regime, a measure of the intensity is typically taken to be $|E_z|^2$ and the detailed consideration of the Poynting vector is, to a large extent, neglected (this is also true for earlier paraxial-based analysis of pre-fractal diffraction phenomena by Christian *et. al.*). Here the full electromagnetic character of the wave scattering problem is addressed and non-trivial qualitative differences are found. For instance, Fig. 2.10 shows a noticeable difference between the estimated dimensions for $\left|\frac{E_z}{E_0}\right|^2$ and the formal intensity from Eq. (2.24). Although the qualitative features of the two curves are similar, $\left|\frac{E_z}{E_0}\right|^2$ is typically associated with a higher dimension than $\frac{I}{c^2\epsilon_0 E_0 B_0}$.

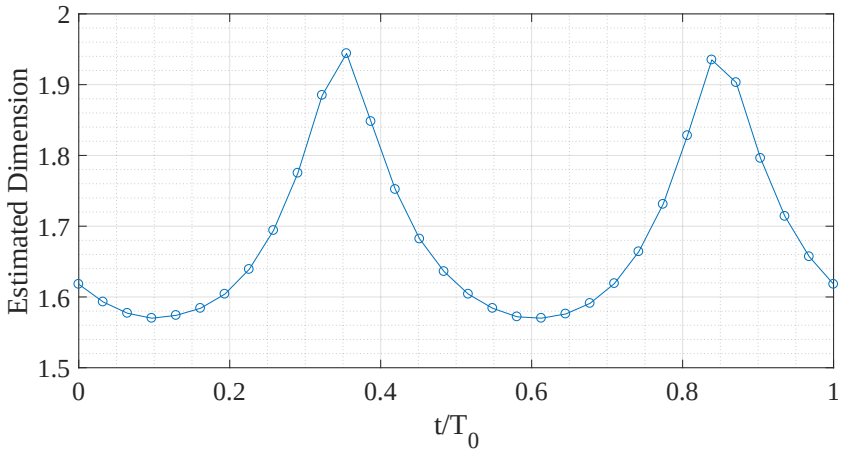

Figure 2.9: The estimated dimension for $\Re e\left(\frac{E_z}{E_0}\right)$ for the diffraction of a truncated-Weierstrass function with $D_0 = 1.5$ at $y = 10^{-1}\lambda$ as a function of time.

Looking at Fig. 2.11 the most immediate thing to notice is the connection between the erratic-ness of the estimated dimension of the intensity, $\left|\frac{E_z}{E_0}\right|^2$, and D_0 values – the smaller D_0 values have a much smoother curve compared to the various peaks and troughs which start appearing for $D_0 = 1.5$ and become more and more prominent as D_0 rises. What is important to state is that the aforementioned fluctuations are at the same distances no matter what the D_0 values are. An interesting quirk of the dimensions calculated is that when the y values are small/ around the distances of λ, the higher D_0 values (1.7, 1.9) actually have a lower estimated dimension. Only as y increases does the estimated dimension of the higher D_0 values become larger. The estimated dimension of the lower D_0 values falls steadily towards unity as the distance increases. This pattern also appears in Fig. 2.12. In both the intensity and real electric field plots, the difference in the estimated dimension in the $D_0 = 1.9$ and the others is large.

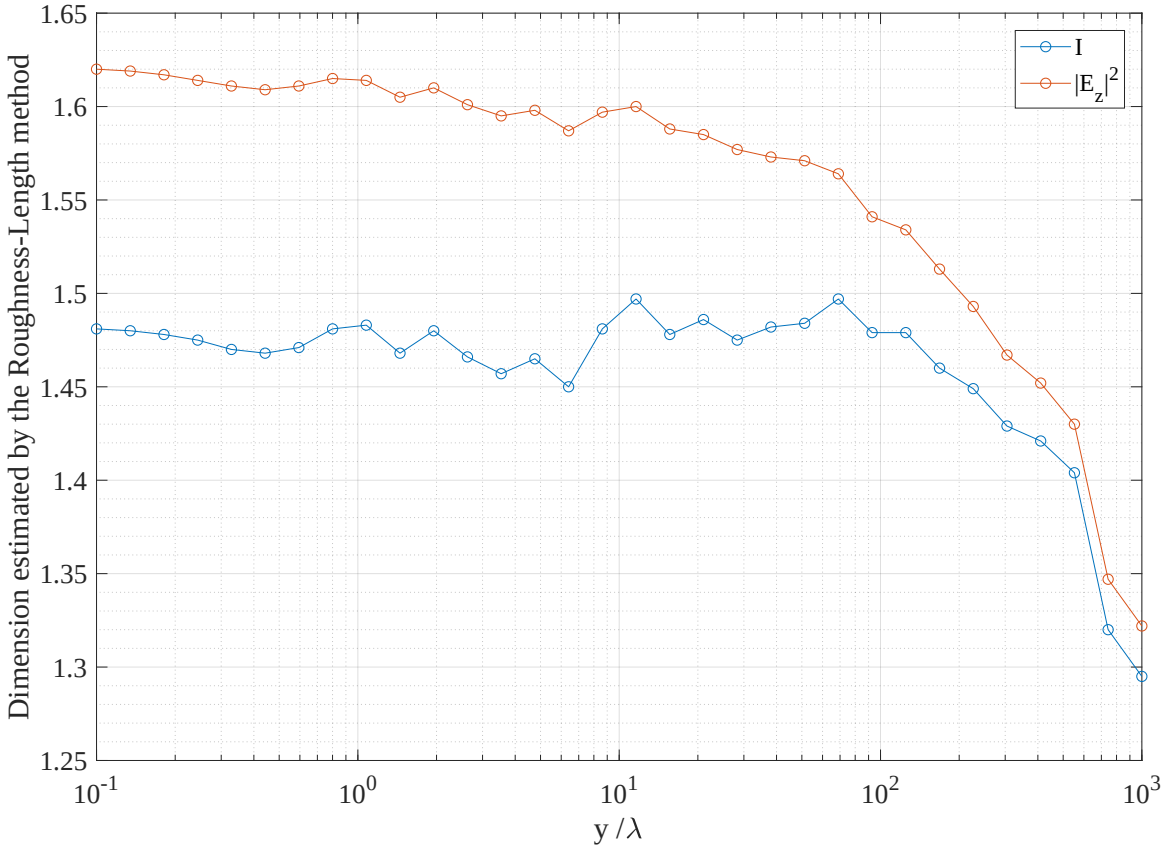

Figure 2.10: Comparison of the estimated dimension for $D_0 = 1.5$ for the intensity, $\frac{I}{c^2\epsilon_0 E_0 B_0}$, and $\left|\frac{E_z}{E_0}\right|^2$.

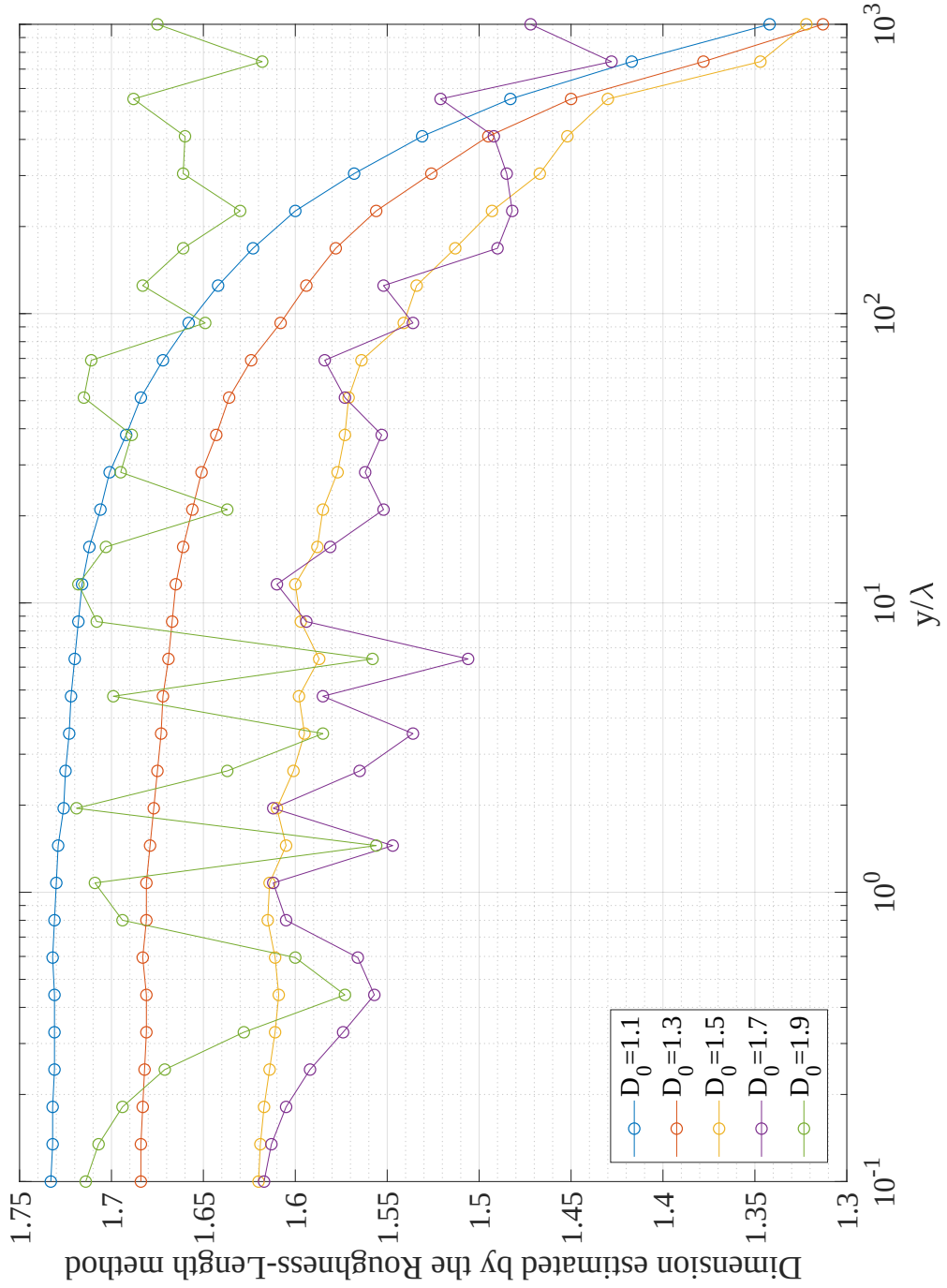

Figure 2.11: The estimated dimension for intensity, $\left|\frac{E_z}{E_0}\right|^2$, diffracted from a screen.

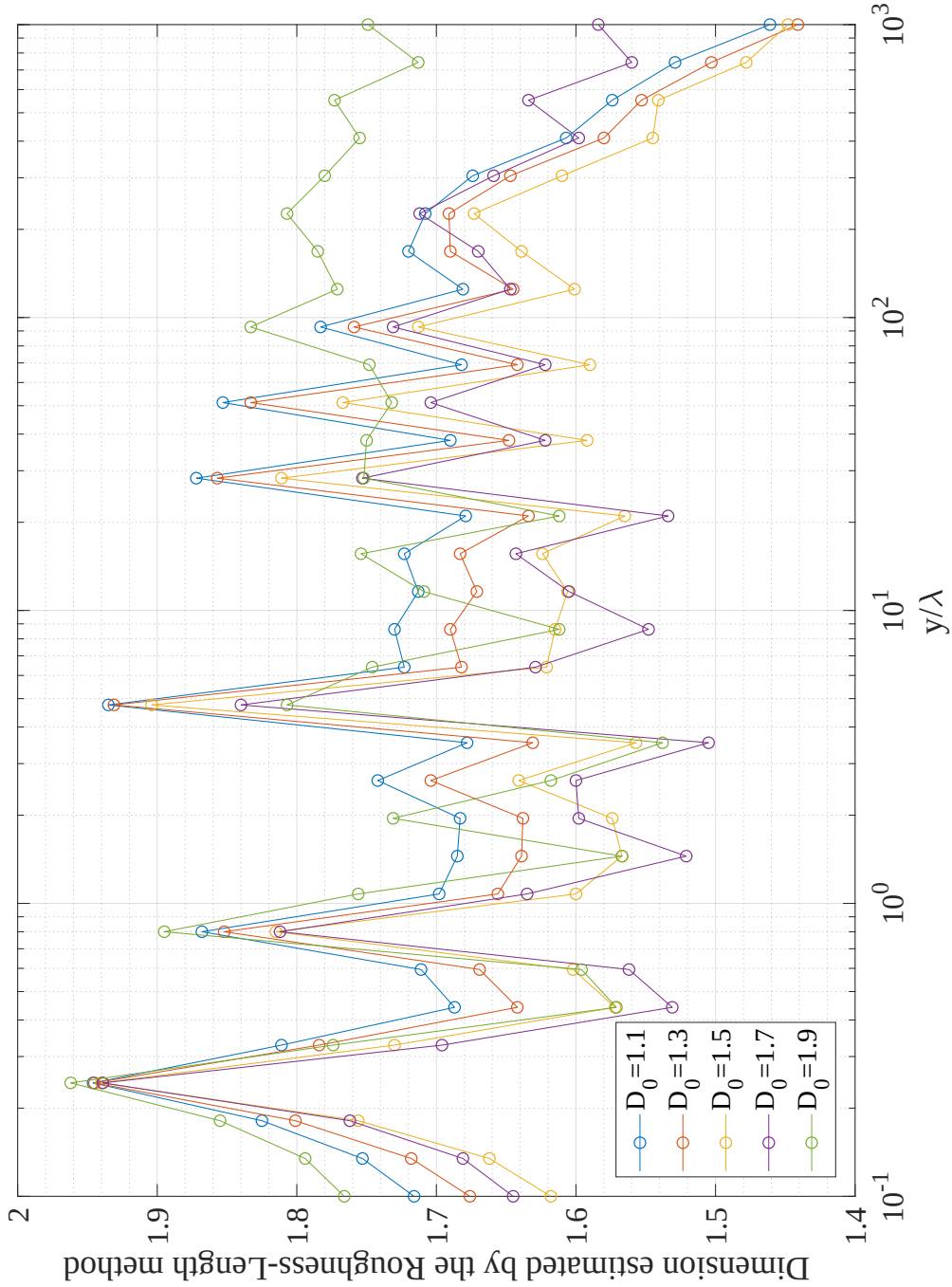

Figure 2.12: The estimated dimension for the electric field, $2\Re e\left(\frac{E_z}{E_0}\right)$, diffracted from a screen.

2.5 Paraxial Theory

To establish the paraxial limit of the Weierstrass-Lamb TE wave, is it necessary to discard any component associated with the reflected wave, $\exp(i\mathbf{k_{ref}}\cdot\mathbf{x})$. An approximate wave travelling in the forward y direction from contribution ν is then given by

$$\frac{E_z}{E_0}\Big|_{\text{fwd}}^{(\nu+)} \approx \frac{1}{\gamma^{(2-D_0)\nu}}\exp(i\mathbf{k}_{\mathbf{inc}}^{(\nu+)}\cdot\mathbf{x})\Big[\frac{1}{2}-\frac{1+i}{2i}F(\chi_-^{(\nu+)})\Big]. \tag{2.25}$$

In the paraxial regime, one views the wave at a large distance from the knife-edge in the forward direction, and where the range of x is small. That is, where $y>0$ and $y\gg|x|$. It then follows that

$$\mathbf{k_{inc}}\cdot\mathbf{x} = -k_{incx}x + k_{incy}y \approx -k_{incx}x - \frac{k_{incx}^2 y}{2k} + k_{incy}, \tag{2.26}$$

since $k_y = +\sqrt{k^2-k_x^2}$ and $|k_x|\ll k$. By applying the same sort of analysis to $\chi_-^{(\nu+)}$, it follows that

$$\chi_-^{(\nu+)} \approx \Big(\frac{k}{\pi y}\Big)^{\frac{1}{2}}\Big(x-\frac{k_x y}{k}\Big) \equiv \chi_-^{(\nu+)\text{par}}. \tag{2.27}$$

Hence, one finds that $\frac{E_z}{E_0}\Big|_{\text{fwd}}^{(\nu+)}$ may be approximated as

$$E_z^{(\nu+)} \approx \exp(iky)u(x,y), \tag{2.28}$$

where

$$u(x,y) \equiv \frac{E_0}{2}\Big[1-\frac{1+i}{i}F(\chi^{\text{par}})\Big]\exp\Big(-ik_x x - i\frac{k_x^2 y}{2k}\Big), \tag{2.29}$$

satisfies the paraxial diffraction equation [*cf* Eq. (1.48)] exactly. This type of approximation procedure can be applied to each component of the Weierstrass-Lamb solution.

Figure 2.13 shows that for $|x|/y \ll \mathcal{O}(1)$, the paraxial solution mimics almost exactly the formal Weierstrass-Lamb solution when the input field corresponds to a normally-incident plane wave. For a fixed distance y, the paraxial approximation begins to break down for increasing $|x|$ since the assumption of small propagation angles is violated. It is now natural so consider whether or not the paraxial approximation yields reliable results once one allows for a pre-fractal input field (e.g. Weierstrass-type illumination).

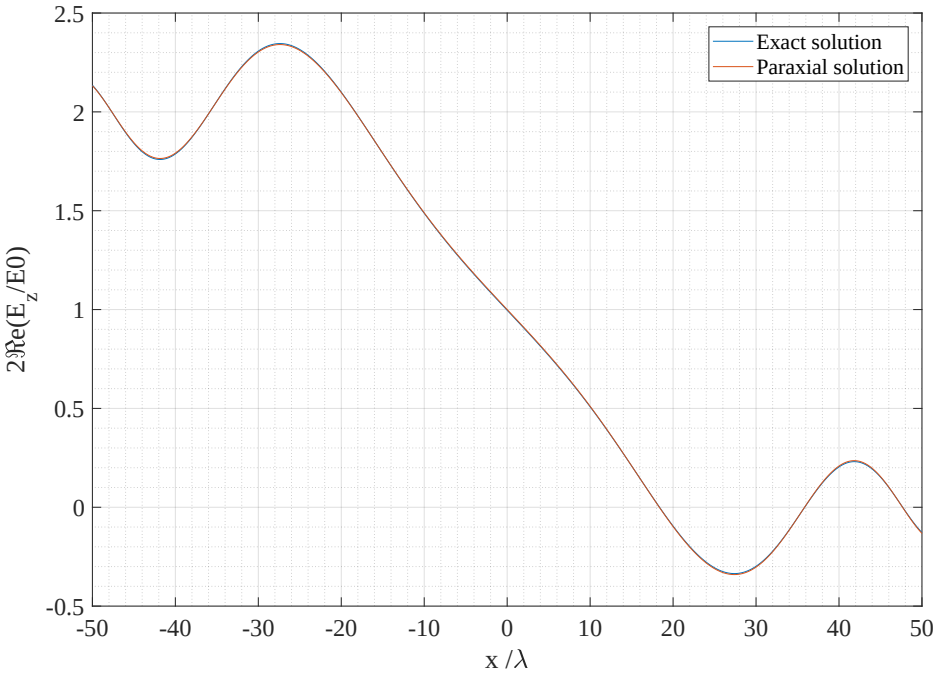

Figure 2.13: A comparison between the TE and paraxial solutions for the electric field of a plane-wave at $y = 10^3\lambda$ downstream from the screen.

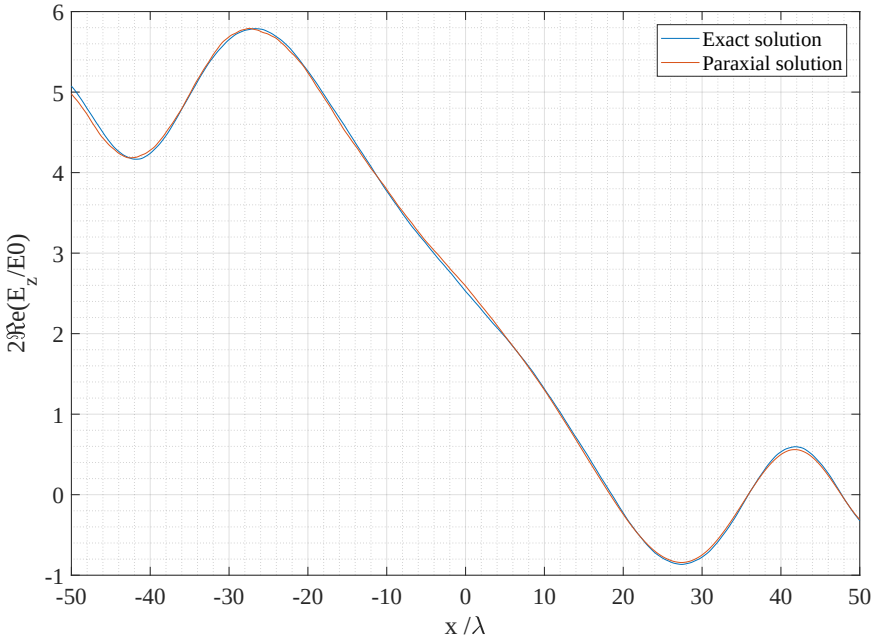

Figure 2.14: A comparison between the TE Weierstrass-Lamb and paraxial solutions for the electric field of a truncated-Weierstrass wave with $D_0 = 1.1$, $\Lambda = 2500\lambda$, $\gamma = 3$ and $\epsilon = 1$ at $y = 10^3\lambda$ downstream from the screen.

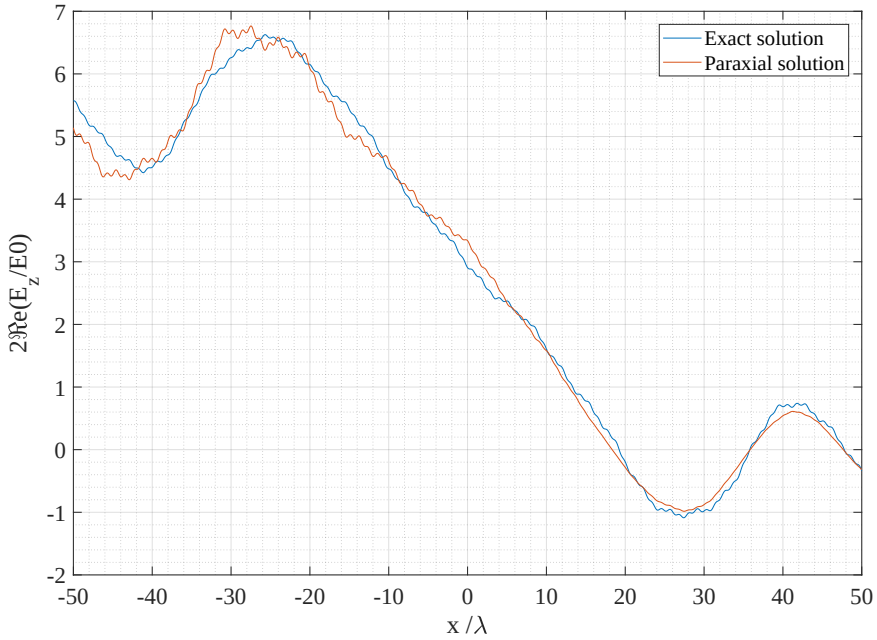

Figure 2.15: A comparison between the TE Weierstrass-Lamb and paraxial solutions for the electric field of a truncated-Weierstrass wave with $D_0 = 1.5$, $\Lambda = 2500\lambda$, $\gamma = 3$ and $\epsilon = 1$ at $y = 10^3\lambda$ downstream from the screen.

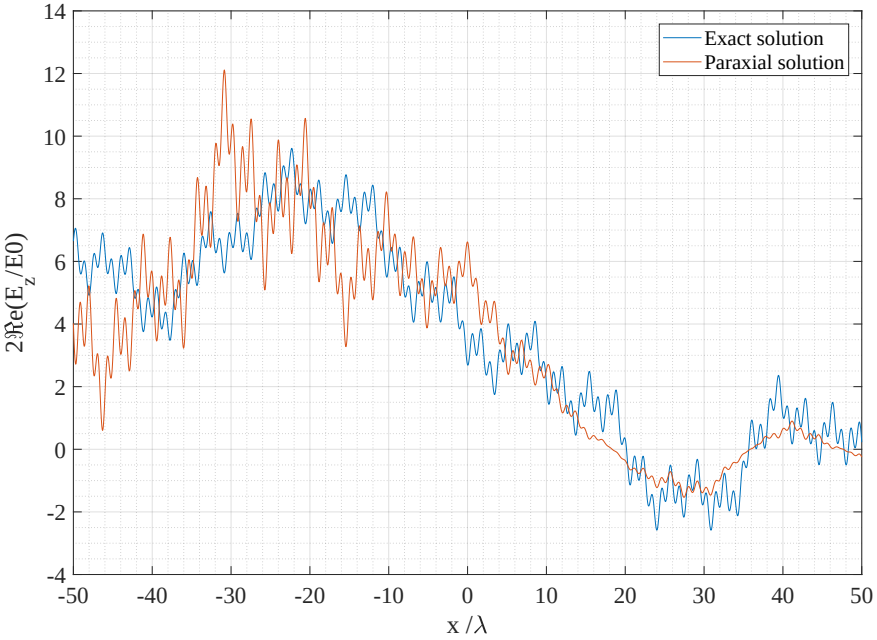

Figure 2.16: A comparison between the TE Weierstrass-Lamb and paraxial solutions for the electric field of a truncated-Weierstrass wave with $D_0 = 1.9$, $\Lambda = 2500\lambda$, $\gamma = 3$ and $\epsilon = 1$ at $y = 10^3\lambda$ downstream from the screen.

The paraxial approximation holds for input waves with low complexity (e.g. $D_0 = 1.1$; see Fig. 2.14). However, one can see that this agreement begins to falter for mid-range dimensions (e.g. in Fig 2.15 where $D_0 = 1.5$). For these mid-range D_0 values, one can see that the general trend of the diffraction pattern is similar for both Weierstrass-Lamb and paraxial solutions, but there are obvious quantitative differences. For large D_0 values (e.g. $D_0 = 1.9$; see Fig. 2.16), the paraxial solution fails entirely and one may therefore conclude that the small-angle approximation underpinning earlier work is potentially problematic. Subsequent chapters in this thesis will dispense almost entirely with the paraxial approximation on the basis that it does not provide a quantitatively accurate picture of how fractal and pre-fractal waves diffract.

CHAPTER 3

PLANE WAVE ILLUMINATION ON A CANTOR GRATING

This chapter begins the formal analysis of plane waves scattering from complex domains. The candidate multi-scale object that will be used is the Cantor set [10] or, more precisely, a slightly modified version of what might be interpreted as the 'traditional' Cantor set from Sec. 1.2.1. Here, one takes the traditional '$\frac{1}{3}$' Cantor set and, in a sense, inverts it so that all the regions that originally corresponded to gaps are filled in, and all the filled-in regions become gaps. At the initiator stage ($n = 0$), one now has a slit that maps easily onto a simple optics experiment. At the first pre-fractal level ($n = 1$), the central third of the initial slit is filled-in, and so produces a double-slit experiment where the slit width and separation happen to be equal to one another. The pre-fractal level $n = 2$ then produces four slits, and so on, (see Fig. 3.1). As $n \to \infty$, a Cantor-type diffraction grating is produced where all the constituent sub-apertures have the same size, but which are non-uniformly separated and also occupy a region of space that is bounded by the initial $n = 0$ slit. Hence, the Cantor-type grating is fundamentally different from classic gratings considered in optics, which tend to be periodic and thus be of infinite extent (a good example being the Talbot effect, [31, 37, 38]).

Figure 3.1: The first four pre-fractal levels of the Cantor grating.

The purpose of this chapter, then, is to investigate the diffraction patterns obtained as a normally-incident plane wave illuminates increasing levels of the Cantor grating. Having detailed the complex domain of interest, attention must now be turned to which analytical framework to deploy. Far-field studies of the Cantor-set diffraction problems typically require only Fourier transforms through the Fraunhofer approximation [34, 39, 40]. Nearer-field considerations must use the Fresnel approximation [28, 34]. Here, the RS diffraction-integral formulation will be used.

3.1 The Cantor-type grating

For every pre-fractal level $n = 1, 2, 3\ldots$ the individual slit half-width, a_n, is taken to be $\frac{a_0}{3^n}$, where a_0 is the half-width of the initiator slit (typically specified here in units of wavelength), and the total number of slits at stage n is simply 2^n. Evaluation of the diffraction integral requires one to know the location of all the constituent slit edges in the x' coordinate.

Figure 3.2: The second pre-fractal level of the Cantor grating.

For example, Fig. 3.2 shows the second pre-fractal level of the Cantor set. The midpoint of each slit is labelled Ξ_0, Ξ_1, $\Xi_2 \ldots \Xi_{n-1}$ and the subscript index is subsequently converted into a binary representation:

$$0 \rightarrow (000),$$
$$1 \rightarrow (001),$$
$$2 \rightarrow (010),$$
$$3 \rightarrow (011).$$

Those binary representations are then treated as an array of numbers in the style of (b_n b_{n-1} … b_0), which can be used to derive an equation for the location for each slit midpoint:

$$\Xi_j = 2a_0 \sum_{j=0}^{n-1} \frac{(-1)^{b_j}}{3^j}. \tag{3.1}$$

For the example in Fig. 3.2, the midpoints are calculated to be $\Xi_0 = \frac{-8a_0}{9}$, $\Xi_1 = \frac{-4a_0}{9}$, $\Xi_2 = \frac{4a_0}{9}$, and $\Xi_3 = \frac{8a_0}{9}$. It is then simply a matter of adding and subtracting a_n to find the locations of each slit edge.

From the Eq. (1.34), one can show that the expression for the electric field diffracted by pre-fractal level n of a Cantor-type grating is

$$E_z(x,y) = \frac{iky}{2} E_0 \sum_{j=0}^{2^n-1} \int_{a_-(\Xi_j)}^{a_+(\Xi_j)} dx' \frac{H_1^{(1)}(kR)}{R}, \tag{3.2}$$

where E_0 is the (complex) amplitude of the incident wave. For definiteness, the Cantor-type grating is oriented so that the longitudinal extent of the slits is aligned along the z axis. Furthermore, TE illumination is considered so that the spatial part of the cw electric field is described by $\mathbf{E} = (0, 0, E_z)$ throughout.

Here, attention of paid solely to the Dirichlet problem, where the electric field E_z must vanish everywhere on the surface of the screen (assumed to be perfectly conducting and with zero thickness) [34]. In the aperture regions (transparent parts), the Kirchhoff approximation $E_z(x', 0) \approx E_0$ is used, where E_0 is the complex amplitude of the incident plane wave. This level of approximation holds true generally, except in regions close to the edges of the obstructions that make up the screen. Hence, one may expect the Kirchhoff approximation to break down close to the screen and when the constituent sub-apertures are smaller than the wavelength. In other words, the approach used here cannot access the regime of a fully-fractal screen where one finds $|E_z| \to 0$ for $y > 0$ as $n \to \infty$ [c.f. Eq. (3.2)]. Such a regime can be described, however, with deployment of functional analysis methods and boundary-integral equations [7].

3.1.1 Computational Method

All integration within this thesis has been performed with the built-in MATLAB `integral` subroutine. This 'off-the-shelf' method was chosen over a custom (in-house) algorithm due to its robust and generally very reliable performance. The absolute and relative error tolerances were kept to default settings (10^{-10} and 10^{-6}, respectively). In practice, one integrates over each finite sub-domain [as suggested by Eq. (3.2)] rather than integrating over an implicitly pre-fractal domain directly. Another benefit of using `integral` is its ability to self-identify whenever the numerical result fails to converge as desired.

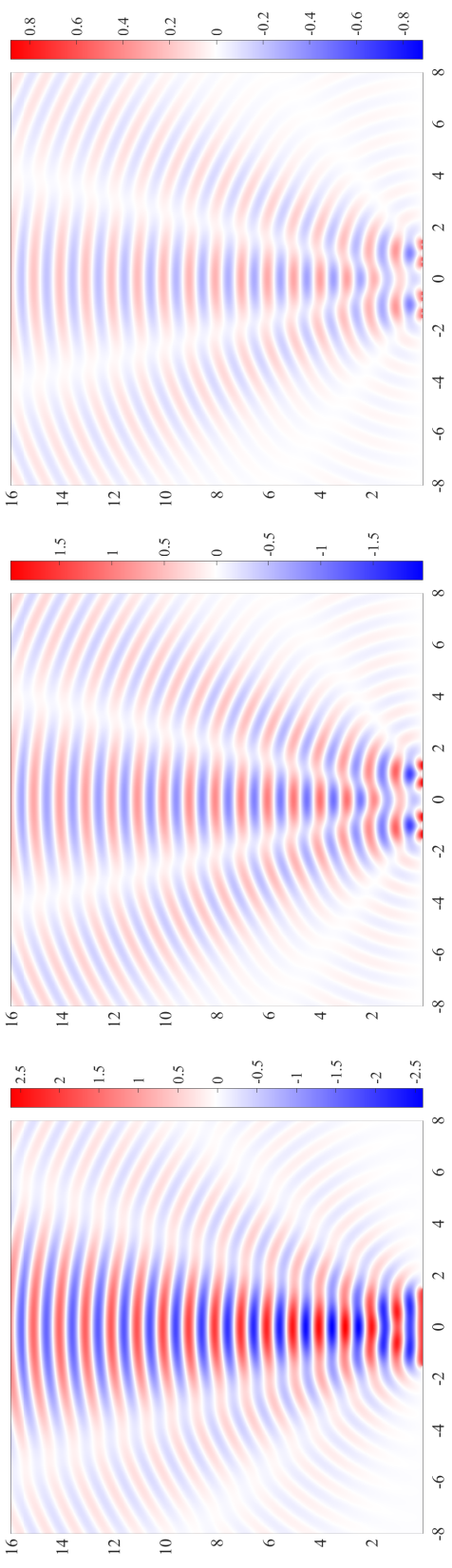

Figure 3.3: A comparison between the $2\Re e\left(\frac{E_z}{E_0}\right)$ for the zeroth *(left)*, third *(middle)* and fifth *(right)* pre-fractal level of the Cantor grating for $a_0 = 1.5\lambda$. Due to the relatively small half-width, the pattern converges extremely quickly.

From Fig. 3.3, it seems clear that when a_0 is comparable to the wavelength, the diffraction pattern quickly converges. No matter how much one moves up the pre-fractal levels of the Cantor slit, almost the same pattern would still appear (although the amplitude tends to fall off). For a larger a_0 it takes more iterations in n for the pattern to converge. No matter the size of a_0, there will always eventually be convergence due to the lack of presence of sub-wavelength structure. Figure 3.4 shows the field from the first, second and third pre-fractal level of a Cantor-type grating with $a_0 = 10\lambda$. After the third level, the diffracted pattern converges and almost no additional complexity is found as n increases further. Although the pattern converges at $n = 3$, the actual converged pattern formed is a rather interesting.

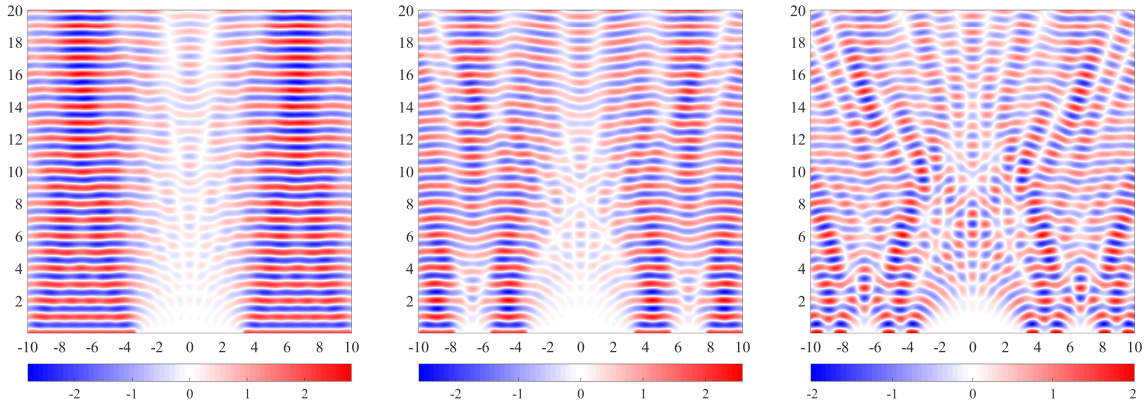

Figure 3.4: A zoomed comparison between $2\Re e\left(\frac{E_z}{E_0}\right)$ for the first *(left)*, second *(middle)* and third *(right)* pre-fractal level of the Cantor grating for $a_0 = 10\lambda$ (general plots can be found in Figs. C.24, C.26, and C.28).

To map the predictions of Eq. (3.2) onto an experiment (e.g. in a typical undergraduate optics laboratory), one might consider a single-slit aperture with a width of around 0.2mm so that, for green laser light with a wavelength of 534nm, $a_0 \approx 250\lambda$. Figure 3.5 shows the intensity (i.e., what would be observed visually) for the zeroth (i.e., single slit), third, and fifth pre-fractal level. The corresponding electric field distributions vary extremely rapidly on the spatial scales considered here and are not shown here. However, they can be found in Appendix C, along with a wide selection of illustrative results.

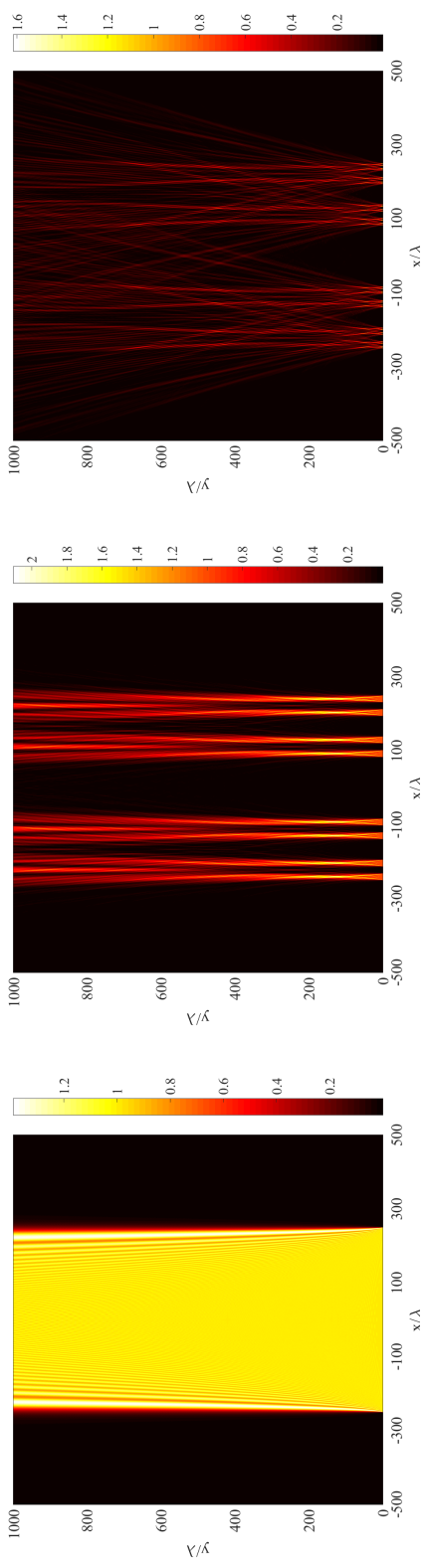

Figure 3.5: A comparison between $\left|\frac{E_z}{E_0}\right|^2$ for the zeroth *(left)*, third *(middle)* and fifth *(right)* pre-fractal level of the Cantor grating with $a_0 = 250\lambda$.

3.2 Roughness-length dimension estimation

In order to seek a quantitative measure of both the intensity and the electric field, one must once again consider dimension estimation using the roughness-length measure. Figure 3.6 shows a fundamental flaw of dimensional estimation – non-integer dimension is assigned to an object that is inherently non-complex, such as one can see in the diffraction of a plane wave from a single slit (such as the $n = 0$ line in Fig. 3.6). This phenomenon has already been found in laser optics when using the power-spectrum method of dimension estimation in single-slit configurations [41] and will be generalized to the Cantor-type grating (i.e., a multi-slit problem) in a later section. After consideration, it was decided that a domain $x \in [-2a_0, 2a_0]$ was most appropriate – even when approaching the far-field regime effectively all of the diffraction pattern is captured. A spatial resolution of $\Delta x = \frac{\lambda}{32}$ was chosen so that the field at the wavelength scale is sufficiently sampled for the BENOIT analysis.

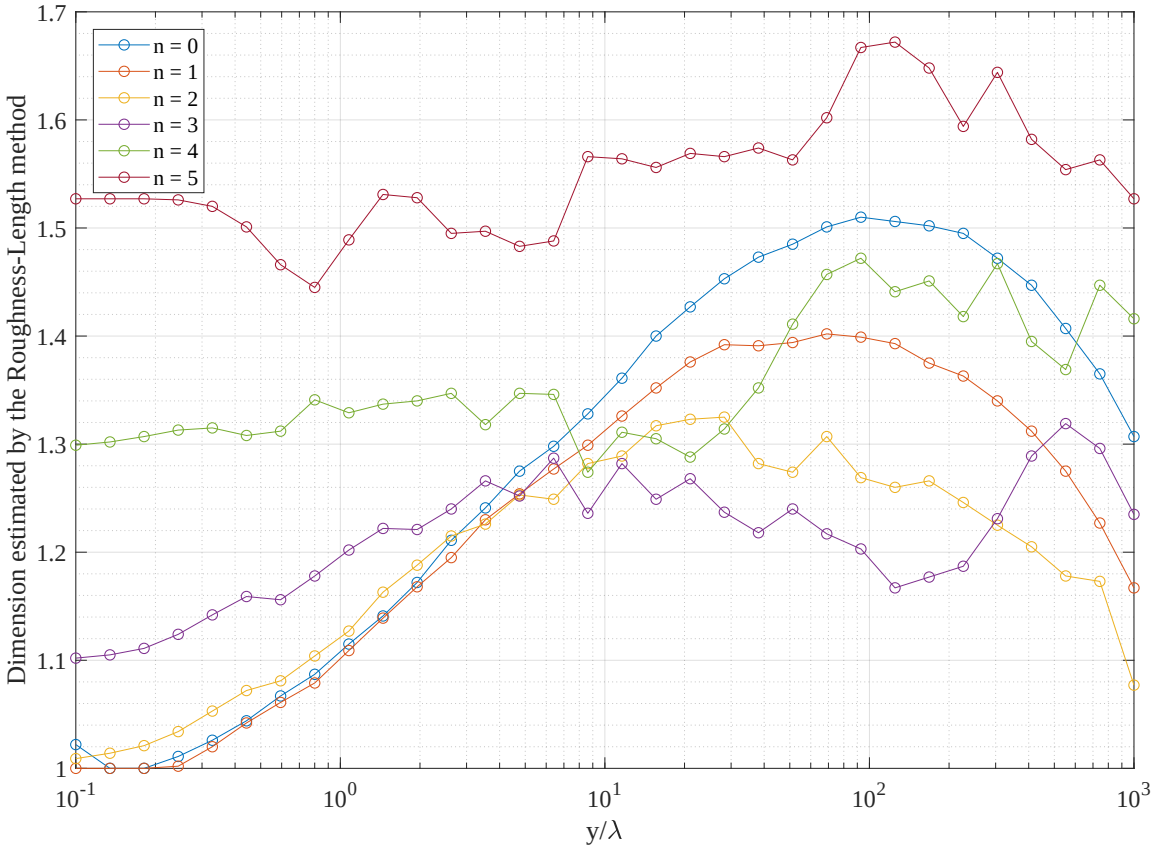

Figure 3.6: Roughness-length estimation of dimension of $\left|\frac{E_z}{E_0}\right|^2$ due to a Cantor grating with $a_0 = 250\lambda$.

The results shown in Figs. 3.6 and 3.7 can be used in Chapters 4 and 5 to help establish which

features of the roughness-length plots are due to the multi-scaledness of the complex input wave, and which are due to the estimation method itself. The a_0 in Figs. 3.6 and 3.7 is fixed at 250λ and hence as n increases, naturally a_n will decrease. For $n = 5$, the half-width of the individual slits is then $a_n \approx 1.03\lambda$ wide. As discussed in Chapter 1, an exact Helmholtz solution away from the screen contains no sub-wavelength structure and hence diffraction from so narrow a slit would certainly destroy detail otherwise found in patterns from broader slits. This effect can also be seen in Fig 3.3, where the pattern quickly converges with n. It is hence extremely important to confirm if any perceived dimensionality is an effect of the grating itself or from the size of the constituent slits.

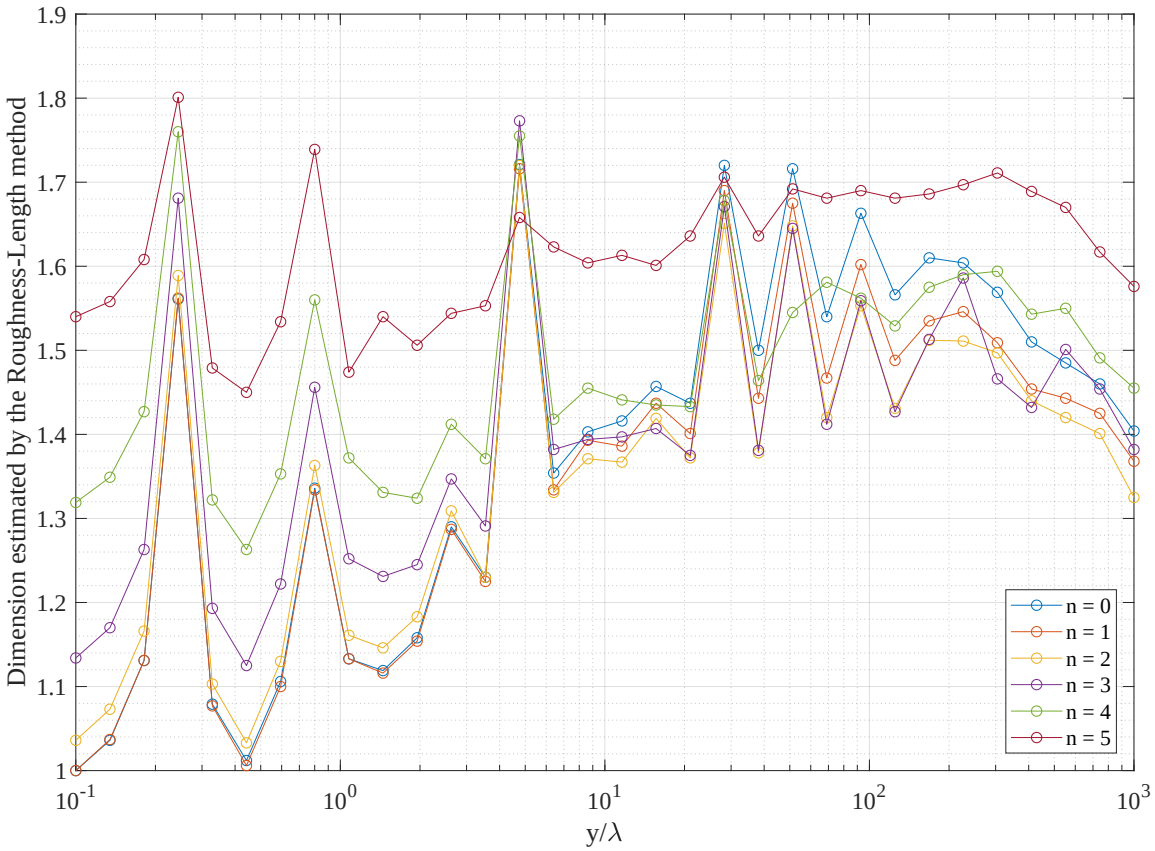

Figure 3.7: Roughness-length estimation of dimension $2\Re e\left(\frac{E_z}{E_0}\right)$ due to a Cantor grating with $a_0 = 250\lambda$.

In order to find out whether the changes in dimension are due to n increasing or the individual slit sizes, a modified construction of the Cantor set was introduced whereby a_n is held fixed (e.g. at 250λ) for all pre-fractal levels. In this alternative structure, the "effective a_0 size" is equal to $a_n 3^n$. An important factor to maintain is the numerical extent of screen on either side of the outer slits. Figure 3.8 shows how quickly a_0 grows with n. Since $\Delta x = \frac{\lambda}{32}$ must be preserved (to

ensure consistency in the BENOIT output), the computation time quickly ramps up with n.

Figure 3.8: A modified Cantor grating with a static a_n value. One can see how quickly the overall grating size grows as n increases.

Unfortunately, when one deploys the modified Cantor set one quickly hits a computational wall; when keeping $\Delta x = \frac{\lambda}{32}$ fixed, for $n = 4$ and $n = 5$ one would require x array sizes of 2,592,001 and 7,776,001 points respectively (and where the a_0 values in the traditional Cantor set would be $20,250\lambda$ and $60,750\lambda$) – far too large for conventional desktop computers to handle in realistic time-scales! Therefore, at this time, only results up to $n = 3$ can be analysed for the modified Cantor set.

n	x domain size	Approx. time for one calculation	No. of calculations	Approx. overall time
0	48,001	150s	1	150s
1	96,000	450s	1	450s
2	288,001	1450s	2	48mins
3	864,001	2600s	4	240 mins

Table 3.1: Approximate computation times for the calculation of the diffracted field at $y \approx 8\lambda$ (the middle y value for logarithmically evenly-spaced y array) for a modified Cantor set with $a_n = 250\lambda$. "No. of calculations" refers to the number of constituent diffraction patterns that must be computed at pre-fractal level $n = 1,2,3$ (divided by 2 for $n > 0$ due to the spatial symmetry of the system).

Deploying the modified Cantor set changes the datasets entirely: instead of an increase of erraticness (cf. Fig. 3.6) Fig. 3.9 presents a similar parabolic shape which is largely preserved in n. Before this second analysis was undertaken, it was completely unknown whether the estimated dimension would be higher or lower as n increases. This work shows that generally it seems to gets lower and therefore it can be said that merely diffracting a plane-wave from a pre-fractal grating does not tend to produce a complex diffracted field. It is difficult to draw any solid conclusions from studying the electric-field results. Both Figs. 3.7 and 3.10 are similar in nature to Fig. 2.12. One could assume that no matter what is studied the estimated dimension appears to be dominated by phase effects [if one wishes to quantify the electric field with distance from the slit, one is probably going to be presented with a graph full of peaks and troughs]. This is a shame as it means one cannot have a good quantitative measure of how electric fields diffracted from complex domains vary in space.

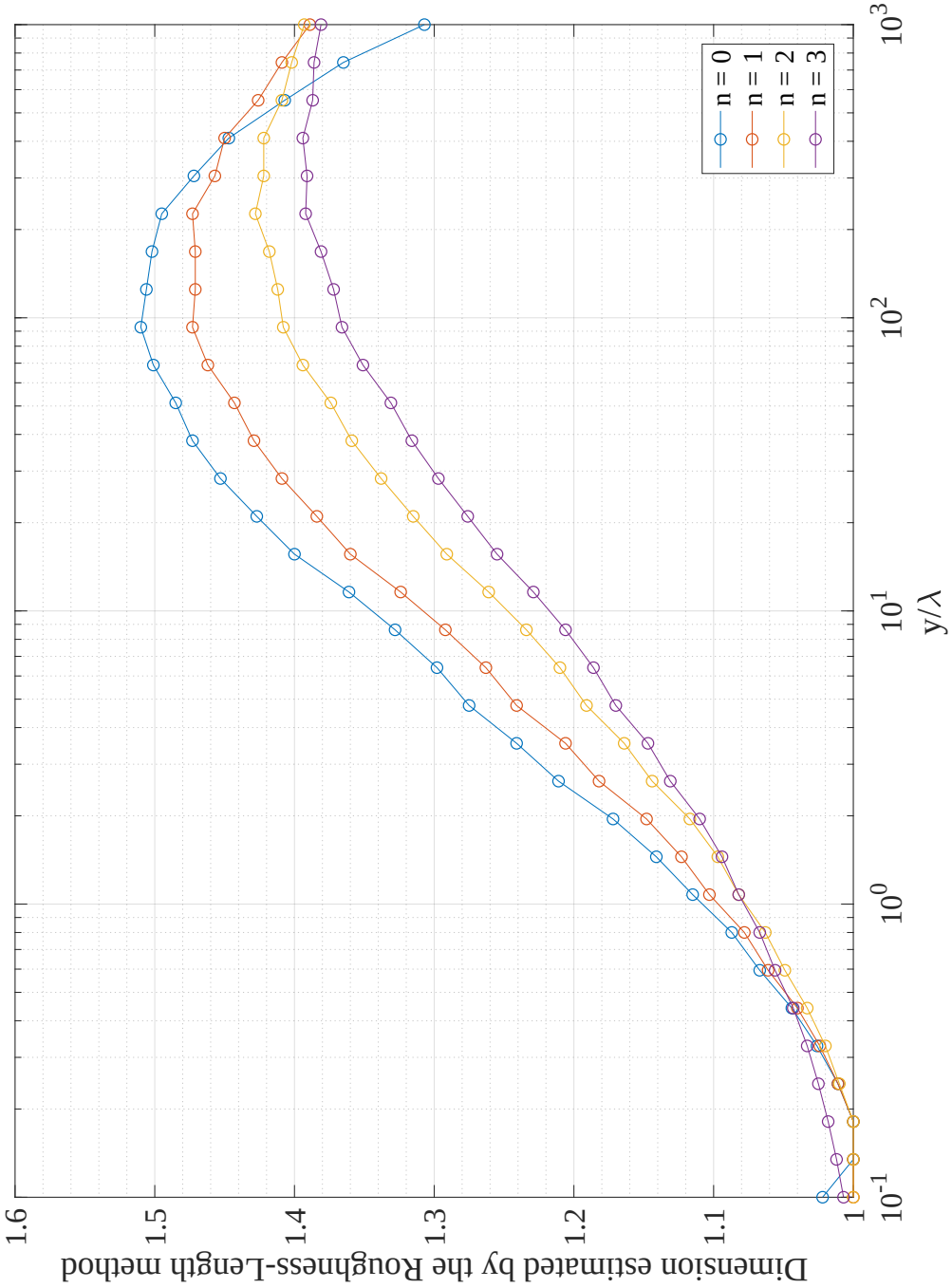

Figure 3.9: Roughness-length estimation of dimension of $\left|\frac{E_z}{E_0}\right|^2$ for a modified Cantor grating with $a_n = 250\lambda$.

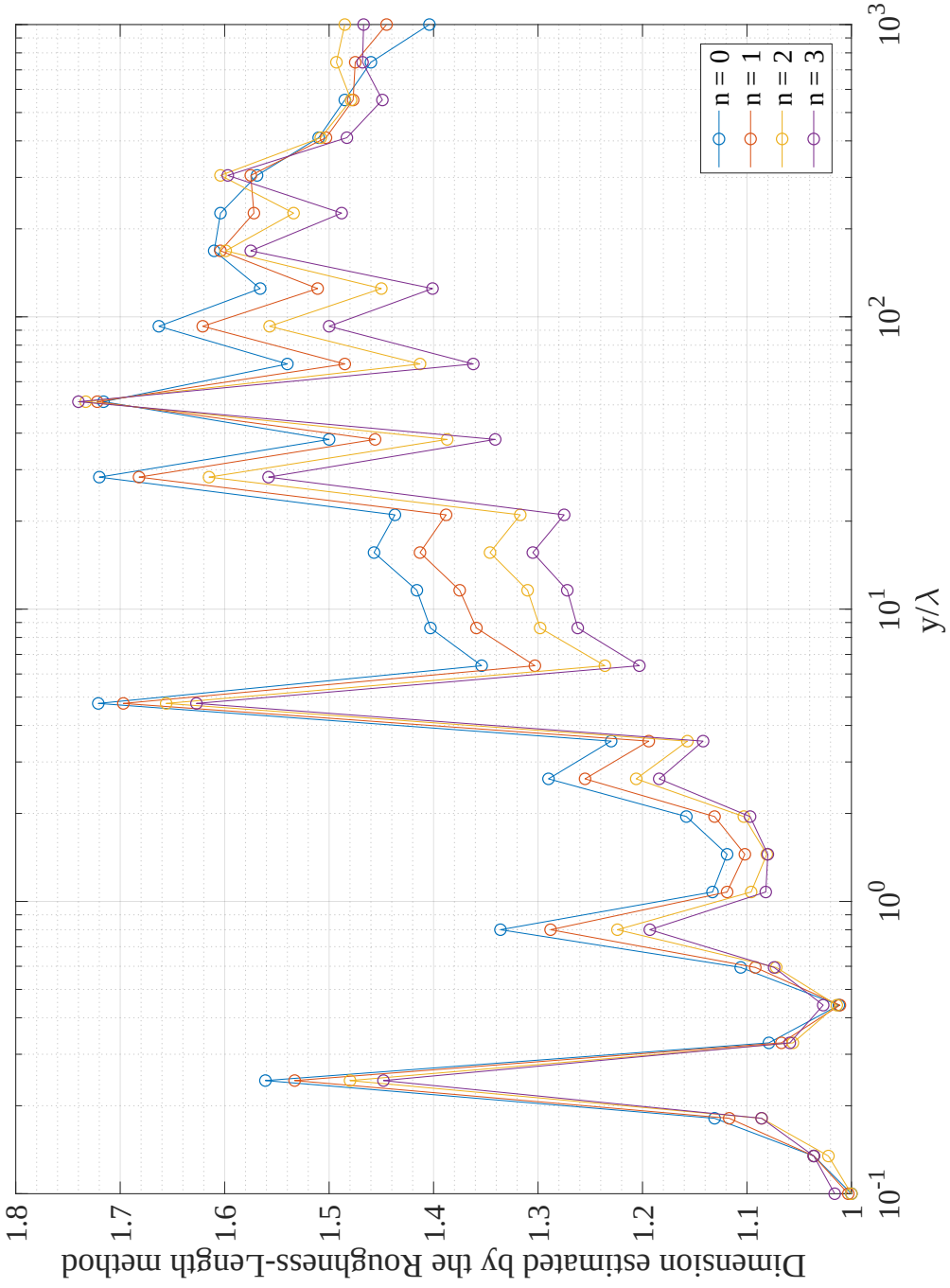

Figure 3.10: Roughness-length estimation of dimension of electric field, $2\Re e\left(\frac{E_z}{E_0}\right)$ for a modified Cantor grating with $a_n = 250\lambda$.

3.3 Magnetic flux density

From knowing the electric field $\mathbf{E}$, one can determine the components of magnetic flux density $\mathbf{B}$ through Maxwell's equations. Since $\mathbf{E} = (0, 0, E_z)$, where for a single-slit aperture

$$E_z(x,y) = \frac{iky}{2} E_0 \int_{-a_0}^{a_0} dx' \frac{H_1^{(1)}(kR)}{R}, \tag{3.3}$$

it follows that $\mathbf{B}$ may be obtained from

$$\mathbf{B} = \frac{1}{i\omega} \nabla \times \mathbf{E} = \frac{1}{i\omega} \begin{vmatrix} \hat{\mathbf{e}}_x & \hat{\mathbf{e}}_y & \hat{\mathbf{e}}_z \\ \frac{\partial}{\partial x} & \frac{\partial}{\partial y} & \frac{\partial}{\partial z} \\ 0 & 0 & E_z \end{vmatrix}. \tag{3.4}$$

Combining Eqs. (3.3) and (3.4), one can show that the B_x and B_y components of the electromagnetic field in the forward half-plane $y > 0$ are given by

$$B_x(x,y) = \frac{1}{i\omega} \frac{\partial}{\partial y} E_z(x,y) \tag{3.5}$$

and

$$B_y(x,y) = -\frac{1}{i\omega} \frac{\partial}{\partial x} E_z(x,y), \tag{3.6}$$

so that

$$B_x(x,y) = \frac{B_0}{2} \int_{-a_0}^{a_0} dx' \frac{H_1^{(1)}(kR)}{R} - y \frac{B_0}{2} \int_{-a_0}^{a_0} dx' ky \frac{H_2^{(1)}(kR)}{R^2} \tag{3.7}$$

and

$$B_y(x,y) = y \frac{B_0}{2} \int_{-a}^{a} dx' \frac{k(x-x')}{R^2} H_2^{(1)}(kR). \tag{3.8}$$

For the TE solution to Maxwell's equations, one immediately sees that B_z must necessarily vanish. Also, one expects B_x to be the dominant part of $\mathbf{B}$ (which is verified numerically). The cylindrical-polar components can be obtained from $B_\phi = \cos(\phi) B_x + \sin(\phi) B_y$ and $B_r = -\sin(\phi) B_x + \cos(\phi) B_y$ [20]. Finally, it can be shown that $\nabla \cdot \mathbf{B} = 0$.

Equations (3.7) and (3.8) can simply be generalized for diffraction from a Cantor-type grating:

$$B_x(x,y) = \frac{B_0}{2} \sum_{j=0}^{2^n-1} \left[\int_{a_-(\Xi_j)}^{a_+(\Xi_j)} dx' \frac{H_1^{(1)}(kR)}{R} - y \int_{-a_0}^{a_0} dx' ky \frac{H_2^{(1)}(kR)}{R^2} \right], \tag{3.9}$$

and

$$B_y(x,y) = y \frac{B_0}{2} \sum_{j=0}^{2^n-1} \int_{-a}^{a} dx' \frac{k(x-x')}{R^2} H_2^{(1)}(kR). \tag{3.10}$$

Results for the electric and magnetic fields (in Cartesian and cylindrical polar forms) for both the traditional and modified Cantor sets (the former with $a_0 = 1.5\lambda$ and latter with $a_n = 1.5\lambda$) are given in the following five pages.

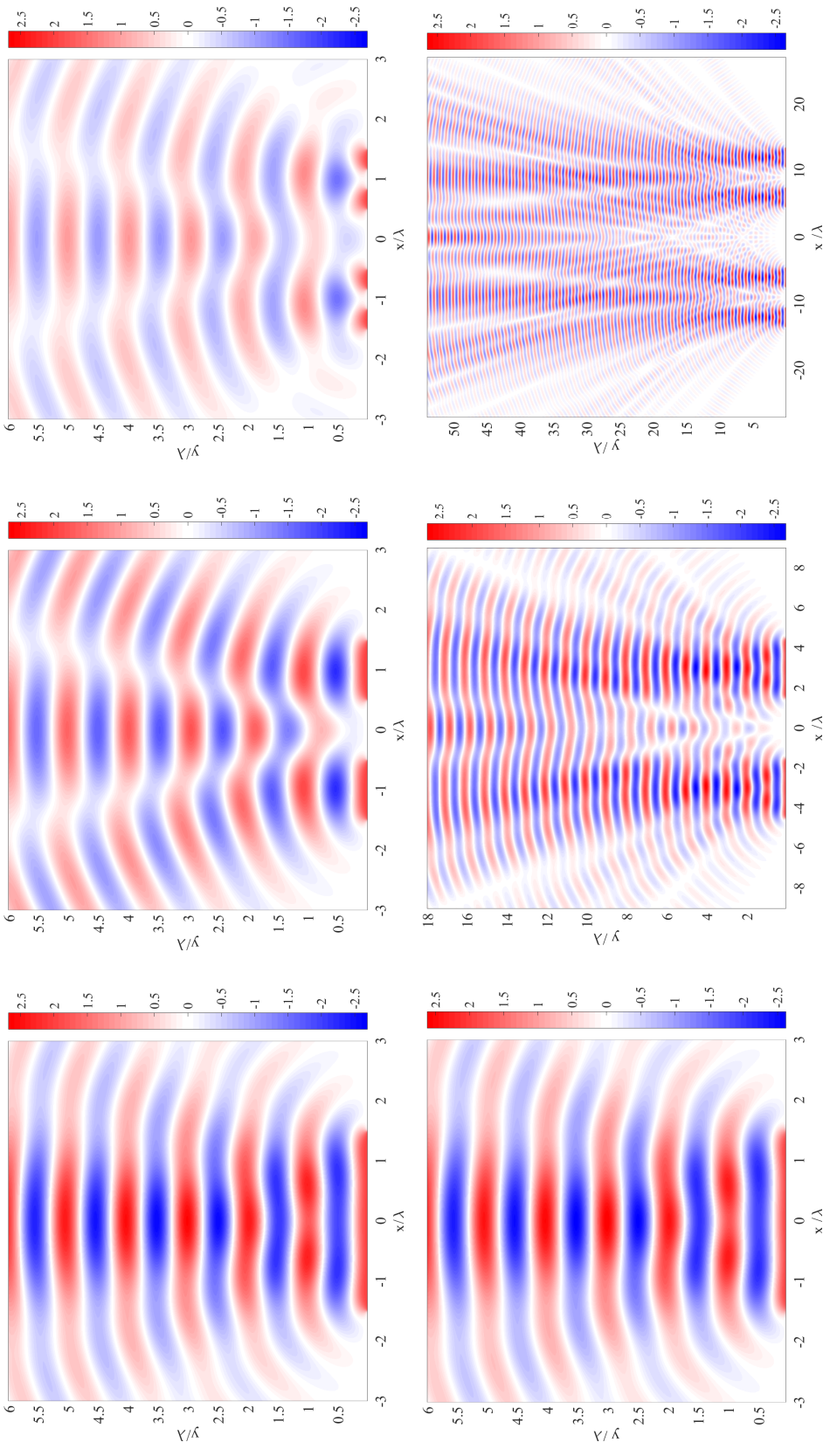

Figure 3.11: A comparison between of the $2\Re e\left(\frac{E_z}{E_0}\right)$ for the zeroth *(left)*, first *(middle)* and second *(right)* pre-fractal level of the Cantor grating for $a_0 = 1.5\lambda$ *(top row)* and $a_n = 1.5\lambda$ *(bottom row)*.

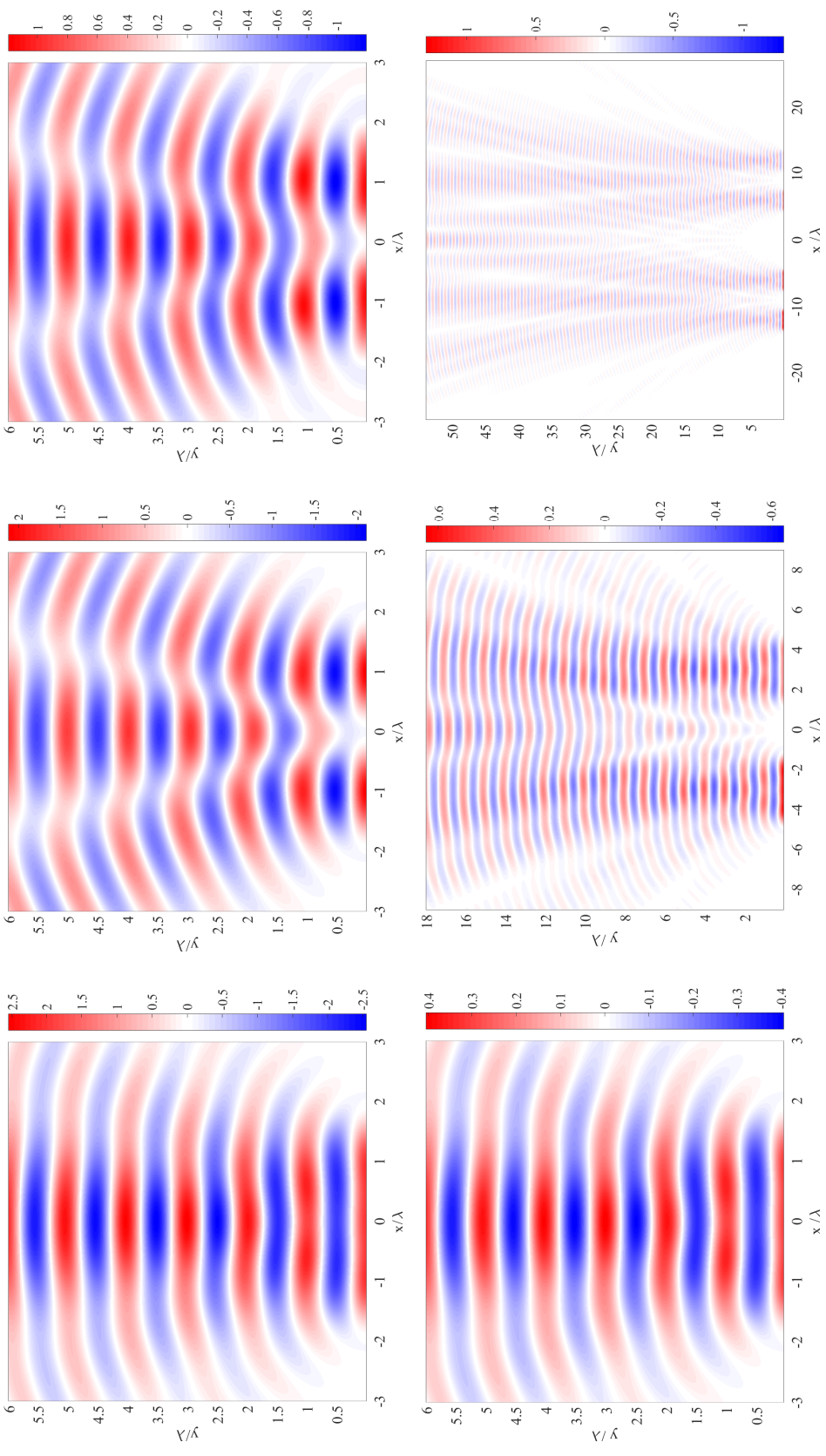

Figure 3.12: A comparison between of the $2\Re e\left(\frac{B_x}{B_0}\right)$ for the zeroth *(left)*, first *(middle)* and second *(right)* pre-fractal level of the Cantor grating for $a_0 = 1.5\lambda$ *(top row)* and $a_n = 1.5\lambda$ *(bottom row)*.

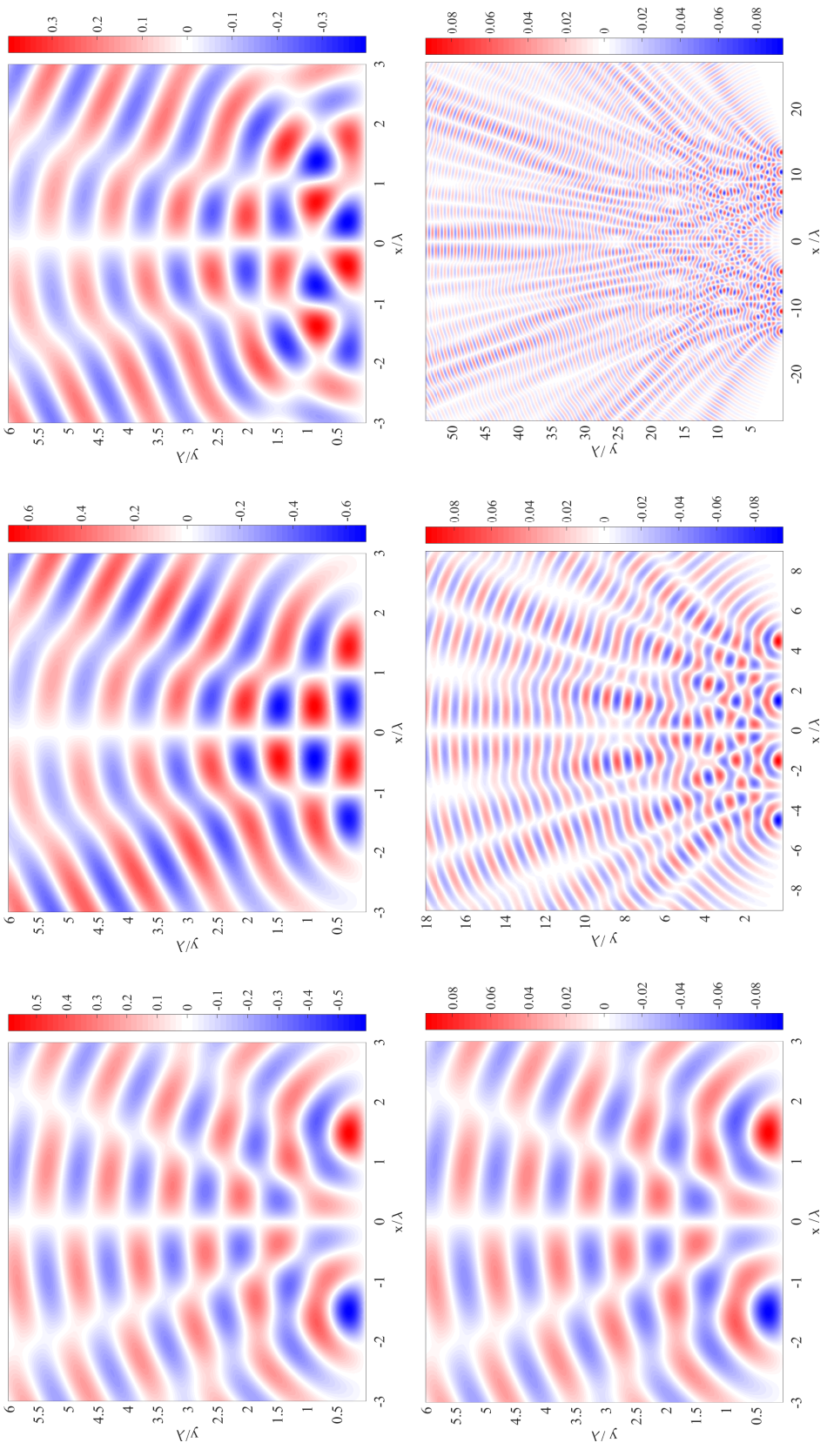

Figure 3.13: A comparison between of the $2\Re e\left(\frac{B_y}{B_0}\right)$ for the zeroth *(left)*, first *(middle)* and second *(right)* pre-fractal level of the Cantor grating for $a_0 = 1.5\lambda$ *(top row)* and $a_n = 1.5\lambda$ *(bottom row)*.

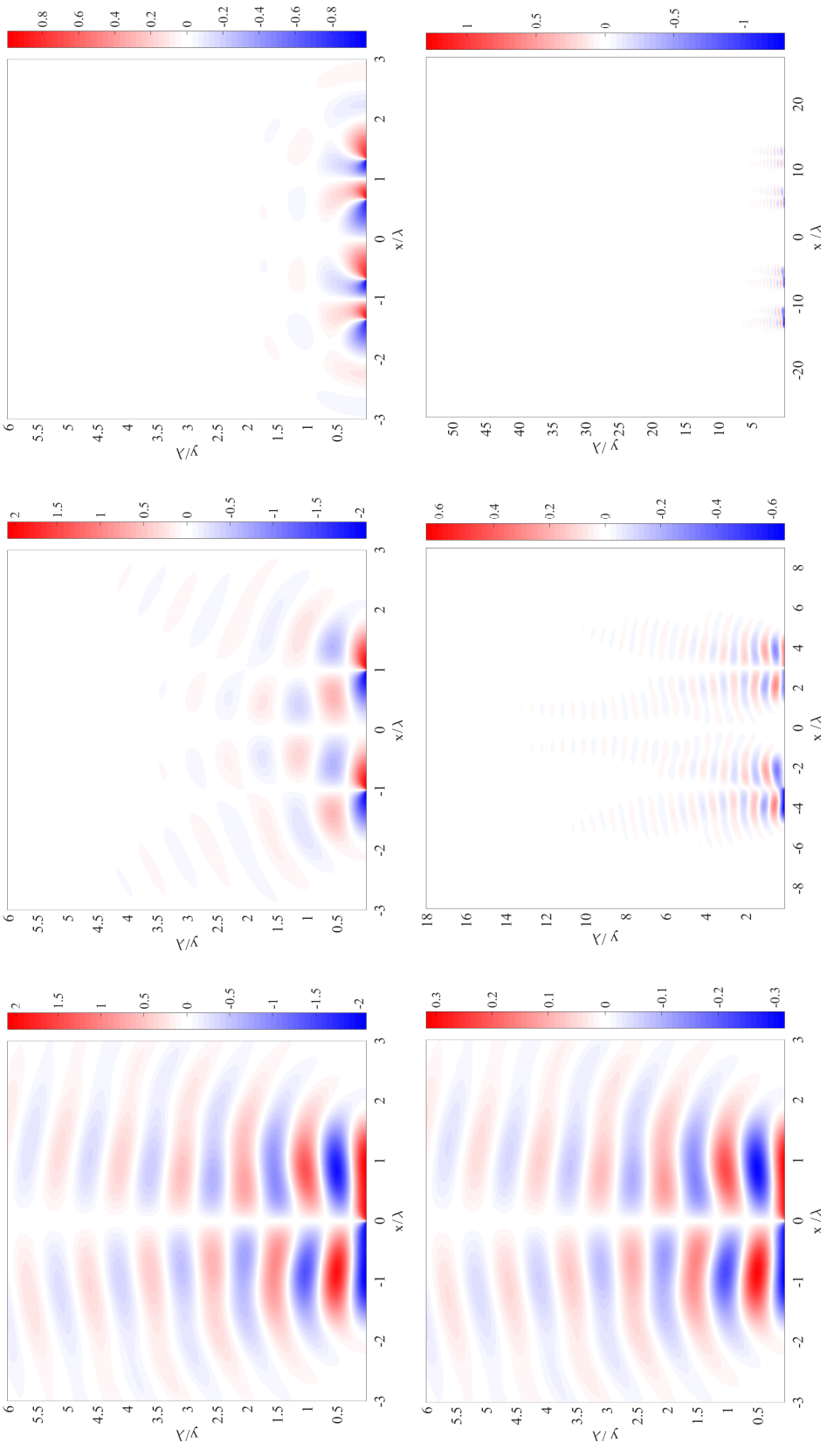

Figure 3.14: A comparison between of the $2\Re e\left(\frac{B_r}{B_0}\right)$ for the zeroth *(left)*, first *(middle)* and second *(right)* pre-fractal level of the Cantor grating for $a_0 = 1.5\lambda$ *(top row)* and $a_n = 1.5\lambda$ *(bottom row)*.

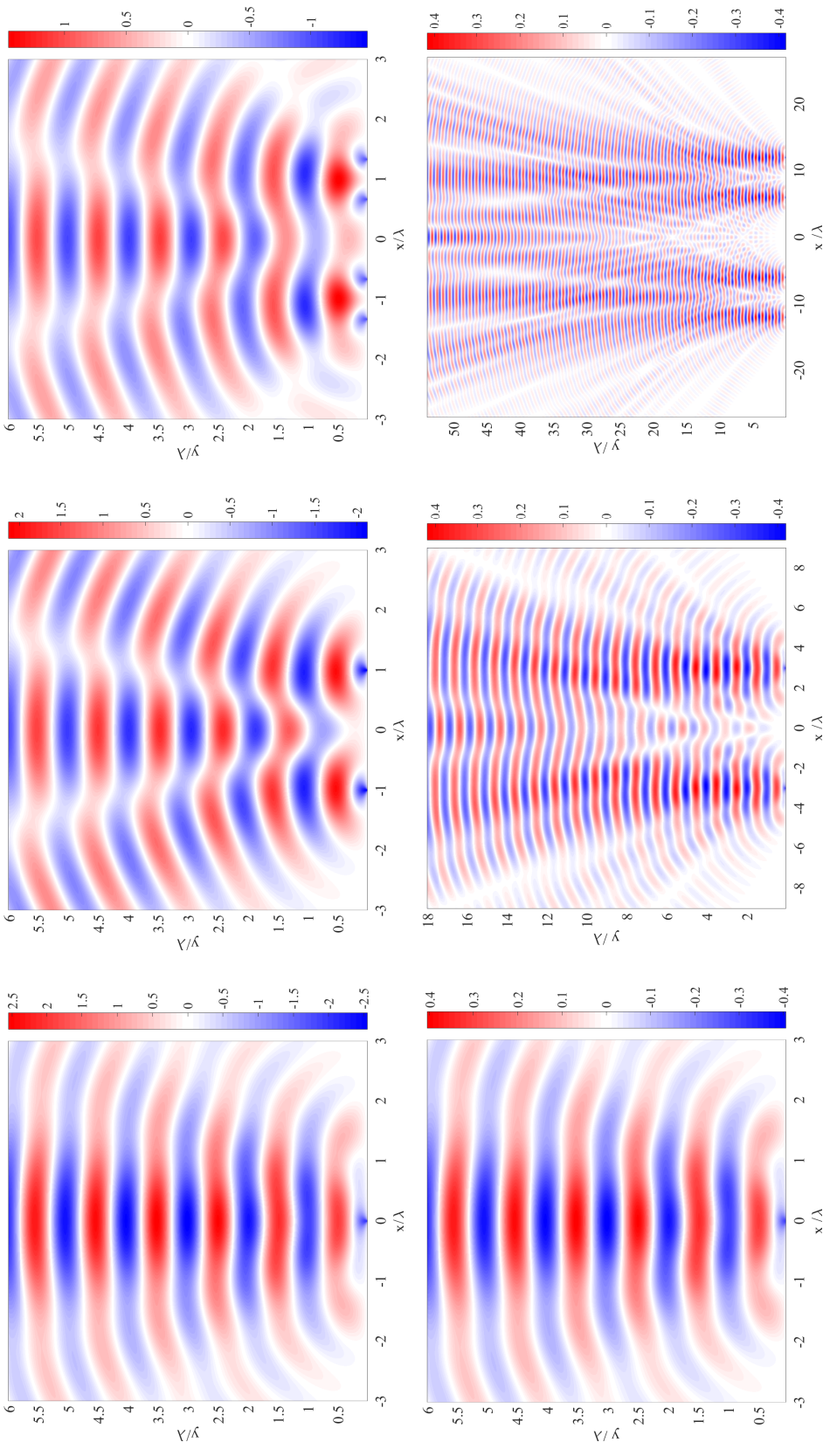

Figure 3.15: A comparison between of the $2\Re e\left(\frac{B_\psi}{B_0}\right)$ for the zeroth *(left)*, first *(middle)* and second *(right)* pre-fractal level of the Cantor grating for $a_0 = 1.5\lambda$ *(top row)* and $a_n = 1.5\lambda$ *(bottom row)*.

3.4 Intensity power spectrum

It is well known that in scalar wave optics, where the Fresnel approximation holds true, the power spectrum for the diffracted electric field in the forward half-plane $y > 0$ beyond the aperture of half-width a_0 is

$$|FT[E_z(x,y)]|^2 = |E_0|^2 \frac{\mathrm{sinc}^2(k_x a_0)}{\pi^2}, \tag{3.11}$$

where k_x is the transverse spatial frequency and FT is the Fourier transform across the x-domain for a fixed y value. In Fourier space, the spectrum extends infinitely along the k_x axis and is independent of y. However, New and Albaho [2] were able to show that the power spectrum for the diffracted intensity has a well-defined cut-off at a spatial frequency $k_c = \frac{2ka_0}{y}$ such that

$$P(k_x,y) = |FT(|E_z|^2)|^2 \begin{cases} |E_0|^2 \frac{\sin^2[k_x a_0(1-\frac{k_x}{k_c})]}{(k_x\pi)^2}, & k_x < k_c \\ 0, & k_x > k_c \end{cases}. \tag{3.12}$$

The intensity power spectrum is often of importance to physics, for instance in the modelling of unstable-resonator modes. It has previously been shown by New *et. al.* [2, 41, 42] that the $\frac{1}{k^2}$ dependence of $P(k_x,y)$ leads to a power-spectrum fractal dimension of $D_{PS} = 1.5$, even though there is no source of multi-scaledness in the problem at hand (namely normal incidence of a plane wave on a single slit). One therefore has to be rather careful when interpreting results even from well-known fractal dimension measures (in particular, the power spectrum method tends to be most widely applicable to random fractals [43, 44]). The idea of New and Alberto, of considering diffracted intensity, may now be applied to the Cantor-grating problem. Figure 3.16 shows the intensity power spectrum,

$$P(k_x,y) = \left|FT[|E_z(x,y)|^2]\right|^2 \tag{3.13}$$

for a single slit with $a_0 = 250\lambda$ at a distance of $y = 10^3\lambda$. The general trend of the log-log plot is evidently a straight line with gradient

$$\beta \equiv \frac{d\log[P(k_x,y)]}{d\log(k_x)} \tag{3.14}$$

and which corresponds to a power spectrum dimension of $D_{PS} = \frac{5-\beta}{2} \approx 1.5$. The recovery of this result demonstrates that the same caution must be exercised when considering RS solutions (where a fractal dimension is obtained for an inherently non-fractal object). Light numerical evidence has been obtained to show that the power-spectrum method fails to give a meaningful prediction for D_{PS} not only for uniform illumination [2] (i.e., in the absence of multiscaled features), but also in the more general case where the input waveform possesses multiscale (pre-fractal) structure. The power spectrum model is unfortunately ever-present in Physics, both theoretical and experimental, even with its shortcomings. More information on exactly why and where it fails is given in [21].

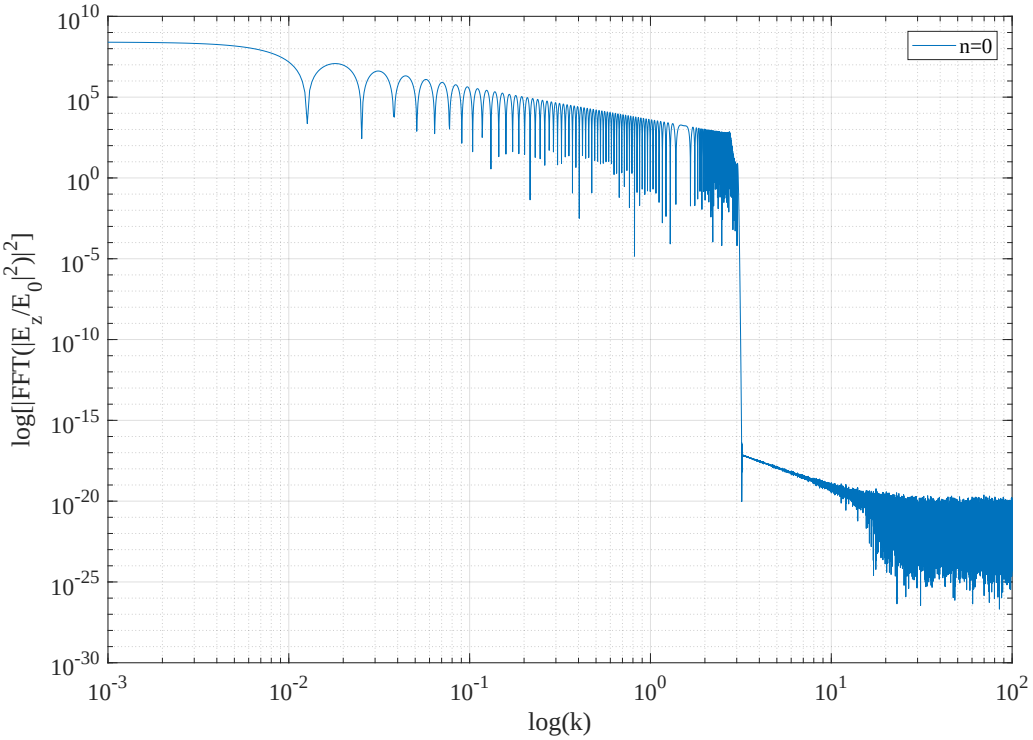

Figure 3.16: Power spectrum of the diffracted intensity for a single slit, width $a_0 = 250\lambda$ at a distance of $y = 10^3\lambda$. The cut-off is at $\lambda k_c \approx \pi$ which is broadly in line with the prediction in [2] (which is not surprising for this quasi-paraxial regime).

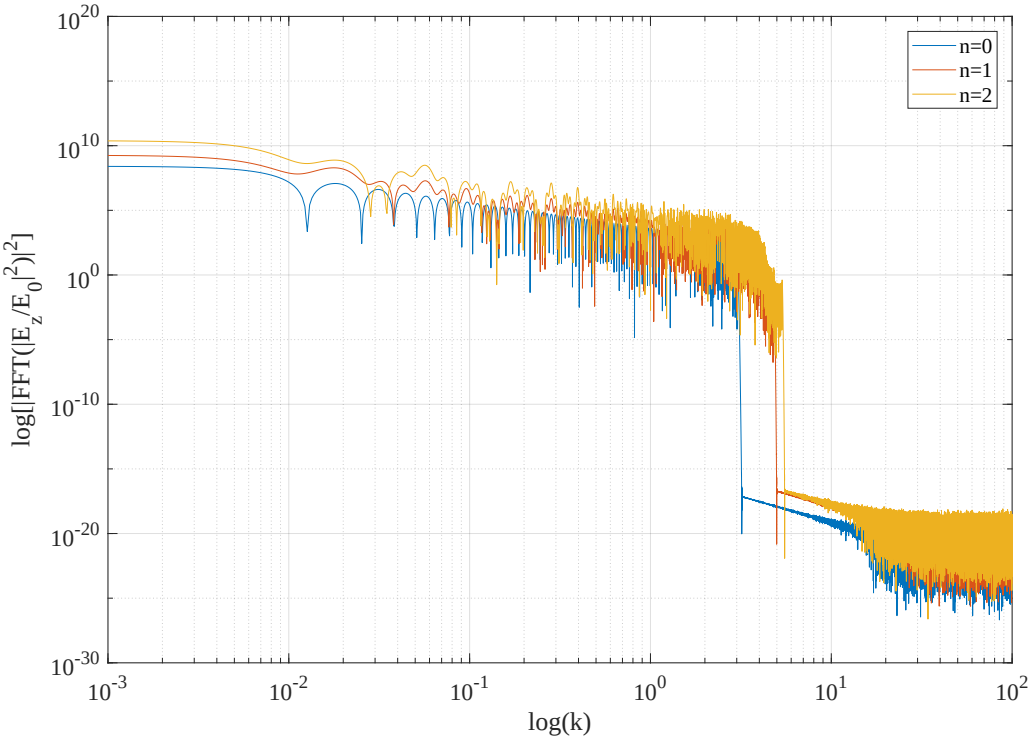

Figure 3.17: The power spectrum of the diffracted intensity for the first three pre-fractal levels of the modified Cantor set with $a_n = 250\lambda$ at a distance of $y = 10^3\lambda$.

Figure 3.17 shows that even for diffraction from multiple slits, the intensity power spectrum gives largely the same quantitative result as for the single slit – the average trend of each of these lines is the same, even if the actual results are shifted slightly. The intensity cut-offs (where the gradients suddenly drop off at around $k = \pi\lambda^{-1}$) for each n are different. This is perhaps due to the quadratic nature of the intensity calculation and the presence of multiple slits. However, it can be seen that the average trend in the gradients is essentially independent of n.

CHAPTER 4

DIFFRACTION OF THE WEIERSTRASS FUNCTION ON A SINGLE SLIT

The previous chapter considered physical geometries concerning the scattering of a normally-incident plane wave from pre-fractal Cantor-set gratings. These scenarios pertain to one particular class of complex-domain problem, where a simple input wave (that is, one with typically uniform, or at most slowly-varying parameters) encounters a multi-scale obstacle. Here, attention is now paid to a different class of problem, namely that where a multi-scale input wave encounters a simple aperture (in this case, a single slit). The single-slit configuration is where most of the early paraxial analyses of fractal diffraction, based on the Fresnel approximation, have been focused. That formulation was in terms of Eq. (1.48), where it was possible to write down an expression for the diffracted field in terms of auxiliary Fresnel functions and Hastings's rational approximations [5, 30]. As discussed in Chapter 2, the paraxial description of the fractal generalization of the knife-edge problem failed in a number of ways. It is not difficult to see that the same level of approximation will also inevitably fail for the single-aperture geometry. In this chapter, Weierstrass illumination of a single slit is revisited but using the RS diffraction integral instead. The deployment of that foundation eliminates altogether the prospect of finding semi-analytical solutions analogous to these of paraxial theory. However, the benefit is that the predictions it makes stand some chance of being quantitatively accurate. For all computations in this chapter, $\Lambda = 2500\lambda$, $\gamma = 3$ and $\epsilon = 1$.

4.1 Illumination with a truncated-Weierstrass wave

The illuminating field $E_z(x',0)$ is taken to be E_0 across the domain of the single slit, $-a_0 \leq x' \leq a_0$ and where $E_z(x',0) = 0$ outside that region. By choosing a truncated-Weierstrass wave at $y = 0$,

the RS diffraction integral of Eq. (1.34) becomes

$$E_z(x,y) = \frac{iky}{2} E_0 \int_{-a_0}^{a_0} dx' \frac{H_1^{(1)}(kR)}{R} \left[1 + \epsilon \sum_{\nu=0}^{N} \frac{1}{\gamma^{(2-D_0)\nu}} \cos\left(\frac{2\pi}{\Lambda} \gamma^\nu x' + \phi_\nu \right) \right], \tag{4.1}$$

where, recall, ϵ controls the strength of the pre-fractal modulation and N determines the cut-off spatial frequency. In contrast to the Fresnel case [5], the RS problem is predominately numerical because one cannot evaluate exactly the constituent integrals (involving products of $\frac{1}{R}$, Hankel functions and cosines); moreover, to introduce approximations at this stage would undermine the purpose of the research. However, one may, of course, recover all the previous analytical predictions from paraxial theory in the limit $kR \gg \mathcal{O}(1)$ and $\frac{|x|}{y} \ll \mathcal{O}(1)$ (see the asymptotic analysis of Section 1.3.1), beginning with

$$u(x,y) \approx E_0 \sqrt{\frac{k}{\pi y}} \frac{1+i}{2i} \int_{-a_0}^{a_0} dx' \exp\left[\frac{ik(x-x')^2}{2y} \right] \left[1 + \epsilon \sum_{\nu=0}^{N} \frac{1}{\gamma^{(2-D_0)\nu}} \cos\left(\frac{2\pi}{\Lambda} \gamma^\nu x' + \phi_\nu \right) \right]. \tag{4.2}$$

Previously, it has been argued that the Weierstrass summation must have a cut-off (here, at $\nu = N$) to avoid an unphysical (i.e., complex) propagation angle, θ_ν (see Sec. 2.2). Another reason is that for $N \to \infty$, the integrand becomes continuous everywhere but differentiable nowhere. This second feature is potentially problematic from another physical perspective, since it would seem to rule out the possibility of an arbitrarily "rough" electromagnetic wave having a magnetic component. That is, in the TE solution, the component $B_y = \frac{1}{-i\omega} \frac{\partial E_z}{\partial x}$ is unlikely to exist and $\nabla \cdot \mathbf{B}$ would be undefined in the plane of the screen. However, the RS integral would appear to smooth out structure even on vanishingly-small scales so that, away from the screen, the components of the electromagnetic field become well-behaved and uniformly differentiable.

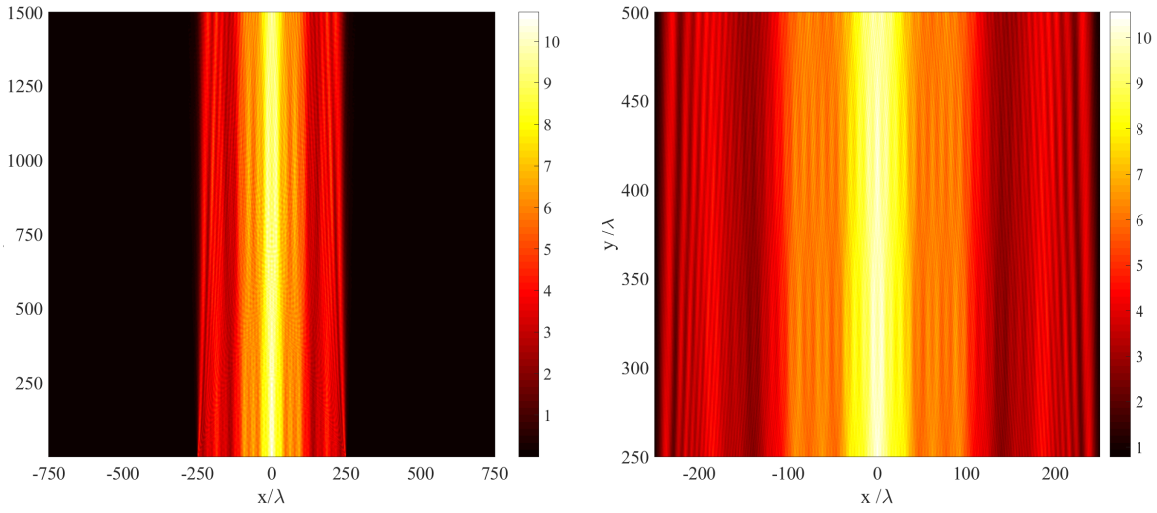

Figure 4.1: Intensity $\left| \frac{E_z}{E_0} \right|^2$ for a diffracted Weierstrass-type wave with $D_0 = 1.5$ at a single-slit aperture with $a_0 = 250\lambda$. A section of the (x, y) forward half-plane (*left*) and magnification beginning to show some smaller-scale features (*right*).

For illustrative purposes, one might compare the predictions of Eq. (4.1) that are shown in Fig. 4.1 to the left hand plot in Fig 3.5. There are some noticeable differences. Firstly, the peak intensity is much greater for the case of pre-fractal illumination – this is not surprising due to the relatively large amplitude coefficients at low ν and when D_0 is moderate to large. Secondly, one can perceive a 'knotted structure' running through the intensity pattern (*cf* right-hand pane of Fig. 4.1).

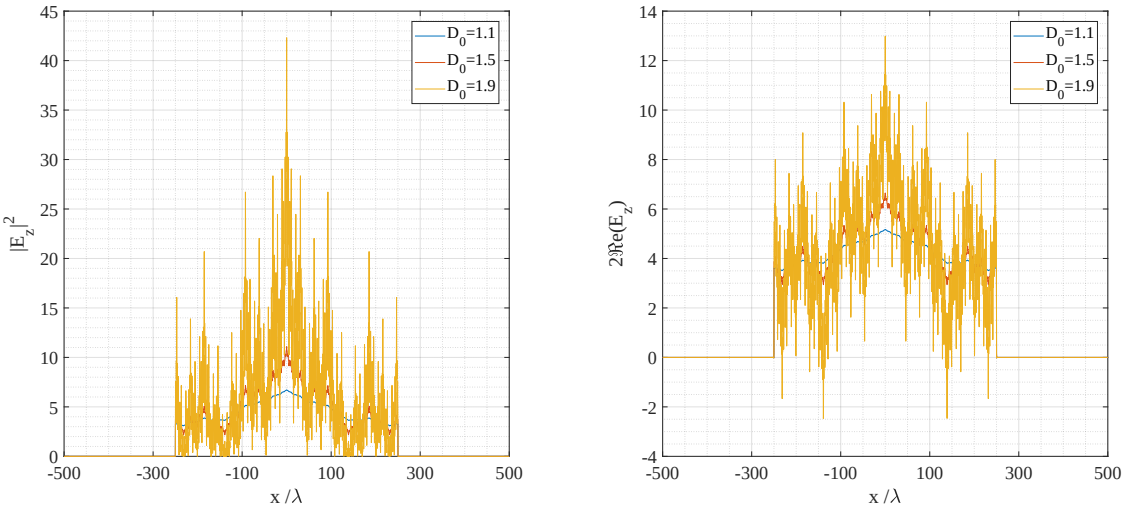

Figure 4.2: 1D slices of the diffraction of the Weierstrass-type input wave at $a_0 = 250\lambda$ and $y = 10^{-1}\lambda$. Intensity $\left|\frac{E_z}{E_0}\right|^2$ (*left*) and electric field $2\Re e\left(\frac{E_z}{E_0}\right)$ (*right*).

The more detailed magnifications shown in Figs. 4.3 to 4.5 reveal how as D_0 grows, the 'knotted' structure becomes increasingly prevalent.

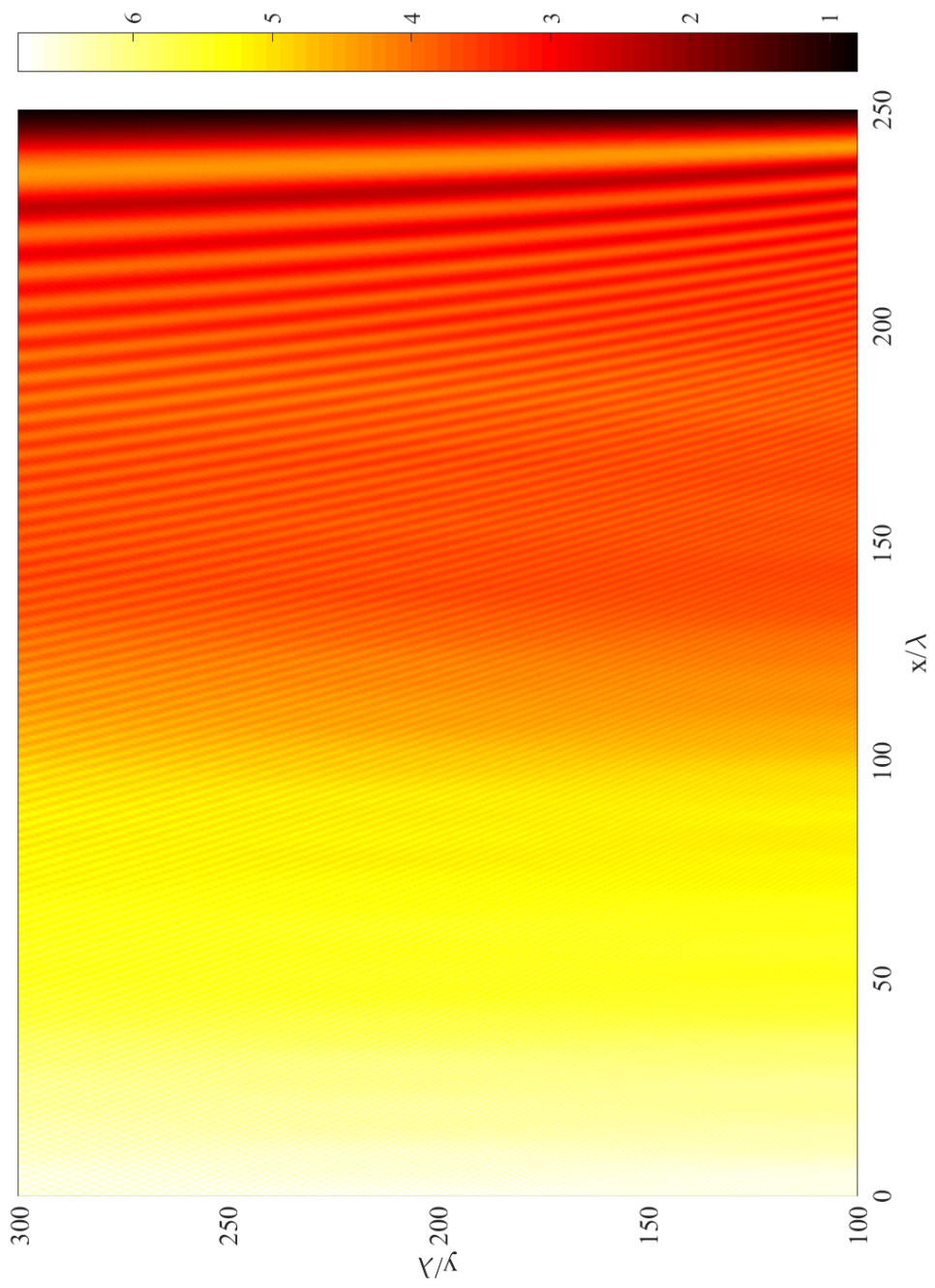

Figure 4.3: A detailed plot of the intensity, $\left|\frac{E_z}{E_0}\right|^2$, of the diffraction pattern formed from a truncated-Weierstrass input wave with $D_0 = 1.1$.

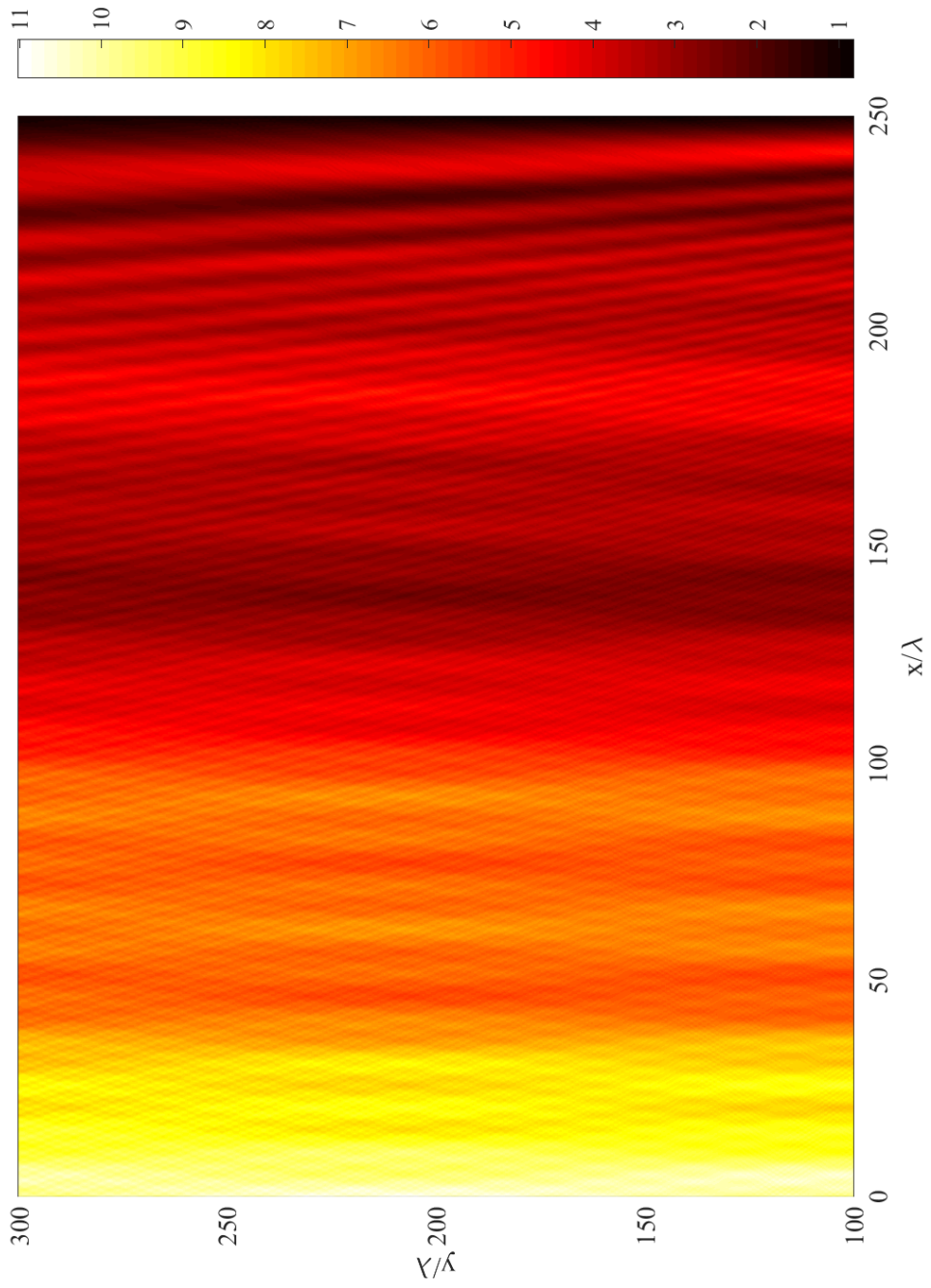

Figure 4.4: A detailed plot of the intensity, $\left|\frac{E_z}{E_0}\right|^2$, of the diffraction pattern formed from a truncated-Weierstrass input wave with $D_0 = 1.5$.

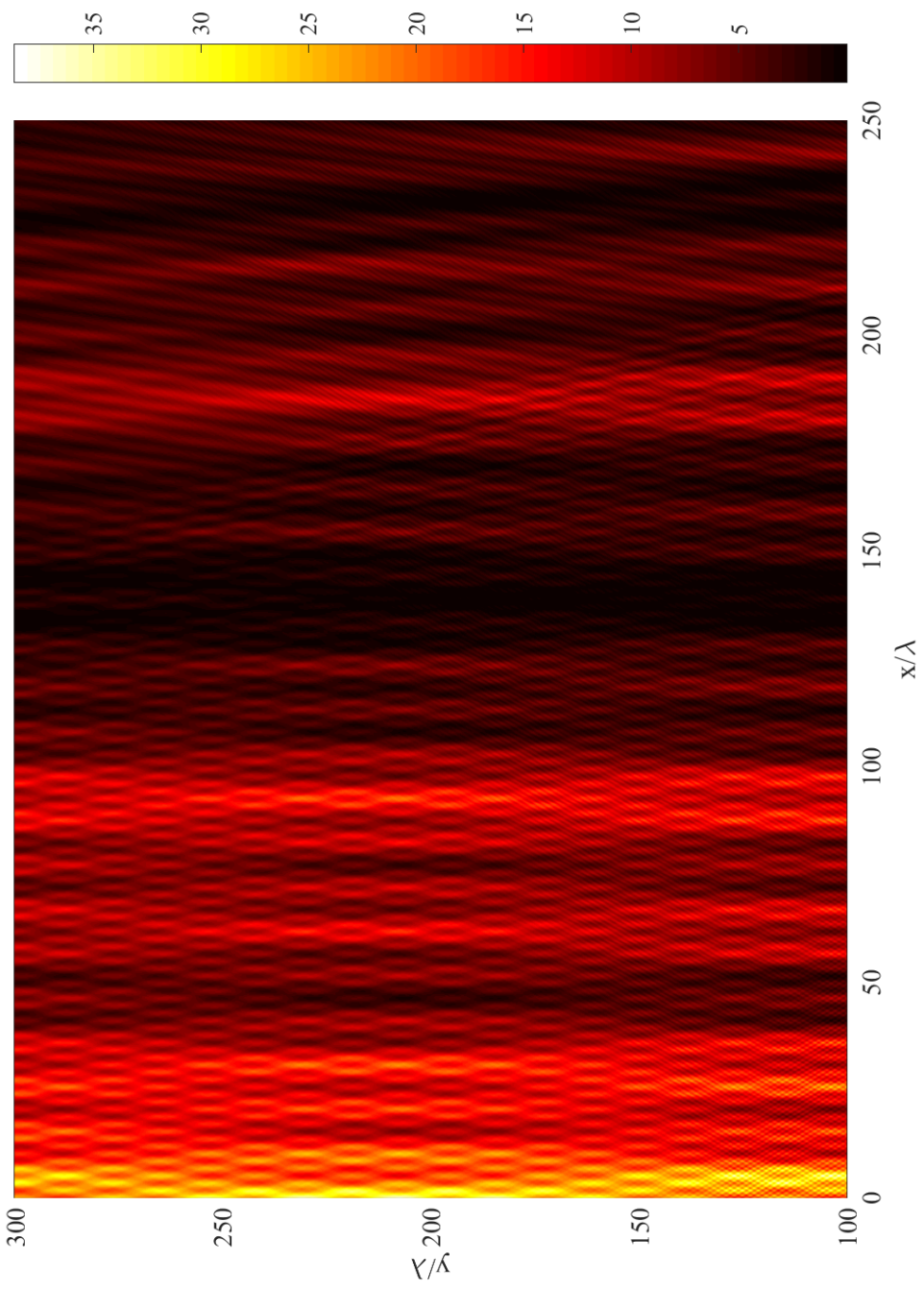

Figure 4.5: A detailed plot of the intensity, $\left|\frac{E_z}{E_0}\right|^2$, of the diffraction pattern formed from a truncated-Weierstrass input wave with $D_0 = 1.9$.

4.2 Dimension estimation

A preliminary analysis of the dimension associated with RS intensity patterns begins by considering the relative importance of the plane-wave component in isolation (i.e., where one sets $\epsilon = 0$). The roughness-length dimension in that case is relatively smooth and well-behaved when seeking variations with distance y (see Fig. 4.6); one finds essentially the same curve as the $n = 0$ result in Fig. 3.6, as expected.

One might then consider the dimension associated solely with the Weierstrass-type component of the illumination. The corresponding curve is much more erratic, with a region of fairly rapid fluctuations. Perhaps the more striking feature is that, beyond $y \approx 3\lambda$, the estimated dimension of the pattern associated with a complex waveform is actually **less** than that associated with the uniform waveform. This result is unexpected and, at present, no obvious explanation for such a strange feature is immediately apparent. It might, for instance, be regarded as a limitation inherent to the roughness-length dimension measure, just as the power-spectrum is potentially problematic is assessing dimension for a diffracted plane wave. But whatever the explanation, it is a good example to illustrate the difficulties found when trying to quantify the complexity of scattered pre-fractal waves.

Figure 4.6 also shows the combined effect of the estimated dimension for the total field (including plane wave and Weierstrass components). The curve lies somewhere between the 'plane-wave only' and the 'Weierstrass-only' results. Similar qualitative effects have been observed for the electric field (see Fig. 4.7).

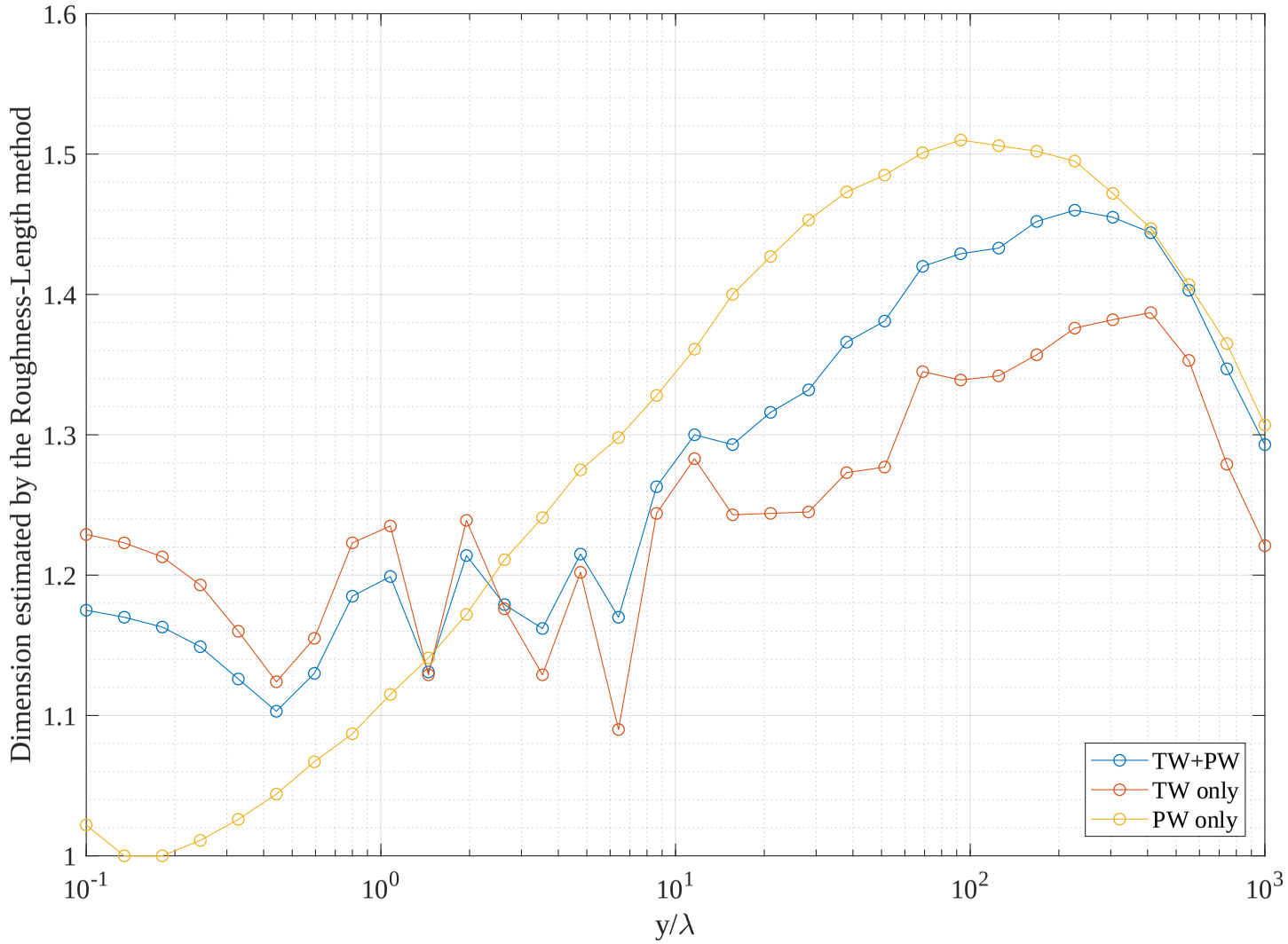

Figure 4.6: Estimated roughness-length dimension for $\left|\frac{E_z}{E_0}\right|^2$ when considering the components in isolation and when combined for $D_0 = 1.3$ where "TW" stands for an input wave of a single truncated-Weierstrass wave input wave and "PW" stands for a plane input wave. "TW+PW" is a combination of the two (i.e., in Eq. (4.1)).

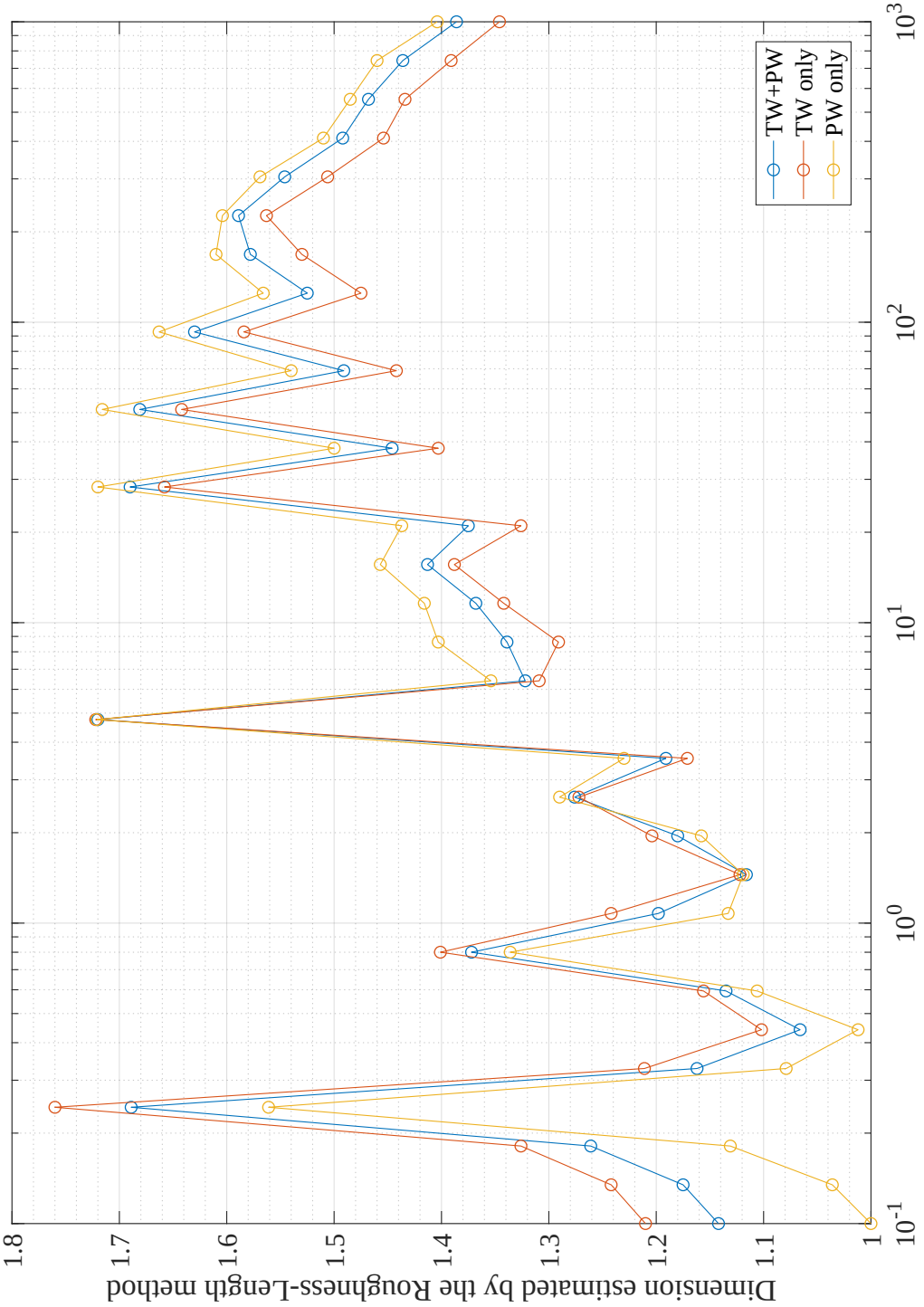

Figure 4.7: Estimated roughness-length dimension for electric field, $2\Re e\left(\frac{E_z}{E_0}\right)$, when considering components in isolation and when combined for $D_0 = 1.3$ where "TW" stands for an input wave of a single truncated-Weierstrass wave input wave and "PW" stands for a plane input wave. "TW+PW" is a combination of the two (i.e., in Eq. (4.1)).

Attention is now turned to estimating the roughness-length dimension for complete intensity patterns (when both plane-wave and Weierstrass components are included) (see Fig. 4.8). For lower D_0 values, the curve follows quite closely the pure plane-wave result. This is not surprising since the amplitudes in the Weierstrass function $\gamma^{-(2-D_0)\nu}$ fall off rapidly with ν. However, as D_0 increases, the curves start to become more erratic, developing quite profound peaks and troughs whose position in y appear to be largely independent of D_0. Some trends in the dataset can now be identified from Figs. 4.8 and 4.9:

- As distance from the slit increases, the dimension estimation seems to begin converging (of course, longer distances are required to test that idea more rigorously). However, one may reasonably expect the dimension to approach 1 as $y \to \infty$. This is because in the far-field limit, the diffraction pattern must approach a sequence of geometrically-separated *sinc* functions, each of which has the same scale-length. Such a pattern, by any measure, cannot be fractal.

- The estimated dimension at very short distances (e.g. $y = 10^{-1}\lambda$) is always less than D_0. This feature is perhaps to be expected whenever one truncates the Weierstrass at any finite N. That is, the truncated series $w_N(x)$ from Eq. (1.18) can never be as complex or area-filling as the curve $W(x)$ in Eq. (1.3) for $N < \infty$.

- Beyond a distance of $y = 10^2\lambda$, the erratic fluctuations in the curves tend to settle down and the estimated dimension appears to be slightly better behaved.

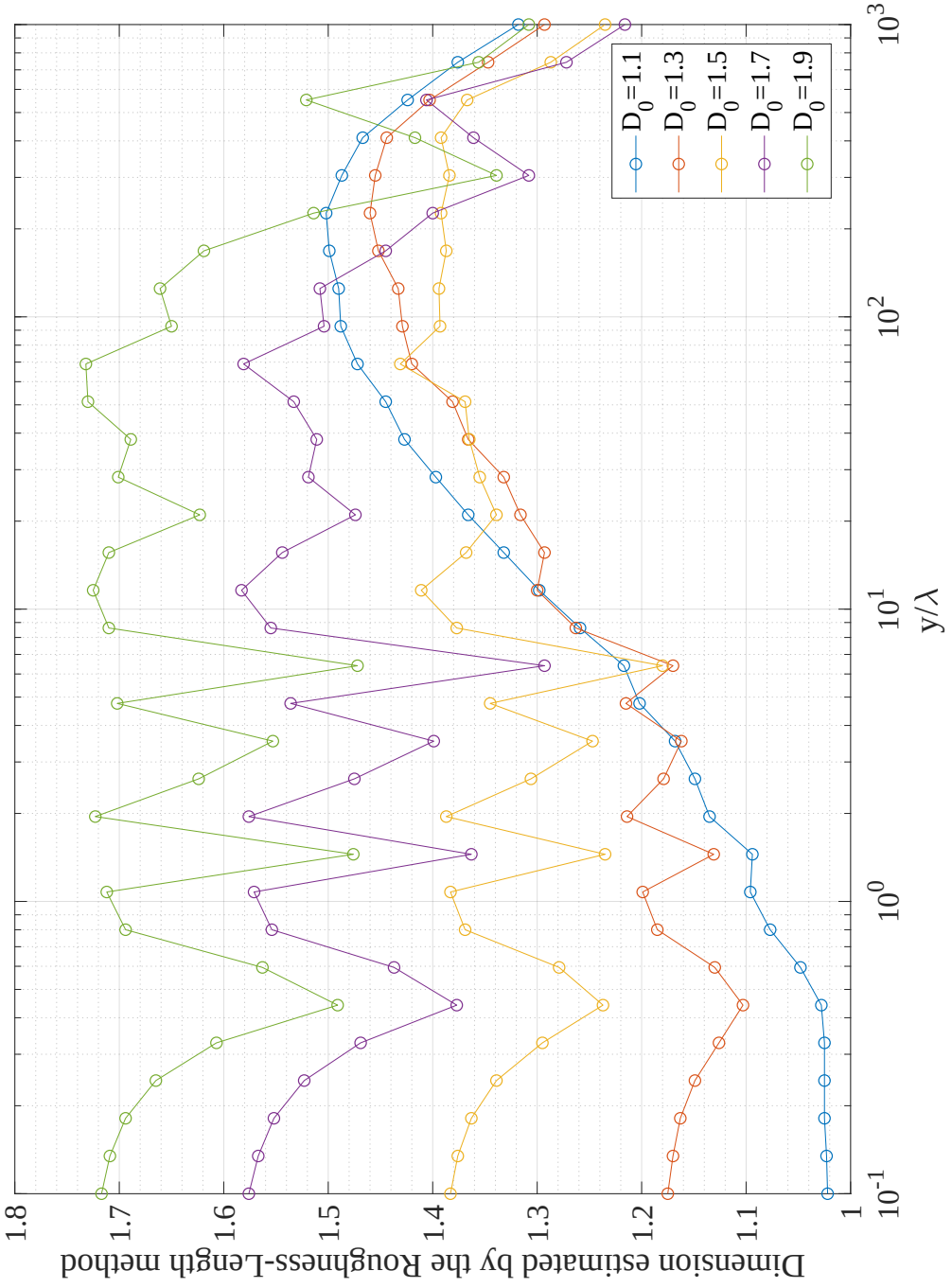

Figure 4.8: Comparisons of roughness-length estimation of dimension for intensity, $\left|\frac{E_z}{E_0}\right|^2$ when the illuminating field is of the Weierstrass type.

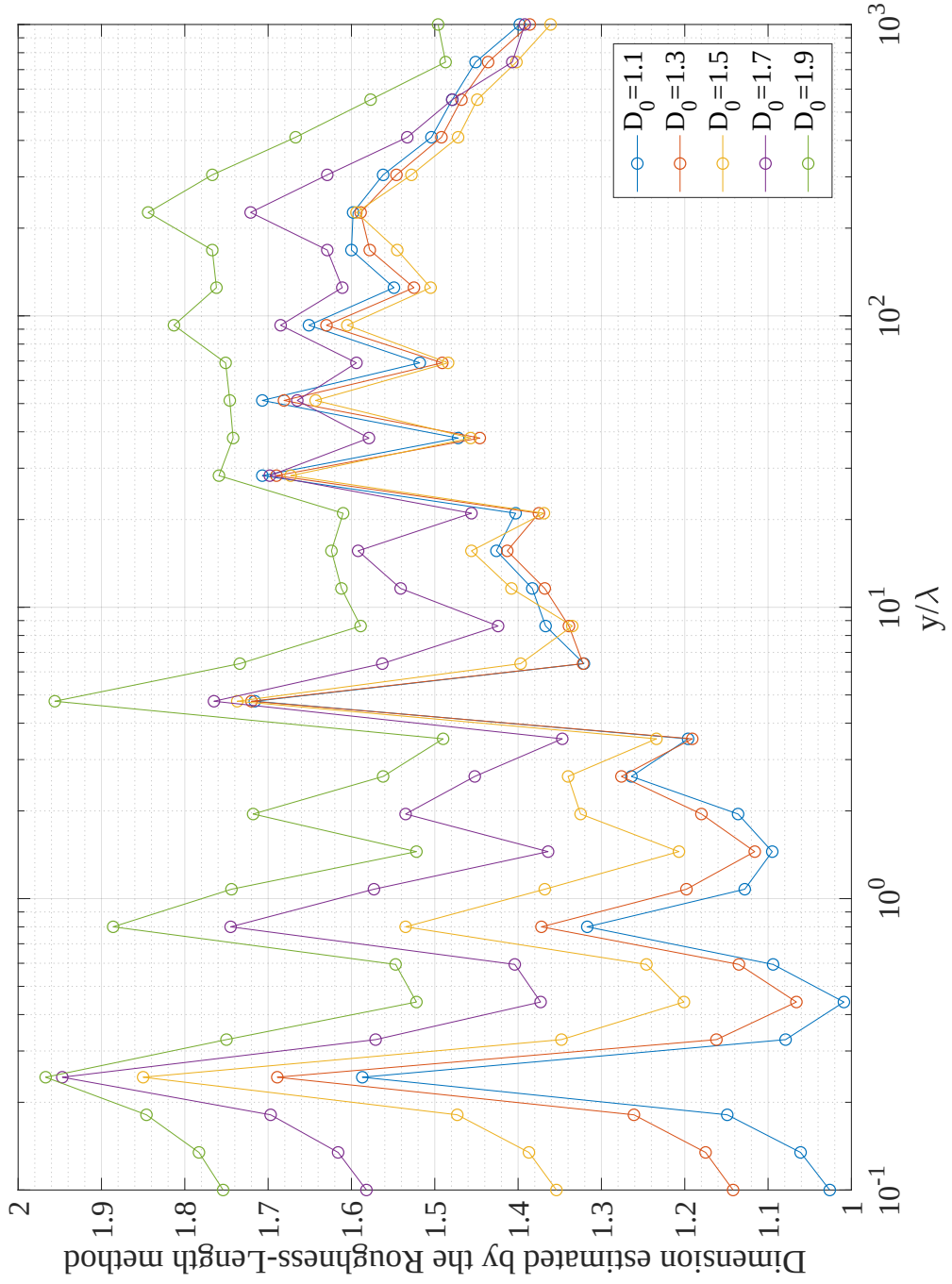

Figure 4.9: Comparisons of roughness-length estimation of dimension for electric field, $2\Re e(\frac{E_z}{E_0})$ when the illuminating field is of the Weierstrass type.

4.3 Variations of the Weierstrass single slit problem

All the numerical work considered in the previous section has been, specifically, for the case of $\phi_\nu = 0$ – i.e., all the phase shifts in the Weierstrass summation were inherently set to zero. There were two main reasons for that. Firstly, the parameter D_0 has been proven to be the Hausdorff dimension for the Weierstrass function for the case of $\phi_\nu = 0$, $\forall \nu$. Secondly, non-zero phases generally produce an asymmetric function; diffraction will then transform one asymmetric signal into another similarly asymmetric signal (and therefore it is difficult to identify the effect of diffraction). Two particular cases for non-vanishing phases are given in Fig. 4.10.

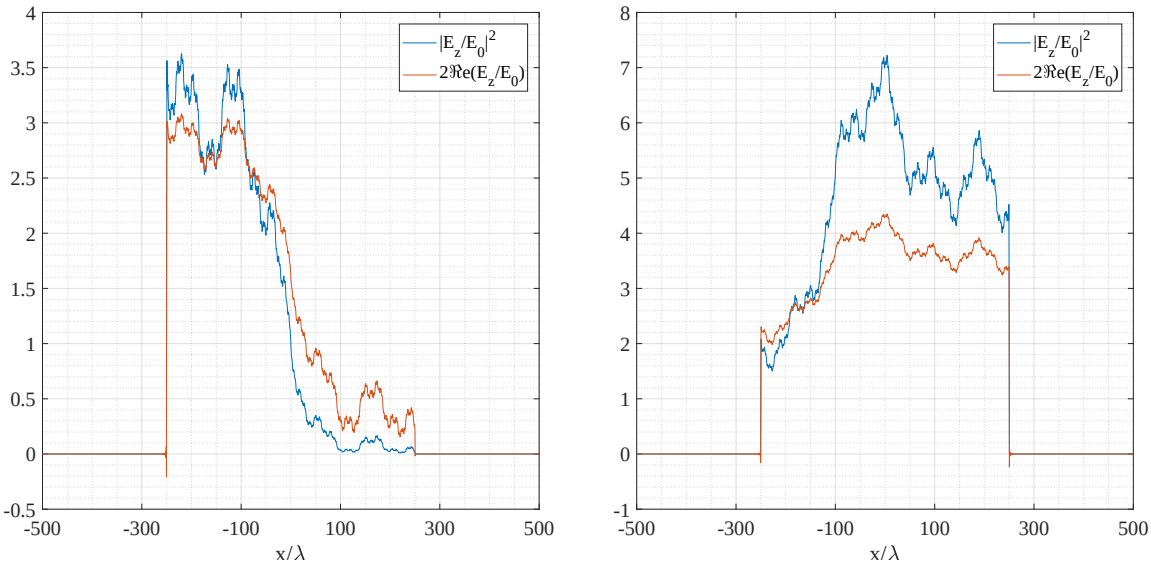

Figure 4.10: Diffracted field at $y = 10^{-1}\lambda$ for $\phi = \frac{\pi}{2}$ (*left*) and a ϕ_ν chosen uniformly at random in the interval $[0, 2\pi)$ (*right*).

Results are shown in Figs. 4.11 and 4.12 for $D_0 = 1.3$ when the phase shifts change. In each graph, seven of the eight curves are for cases where ϕ_ν all assume the same value, whereas the last curve in each graph has randomly chosen $\{\phi_\nu\}$. This 'misfit' result happens for $\phi_\nu = \pi$, whose effect with regards to the input wave is to simply implement the inversion $\epsilon \to -\epsilon$ (and therefore the Weierstrass-type wave is in anti-phase relative to the normally-incident plane wave component). All the other results for the different ϕ_ν values generally follow the results of the $\phi_\nu = 0$ curve and show a very strong qualitative and quantitative similarities – even when the input waves look rather different.

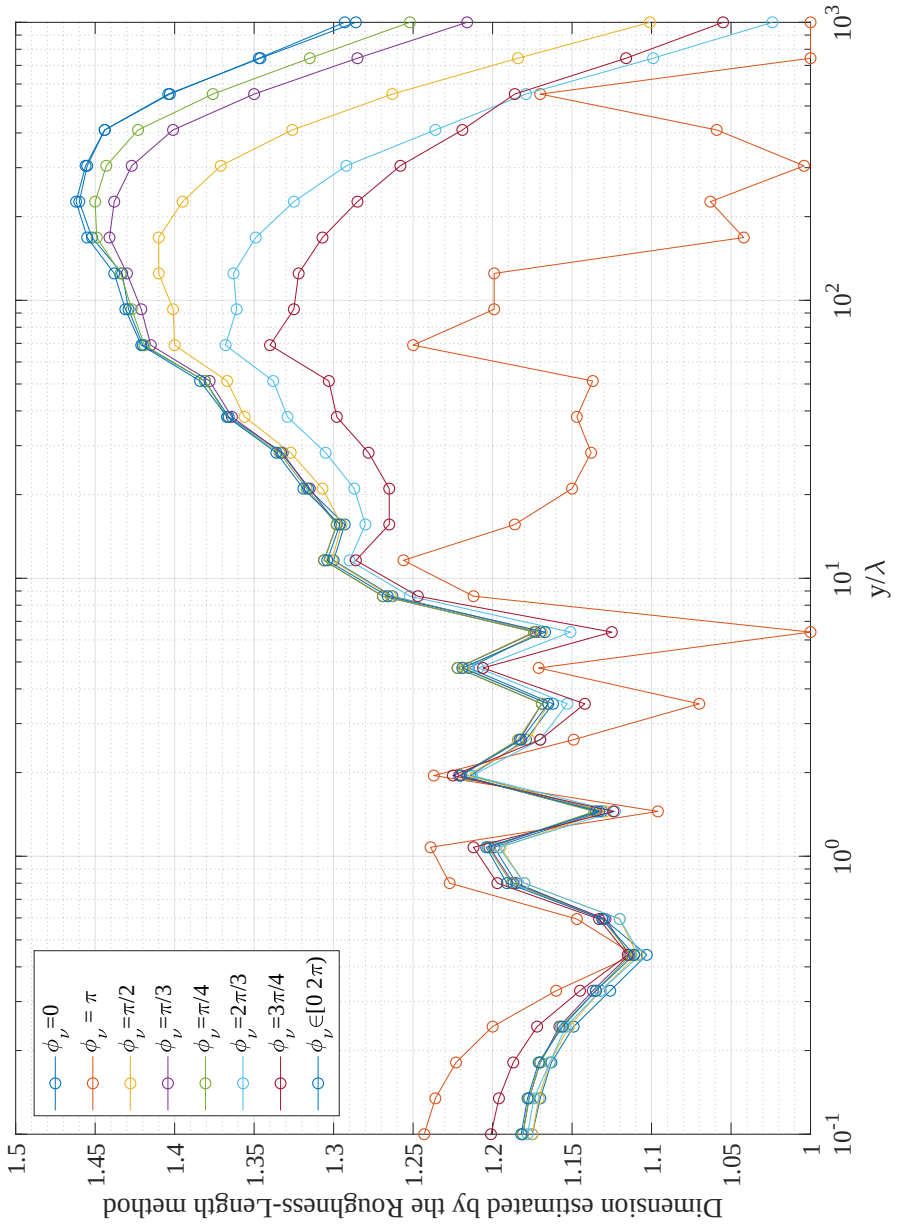

Figure 4.11: Graph showing the differences in the estimated dimension of intensity $\left|\frac{E_z}{E_0}\right|^2$ when a single slit is illuminated by a truncated-Weierstrass wave with $D_0 = 1.3$. The varying parameter is the phase, ϕ_ν.

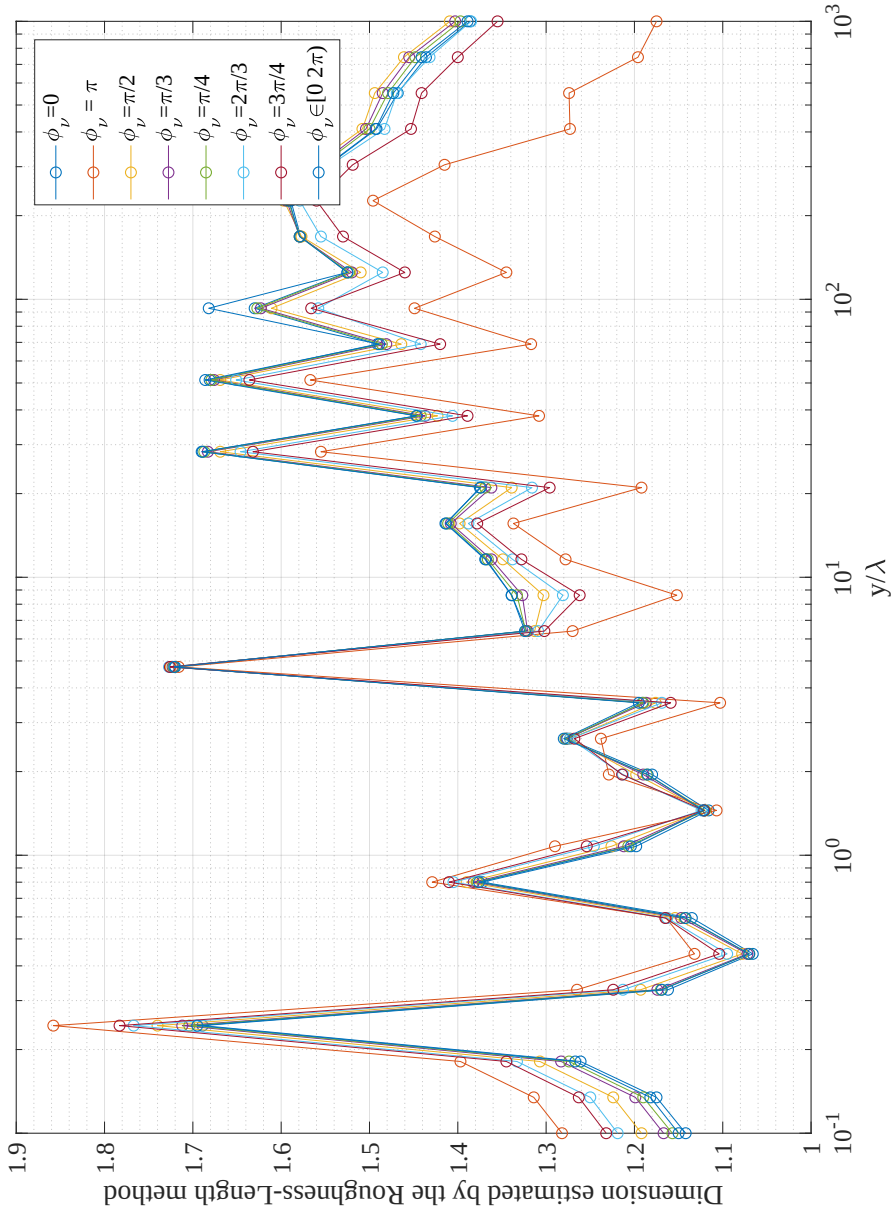

Figure 4.12: Graph showing the differences in the estimated dimension of $2\Re e\left(\frac{E_z}{E_0}\right)$ when a single slit is illuminated bu a truncated-Weierstrass wave with $D_0 = 1.3$. The varying parameter is the phase, ϕ_ν.

4.4 Fractal dimension and limits

At this juncture, it seems appropriate to consider and comment on the notion of fractal dimension and how it pertains to the work in this thesis (particularly in this chapter). The BENOIT analysis of Sections 4.2 and 4.3 have been concerned with trying to quantify the complexity of diffracted Weierstrass-type waves at various distances downstream from the slit in the forward-half plane. The results so far obtained have proved extremely difficult to interpret physically. One possibility is that such an endeavour is bound to fail, in the sense that it can never be accomplished satisfactorily based on the following argument.

The dimension D_0 of the input Weierstrass-wave holds only in the limit that $N \to \infty$. That is, the Hausdorff dimension is as asymptotic property of a fractal set that has meaning only in the limit. The question should be – *by how much can one truncate* $W(x)$ *and still have the value of* D_0 *accurately reflect the complexity of* $w_N(x)$? This is, in effect, always a question one must consider when trying to estimate the dimension of any real (i.e., finite) datasets such as those considered here.

The parameters considered in this thesis have imposed a physical small-scale limit of λ (the optical wavelength), and the largest scale-length is $\Lambda = 2500\lambda$. This range captures just over three decimal orders of scale contained in the input fields whereas the true Weierstrass function (which more rigorously accommodates D_0) comprises an infinite number of scales. There is, hence, a discrepancy between what may be allowed physically and what one might expect to be the case mathematically. Going much beyond three decimal orders of spatial scale was not practical (or possible), given the available computational resources. The case might be that the 'diffracted fractals' scenario considered here falls short of what may be required for a fuller analysis. This point will be revisited at the end of the next chapter.

4.5 Intensity power spectrum

In Section 3.4, a preliminary numerical analysis was undertaken which demonstrated, at least in quasi-paraxial regimes, that the average trend of the log-log intensity power spectrum for normally-incident plane waves diffracted by a Cantor-type grating was linear in nature. More precisely, the (negative) gradient of $\beta \approx -2$ was found to be more-or-less insensitive to the pre-fractal level n, and which is indicative of a power-spectrum dimension $D \approx 1.5$, *irrespective* of n. One might now consider a similar analysis for the single-slit aperture illuminated by a truncated-Weierstrass input wave. Figure 4.13 shows a selection of results for the intensity power spectrum across a range of D_0 values. The average trends of the log-log graphs are found to be largely insensitive of D_0 and again they have a gradient of $\beta \approx -2$. This type of behaviour (which, it turns out, is also present in paraxial analysis of single slit diffraction patterns) suggests that the intensity power spectrum dimension for Weierstrass waves is always going to be approximately 1.5, irrespective of D_0. The spatial frequency cut-off, k_c, is found to be $\lambda k_c \approx \pi$, in good agreement

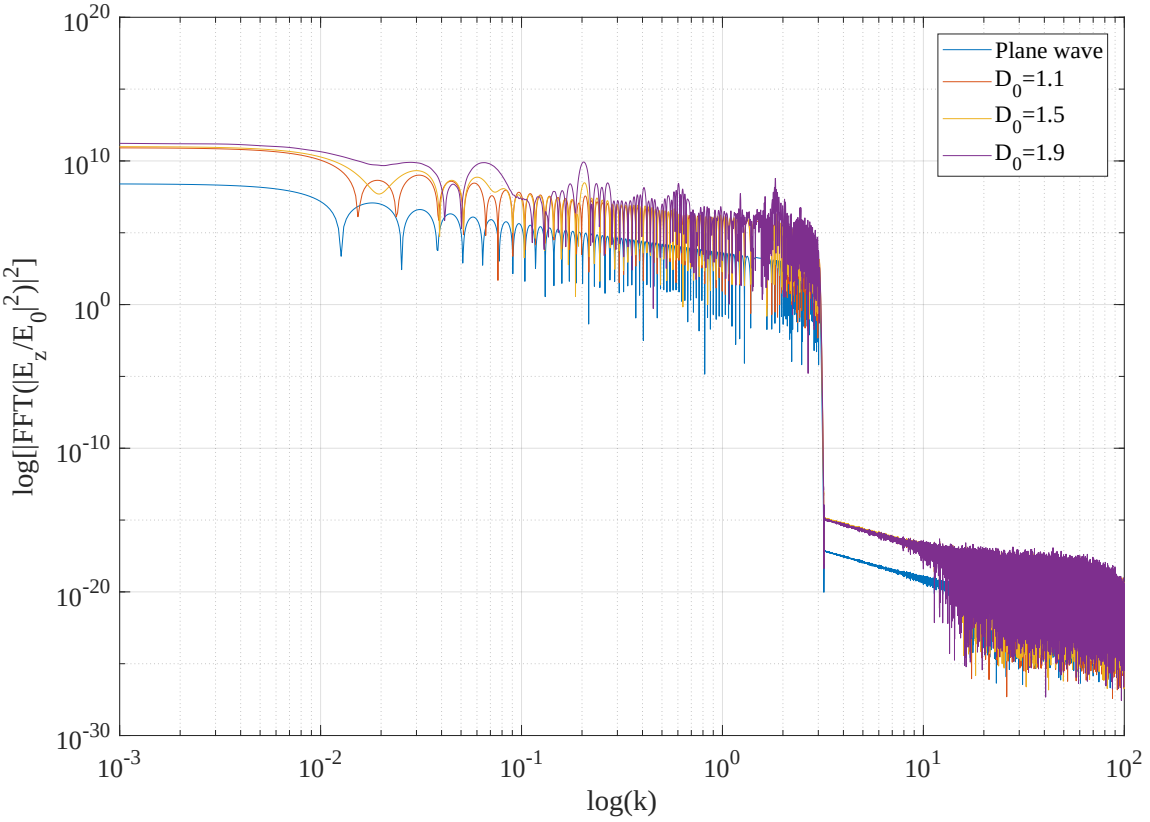

Figure 4.13: Comparison of the intensity power spectra for a single slit of half width $a_0 = 250\lambda$ computed at distance $y = 10^3\lambda$ for different D_0 values. The plane-wave result ($\epsilon = 0$) provides a reference.

with New and Albaho [2] in this quasi-paraxial regime.

CHAPTER 5

DIFFRACTION OF THE WEIERSTRASS FUNCTION ON CANTOR GRATINGS

In this final chapter, attention is paid to a new class of problem – the scattering of a pre-fractal input wave by a pre-fractal obstacle. For modelling this type of scenario, the obvious way forward is to combine the Weierstrass illumination deployed in Chapter 4 with the Cantor sets identified in Chapter 3 (firstly the traditional version, with fixed a_0, then the modified version with fixed a_n). For consistency with that earlier work, the half width in question is 250λ. Other parameters (such as $\Lambda = 2500\lambda$, $\gamma = 3$ and $\epsilon = 1$) are also preserved in order to keep the corresponding numerical calculations comparable.

When the incident waveform is TE-polarized, the electric field $E_z(x,y)$ at some distance $y > 0$ beyond the Cantor grating is given by

$$E_z(x,y) = \frac{iky}{2} E_0 \sum_{j=0}^{2^n-1} \int_{a_-(\Xi_j)}^{a_+(\Xi_j)} dx' \frac{H_1^{(1)}(kR)}{R} \left[1 + \epsilon \sum_{\nu=0}^{N} \frac{1}{\gamma^{(2-D_0)\nu}} \cos\left(\frac{2\pi}{\Lambda} \gamma^\nu x' + \phi_\nu \right) \right], \tag{5.1}$$

where $R \equiv \sqrt{(x-x')^2 + y^2}$. In Chapter 4, it was found that most $\{\phi_\nu\}$ values had little impact towards the complexity of the diffracted pattern and hence the phase parameters are kept as zeros in this chapter.

5.1 Diffraction from the traditional Cantor set

The numerical analysis begins by restricting the parameter space in the problem to a slightly more manageable size. The initiator single-slit of the Cantor set is chosen to have $a_0 = 250\lambda$ and D_0 values have been chosen in the range of $D_0 = 1.1$ to $D_0 = 1.9$.

Some of the same general trends are uncovered here are remarkably similar to those encountered

earlier in the thesis. Most notably, the BENOIT plots for the electric field tend to be somewhat irregular in comparison to those for the intensity plots. Moreover, after a distance of around $y = 10^2\lambda$, the latter seem to settle down a little, behaving less erratically. At low D_0 (e.g. $D_0 = 1.1$ and 1.3) the estimated dimension changes relatively slowly as one progresses up through the hierarchy of Cantor-set pre-fractal levels. As n increases, the constituent slits become narrower and the corresponding dimension estimations increasingly irregular. Qualitatively similar phenomena appear in Chapter 3 (cf. Fig. 3.6). A prevalent feature to emerge can be seen in Fig. 5.1, where at pre-fractal level $n = 5$ of the Cantor-set algorithm there is some evidence of a convergence phenomena. At $n = 5$, the slit widths are $a_n = \frac{250\lambda}{3^5} \approx 1.03\lambda$. Hence for $n = 6$ the apertures will all be sub-wavelength and one then may expect no further significant diffraction effects. Only the curve for $D_0 = 1.9$ shows any discriminable deviation and even then, only in two regimes – near $y \approx 10^{-1}\lambda$ and $y \approx 10^2\lambda$. A similar kind of convergence is also found for the estimated dimension result for the electric field (Fig. 5.2), where again only the curve for $D_0 = 1.9$ deviates slightly from the general trend.

The existence of the general convergence property is a desirable feature from a physical perspective: one does not expect arbitrarily-small changes to the scattering obstacle to produce arbitrarily large changes in the diffraction patterns.

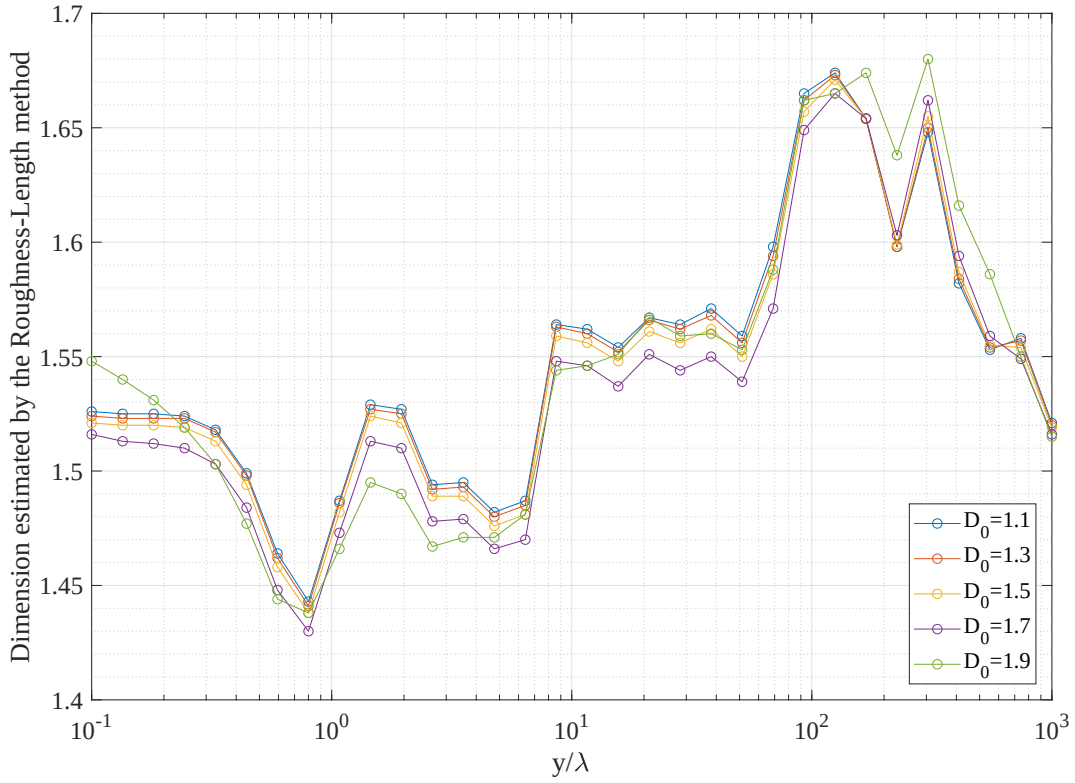

Figure 5.1: Estimated roughness-length dimension of intensity, $\left|\frac{E_z}{E_0}\right|^2$, for a pre-fractal Weierstrass-type incident wave for pre-fractal level $n = 5$ of the traditional Cantor set grating.

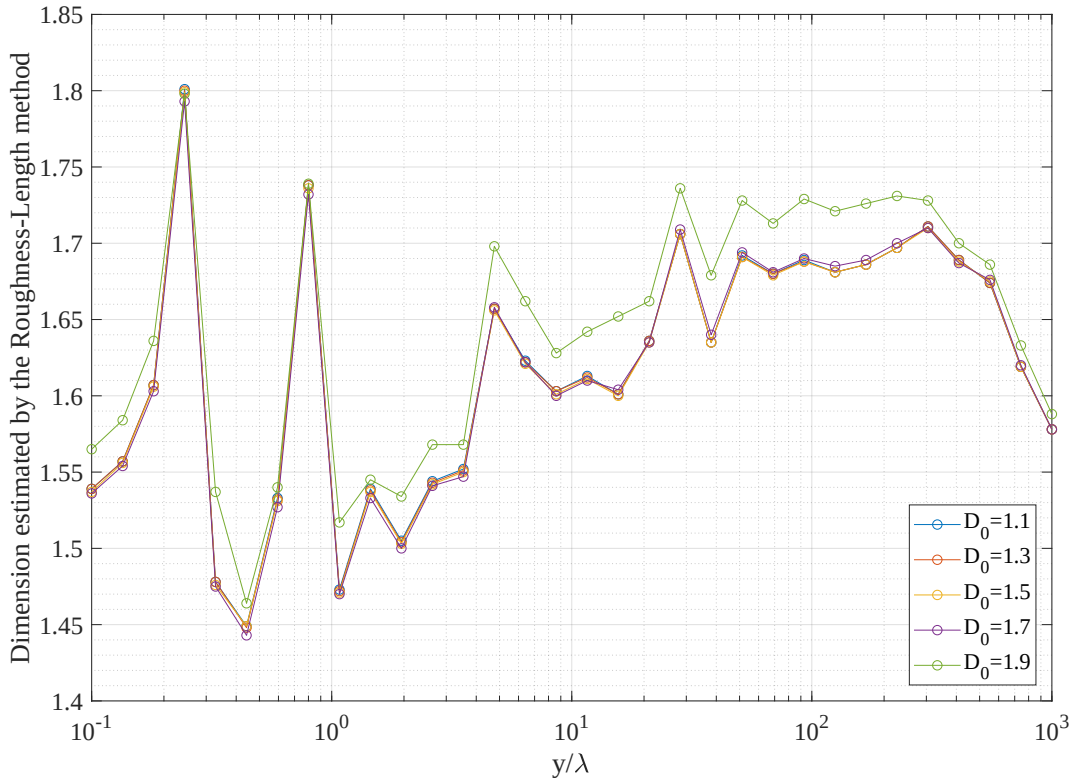

Figure 5.2: Estimated roughness-length dimension of electric field, $2\Re e\left(\frac{E_z}{E_0}\right)$, for a pre-fractal Weierstrass-type incident wave for pre-fractal level $n = 5$ of the traditional Cantor set grating.

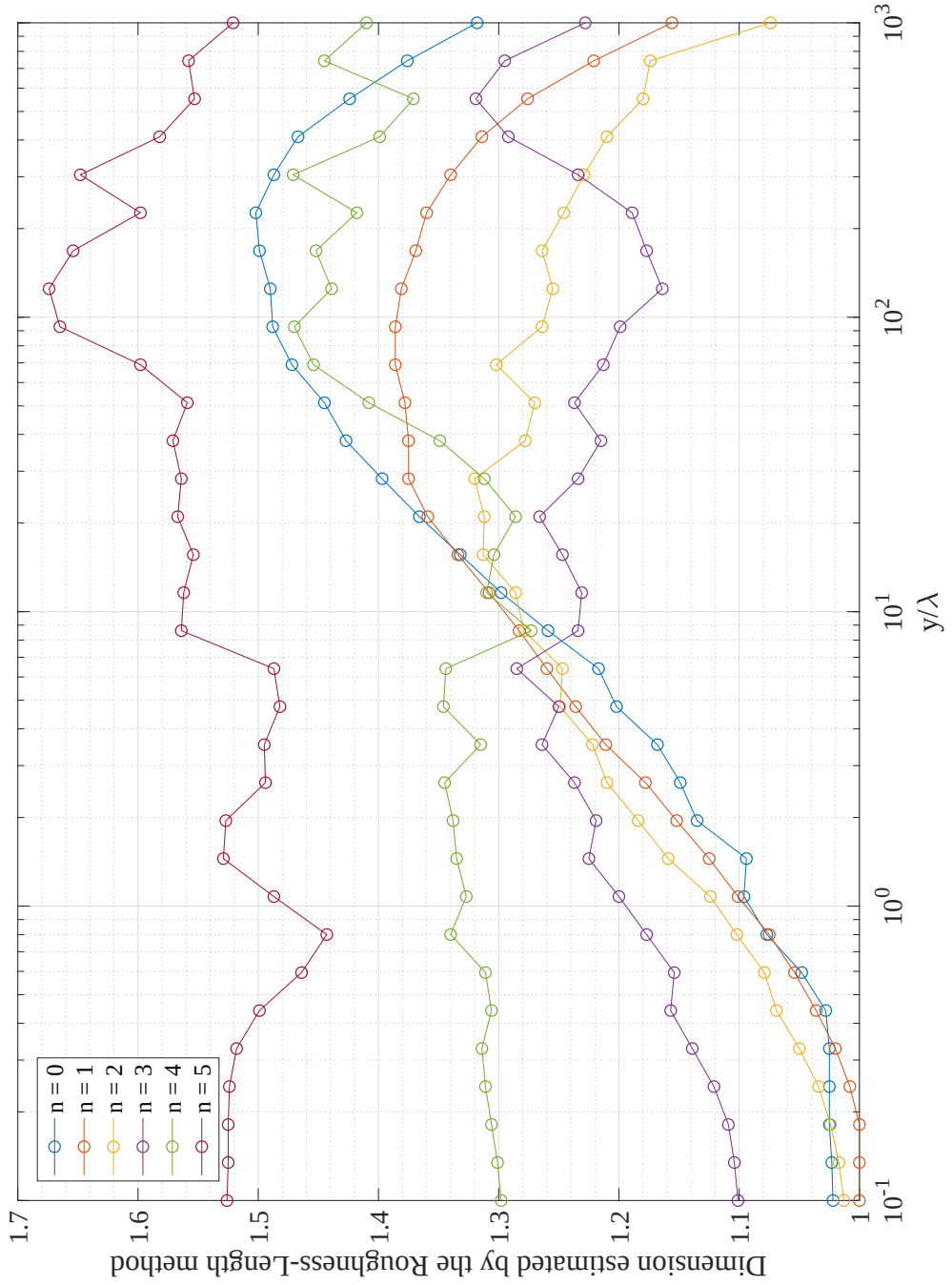

Figure 5.3: Estimated roughness-length dimension for diffracted intensity, $\left|\frac{E_z}{E_0}\right|^2$, of a truncated-Weierstrass waveform with $D_0 = 1.1$ from a traditional Cantor set with $a_0 = 250\lambda$.

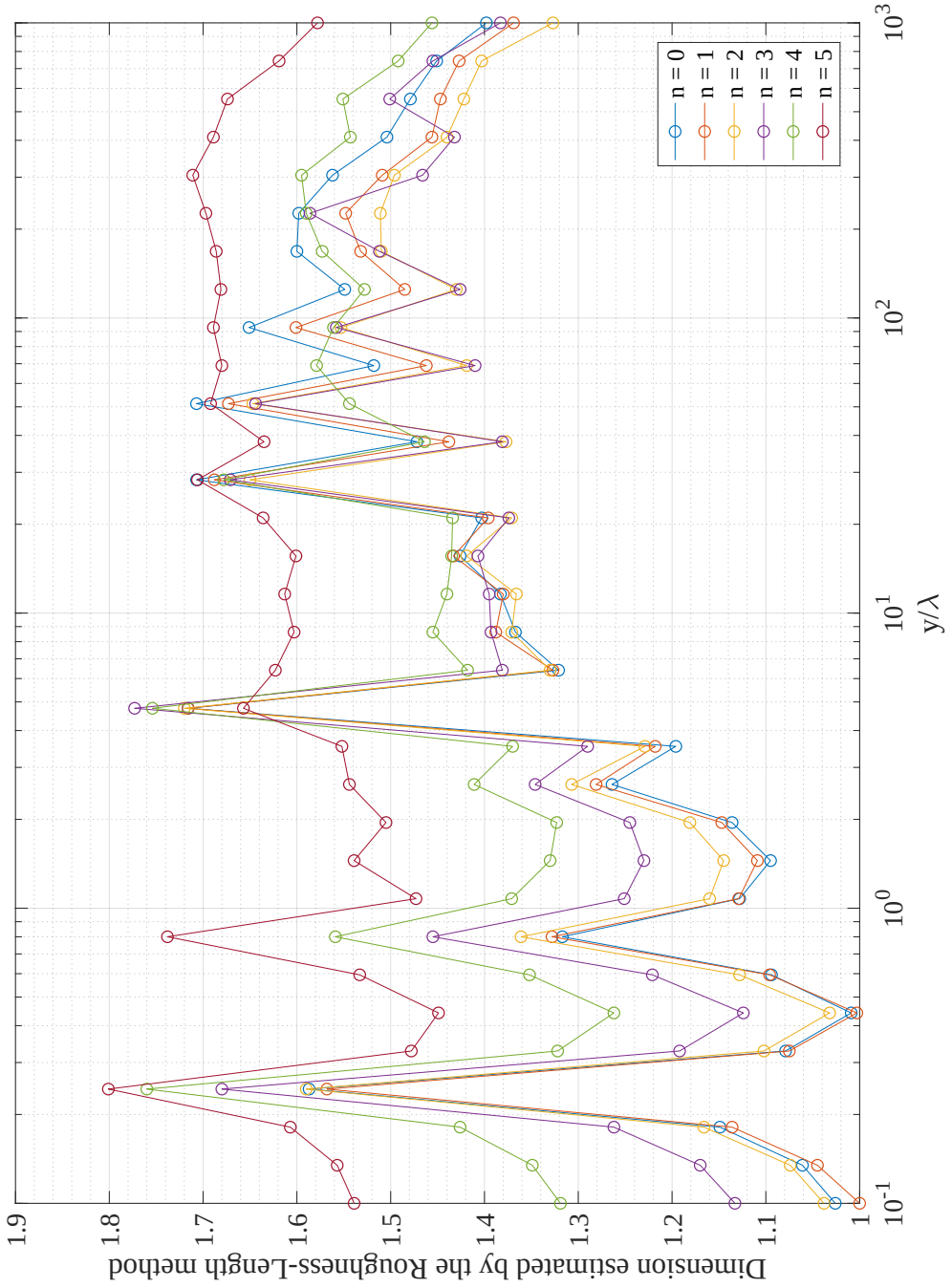

Figure 5.4: Estimated roughness-length dimension for diffracted electric field, $2\Re e(\frac{E_z}{E_0})$, of a truncated-Weierstrass waveform with $D_0 = 1.1$ from a traditional Cantor set with $a_0 = 250\lambda$.

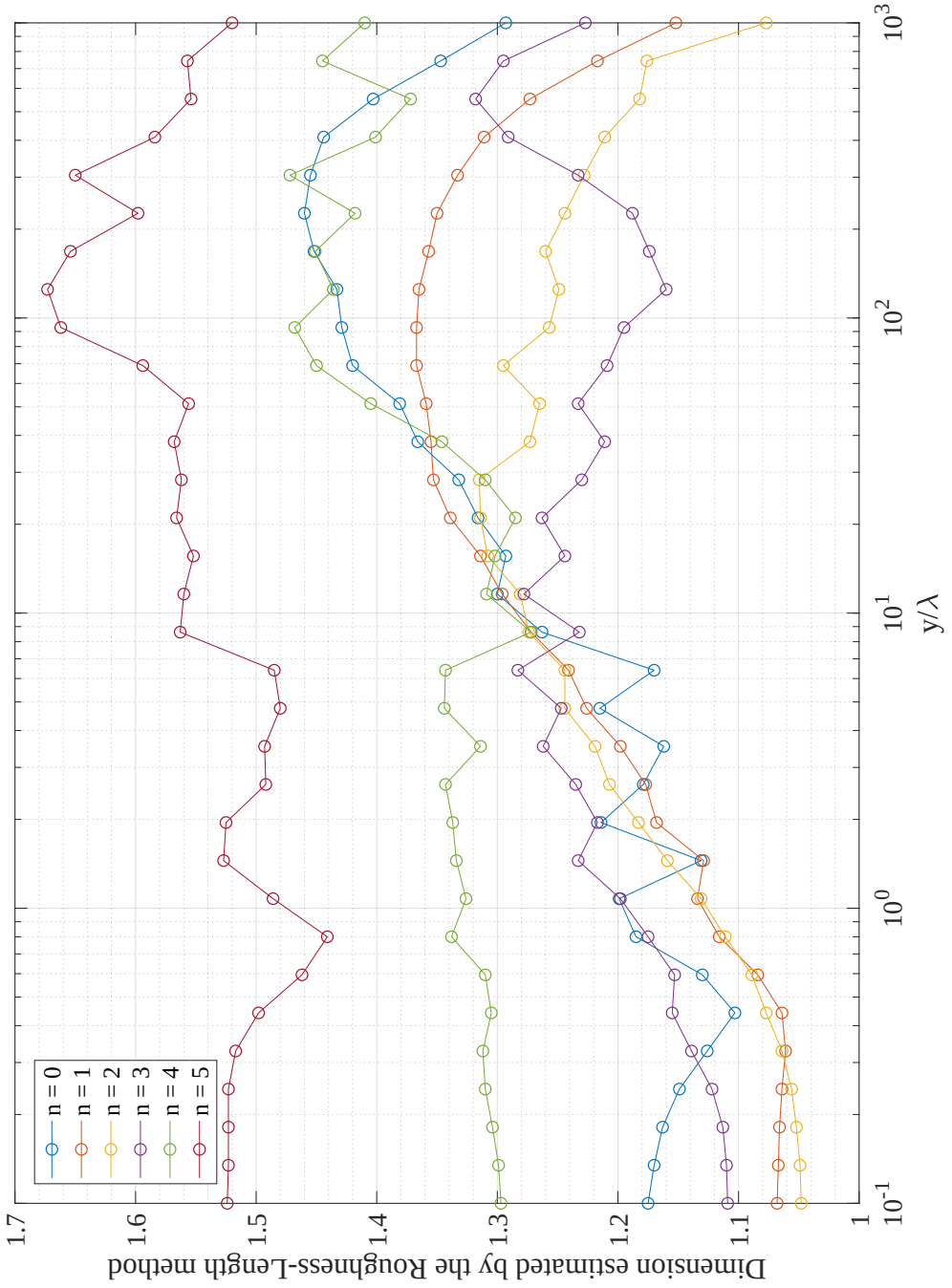

Figure 5.5: Estimated roughness-length dimension for diffracted intensity, $\left|\frac{E_z}{E_0}\right|^2$, of a truncated-Weierstrass waveform with $D_0 = 1.3$ from a traditional Cantor set with $a_0 = 250\lambda$.

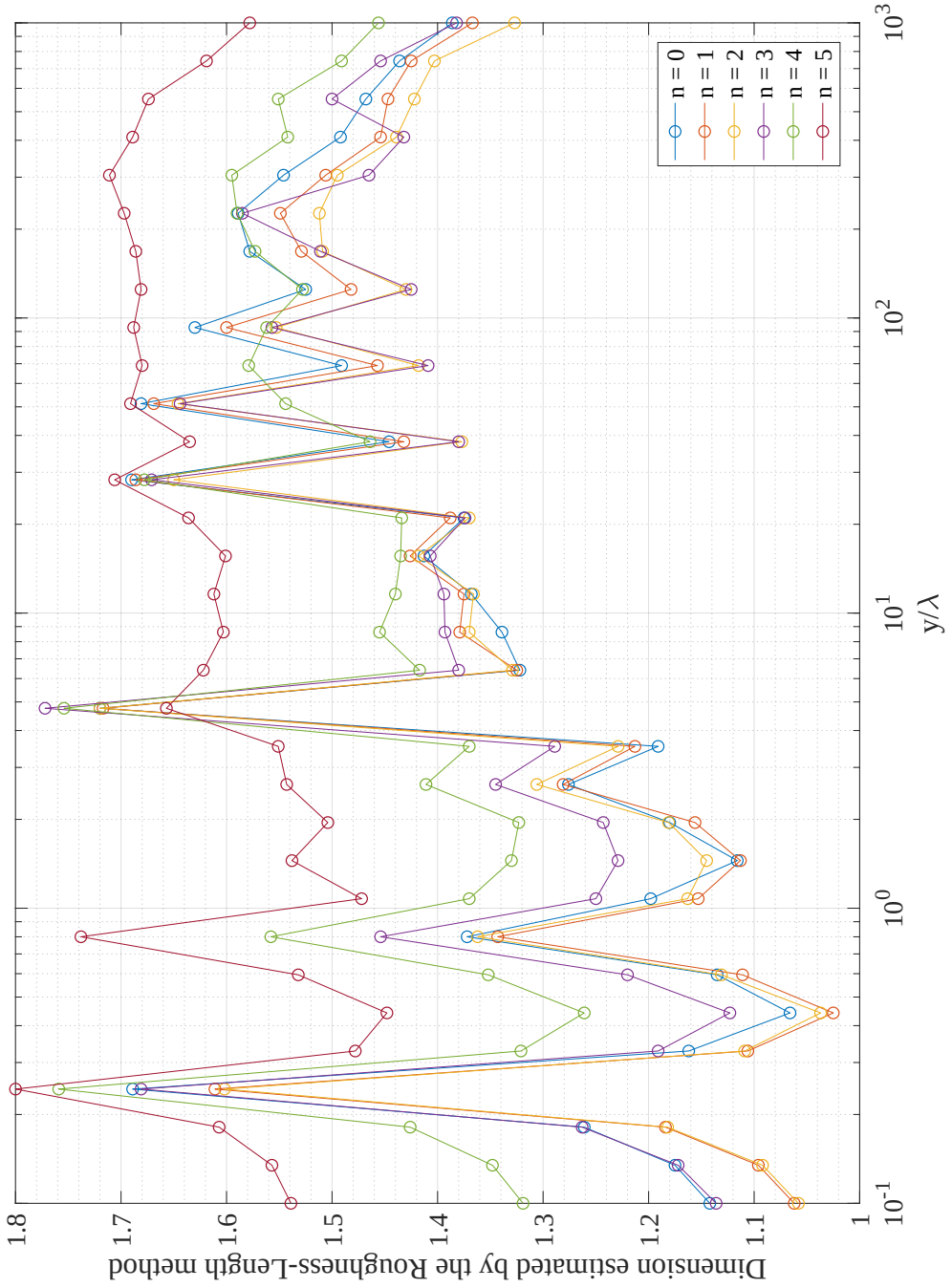

Figure 5.6: Estimated roughness-length dimension for diffracted electric field, $2\Re e(\frac{E_z}{E_0})$, of a truncated-Weierstrass waveform with $D_0 = 1.3$ from a traditional Cantor set with $a_0 = 250\lambda$.

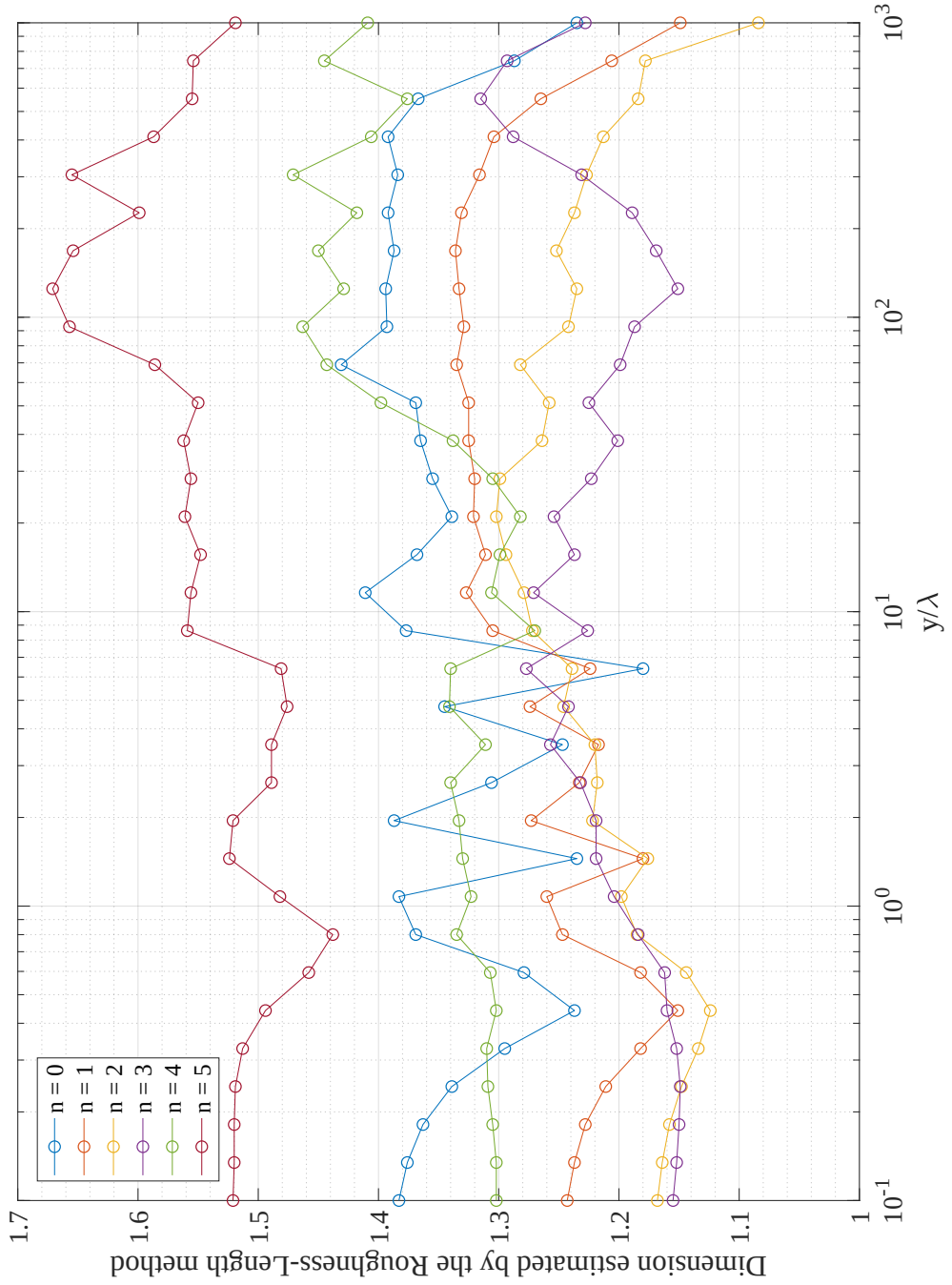

Figure 5.7: Estimated roughness-length dimension for diffracted intensity, $\left|\frac{E_z}{E_0}\right|^2$, of a truncated-Weierstrass waveform with $D_0 = 1.5$ from a traditional Cantor set with $a_0 = 250\lambda$.

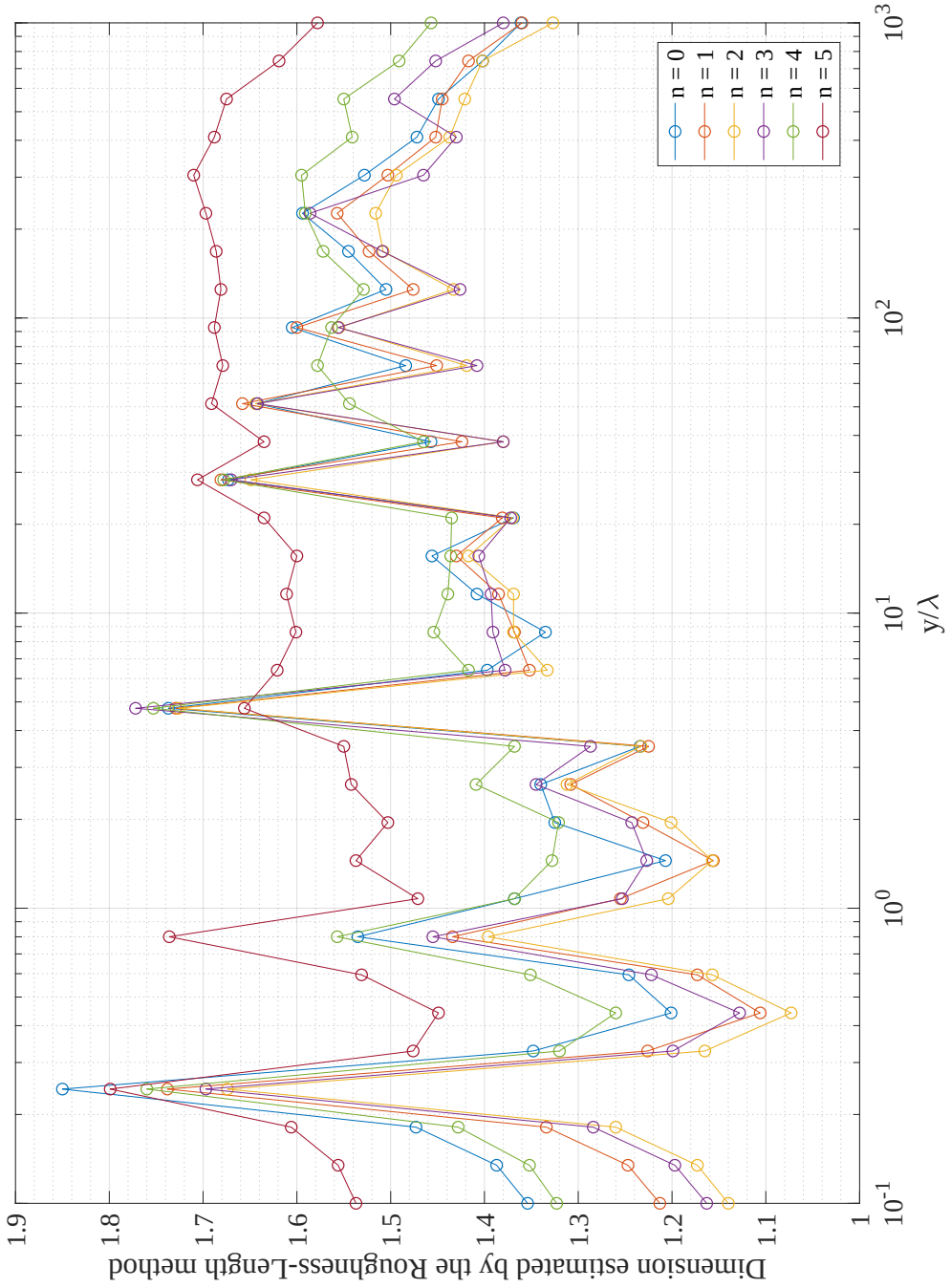

Figure 5.8: Estimated roughness-length dimension for diffracted electric field, $2\Re e(\frac{E_z}{E_0})$, of a truncated-Weierstrass waveform with $D_0 = 1.5$ from a traditional Cantor set with $a_0 = 250\lambda$.

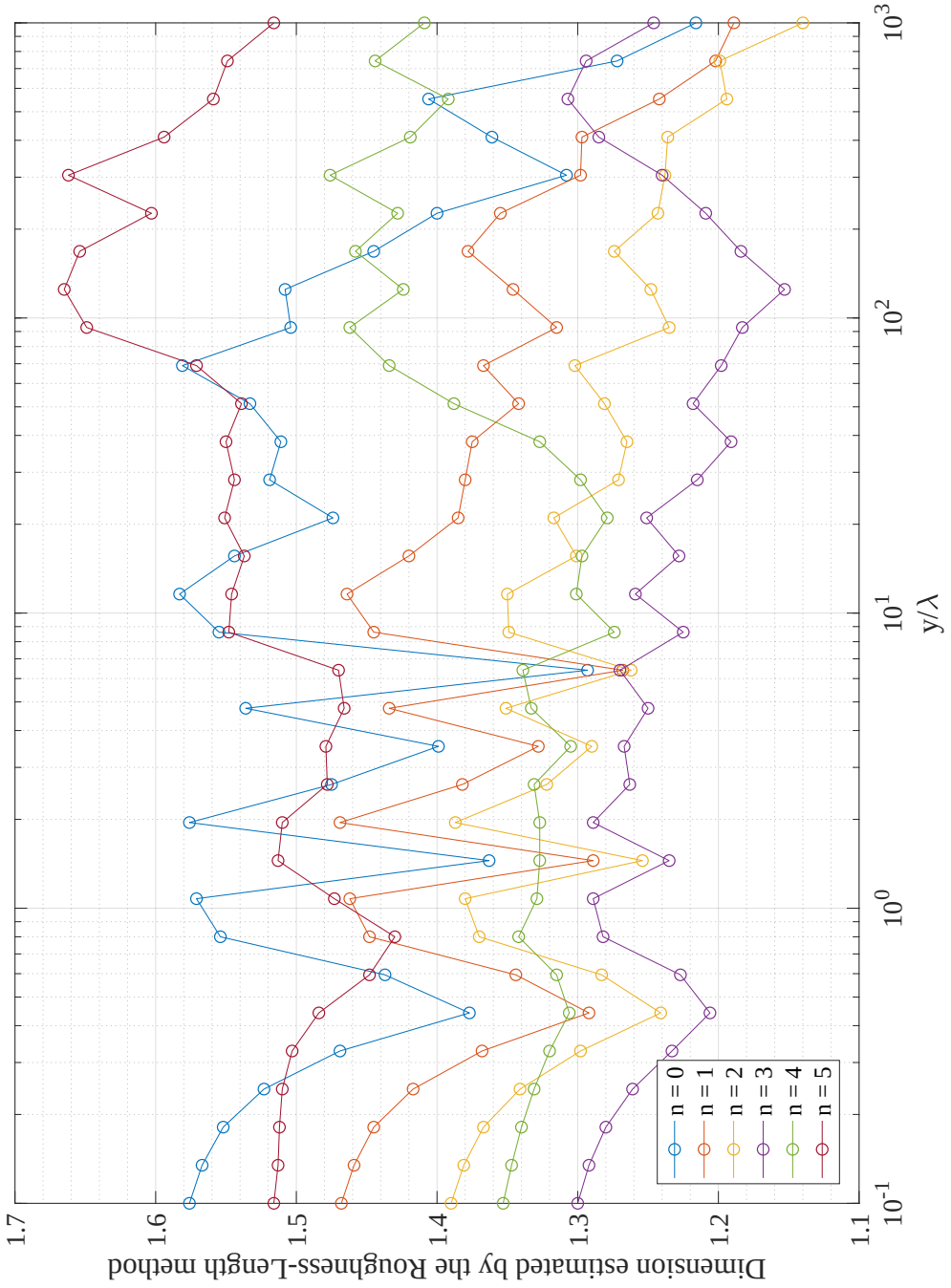

Figure 5.9: Estimated roughness-length dimension for diffracted intensity, $\left|\frac{E_z}{E_0}\right|^2$, of a truncated-Weierstrass waveform with $D_0 = 1.7$ from a traditional Cantor set with $a_0 = 250\lambda$.

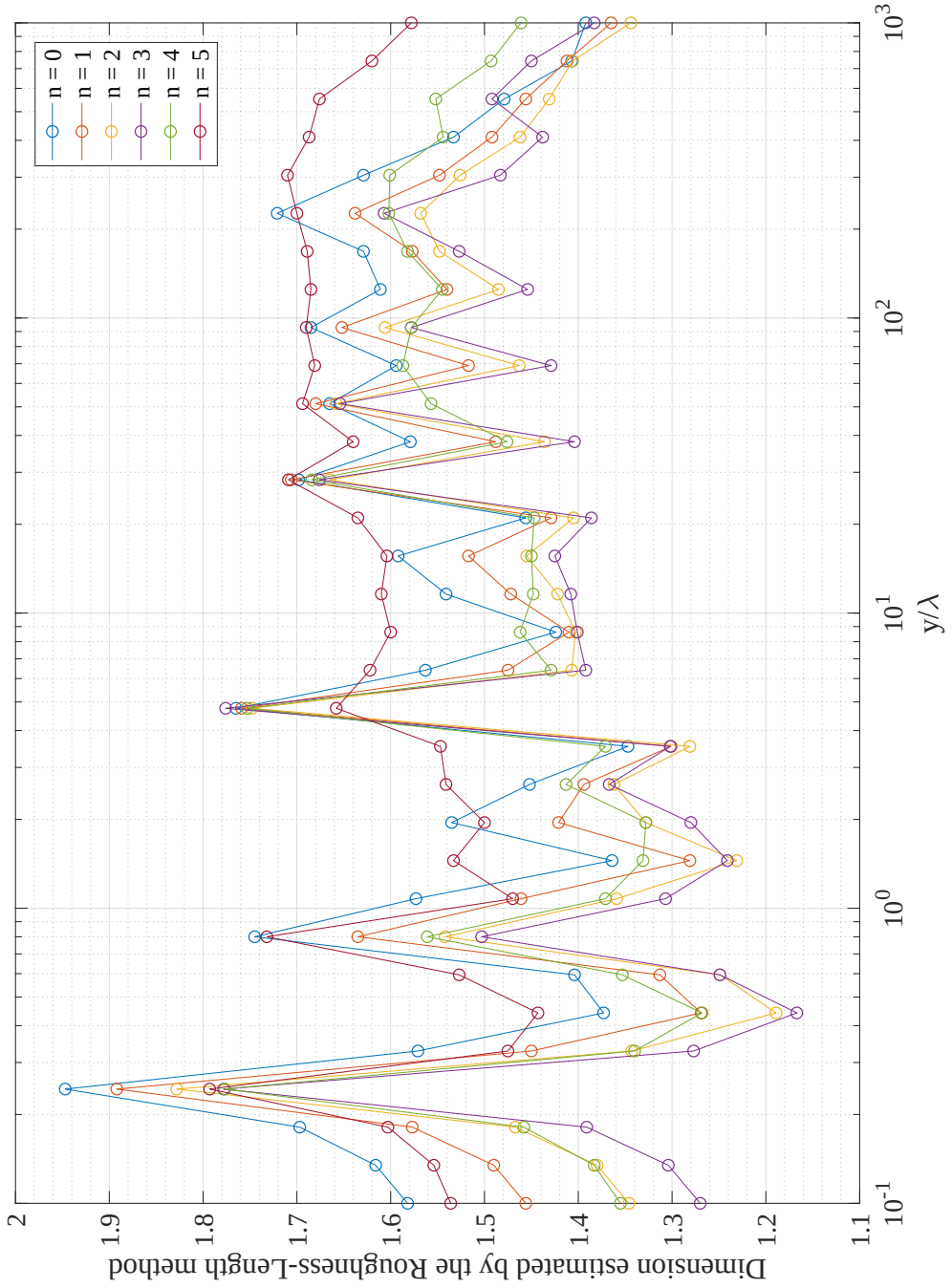

Figure 5.10: Estimated roughness-length dimension for diffracted electric field, $2\Re e\left(\frac{E_z}{E_0}\right)$, of a truncated-Weierstrass waveform with $D_0 = 1.7$ from a traditional Cantor set with $a_0 = 250\lambda$.

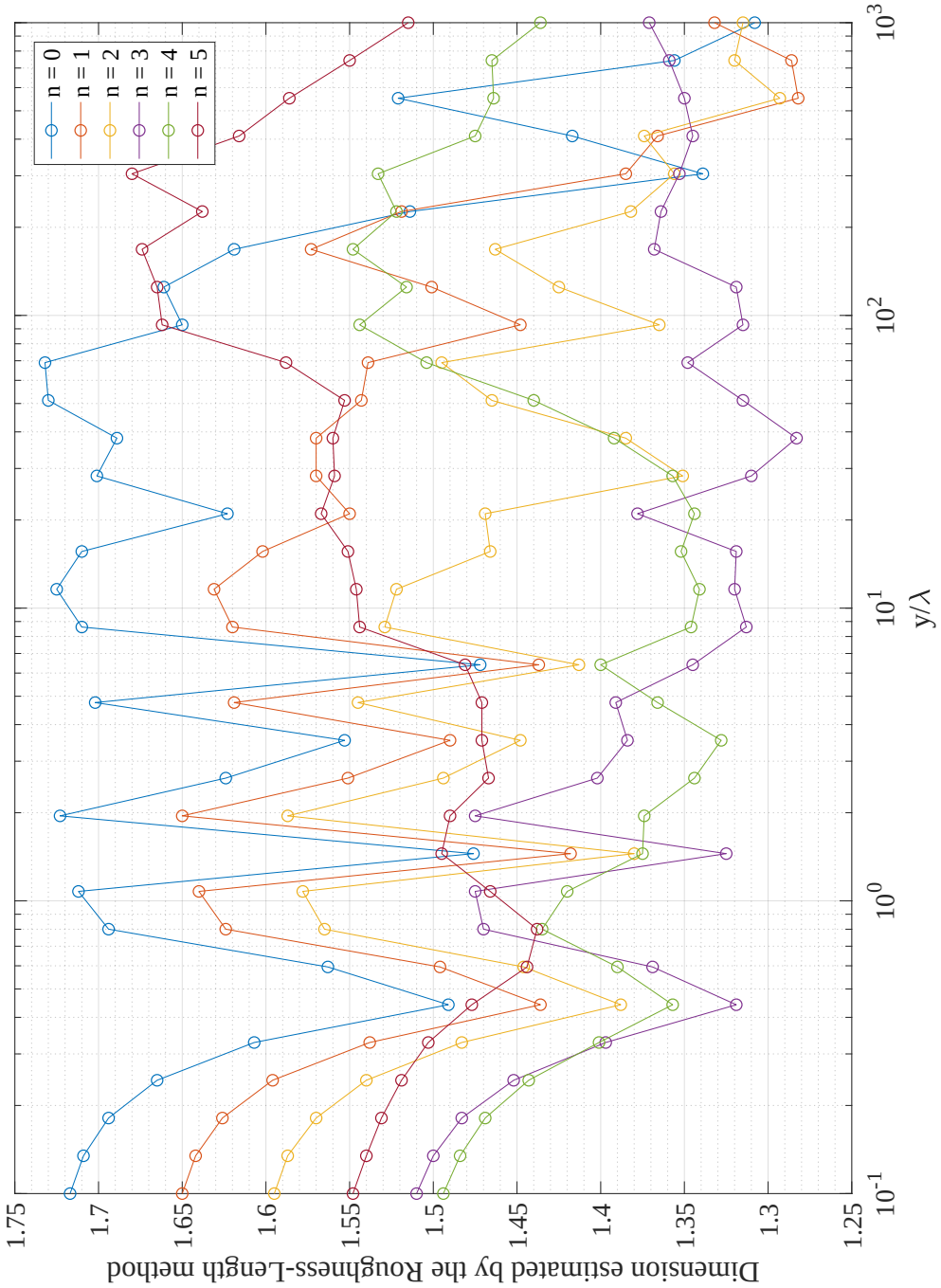

Figure 5.11: Estimated roughness-length dimension for diffracted intensity, $\left|\frac{E_z}{E_0}\right|^2$, of a truncated-Weierstrass waveform with $D_0 = 1.9$ from a traditional Cantor set with $a_0 = 250\lambda$.

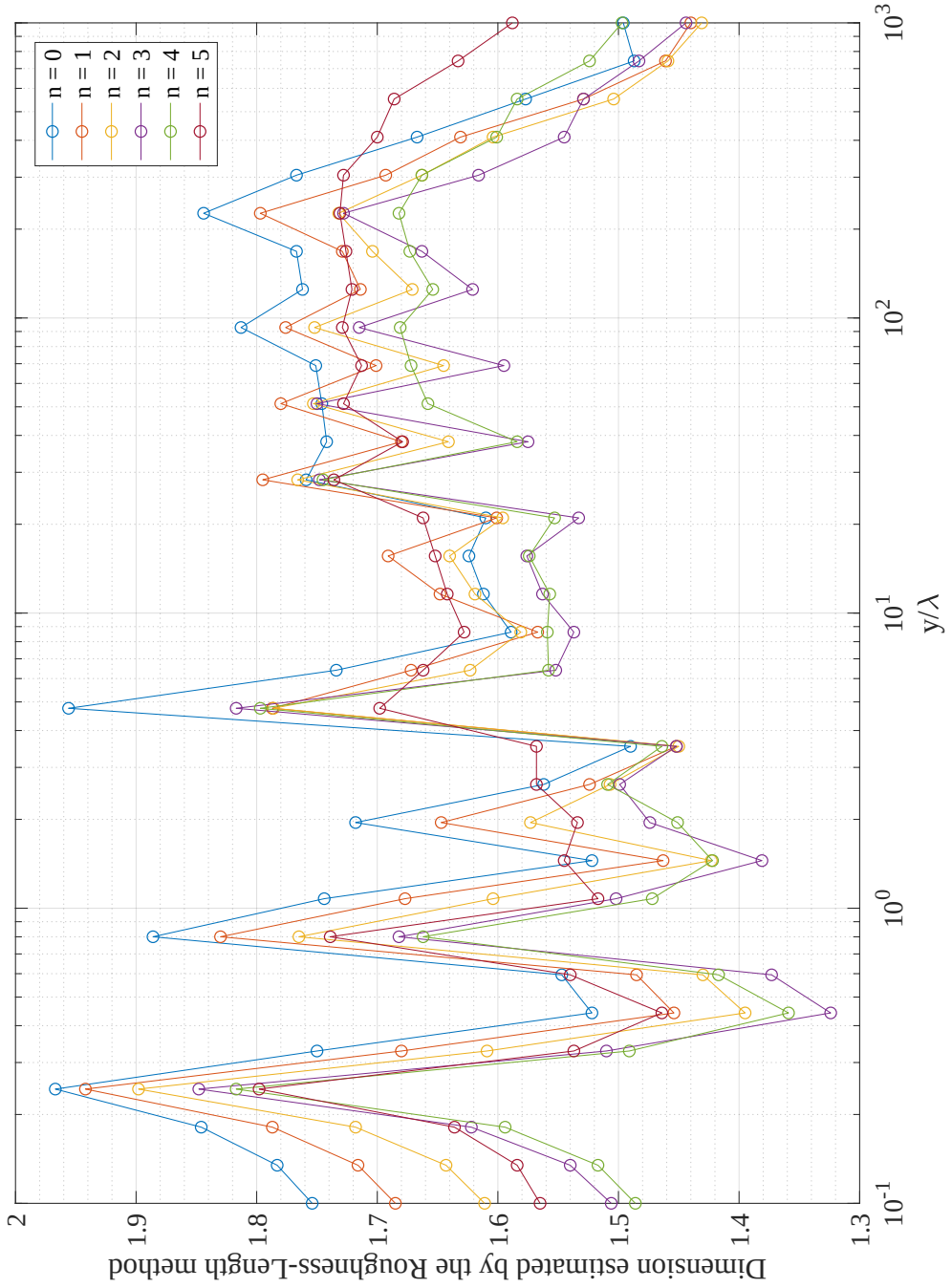

Figure 5.12: Estimated roughness-length dimension for diffracted electric field, $2\Re e\left(\frac{E_z}{E_0}\right)$, of a truncated-Weierstrass waveform with $D_0 = 1.9$ from a traditional Cantor set with $a_0 = 250\lambda$.

5.2 Diffraction from the modified Cantor set

After analysing the results from the traditional Cantor set one must now look at the modified Cantor set (akin to in Chapter 3). Once again, the half-width of the individual slits is kept at $a_n = 250\lambda$. The main difficulty here (which was largely unforeseen at the start of the research project) is the 'wall' that is encountered very rapidly in terms of required computational times. Unlike for the traditional Cantor set, it has not been possible to progress beyond pre-fractal level $n = 3$ for the modified Cantor set. To preserve the integrity of the sampling (i.e., keeping the resolution of the plot, $\Delta x = \frac{\lambda}{32}$, fixed - this is essential to keep the roughness-length analysis in BENOIT as consistent as possible as discussed in Subsection 1.2.4.3) and to accommodate a sufficiently wide transverse domain, the number of x grid points ramps up geometrically. For $n = 3$, the number of x points is $864,001$. This increase in points is augmented by the fact that, for regimes with pre-fractal illumination (i.e., a Weierstrass wave with $N = 7$ and $\Lambda = 2,500\lambda$), multiple diffraction patterns need to be computed for each n. This type of double-barrelled fractality has largely exceeded available computational resources and resulted in exhaustive wait times (effectively six months to generate the data in this chapter!). Unfortunately, there does not seem to be any short-cut to performing numerical calculations with Weierstrass functions: increasing Δx to speed-up calculations risks under-sampling the higher frequencies, while truncating the summation before reaching N eliminates these contributions altogether (neither scenario is satisfactory).

n	x domain size	Approx. time for one calculation	No. of calculations	Approx. overall time
0	48,001	180s	9	27 minutes
1	96,001	600s	9	90 minutes
2	288,001	2000s	18	10 hours
3	864,001	5000s	36	50 hours

Table 5.1: Approximate computation times for the diffracted field at a single y value with a modified Cantor-grating and truncated-Weierstrass illumination (here, times are given for the patterns at $\nu = 4$). The parameters are $D_0 = 1.5$ and $y \approx 8.6\lambda$ (the middle value of the logarithmically-spaced y array). "No. of calculations" refers to the number of constituent diffraction patterns that must be computed at pre-fractal level $n = 1, 2, 3, \ldots$. For $N + 1$ contributions from truncated-Weierstrass illumination, and the normally-incident plane wave, a total of $(N + 2) \times 2^{n-1}$ patterns must be calculated.

Some typical computation times are shown in Table 5.1 for a single value of y. These numbers depend critically upon both y and the index ν. The time required to compute any particular integral increases as $y \to 0$ and for increasing ν (see Fig. 5.13). Either of these parameters can give rise to a very rapidly-varying integrand in x' and desired convergence of the MATLAB library function `integral` takes longer and longer to reach. Sources of long computation times thus include:

- High number of points in x (needed to preserve the integrity of the calculation and avoid under-sampling),
- High number of slits (with a geometric divergence 2^n),
- High number of spatial-frequency components in $E_z(x',0)$.

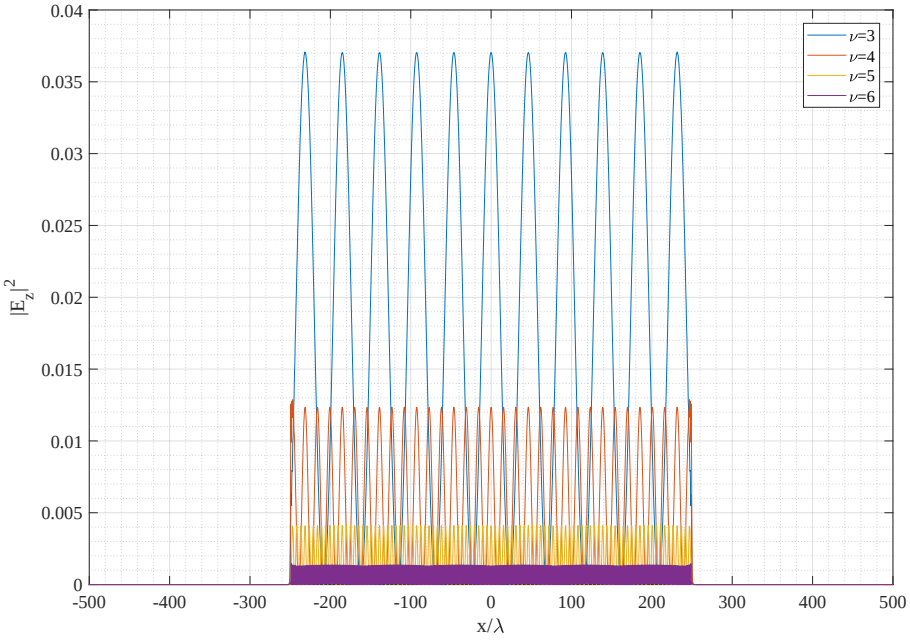

Figure 5.13: The contributions for $\nu = 3,4,5$ and 6 of intensity of the diffracted field at $y = 1\lambda$ for a $D = 1.5$.

It is true to say that similar considerations were present, to some extent, in the analysis of Chapter 4, which addressed the single-slit problem (or pre-fractal level $n = 0$ of the Cantor set). The computation time really becomes problematic with combining pre-fractal waves with pre-fractal scattering obstacle which leads to prospect that studying such a phenomena in any detail, and for high n, is likely not possible with currently-available computing measures. One way of knocking down the computation wall is to use the natural symmetry of the Cantor grating so that patterns from only half of the total number of slits need to be calculated and the result mirrored. Even then, the time required to calculate the diffraction at a single y value is on the scale of days. Some qualitatively similar effects are found for the modified Cantor set as with the traditional Cantor set (see Figs. 5.14 to 5.19). Illuminating waves with low D_0 tend to have roughness-length dimensions that are generally better behaved [variations in estimation with y are again smoother and more gradual for $\left|\frac{E_z}{E_0}\right|^2$ than for $2\Re e\left(\frac{E_z}{E_0}\right)$]. There is also some mild evidence for convergence, however it has not been possible to progress onto higher n values here.

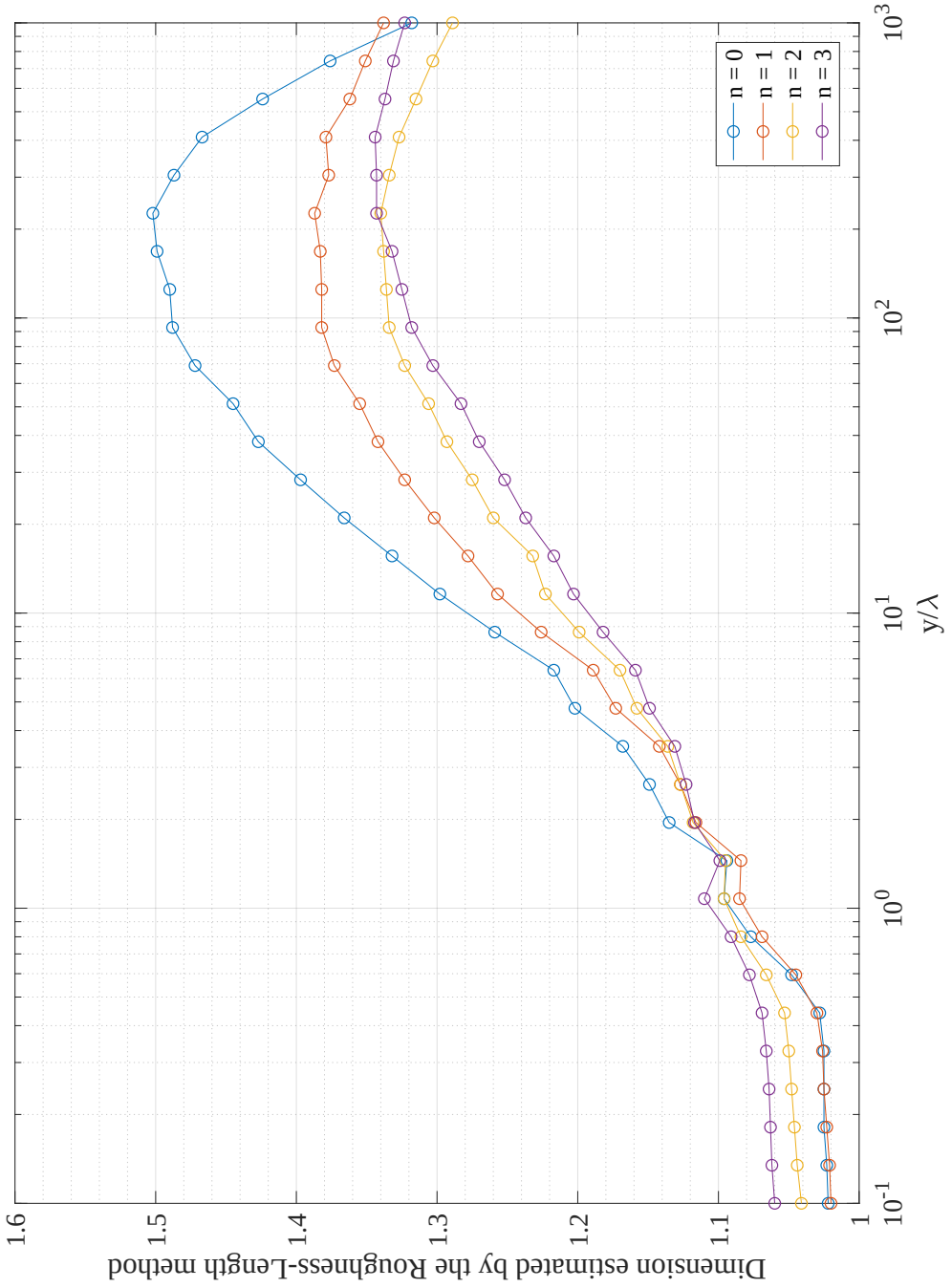

Figure 5.14: Estimated roughness-length dimension for diffracted intensity, $\left|\frac{E_z}{E_0}\right|^2$, of a truncated-Weierstrass waveform with $D_0 = 1.1$ from a modified Cantor set with $a_0 = 250\lambda$.

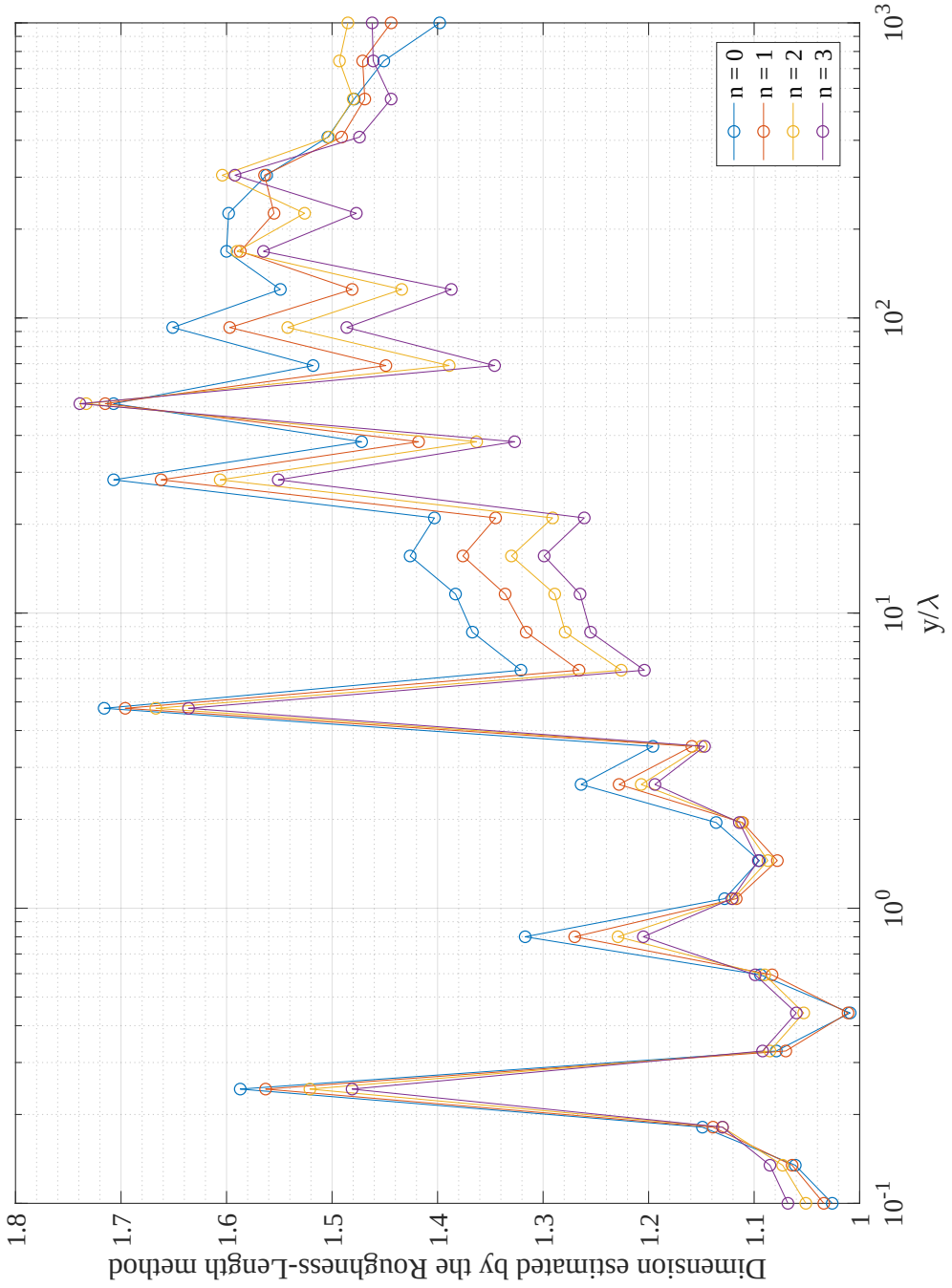

Figure 5.15: Estimated roughness-length dimension for diffracted electric field, $2\Re e\left(\frac{E_z}{E_0}\right)$, of a truncated-Weierstrass waveform with $D_0 = 1.1$ from a modified Cantor set with $a_0 = 250\lambda$.

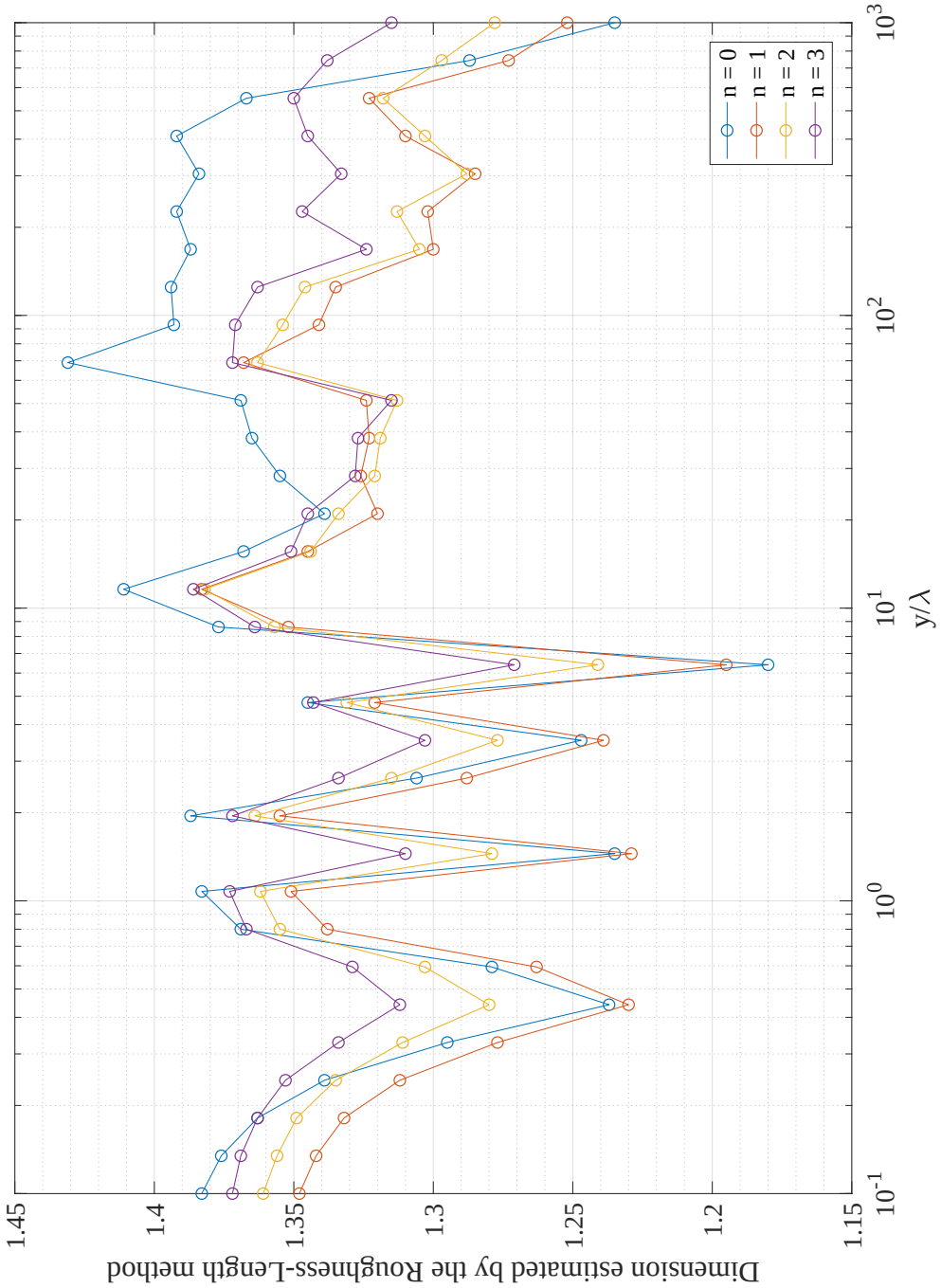

Figure 5.16: Estimated roughness-length dimension for diffracted intensity, $\left|\frac{E_z}{E_0}\right|^2$, of a truncated-Weierstrass waveform with $D_0 = 1.5$ from a modified Cantor set with $a_0 = 250\lambda$.

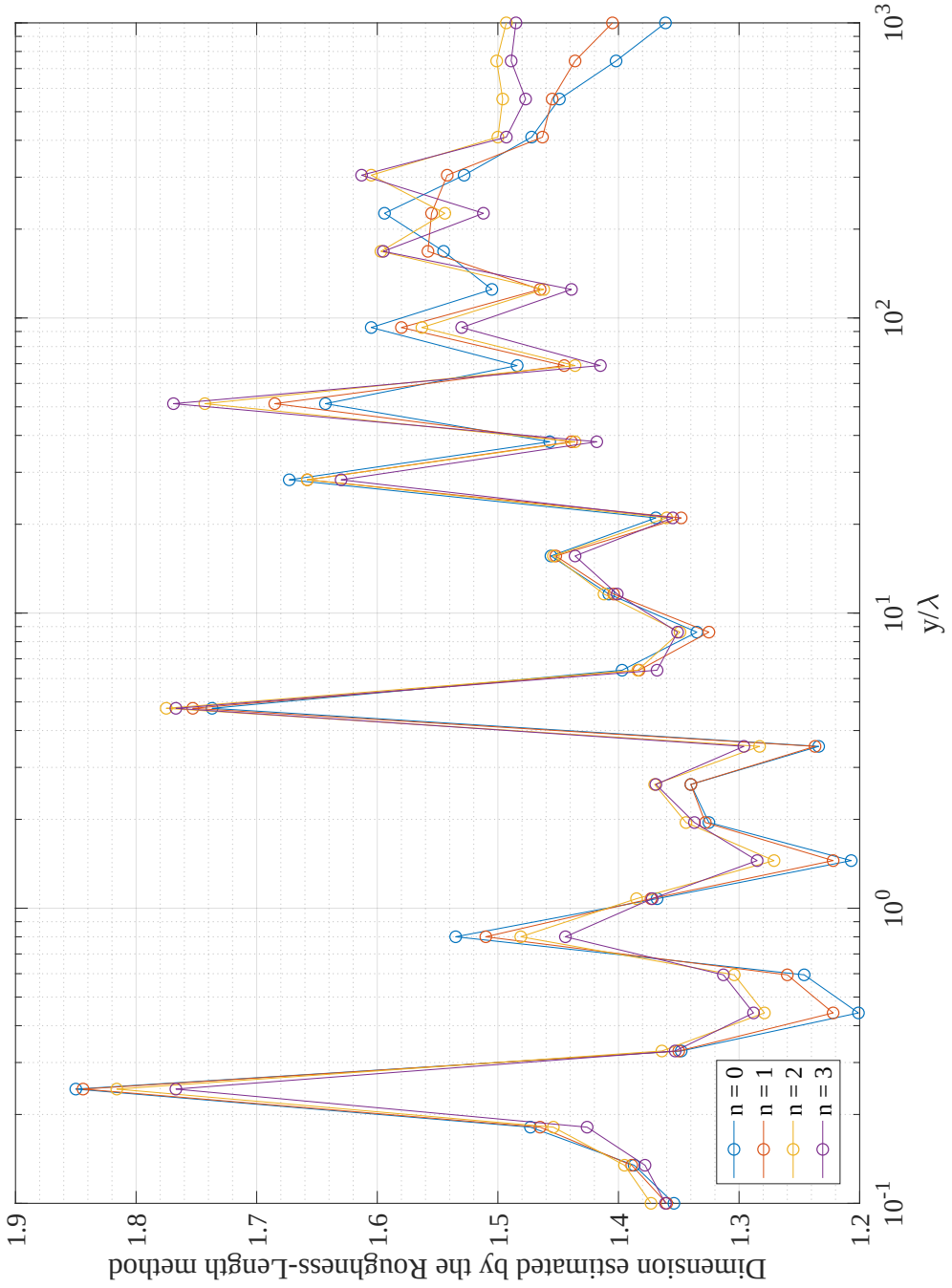

Figure 5.17: Estimated roughness-length dimension for diffracted electric field, $2\Re e\left(\frac{E_z}{E_0}\right)$, of a truncated-Weierstrass waveform with $D_0 = 1.5$ from a modified Cantor set with $a_0 = 250\lambda$.

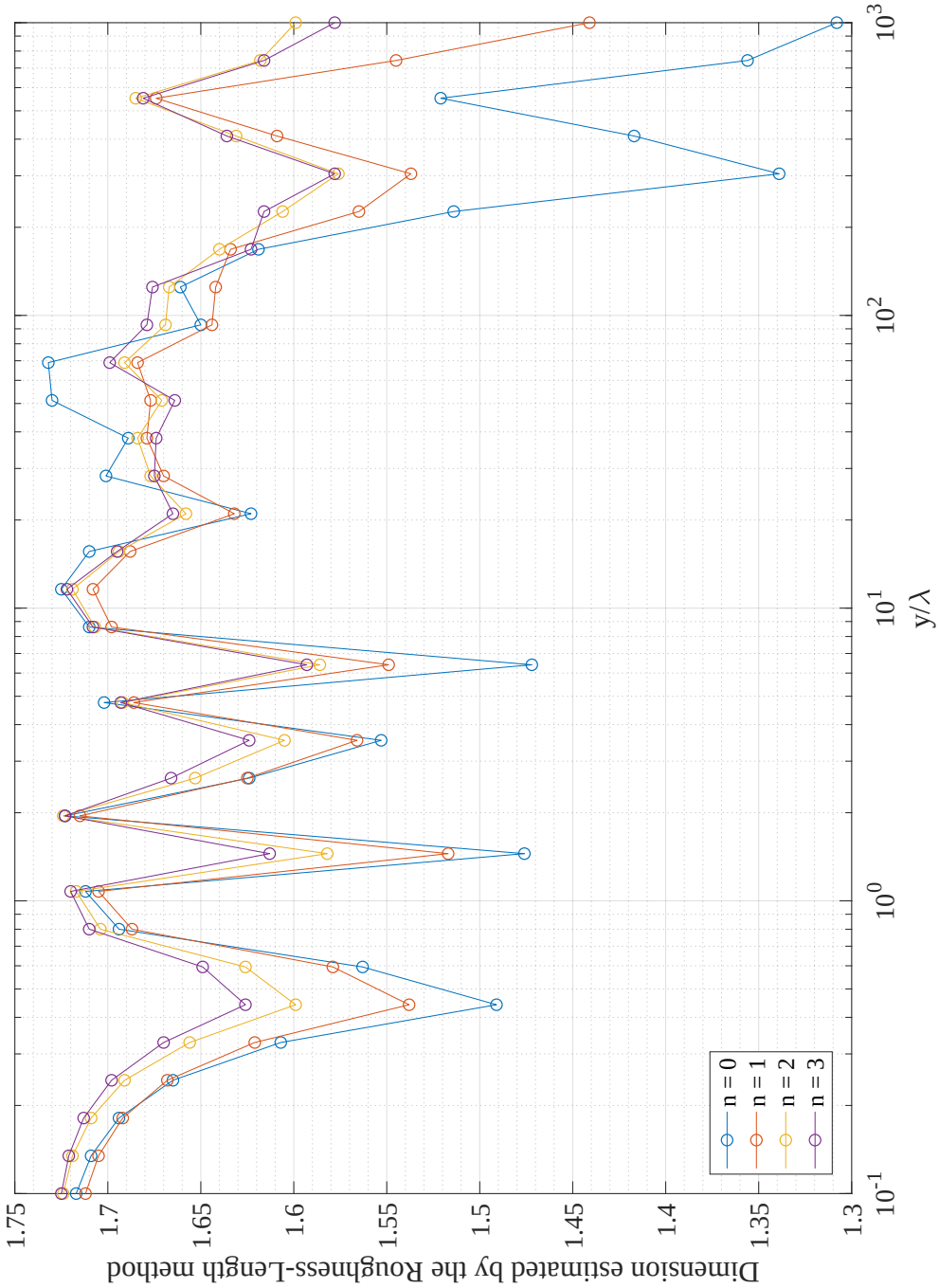

Figure 5.18: Estimated roughness-length dimension for diffracted intensity, $\left|\frac{E_z}{E_0}\right|^2$, of a truncated-Weierstrass waveform with $D_0 = 1.9$ from a modified Cantor set with $a_0 = 250\lambda$.

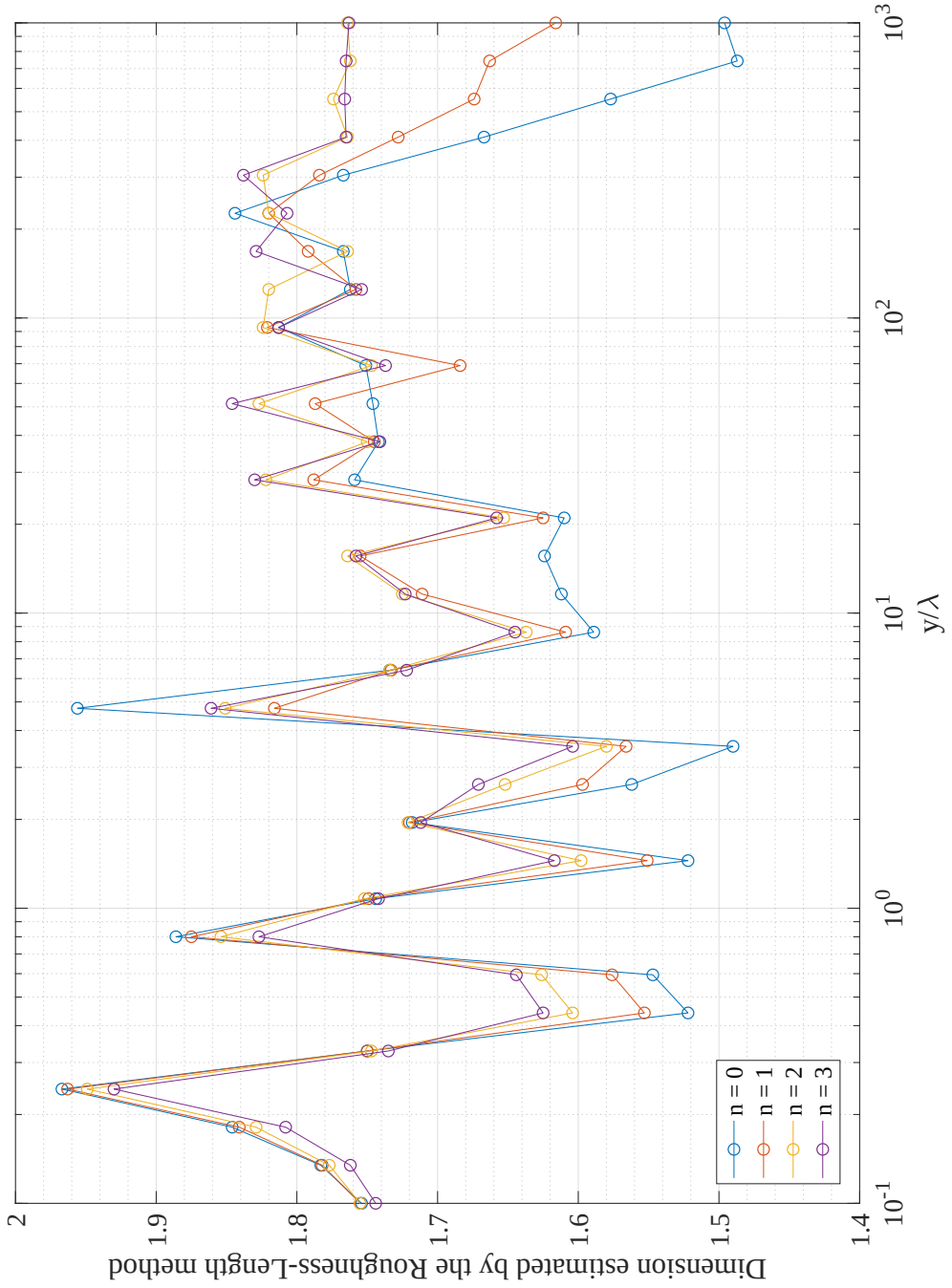

Figure 5.19: Estimated roughness-length dimension for diffracted electric field, $2\Re e\left(\frac{E_z}{E_0}\right)$, of a truncated-Weierstrass waveform with $D_0 = 1.9$ from a modified Cantor set with $a_0 = 250\lambda$.

CHAPTER 6

CONCLUSIONS AND FURTHER WORK

The programme of work undertaken in this MSc has been intended to re-start some of the research activity on 'fractal diffraction' that had ended in 2016, but exploring different possible directions. This approach has involved beginning from scratch, essentially replacing the paraxial approximation with a new formulation based on the RS diffraction integral (which is free from angular limitations and hence much more appropriate for modelling high-frequency problems). While closed-form mathematical predictions are not so forthcoming from this more sophisticated and predominantly numerical approach, one can reasonably expect the results to be more physically meaningful.

The classic knife-edge problem has been solved, and the solution first derived by Sommerfeld revisited in rather a high level of detail. This type of preparatory detailed investigation provided the mathematical 'blueprint' for how to approach generalizing the knife-edge problem in order to accommodate illuminating and scattered fields that are complex in nature (in the sense of comprising structure across, in principle, many decimal order of scale). Fundamental TE and TM Weierstrass-Lamb waves have been obtained, wherein the incident phase fronts are always perpendicular to the (x, y) plane, and a provisional analysis using BENOIT has also considered the fractal-dimension properties of the TE wave. In the somewhat restrictive parameter regimes allowed by paraxial theory, a known solution first derived in 2013 emerges asymptotically. In terms of taking this work forward, there are two main outstanding tasks: (i) for maximum generality, it is desirable to derive Weierstrass-Lamb waves where the constituent waveforms may be polarized in any arbitrary direction relative to the screen (one might use, for instance, the methods found in tomes by Born and Wolf [34] or Stamnes [28] as a starting point). (ii) The BENOIT analysis needs to be extended. Here, the range of x considered has been limited by available computer resources and also the 12-month duration of the MSc programme. A

wider spatial domain needs to be considered (for instance, allowing for x to be bounded between $-\Lambda \leq x \leq \Lambda$ to ensure that all scales in the Weierstrass waveform are captured), and these larger datasets may well provide some more conclusive insight. There is also the question of how (if at all) the fractal-dimension characteristics change between the TE and TM waves.

Scattering of normally-incident plane waves by a Cantor set-type complex domain has been addressed. While this geometry has previously been considered in the literature, more analyses appear to be concerned with the far-field region [39, 40] where diffraction patterns can be described using Fourier transforms. In this thesis, a prescription was developed based on the RS diffraction integral and interesting qualitative agreement has been found with the boundary element numerical method used by other research groups considering Neumann screens [45]. While gratings based on the traditional Cantor set generated some fascinating patterns, a greater level of complexity was often present when using a modified Cantor-set construction (one where the constituent slits have a fixed width across all pre-fractal levels). BENOIT analysis also suggested more regular behaviour in the estimated dimension when using this alternative type of grating. Finally, numerical work using FFTs demonstrated that the power-spectrum dimension remained fixed at around 1.5, irrespective of the pre-fractal level n for the Cantor set. This result suggests that the single-slit analysis by New and Albaho [2] has scope to be generalized to complex domains such as those modelled by the Cantor set but that its key physical prediction (i.e., the spatial-frequency cut-off) will likely survive.

Preliminary investigations using a 2DRS method have been initiated for considering plane-wave scattering by complex domains such as the Cantor dust. These results are given in Appendix E, but they have not been further developed due to a lack to time and computing resources.

A first attempt has been made to go beyond the assumptions underpinning the early (paraxial) analyses that considered the diffraction of the Weierstrass-type waveform at a single aperture. The entire problem has been reformulated with closer attention now being paid to the high-frequency nature of pre-fractal waves (these considerations are outside the scope of paraxial theory). The chosen formulation lies with a RS diffraction integral, which is formally an exact solution to the underlying 2D Helmholtz equation. There naturally remains a small level of approximation here, wherein the precise form of the input wave $E_z(x',0)$ may only ever be specified approximately (e.g., as a uniform wavefront) but this feature is also shared by the more familiar Fresnel integral approach. It was hoped, initially, that basing the field description on the Helmholtz equation – where unphysical sub-wavelength structure is eliminated – might remove some of the difficulties interpreting the BENOIT dimension-estimation curves (e.g., smoothing the graphs, reducing variability, etc.). While such difficulties evidently still persist, some new results have been uncovered that will require closer scrutiny.

Finally, the first steps have been taken towards modelling the physical regime of a pre-fractal wave scattering from a pre-fractal obstacle. To pursue this particular class of problem, the same types of mathematical model and computational techniques deployed elsewhere in the thesis

have been used: the RS diffraction integral, Weierstrass-type illumination, and gratings based on pre-fractal levels of traditional and modified Cantor sets. This work is very much provisional, and it certainly merits further development. Computation times required for these types of calculations, particularly once one goes from the traditional Cantor set to its modified counterpart, have tended to become prohibitive. The number of points requirement in the x domain (in order to avoid under-sampling) increases dramatically with n, and these numerical calculations rapidly start becoming impractical. Within the MSc time-scale, it has been possible to generate results only up to the third pre-fractal level.

The computation time may be reduced significantly by altering the approach to the numerics. For instance, one might use specialised oscillatory quadrature methods that are tailored to these sorts of problems (e.g., where there is a frequency-independent computational cost in high-frequency regimes) [46]. Such methods might be deployed to compute full boundary-element solutions, which is a topic reserved for future research. The main roadblock encountered has been extracting physically-meaningful results from the systematic BENOIT analysis of many large datasets. The inconclusive nature of these investigations suggest that other methods may be required in order to fully understand the dimension of the pre-fractal diffraction patterns. One obvious candidate approach is to consider band-averaging in the fourier domain, as considered by Uozumi et. al. [44]. In conclusion, this thesis has attacked a suite of wave propagation problems with regards to various combinations of pre-fractal waves and a variety of scattering obstacles: from the single knife-edge to a single slit and pre-fractal levels of Cantor sets. The results presented here are just the 'tip of the iceberg', and while some solid progress has clearly been made there remains much research to be followed-up for each of the four main strands.

APPENDIX A

DERIVATION OF THE 1-DIMENSIONAL RAYLEIGH-SOMMERFELD EQUATION

The 1D Rayleigh-Sommerfeld formulation is given by [28] to be

$$E_z(x,y) = \frac{iky}{2}\int_{-\infty}^{\infty} dx' E_z(x',0)\frac{H_1^{(1)}(kR)}{R}. \tag{A.1}$$

This can be shown by first taking the Helmholtz equation,

$$\frac{\partial^2 E_z}{\partial y^2} + \frac{\partial^2 E_z}{\partial x^2} + k^2 E_z = 0. \tag{A.2}$$

Setting $E_z(x,y) = E_0 \exp[i(k_x x + k_y y)]$, one then arrives at the dispersion relation,

$$k_y^2 + k_x^2 = k^2. \tag{A.3}$$

The general solution for $E_z(x,y)$ is a linear superposition of a forward and backward-propagating waves, where $k_y > 0$ is the forward solution and $k_y < 0$ is the backward one, so that

$$E_z(x,y) = E_0^{(+)} \exp[i(k_x x + k_y^{(+)} y)] + E_0^{(-)} \exp[i(k_x x + k_y^{(-)} y)]. \tag{A.4}$$

Next, one needs to find an equation for the y-dependence of the Fourier transform $\tilde{E}_z(k_x,y)$ [20], where

$$\tilde{E}_z(k_x,y) = \frac{1}{2\pi}\int_{-\infty}^{\infty} dx E_z(x,y)\exp(-ik_x x). \tag{A.5}$$

Combining Eqs. (A.2) and (A.5) one gets the equation for the y-dependence of the Fourier Transform,

$$\frac{\partial^2}{\partial y^2}\tilde{E}_z(k_x,y) + (k^2 - k_x^2)\tilde{E}_z(k_x,y) = 0. \tag{A.6}$$

Looking at only the forward solution,

$$E_z(x,y) = \int_{-\infty}^{\infty} dk_x \tilde{E}_z(k_x,0)\exp[i(k_x x + k_y y)]. \tag{A.7}$$

$k_y(k_x) \equiv \sqrt{k^2 - k_x^2}$, therefore

$$E_z(x,y) = \int_{-\infty}^{\infty} dk_x \tilde{E}_z(k_x,0)\exp[ik_y(k_x)]\exp(ik_x x), \tag{A.8}$$

Defining $\exp[-ik_y(k_x)y]$ through its Fourier transform,

$$\tilde{h}(k_x,y) = \frac{1}{2\pi}\int_{-\infty}^{\infty} dx h(x,y) \equiv \exp[-ik_y(k_x)y], \tag{A.9}$$

and therefore

$$E_z(x,y) = \int_{-\infty}^{\infty} dk_x \tilde{E}_z(k_x,0)\tilde{h}(k_x,y)\exp(ik_x x). \tag{A.10}$$

$$\tilde{E}_z(k_x,0) = \frac{1}{2\pi}\int_{-\infty}^{\infty} dx E_z(x,0)\exp(-ik_x x) \rightarrow \frac{1}{2\pi}\int_{-\infty}^{\infty} dx' E_z(x',0)\exp(-ik_x x') \tag{A.11}$$

$$\tilde{h}(k_x,0) = \frac{1}{2\pi}\int_{-\infty}^{\infty} dx h(x,y)\exp(-ik_x x) \rightarrow \frac{1}{2\pi}\int_{-\infty}^{\infty} dx'' h(x'',y)\exp(-ik_x x'') \tag{A.12}$$

Substituting Eq.s (A.11) and (A.12) into Eq. (A.9), one then gets

$$E_z(x,y) = \frac{1}{2\pi}\int_{-\infty}^{\infty} dx' E_z(x',0)h(x-x',y). \tag{A.13}$$

One needs to redefine $h(x,y)$ so that,

$$h(x,y) = \int_{-\infty}^{\infty} dk_x \exp[ik_y(k_x)y]\exp(ik_x x), \tag{A.14}$$

hence,

$$E_z(x,y) = \int_{-\infty}^{\infty} dx' E_z(x',0)h(x-x',y) \equiv E_z(x,0) * h(x,y) \tag{A.15}$$

$$h(x,y) = \frac{1}{i}\frac{\partial}{\partial y}\int_{-\infty}^{\infty} \frac{dk_x}{k_y}\exp[i(k_x x + k_y y)] \tag{A.16}$$

$$\begin{aligned} I &= \int_{-\infty}^{\infty} dk_x \frac{\exp\left\{i[k_x x + \sqrt{(k^2 - k_x^2)}y]\right\}}{\sqrt{(k^2 - k_x^2)}} \\ &= \int_{-\infty}^{\infty} \frac{dk_x}{k_y}\exp(i\mathbf{k}\cdot\mathbf{x}) \end{aligned} \tag{A.17}$$

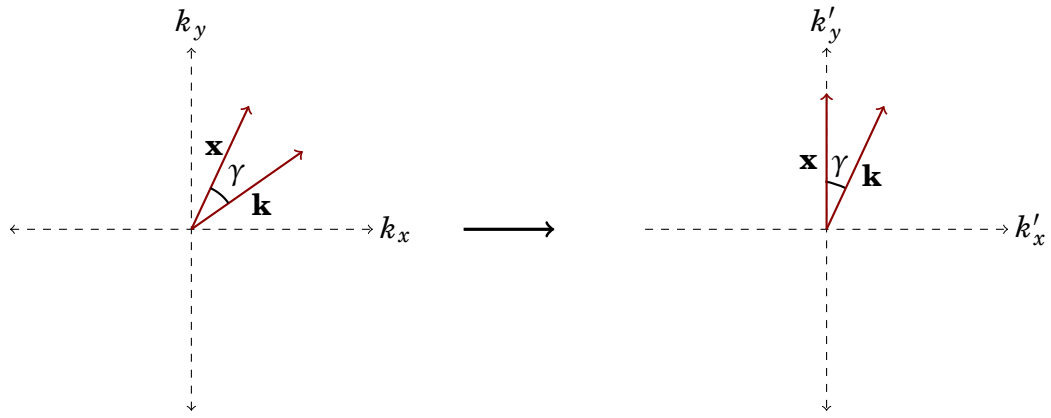

Figure A.1: The coordinate transformation undergone in order to have $\mathbf{k}\cdot\mathbf{x}$ in terms of k'_x and k'_y.

From the transformation shown in figure A.1 it is shown that

$$I = \int_{\frac{\pi}{2}-i\infty}^{-\frac{\pi}{2}+i\infty} d\gamma \exp(ikr\cos\gamma). \tag{A.18}$$

Next is another substitution of $\alpha = -\gamma - \frac{\pi}{2}$ so that the integral is in the form of

$$I = -\int_{-i\infty}^{-\pi-i\infty} d\alpha \exp(-ikr\sin\alpha), \tag{A.19}$$

and therefore [30]

$$I = \pi H_0^{(1)}(kr). \tag{A.20}$$

Substituting Eq. (A.20) back into Eq. (A.14),

$$\begin{aligned} h(x,y) &= \frac{1}{2i}\frac{\partial}{\partial y} H_0^{(1)}(kr), \\ &= \frac{-ky}{2ir} H_1^{(1)}(kr), \end{aligned} \tag{A.21}$$

where $r = \sqrt{x^2+y^2}$ and substituting Eq. (A.21) back into Eq. (A.13) gives the 1DRS equation,

$$E_z(x,y) = \frac{iky}{2}\int_{-\infty}^{\infty} dx' E_z(x',0)\frac{H_1^{(1)}(kR)}{R}, \tag{A.22}$$

where $R = \sqrt{(x-x')^2+y^2}$.

APPENDIX B

DERIVATION FOR THE KNIFE-EDGE DIFFRACTION FROM AN OBLIQUE INCIDENCE ANGLE

In this work, the derivations for two specific incidences of the Sommerfeld solution have been worked through. Firstly, the solution where electric field is transverse to the screen (the TE solution) is considered, and afterwards the solution where magnetic field is, instead, transverse to the screen is derived.

B.1 Derivation of the electric field components for a transverse electric field

In this section, Initially one must consider the Helmholtz equation,

$$(\nabla^2 + k^2)E_z(x,y) = 0, \tag{B.1}$$

where E_z is a summation of an incident field, $E_0 \exp(i\mathbf{k_{inc}} \cdot \mathbf{x})$ and a scattered field, $\Psi_s(x,y)$.

$$E_z(x,y) = E_0 \exp(i\mathbf{k_{inc}} \cdot \mathbf{x}) + \Psi_s(x,y), \tag{B.2}$$

The scattered field $\Psi_s(x,y)$ is composed of an incident part and a reflected part so that,

$$\Psi_s(x,y) = \Psi_{inc} \exp(i\mathbf{k_{inc}} \cdot \mathbf{x}) + \Psi_{ref} \exp(i\mathbf{k_{ref}} \cdot \mathbf{x}), \tag{B.3}$$

so that

$$\left(\frac{\partial^2}{\partial x^2} + \frac{\partial^2}{\partial y^2} + k^2\right)\left[\Psi_{inc} \exp(i\mathbf{k_{inc}} \cdot \mathbf{x}) + \Psi_{ref} \exp(i\mathbf{k_{ref}} \cdot \mathbf{x})\right]. \tag{B.4}$$

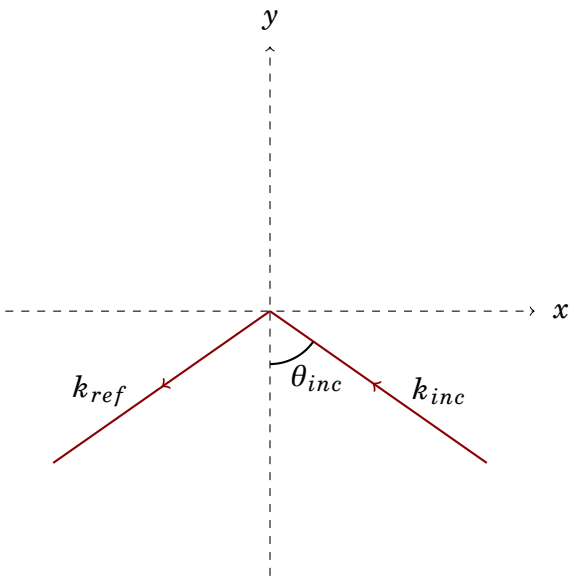

Figure B.1: $\mathbf{k_{inc}}$ and $\mathbf{k_{ref}}$.

where $k_{ref} = k(-\sin\theta_{inc})$. Focusing, for now, on the incident part,

$$\frac{\partial}{\partial x} = \left(\frac{\partial \Psi_{inc}}{\partial x} + ik_{inc_x}\Psi_{inc}\right)\exp(i\mathbf{k_{inc}}\cdot\mathbf{x}),$$
$$\frac{\partial^2}{\partial x^2} = \left(\frac{\partial^2 \Psi_{inc}}{\partial x^2} + i2k_{inc_x}\frac{\partial \Psi_{inc}}{\partial x} - k_{inc_x}^2\Psi_{inc}\right)\exp(i\mathbf{k_{inc}}\cdot\mathbf{x}),$$
$$\frac{\partial}{\partial y} = \left(\frac{\partial \Psi_{inc}}{\partial y} + ik_{inc_y}\Psi_{inc}\right)\exp(i\boldsymbol{k_{inc}}\cdot\boldsymbol{x}),$$
$$\frac{\partial^2}{\partial y^2} = \left(\frac{\partial^2 \Psi_{inc}}{\partial y^2} + i2k_{inc_y}\frac{\partial \Psi_{inc}}{\partial y} - k_{inc_y}^2\Psi_{inc}\right)\exp(i\boldsymbol{k_{inc}}\cdot\boldsymbol{x}).$$

From this, one can see that,

$$\left(\frac{\partial^2}{\partial x^2} + \frac{\partial^2}{\partial y^2} + k^2\right)\left[\Psi_{inc}\exp(i\mathbf{k_{inc}}\cdot\mathbf{x})\right] = \left[\frac{\partial^2 \Psi_{inc}}{\partial x^2} + \frac{\partial^2 \Psi_{inc}}{\partial y^2} + i2\left(k_{inc_x}\frac{\partial \Psi_{inc}}{\partial x} + k_{inc_y}\frac{\partial \Psi_{inc}}{\partial y}\right)\right]. \tag{B.5}$$

Looking at Fig. B.2, it is shown that

$$\begin{pmatrix} x' \\ y' \end{pmatrix} = \begin{pmatrix} \cos\theta_{inc} & \sin\theta_{inc} \\ -\sin\theta_{inc} & \cos\theta_{inc} \end{pmatrix}\begin{pmatrix} x \\ y \end{pmatrix}, \tag{B.6}$$

and therefore

$$x' = x\cos\theta_{inc} + y\sin\theta_{inc}, \tag{B.7}$$

$$y' = y\cos\theta_{inc} - x\sin\theta_{inc}. \tag{B.8}$$

The Helmholtz equation is covariant under transformation and hence

$$\left(\frac{\partial^2 \Psi_{inc}}{\partial x'^2} + \frac{\partial^2 \Psi_{inc}}{\partial y'^2} + i2k\frac{\partial \Psi_{inc}}{\partial y'}\right) = 0. \tag{B.9}$$

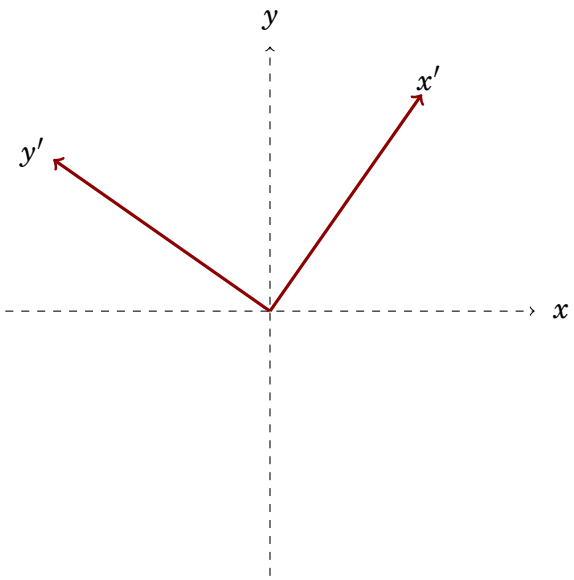

Figure B.2: Coordinate transformation (x, y) to (x', y').

For a coordinate transformation of the reflected plane,

$$\begin{pmatrix} x'' \\ y'' \end{pmatrix} = \begin{pmatrix} -\cos\theta_{inc} & \sin\theta_{inc} \\ -\sin\theta_{inc} & -\cos\theta_{inc} \end{pmatrix} \begin{pmatrix} x \\ y \end{pmatrix}. \tag{B.10}$$

As with B.9,

$$\left(\frac{\partial^2 \Psi_{inc}}{\partial x''^2} + \frac{\partial^2 \Psi_{inc}}{\partial y''^2} - i2k \frac{\partial \Psi_{inc}}{\partial y''} \right) = 0. \tag{B.11}$$

Going from Cartesian to Parabolic-Cylindrical coordinates, the transformations are as follows [20]:

$$\xi' = \sqrt{kr}\cos\frac{\phi'}{2}, \qquad \eta' = \sqrt{kr}\sin\frac{\phi'}{2}, \tag{B.12}$$

$$\xi'' = \sqrt{kr}\cos\frac{\phi''}{2}, \qquad \eta'' = \sqrt{kr}\sin\frac{\phi''}{2}, \tag{B.13}$$

where $\phi' = \phi - \theta_{inc}$ and $\phi'' = \phi + \theta_{inc}$. From this definition, one can see that

$$\begin{aligned} \frac{\partial \Psi_{inc}}{\partial x'} &= \frac{\xi'}{\partial x'}\frac{\partial \Psi_{inc}}{\partial \xi'} + \frac{\partial \eta'}{\partial x'}\frac{\partial \Psi_{inc}}{\partial \eta'} \\ &= \frac{\eta'}{2r}\frac{\partial \Psi_{inc}}{\partial \xi'} - \frac{\xi'}{2r}\frac{\partial \Psi_{inc}}{\partial \eta'}, \end{aligned} \tag{B.14}$$

$$\begin{aligned} \frac{\partial \Psi_{inc}}{\partial y'} &= \frac{\partial \xi'}{\partial y'}\frac{\partial \Psi_{inc}}{\partial \xi'} + \frac{\partial \eta'}{\partial y'}\frac{\partial \Psi_{inc}}{\partial \eta'} \\ &= \frac{\eta'}{2r}\frac{\partial \Psi_{inc}}{\partial \xi'} + \frac{\xi'}{2r}\frac{\partial \Psi_{inc}}{\partial \eta'}, \end{aligned} \tag{B.15}$$

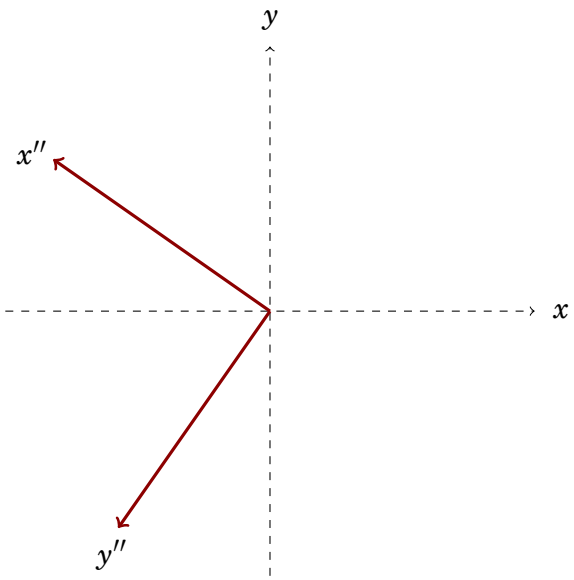

Figure B.3: Coordinate transformation (x, y) to (x'', y'').

$$\frac{\partial^2 \Psi_{inc}}{\partial x^2} = \frac{\partial \xi'^2}{4r^2}\frac{\partial^2 \Psi_{inc}}{\partial \xi'^2} + \frac{\eta'^2}{4r^2}\frac{\partial^2 \Psi_{inc}}{\partial \eta'^2} - \frac{\eta'\xi'}{4r^2}\frac{\partial^2 \Psi_{inc}}{\partial \eta' \partial \xi'} \tag{B.16}$$

and

$$\frac{\partial^2 \Psi_{inc}}{\partial y^2} = \frac{\eta'^2}{4r^2}\frac{\partial^2 \Psi_{inc}}{\partial \xi'^2} + \frac{\xi'^2}{4r^2}\frac{\partial^2 \Psi_{inc}}{\partial \eta'^2} + \frac{\eta'\xi'}{4r^2}\frac{\partial^2 \Psi_{inc}}{\partial \eta' \partial \xi'}. \tag{B.17}$$

All is the same for Ψ_{ref} and therefore

$$\frac{\partial^2 \Psi_{inc}}{\partial \xi'^2} + \frac{\partial^2 \Psi_{inc}}{\partial \eta'^2} + 4i\left[\eta'\frac{\partial \Psi_{inc}}{\partial \xi'} + \xi'\frac{\partial \Psi_{inc}}{\partial \eta'}\right] = 0 \tag{B.18}$$

and

$$\frac{\partial^2 \Psi_{ref}}{\partial \xi''^2} + \frac{\partial^2 \Psi_{ref}}{\partial \eta''^2} - 4i\left[\eta''\frac{\partial \Psi_{ref}}{\partial \xi''} + \xi''\frac{\partial \Psi_{ref}}{\partial \eta''}\right] = 0. \tag{B.19}$$

Taking $\Psi_{inc}, \Psi_{ref}(\xi, \eta) = f(\eta \mp \xi) \equiv f(\zeta)$, Eqs. (B.18) and (B.19) then become

$$\frac{d^2 \Psi_{inc}}{d\zeta'^2} + 2i\zeta'\frac{d\Psi_{inc}}{d\zeta'} = 0 \tag{B.20}$$

and

$$\frac{d^2 \Psi_{ref}}{d\zeta''^2} + 2i\zeta''\frac{d\Psi_{ref}}{d\zeta''} = 0. \tag{B.21}$$

Eqs. (B.20) and (B.21) are standard integrals which integrate to [30]

$$f(\zeta) = a_{inc} + b_{inc}\sqrt{\frac{\pi}{2}}\int_0^{\sqrt{\frac{\pi}{2}}(\eta' - \xi')} d\zeta \exp\left(i\frac{\pi}{2}\zeta^2\right) \tag{B.22}$$

and

$$f(\zeta) = a_{ref} + b_{ref}\sqrt{\frac{2}{\pi}}\int_0^{\sqrt{\frac{\pi}{2}}(\eta''+\xi'')} d\zeta \exp\left(i\frac{\pi}{2}\zeta^2\right) \tag{B.23}$$

respectively. To find the constants a_{inc}, a_{ref}, b_{inc} and b_{ref}, two boundary conditions must be considered. Firstly the case on the boundary far away from the coordinate origin is considered, i.e. $x \to -\infty$ and $y \ll \mathcal{O}(1)$. As $x \to -\infty$, $\phi = \pi$, Ψ_s is negligible and hence,

$$a_{inc} + b_{inc}\sqrt{\frac{2}{\pi}}\int_0^{\infty} \exp\left(i\frac{\pi}{2}\zeta^2\right)d\zeta = 0, \tag{B.24}$$

and

$$a_{ref} + b_{ref}\sqrt{\frac{2}{\pi}}\int_0^{\infty} \exp\left(i\frac{\pi}{2}\zeta^2\right)d\zeta = 0. \tag{B.25}$$

Next, the solution on the half place is considered. On the half-plane, $E_z = 0$, $\phi = 0$ and $x > 0$, hence $\boldsymbol{k_{inc}} \cdot \boldsymbol{x} \to -k\sin\theta_{inc}x$ and $\boldsymbol{k_{ref}} \cdot \boldsymbol{x} \to -k\sin\theta_{inc}x$. At the screen,

$$\eta' - \xi'\Big|_{screen} = -\sqrt{kx}\left[\sin\frac{\theta_{inc}}{2} + \cos\frac{\theta_{inc}}{2}\right] \tag{B.26}$$

and

$$\eta'' + \xi''\Big|_{screen} = \sqrt{kx}\left[\sin\frac{\theta_{inc}}{2} + \cos\frac{\theta_{inc}}{2}\right]. \tag{B.27}$$

Substituting these into Eq. (B.24) and Eq. (B.25) yields

$$1 + a_{inc} + a_{ref} + (b_{inc} - b_{ref})\sqrt{\frac{2}{\pi}}\int_0^{\sqrt{\frac{\pi kx}{2}}\left[\cos\frac{\theta_{inc}}{2}+\sin\frac{\theta_{inc}}{2}\right]} \exp\left(i\frac{\pi}{2}\zeta^2\right)d\zeta = 0. \tag{B.28}$$

The boundary conditions can therefore be deduced as

$$b_{inc} = b_{ref}, \tag{B.29}$$

and

$$a_{inc} + a_{ref} = -E_0. \tag{B.30}$$

Therefore,

$$\begin{aligned}\frac{E_z(x,y)}{E_0} = {} & \exp(i\mathbf{k_{inc}}\cdot\mathbf{x}) - \frac{1+i}{2i}\left[\exp(i\mathbf{k_{inc}}\cdot\mathbf{x})F(\chi_-) - \exp(i\mathbf{k_{ref}}\cdot\mathbf{x})F(\chi_+)\right] \\ & - \frac{1}{2}\left[\exp(i\mathbf{k_{inc}}\cdot\mathbf{x}) + \exp(i\mathbf{k_{ref}}\cdot\mathbf{x})\right],\end{aligned} \tag{B.31}$$

B.2 Magnetic field components for parallel polarization of a plane incident wave

Equation (B.31) can be represented as

$$E_z(x,y) = E_0 \exp(i\mathbf{k_{inc}}\cdot\mathbf{x}) + \Psi_s(x,y). \tag{B.32}$$

In order to find the B components of the solution, one must look at the Maxwell equation

$$\nabla\times\mathbf{E} + \frac{\partial\mathbf{B}}{\partial t} = 0. \tag{B.33}$$

For a cw solution,

$$\mathbf{B} = \frac{-i}{\omega}\nabla\times\mathbf{E}. \tag{B.34}$$

$$\mathbf{B} = \frac{-i}{\omega}\Big[\Big(\frac{1}{r}\frac{\partial E_z}{\partial\phi} - \frac{\partial E_\phi}{\partial z}\Big)\hat{\mathbf{e}}_r + \Big(\frac{\partial E_r}{\partial\phi} - \frac{\partial E_z}{\partial z}\Big)\hat{\mathbf{e}}_\phi + \frac{1}{r}\Big(\frac{\partial}{\partial r}(rE_\phi) - \frac{\partial E_r}{\partial\phi}\Big)\hat{\mathbf{e}}_z\Big], \tag{B.35}$$

and therefore the r and ϕ components of $\mathbf{B}$ are

$$B_r = \frac{-i}{wr}\Big[\frac{\partial}{\partial\phi}E_0\exp(i\boldsymbol{k_{inc}}\cdot\boldsymbol{x}) + \frac{\partial\Psi}{\partial\phi}\Big], \tag{B.36}$$

and

$$B_\phi = \frac{-i}{w}\Big[\frac{\partial}{\partial r}E_0\exp(i\boldsymbol{k_{inc}}\cdot\boldsymbol{x}) + \frac{\partial\Psi}{\partial r}\Big]. \tag{B.37}$$

$$\begin{aligned}\frac{\partial\Psi}{\partial\phi} = &-E_0\frac{1+i}{2i}\exp(i\mathbf{k_{inc}}\cdot\mathbf{x})\frac{\partial}{\partial\phi}F(\chi_-) - E_0\frac{1+i}{2i}F(\chi_-)\frac{\partial}{\partial\phi}\exp(i\mathbf{k_{inc}}\cdot\mathbf{x})\\ &+E_0\frac{1+i}{2i}\exp(i\mathbf{k_{ref}}\cdot\mathbf{x})\frac{\partial}{\partial\phi}F(\chi_+) + E_0\frac{1+i}{2i}F(\chi_+)\frac{\partial}{\partial\phi}\exp(i\mathbf{k_{ref}}\cdot\mathbf{x})\\ &-\frac{E_0}{2}\Big[\frac{\partial}{\partial\phi}\exp(i\mathbf{k_{inc}}\cdot\mathbf{x}) + \frac{\partial}{\partial\phi}\exp(i\mathbf{k_{ref}}\cdot\mathbf{x})\Big].\end{aligned} \tag{B.38}$$

$$\frac{\partial F(\chi_-)}{\partial\phi} = -\frac{\exp(i\frac{\pi}{2}\chi_-^2)}{2}\sqrt{\frac{2kr}{\pi}}\Big[\cos\Big(\frac{\phi-\theta_{inc}}{2}\Big) + \sin\Big(\frac{\phi-\theta_{inc}}{2}\Big)\Big], \tag{B.39}$$

$$\frac{\partial F(\chi_+)}{\partial\phi} = \frac{\exp(i\frac{\pi}{2}\chi_+^2)}{2}\sqrt{\frac{2kr}{\pi}}\Big[\cos\Big(\frac{\phi+\theta_{inc}}{2}\Big) - \sin\Big(\frac{\phi+\theta_{inc}}{2}\Big)\Big], \tag{B.40}$$

$$\frac{\partial}{\partial\phi}\exp(i\mathbf{k_{inc}}\cdot\mathbf{x}) = ikr\cos(\phi-\theta_{inc})\exp(i\mathbf{k_{inc}}\cdot\mathbf{x}) \tag{B.41}$$

and

$$\frac{\partial}{\partial\phi}\exp(i\mathbf{k_{ref}}\cdot\mathbf{x}) = -ikr\cos(\phi+\theta_{inc})\exp(i\mathbf{k_{ref}}\cdot\mathbf{x}). \tag{B.42}$$

$$\begin{aligned}\frac{\partial\Psi}{\partial\phi} = &-E_0 ikr\Big\{-\frac{1+i}{\sqrt{\pi kr}}\exp(ikr)\cos\Big(\frac{\phi}{2}+\frac{\pi}{4}\Big)\\ &+\frac{1+i}{2i}\big[F(\chi_-)\cos(\phi-\theta_{inc})\exp(i\mathbf{k_{inc}}\cdot\mathbf{x})+F(\chi_+)\cos(\phi+\theta_{inc})\exp(i\mathbf{k_{ref}}\cdot\mathbf{x})\big]\\ &+\frac{1}{2}\big[\cos(\phi-\theta_{inc})\exp(i\mathbf{k_{inc}}\cdot\mathbf{x})-\cos(\phi+\theta_{ref})\exp(i\mathbf{k_{ref}}\cdot\mathbf{x})\big]\Big\}\end{aligned} \tag{B.43}$$

Therefore the r component of the magnetic field, $\mathbf{B}$, is

$$\begin{aligned}\frac{B_r}{B_0} = &\cos(\phi+\theta_{ref})-\frac{1+i}{2i}\Big[F(\chi_-)\cos(\phi-\theta_{inc})\exp(i\boldsymbol{k_{inc}}\cdot\boldsymbol{x})+F(\chi_+)\cos(\phi+\theta_{inc})\exp(i\boldsymbol{k_{ref}}\cdot\boldsymbol{x})\Big]\\ &-\frac{1+i}{\sqrt{\pi kr}}\cos\frac{\phi}{2}\cos(\frac{\theta_{inc}}{2}+\frac{\pi}{4})-\frac{1}{2}\Big[\cos(\phi-\theta_{inc})\exp(i\boldsymbol{k_{inc}}\cdot\boldsymbol{x})+\cos(\phi+\theta_{inc})\exp(i\boldsymbol{k_{ref}}\cdot\boldsymbol{x})\Big]\end{aligned} \tag{B.44}$$

$$\frac{\partial}{\partial r}E_0\exp(i\boldsymbol{k_{inc}}\cdot\boldsymbol{x}) = ik\sin(\phi-\theta_{inc})E_0\exp(i\boldsymbol{k_{inc}}) \tag{B.45}$$

$$\begin{aligned}\frac{\partial\Psi}{\partial r} = &-E_0\frac{1+i}{2i}\exp(\boldsymbol{k_{inc}}\cdot\boldsymbol{x})\frac{\partial}{\partial r}F(\chi_-)-E_0\frac{1+i}{2i}F(\chi_-)\frac{\partial}{\partial r}\exp(\boldsymbol{k_{inc}}\cdot\boldsymbol{x})\\ &+E_0\frac{1+i}{2i}\exp(\boldsymbol{k_{ref}}\cdot\boldsymbol{x})\frac{\partial}{\partial r}F(\chi_+)+E_0\frac{1+i}{2i}F(\chi_+)\frac{\partial}{\partial r}\exp(\boldsymbol{k_{ref}}\cdot\boldsymbol{x})\\ &-\frac{E_0}{2}\Big(\frac{\partial}{\partial r}\exp(\boldsymbol{k_{inc}})+\frac{\partial}{\partial r}\exp(\boldsymbol{k_{ref}})\Big).\end{aligned} \tag{B.46}$$

$$\frac{\partial}{\partial r}F(\chi_-) = \frac{\exp(i\frac{\pi}{2}\chi_-^2)}{2r}\chi_-, \tag{B.47}$$

$$\frac{\partial}{\partial r}F(\chi_+) = \frac{\exp(i\frac{\pi}{2}\chi_+^2)}{2r}\chi_+, \tag{B.48}$$

$$\frac{\partial}{\partial r}\exp(\boldsymbol{k_{inc}}\cdot\boldsymbol{x}) = ik\sin(\phi-\theta_{inc})\exp(\boldsymbol{k_{inc}}\cdot\boldsymbol{x}), \tag{B.49}$$

and

$$\frac{\partial}{\partial r}\exp(\boldsymbol{k_{ref}}\cdot\boldsymbol{x}) = -ik\sin(\phi+\theta_{inc})\exp(\boldsymbol{k_{ref}}\cdot\boldsymbol{x}). \tag{B.50}$$

Therefore the ϕ component of the magnetic field, $\mathbf{B}$, is

$$\begin{aligned}\frac{B_\phi}{B_0} = &-\sin(\phi-\theta_{inc})\exp(i\boldsymbol{k_{inc}}\cdot\boldsymbol{x})+\frac{1+i}{2i}\frac{\exp(ikr)}{2ikr}(\chi_--\chi_+)\\ &+\frac{1+i}{2i}\Big[\sin(\phi+\theta_{inc})\exp(i\boldsymbol{k_{inc}}\cdot\boldsymbol{x})F(\chi_+)+\sin(\phi-\theta_{inc})\exp(i\boldsymbol{k_{inc}}\cdot\boldsymbol{x})F(\chi_-)\Big]\\ &+\frac{1}{2}\Big[\sin(\phi-\theta_{inc})\exp(i\boldsymbol{k_{inc}}\cdot\boldsymbol{x})-\sin(\phi+\theta_{inc})\exp(i\boldsymbol{k_{inc}}\cdot\boldsymbol{x})\Big].\end{aligned} \tag{B.51}$$

APPENDIX C

PLANE-WAVE DIFFRACTION FROM CANTOR GRATINGS

This appendix presents a fairly wide selection of results predicting the diffraction patterns from pre-fractal levels 0 through 5 for the traditional and modified Cantor-set illuminated by a normally-incident plane wave. The slit widths (the overall slit size a_0 in the traditional Cantor-set case and the individual a_n for the modified case) are in the rage of 1.5λ to 250λ.

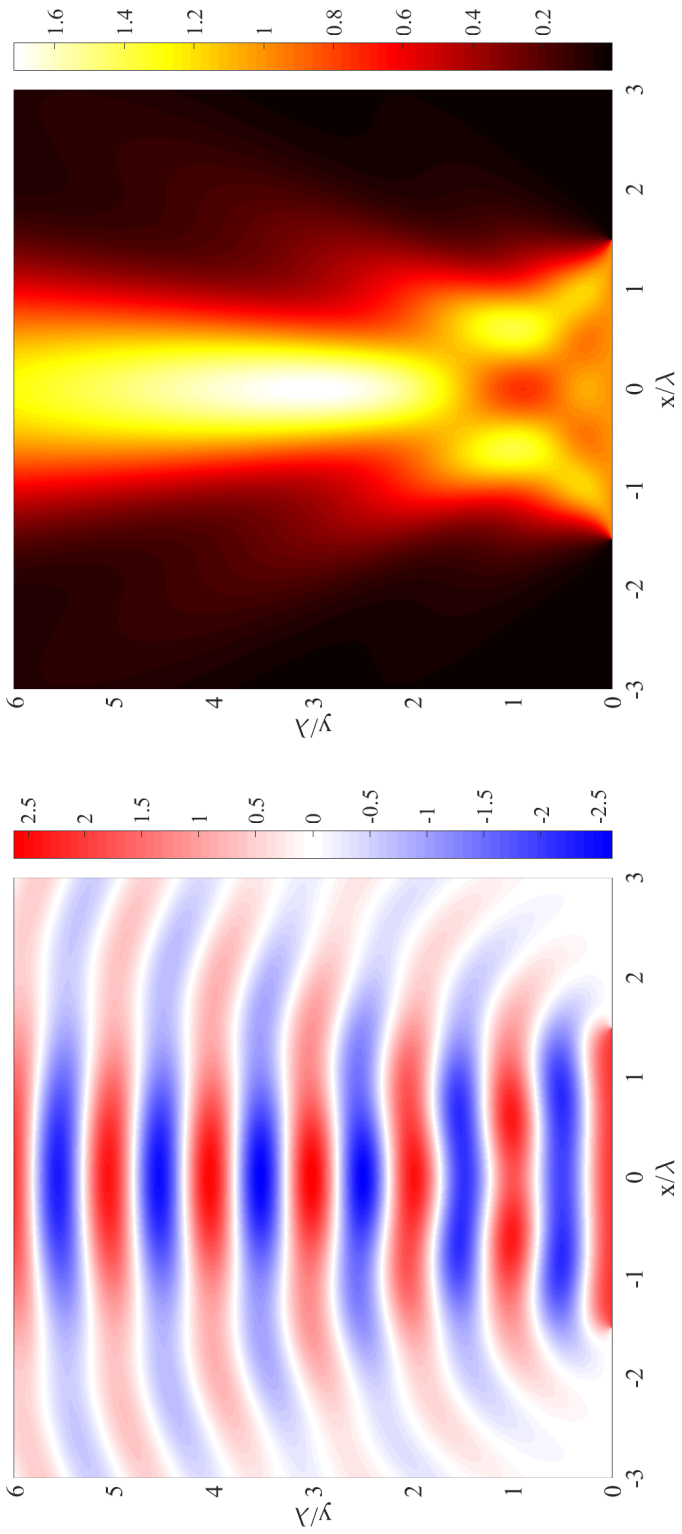

Figure C.1: Diffraction of a plane wave from the $n = 0$th pre-fractal iteration of the Cantor set with an $a_0 = 1.5\lambda$. Electric field, $2\Re e(\frac{E_z}{E_0})$, *(left)* and intensity, $|\frac{E_z}{E_0}|^2$ *(right)*.

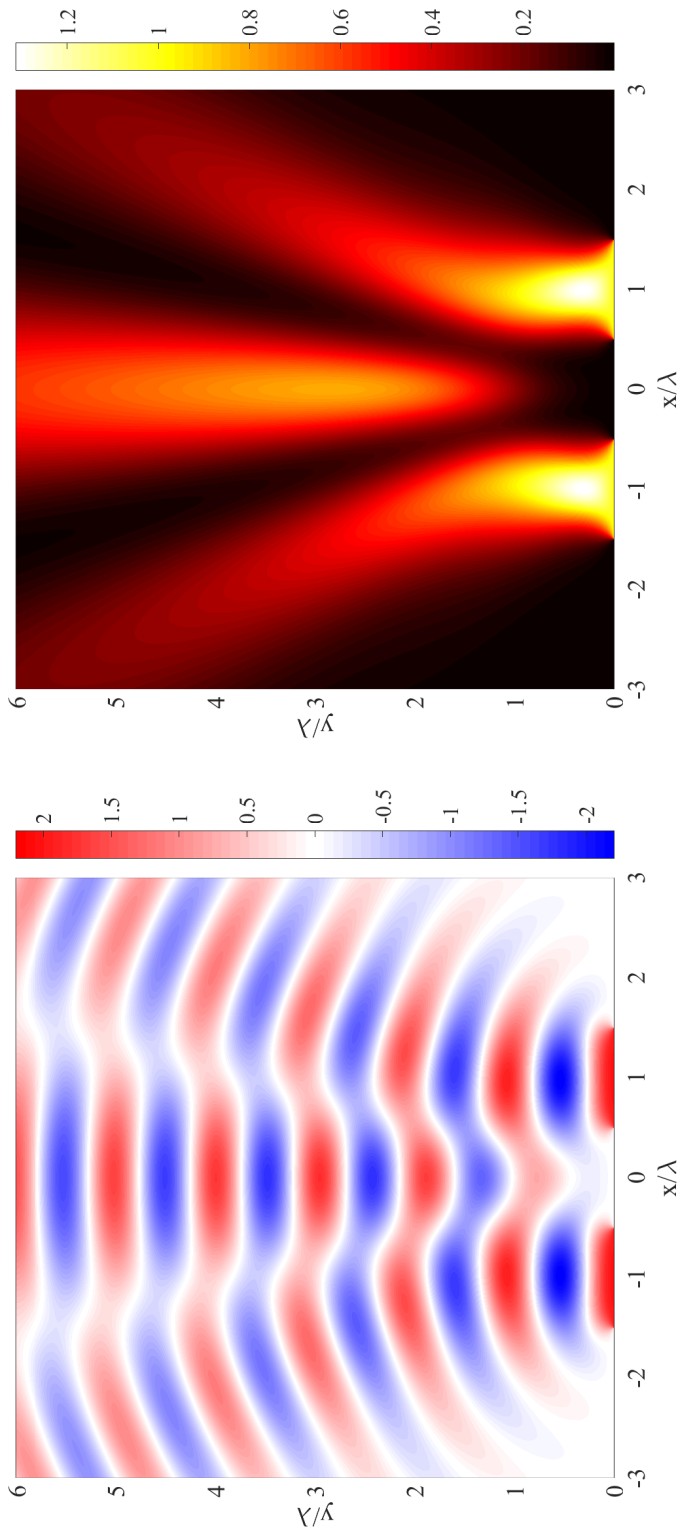

Figure C.2: Diffraction of a plane wave from the $n = 1$th pre-fractal level of the Cantor set with an $a_0 = 1.5\lambda$. Electric field, $2\Re e\left(\frac{E_z}{E_0}\right)$, *(left)* and intensity, $\left|\frac{E_z}{E_0}\right|^2$ *(right)*.

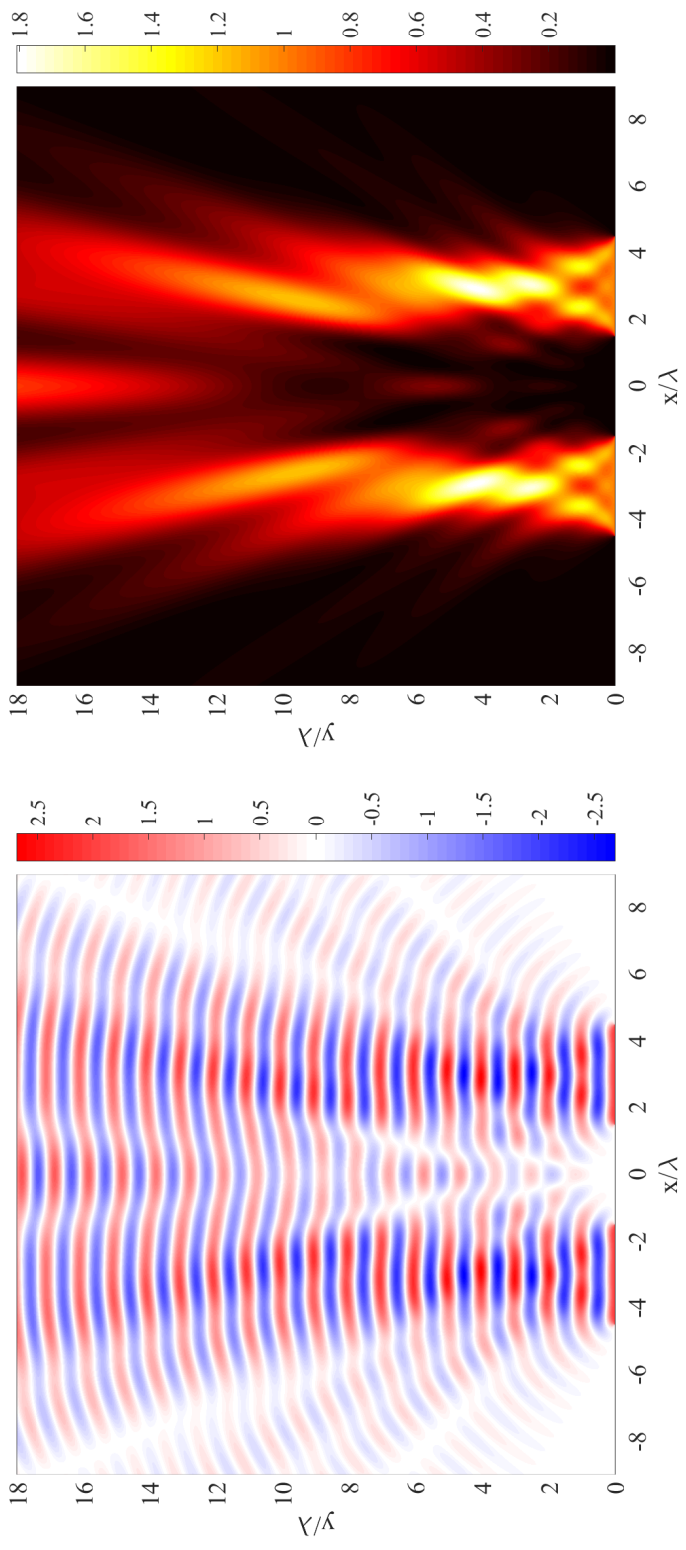

Figure C.3: Diffraction of a plane wave from the $n = 1$th pre-fractal level of the Cantor set with an $a_n = 1.5\lambda$. Electric field, $2\Re e\left(\frac{E_z}{E_0}\right)$, *(left)* and intensity, $\left|\frac{E_z}{E_0}\right|^2$ *(right)*.

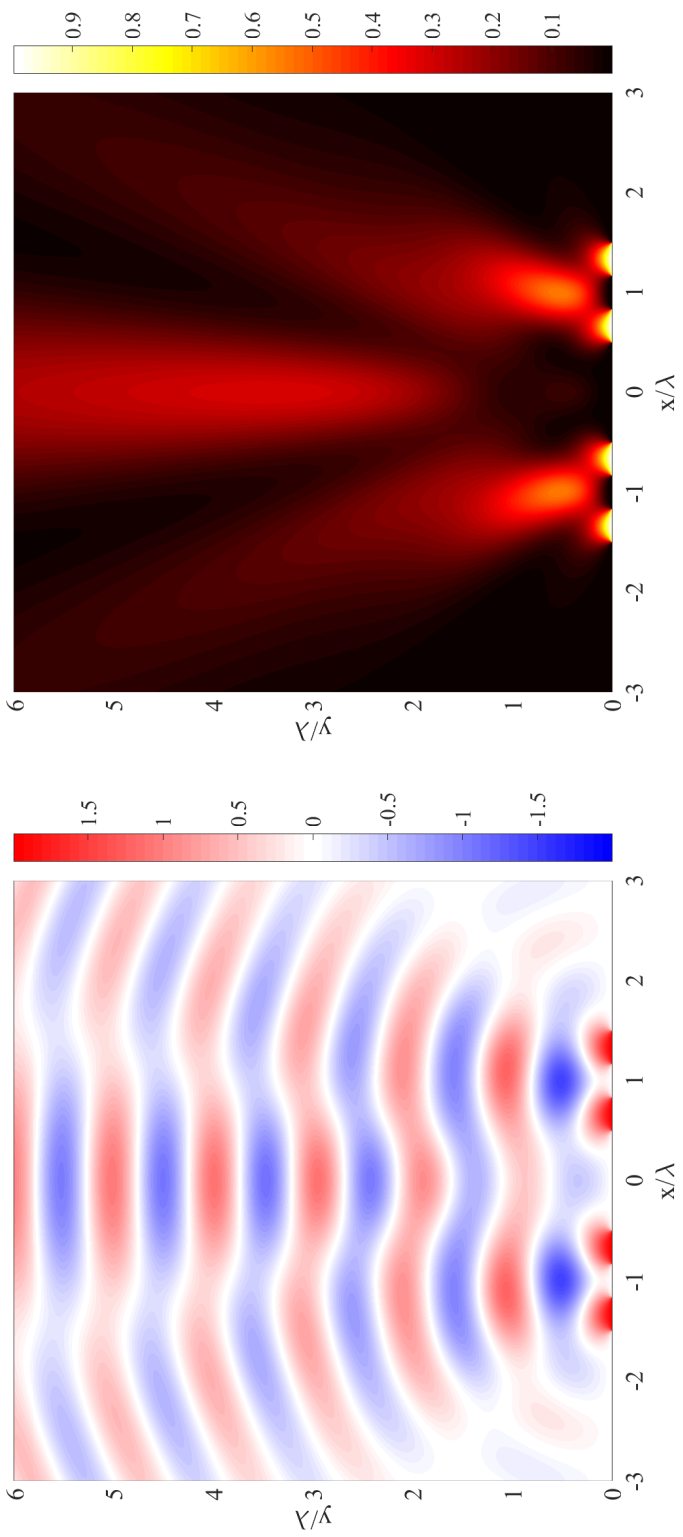

Figure C.4: Diffraction of a plane wave from the $n = 2$th pre-fractal level of the Cantor set with an $a_0 = 1.5\lambda$. Electric field, $2\Re e\left(\frac{E_z}{E_0}\right)$, *(left)* and intensity, $\left|\frac{E_z}{E_0}\right|^2$ *(right)*.

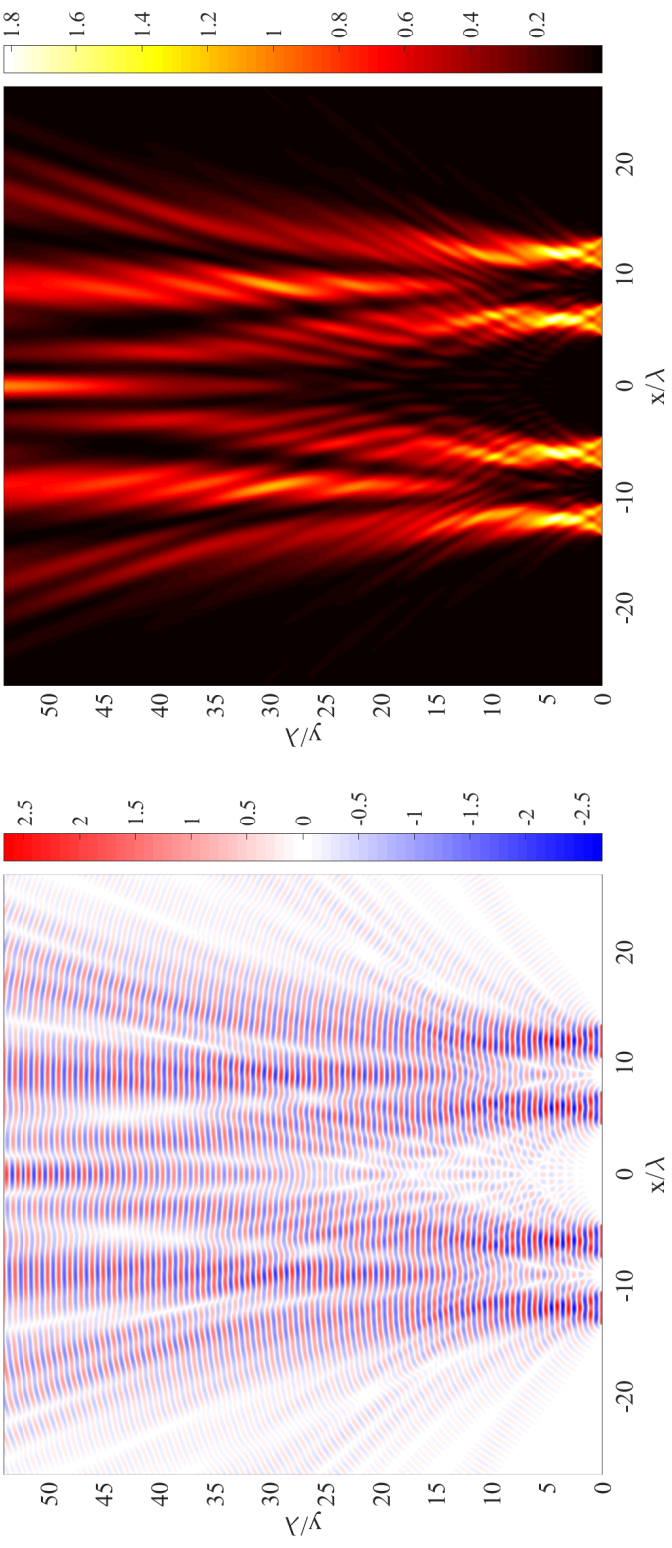

Figure C.5: Diffraction of a plane wave from the $n = 2$th pre-fractal level of the Cantor set with an $a_n = 1.5\lambda$. Electric field, $2\Re e\left(\frac{E_z}{E_0}\right)$, *(left)* and intensity, $\left|\frac{E_z}{E_0}\right|^2$ *(right)*.

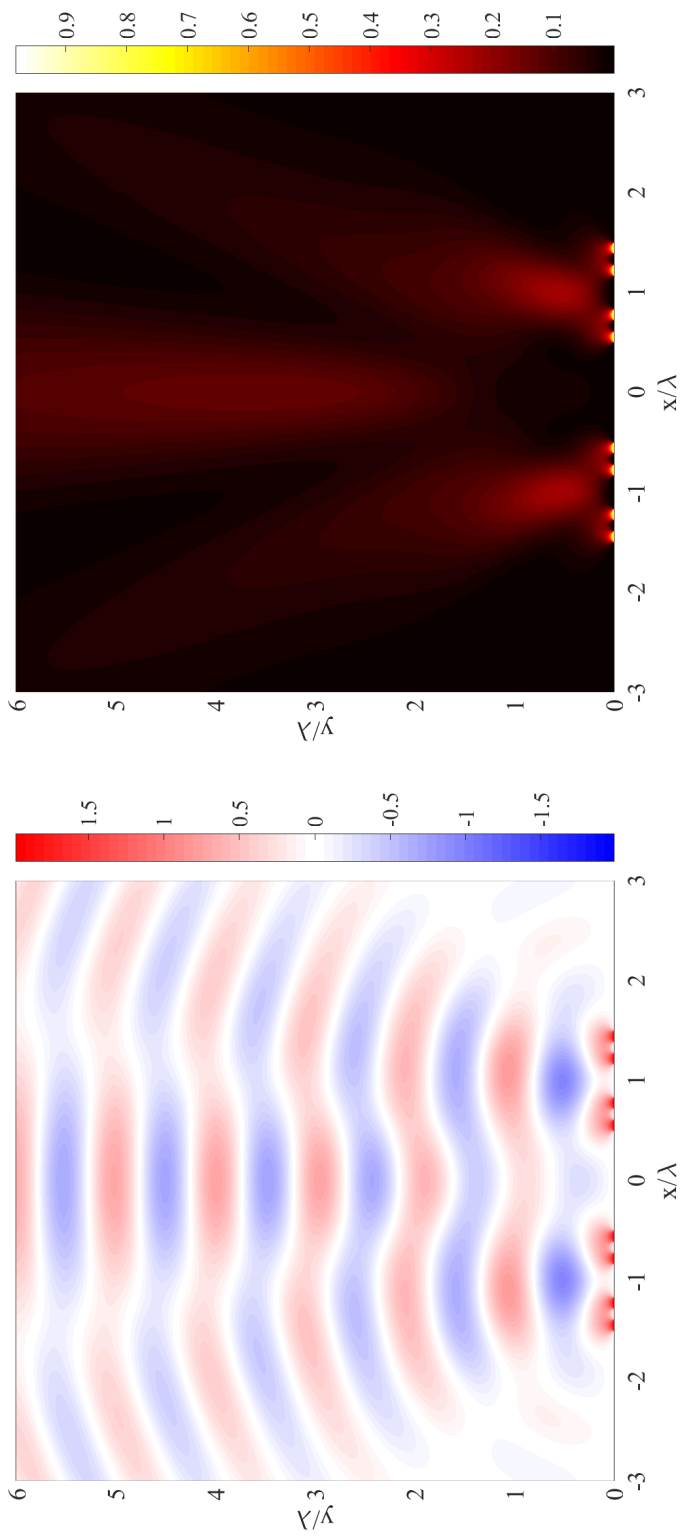

Figure C.6: Diffraction of a plane wave from the $n = 3$th pre-fractal level of the Cantor set with an $a_0 = 1.5\lambda$. Electric field, $2\Re e\left(\frac{E_z}{E_0}\right)$, *(left)* and intensity, $\left|\frac{E_z}{E_0}\right|^2$ *(right)*.

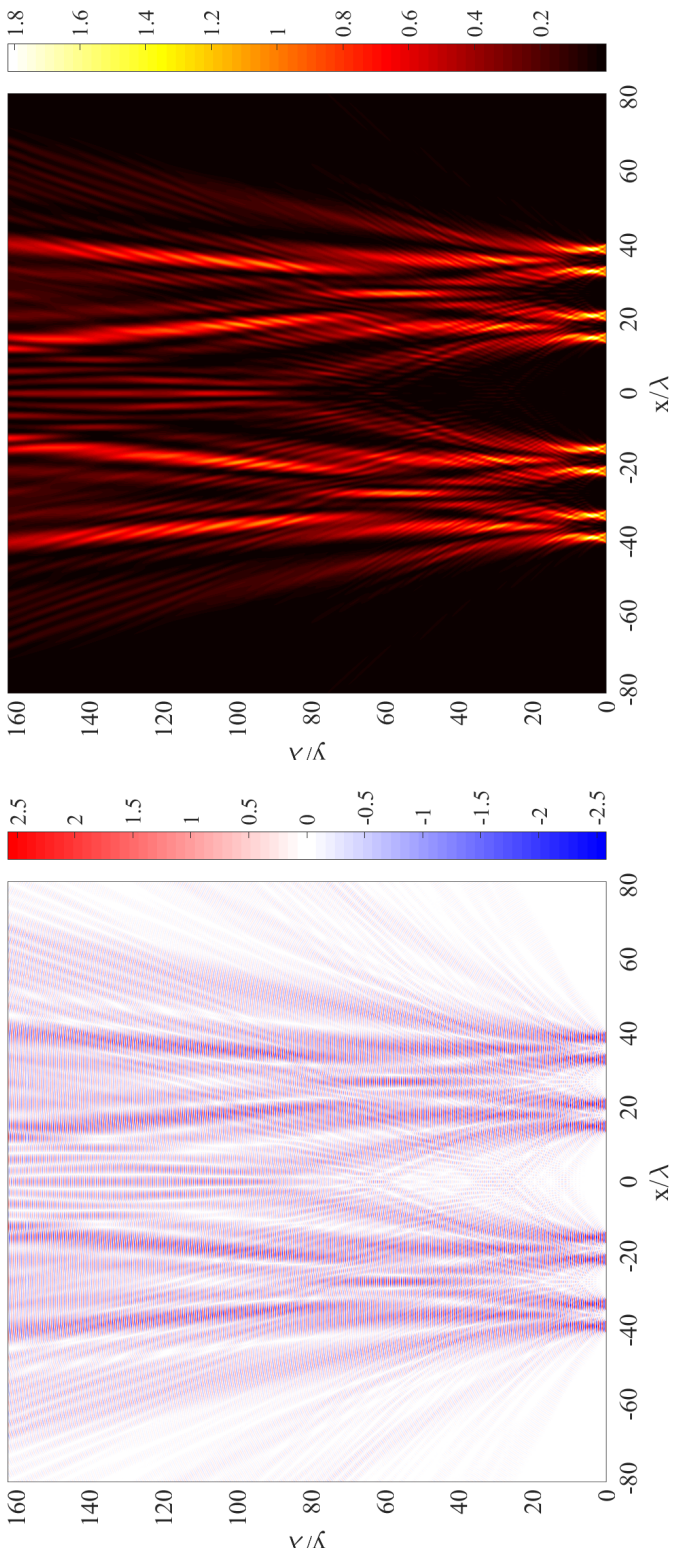

Figure C.7: Diffraction of a plane wave from the $n = 3$th pre-fractal level of the Cantor set with an $a_n = 1.5\lambda$. Electric field, $2\Re e\left(\frac{E_z}{E_0}\right)$, *(left)* and intensity, $\left|\frac{E_z}{E_0}\right|^2$ *(right)*.

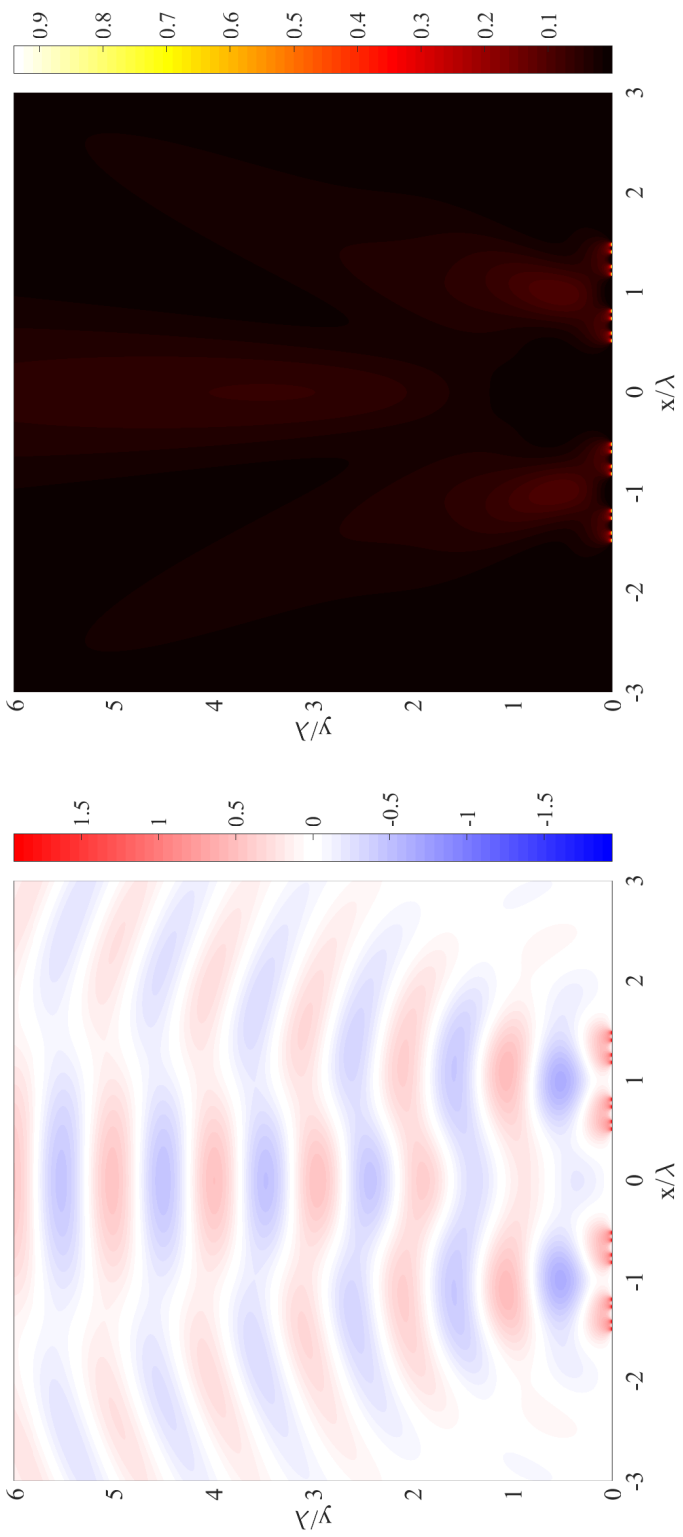

Figure C.8: Diffraction of a plane wave from the $n = 4$th pre-fractal level of the Cantor set with an $a_0 = 1.5\lambda$. Electric field, $2\Re e\left(\frac{E_z}{E_0}\right)$, *(left)* and intensity, $\left|\frac{E_z}{E_0}\right|^2$ *(right)*.

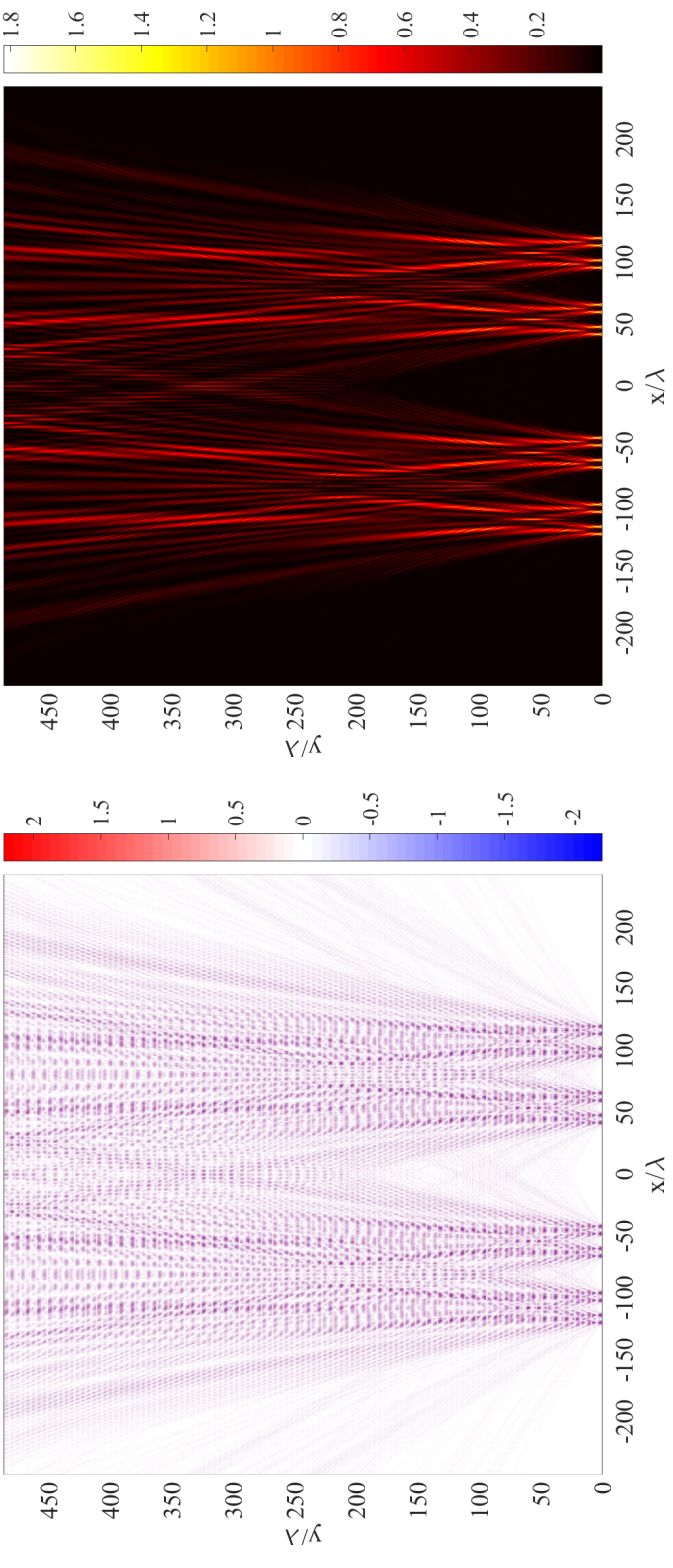

Figure C.9: Diffraction of a plane wave from the $n = 4$th pre-fractal level of the Cantor set with an $a_n = 1.5\lambda$. Electric field, $2\Re e\left(\frac{E_z}{E_0}\right)$, *(left)* and intensity, $\left|\frac{E_z}{E_0}\right|^2$ *(right)*.

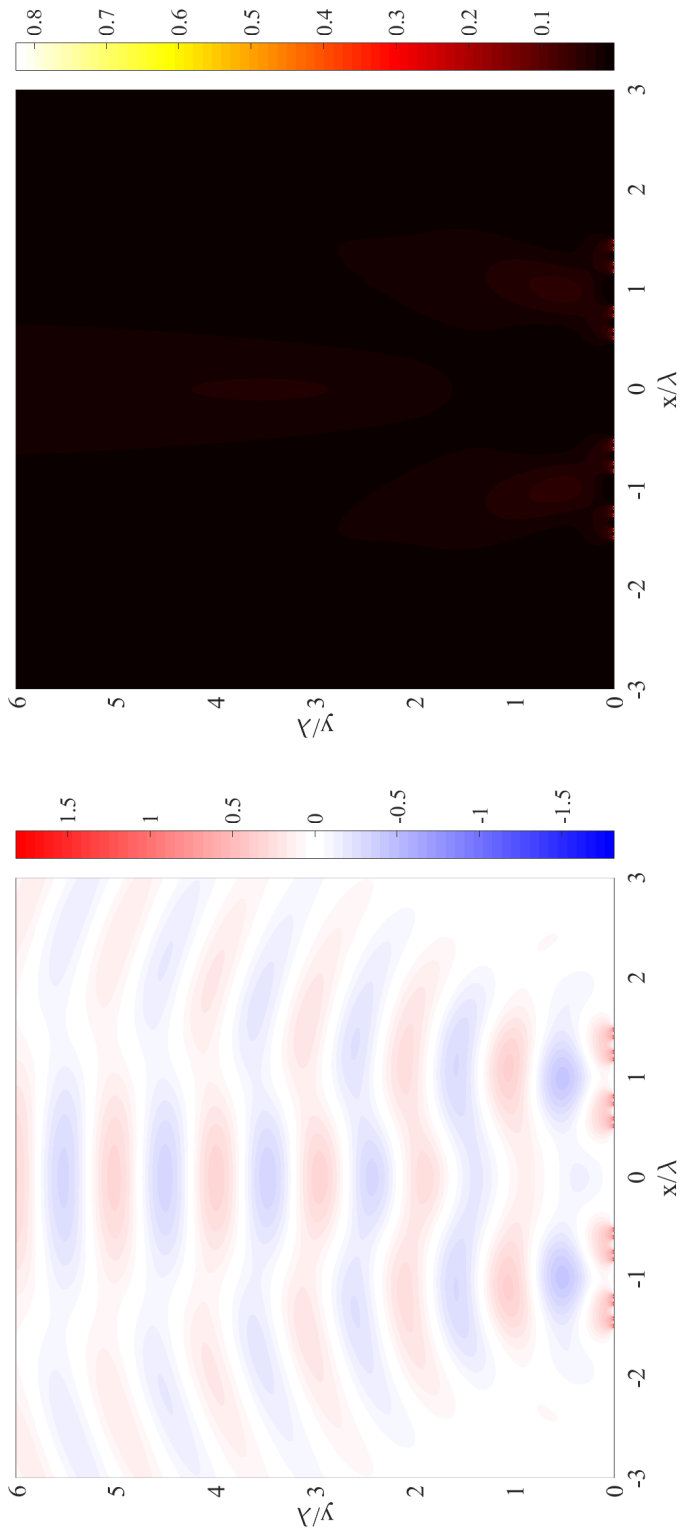

Figure C.10: Diffraction of a plane wave from the $n = 5$th pre-fractal level of the Cantor set with an $a_0 = 1.5\lambda$. Electric field, $2\Re e(\frac{E_z}{E_0})$, *(left)* and intensity, $|\frac{E_z}{E_0}|^2$ *(right)*.

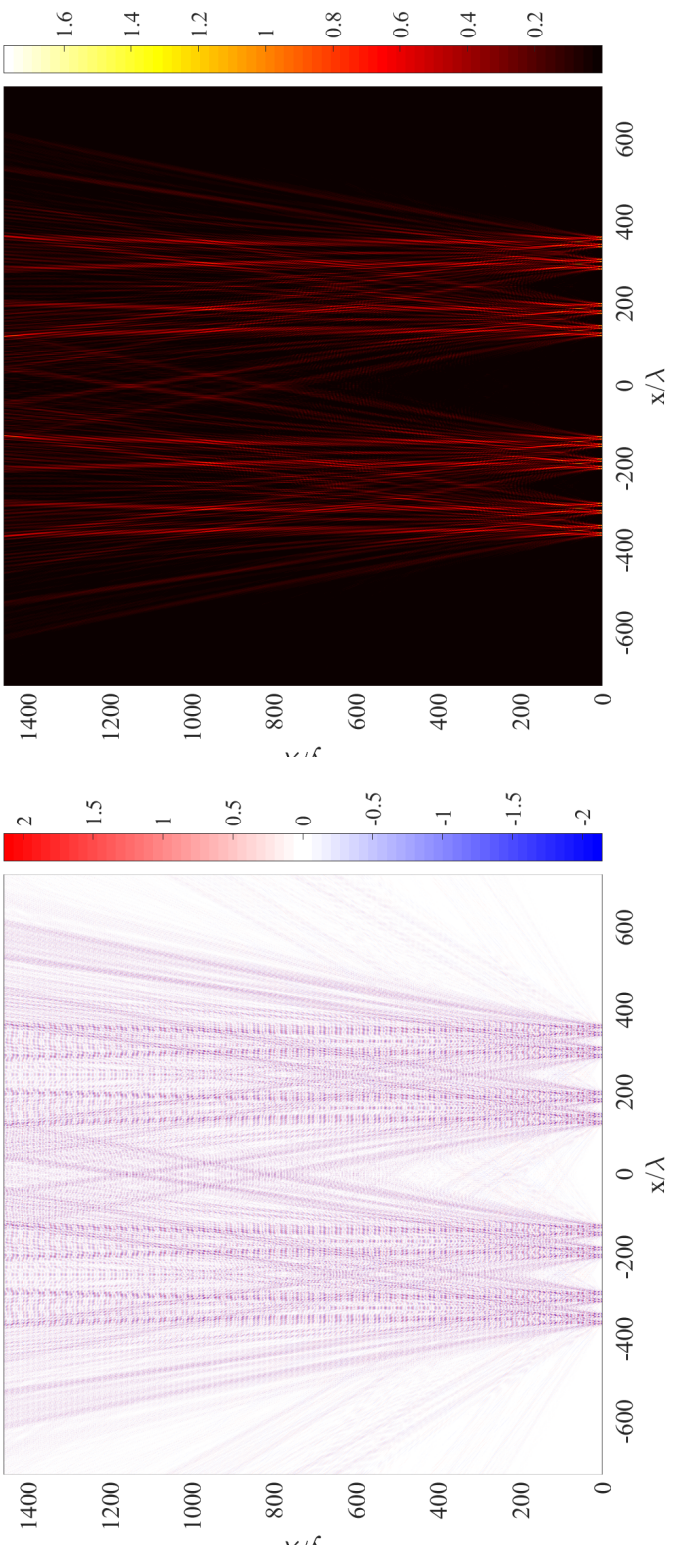

Figure C.11: Diffraction of a plane wave from the $n = 5$th pre-fractal level of the Cantor set with an $a_n = 1.5\lambda$. Electric field, $2\Re e\left(\frac{E_z}{E_0}\right)$, *(left)* and intensity, $\left|\frac{E_z}{E_0}\right|^2$ *(right)*.

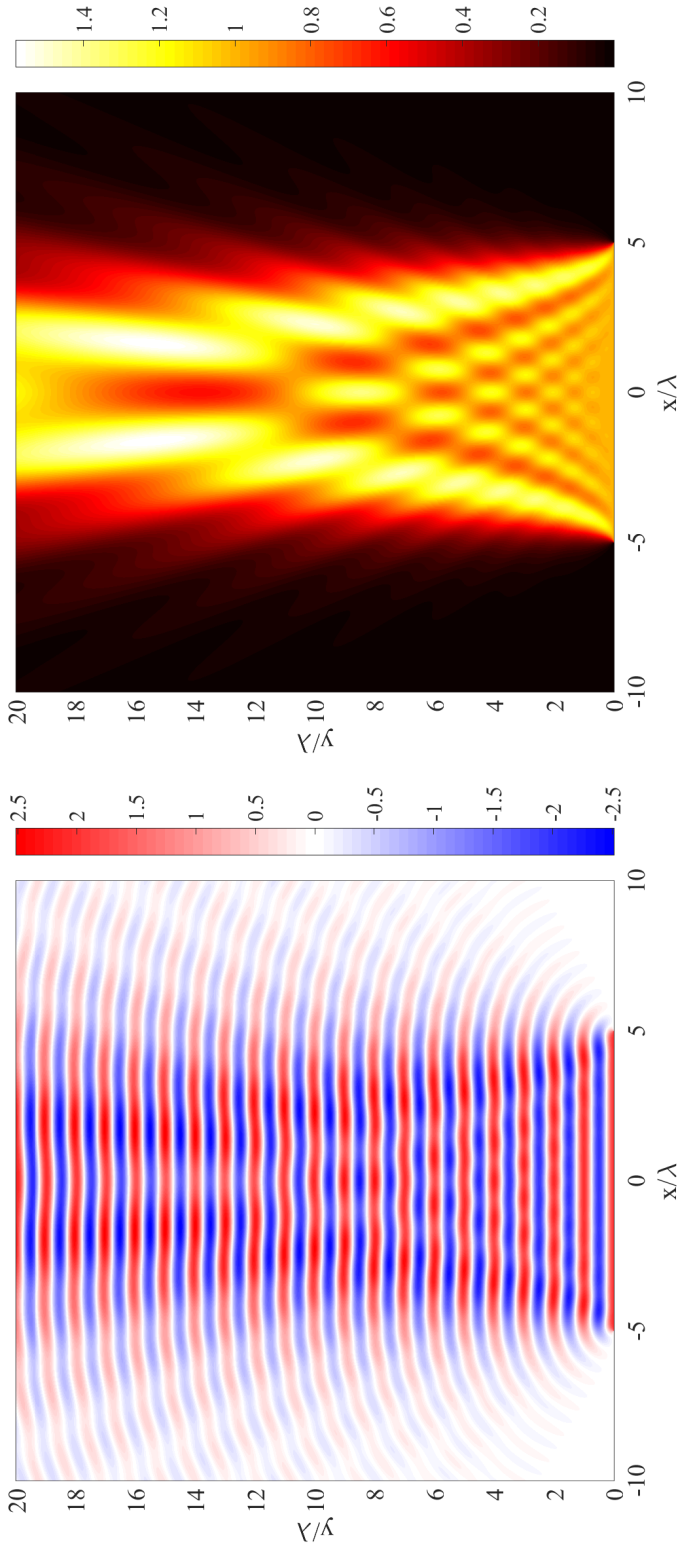

Figure C.12: Diffraction of a plane wave from the $n = 0$th pre-fractal level of the Cantor set with an $a_0 = 5\lambda$. Electric field, $2\Re e\left(\frac{E_z}{E_0}\right)$, *(left)* and intensity, $\left|\frac{E_z}{E_0}\right|^2$ *(right)*.

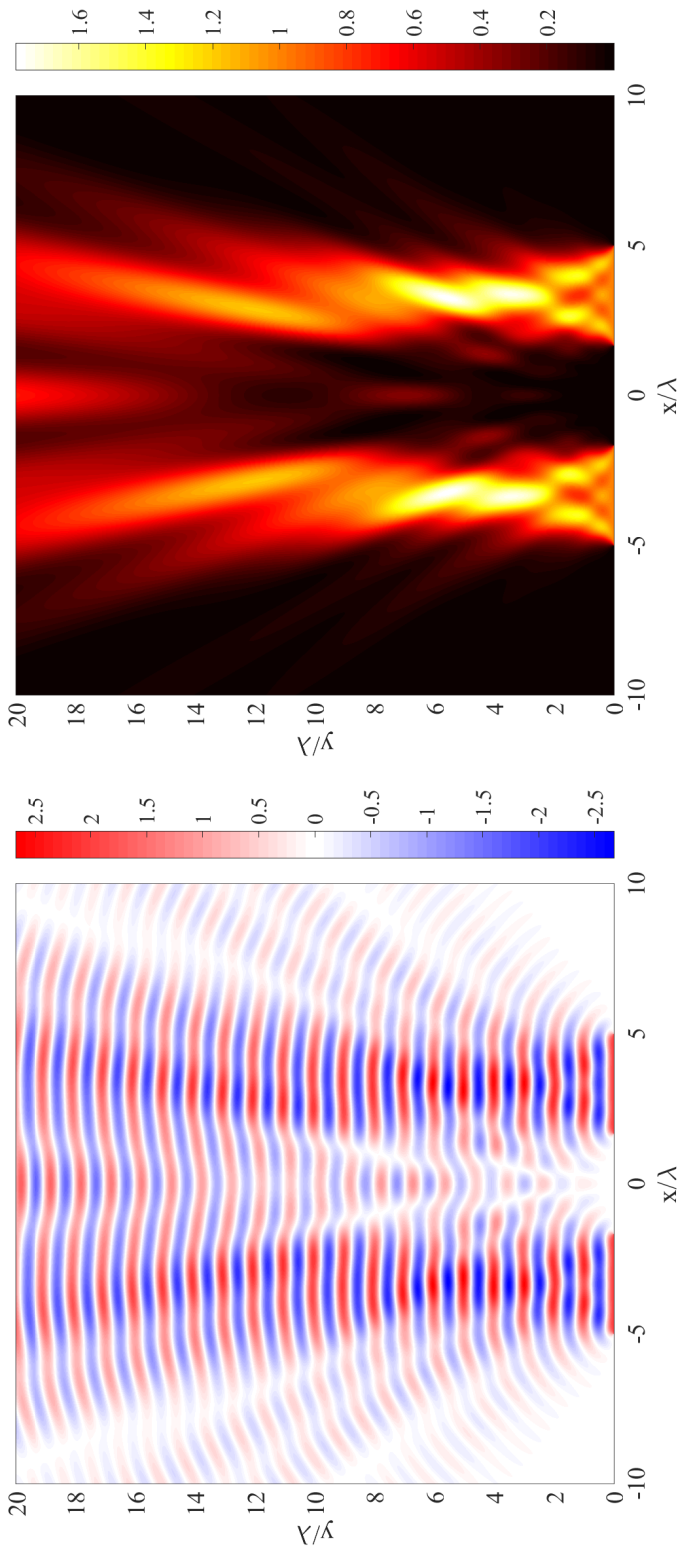

Figure C.13: Diffraction of a plane wave from the $n = 1$th pre-fractal level of the Cantor set with an $a_0 = 5\lambda$. Electric field, $2\Re e\left(\frac{E_z}{E_0}\right)$, *(left)* and intensity, $\left|\frac{E_z}{E_0}\right|^2$ *(right)*.

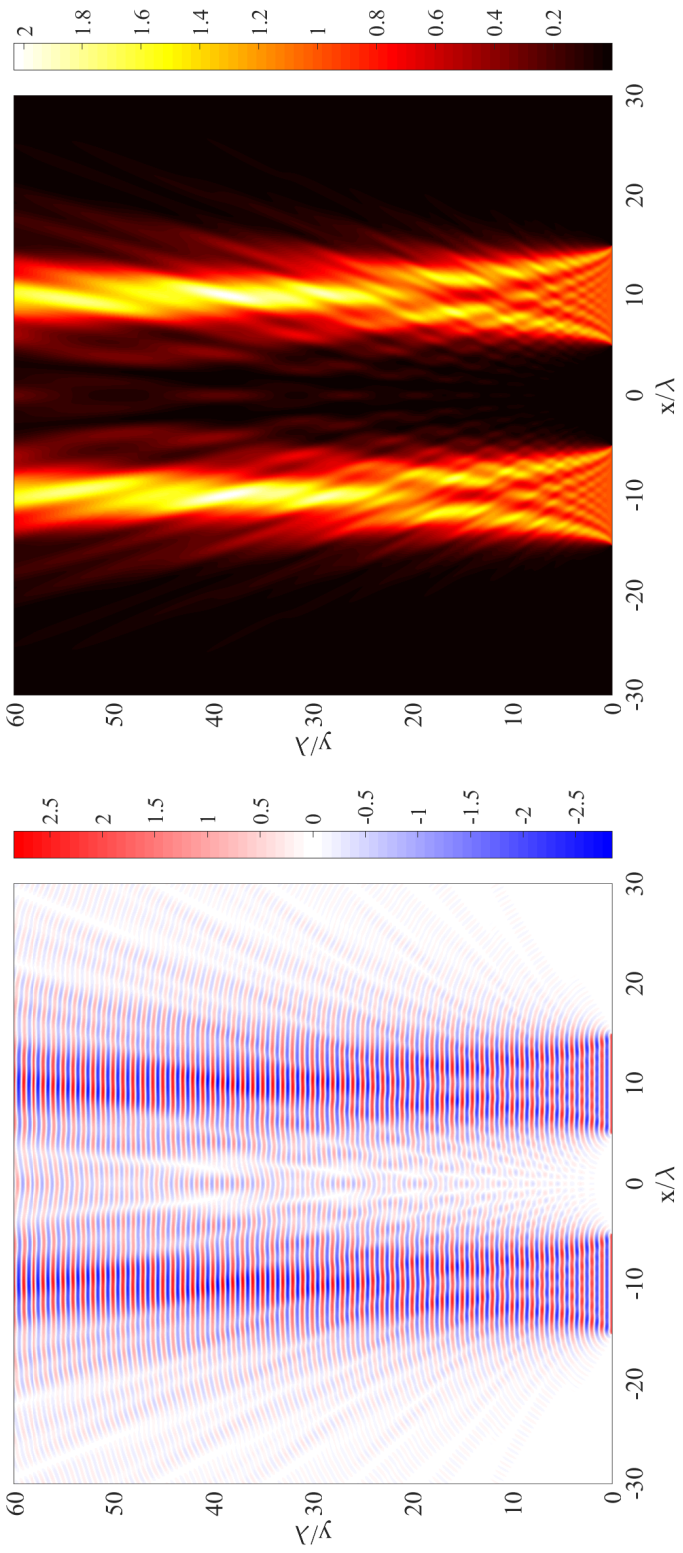

Figure C.14: Diffraction of a plane wave from the $n = 1$th pre-fractal level of the Cantor set with an $a_n = 5\lambda$. Electric field, $2\Re e\left(\frac{E_z}{E_0}\right)$, *(left)* and intensity, $\left|\frac{E_z}{E_0}\right|^2$ *(right)*.

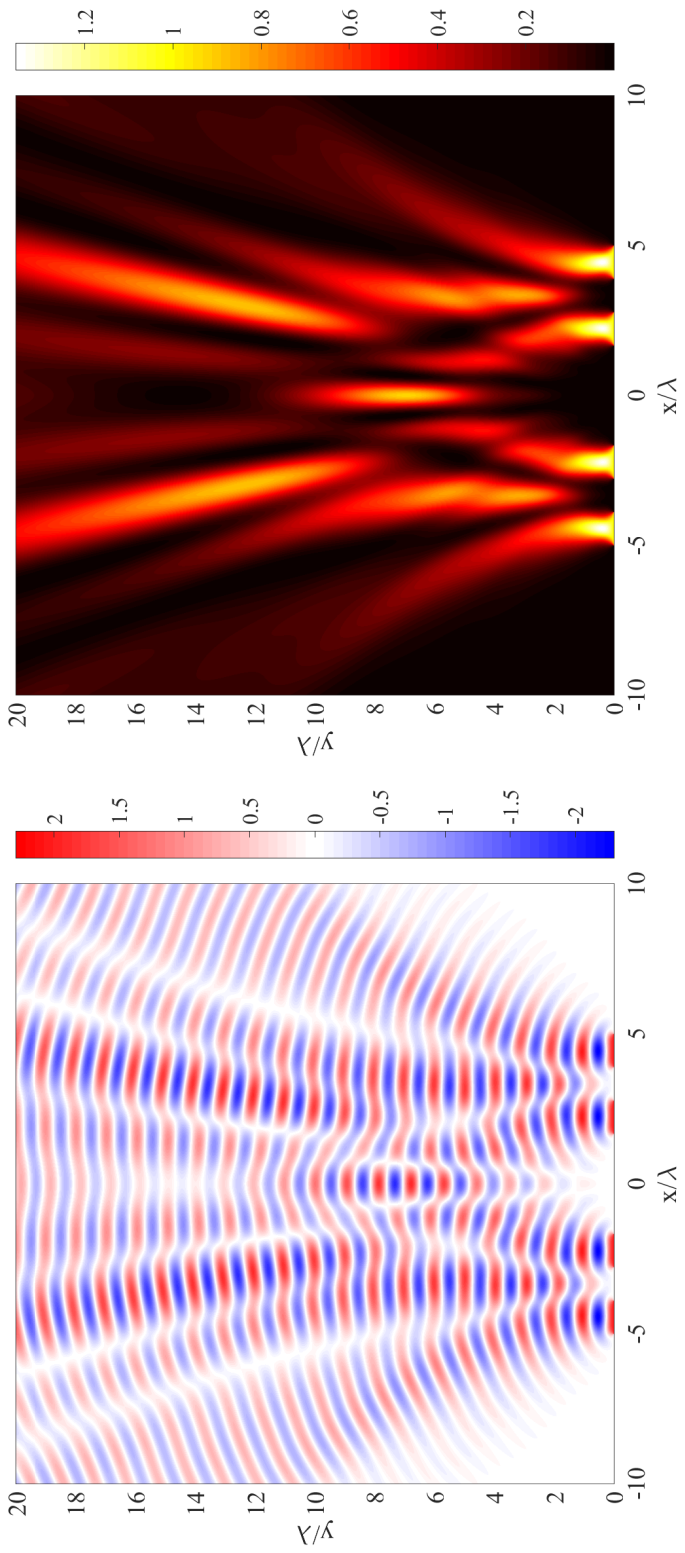

Figure C.15: Diffraction of a plane wave from the $n = 2$th pre-fractal level of the Cantor set with an $a_0 = 5\lambda$. Electric field, $2\Re e\left(\frac{E_z}{E_0}\right)$, *(left)* and intensity, $\left|\frac{E_z}{E_0}\right|^2$ *(right)*.

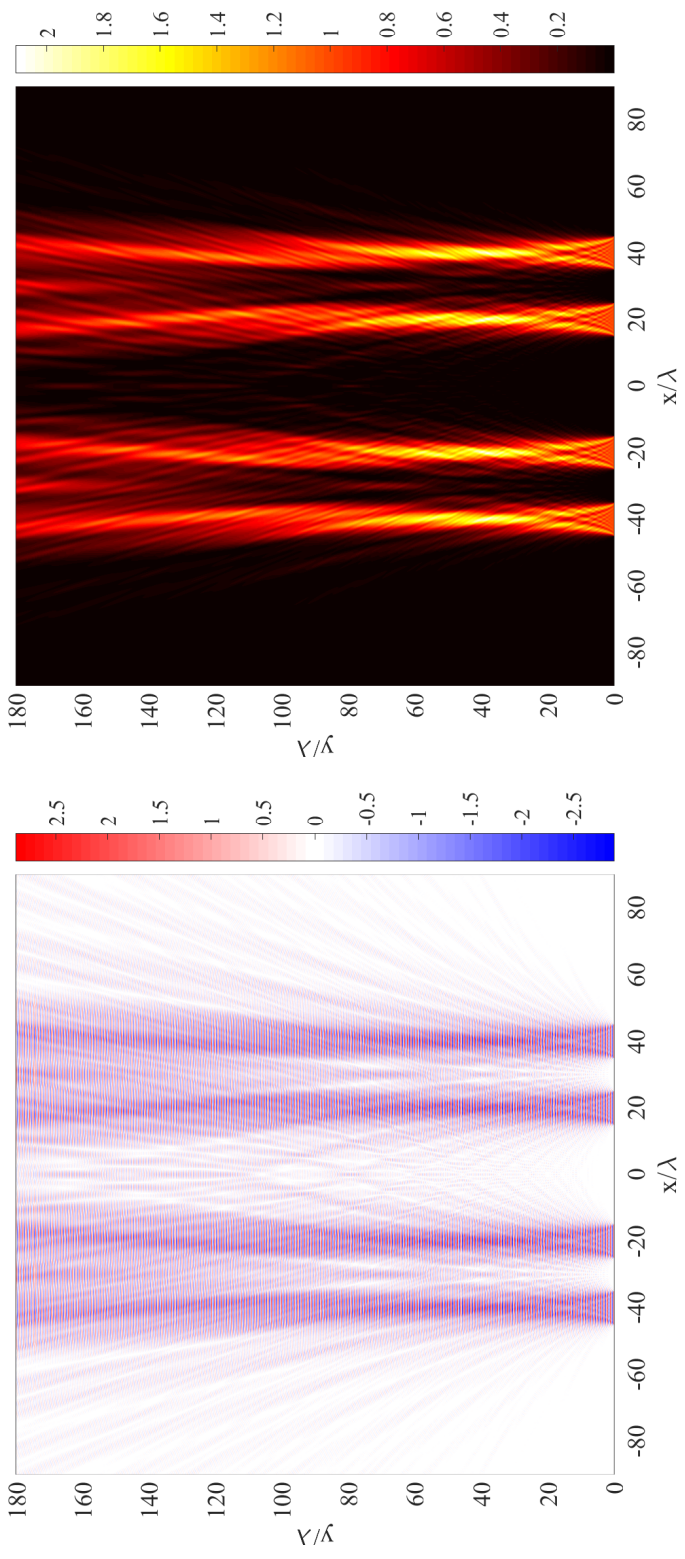

Figure C.16: Diffraction of a plane wave from the $n = 2$th pre-fractal level of the Cantor set with an $a_n = 5\lambda$. Electric field, $2\Re e\left(\frac{E_z}{E_0}\right)$, *(left)* and intensity, $\left|\frac{E_z}{E_0}\right|^2$ *(right)*.

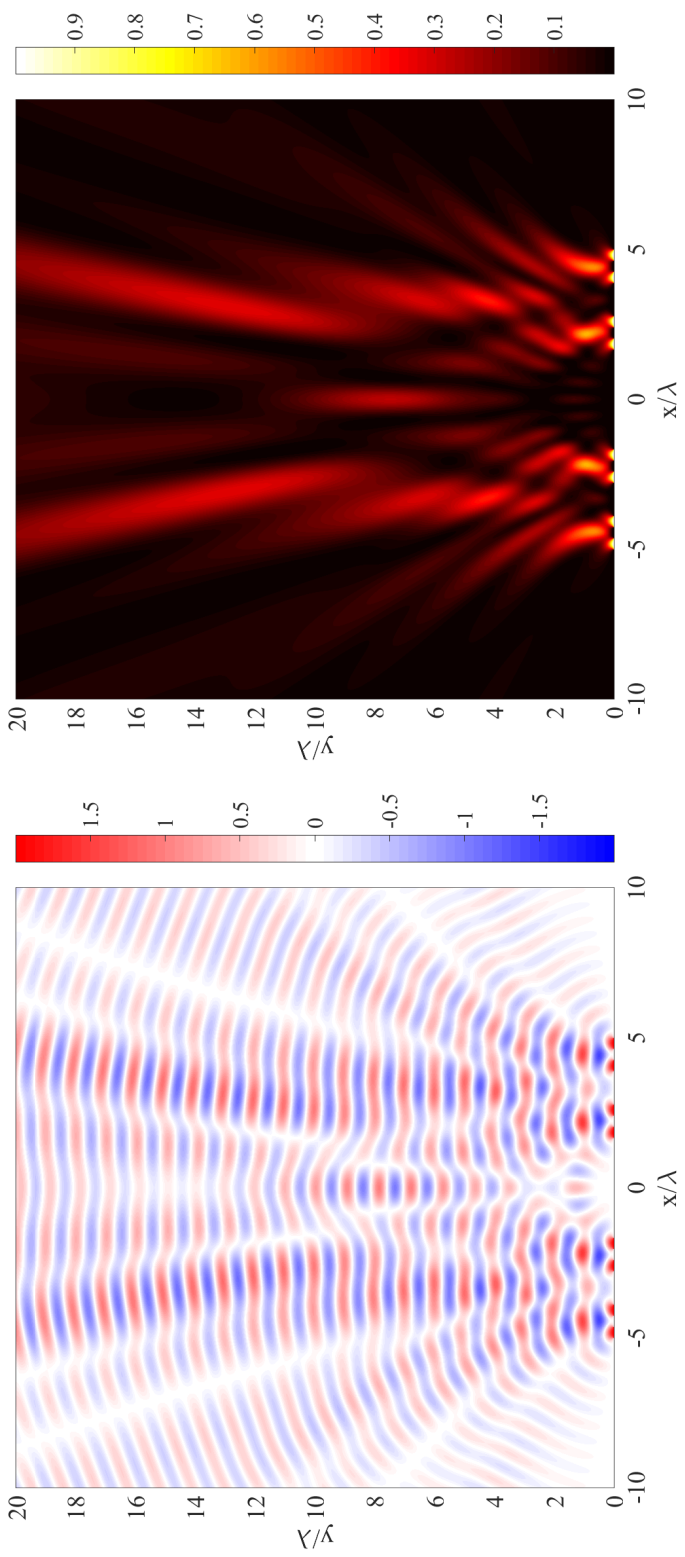

Figure C.17: Diffraction of a plane wave from the $n = 3$th pre-fractal level of the Cantor set with an $a_0 = 5\lambda$. Electric field, $2\Re e\left(\frac{E_z}{E_0}\right)$, *(left)* and intensity, $\left|\frac{E_z}{E_0}\right|^2$ *(right)*.

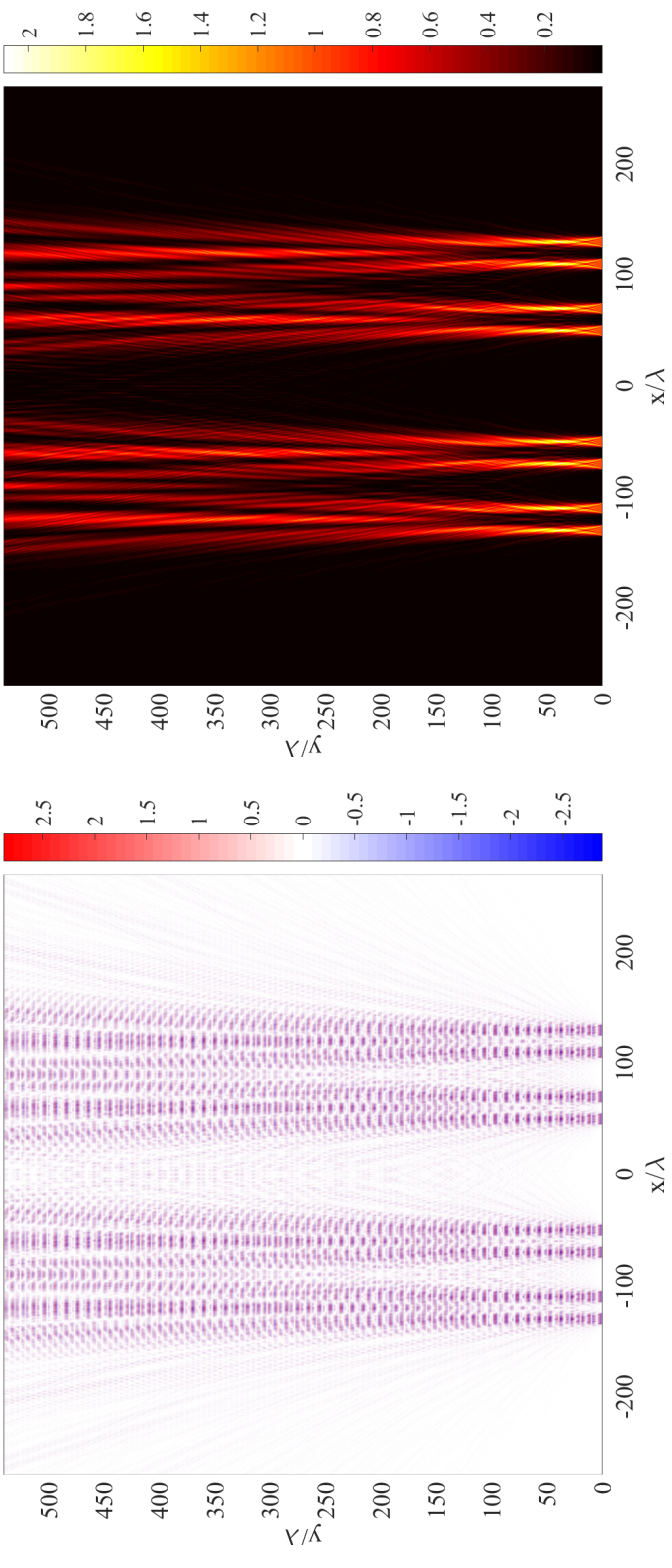

Figure C.18: Diffraction of a plane wave from the $n = 3$th pre-fractal level of the Cantor set with an $a_n = 5\lambda$. Electric field, $2\Re e\left(\frac{E_z}{E_0}\right)$, *(left)* and intensity, $\left|\frac{E_z}{E_0}\right|^2$ *(right)*.

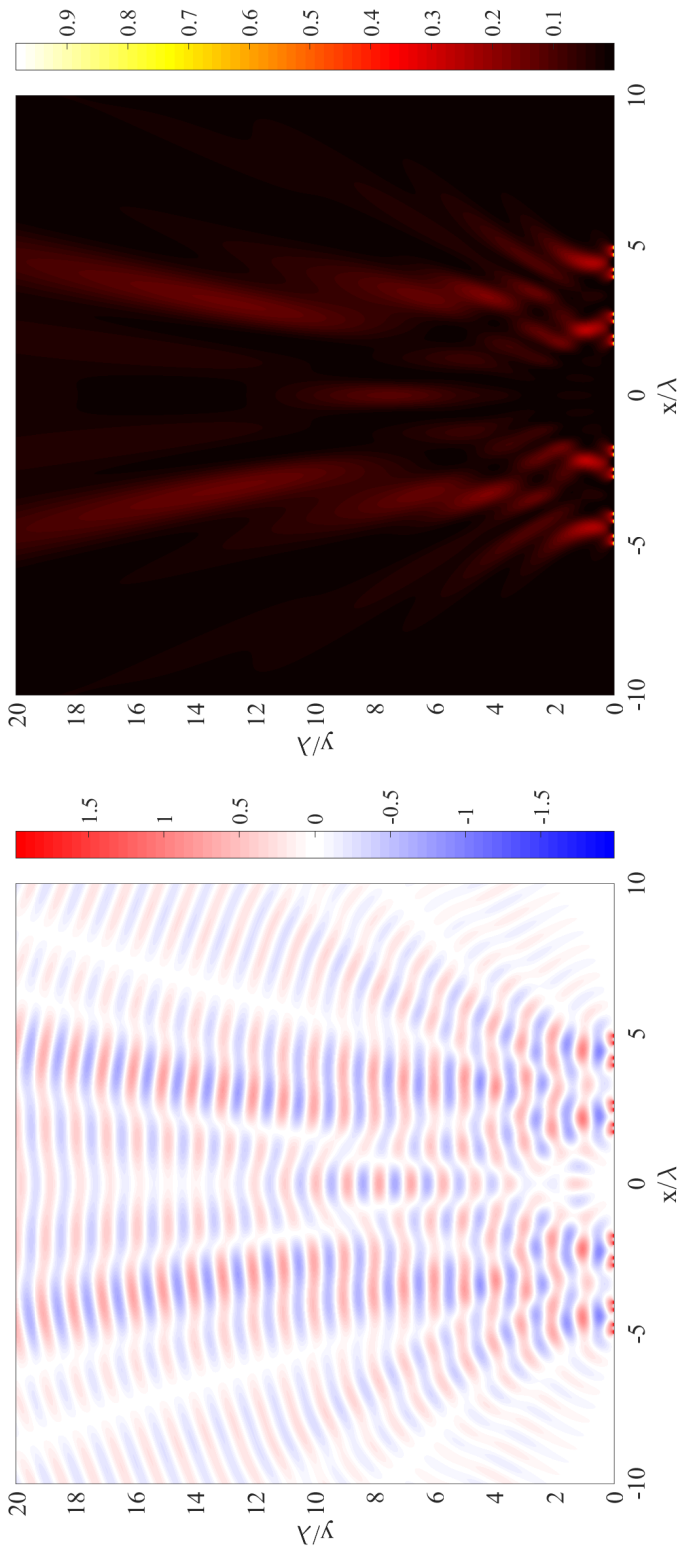

Figure C.19: Diffraction of a plane wave from the $n = 4$th pre-fractal level of the Cantor set with an $a_0 = 5\lambda$. Electric field, $2\Re e\left(\frac{E_z}{E_0}\right)$, *(left)* and intensity, $\left|\frac{E_z}{E_0}\right|^2$ *(right)*.

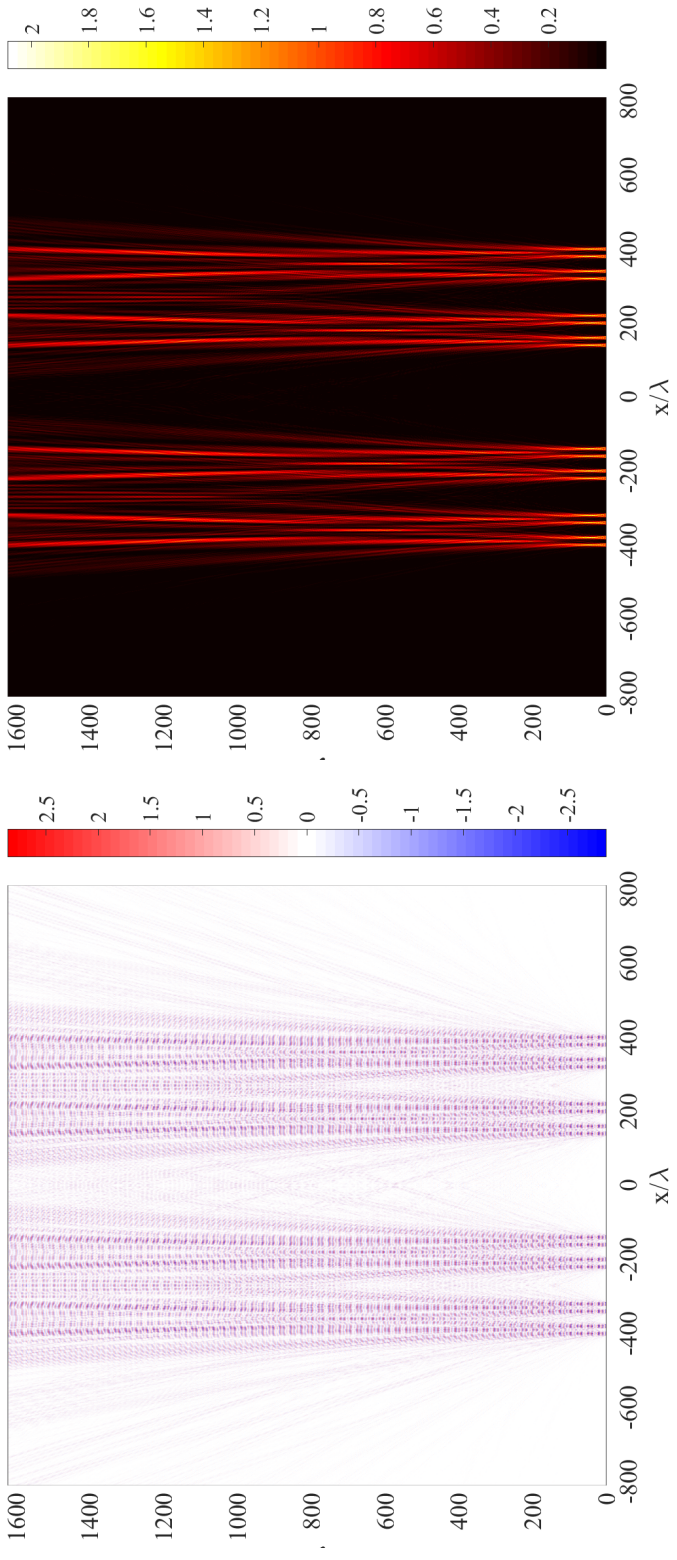

Figure C.20: Diffraction of a plane wave from the $n = 4$th pre-fractal level of the Cantor set with an $a_n = 5\lambda$. Electric field, $2\Re e\left(\frac{E_z}{E_0}\right)$, *(left)* and intensity, $\left|\frac{E_z}{E_0}\right|^2$ *(right)*.

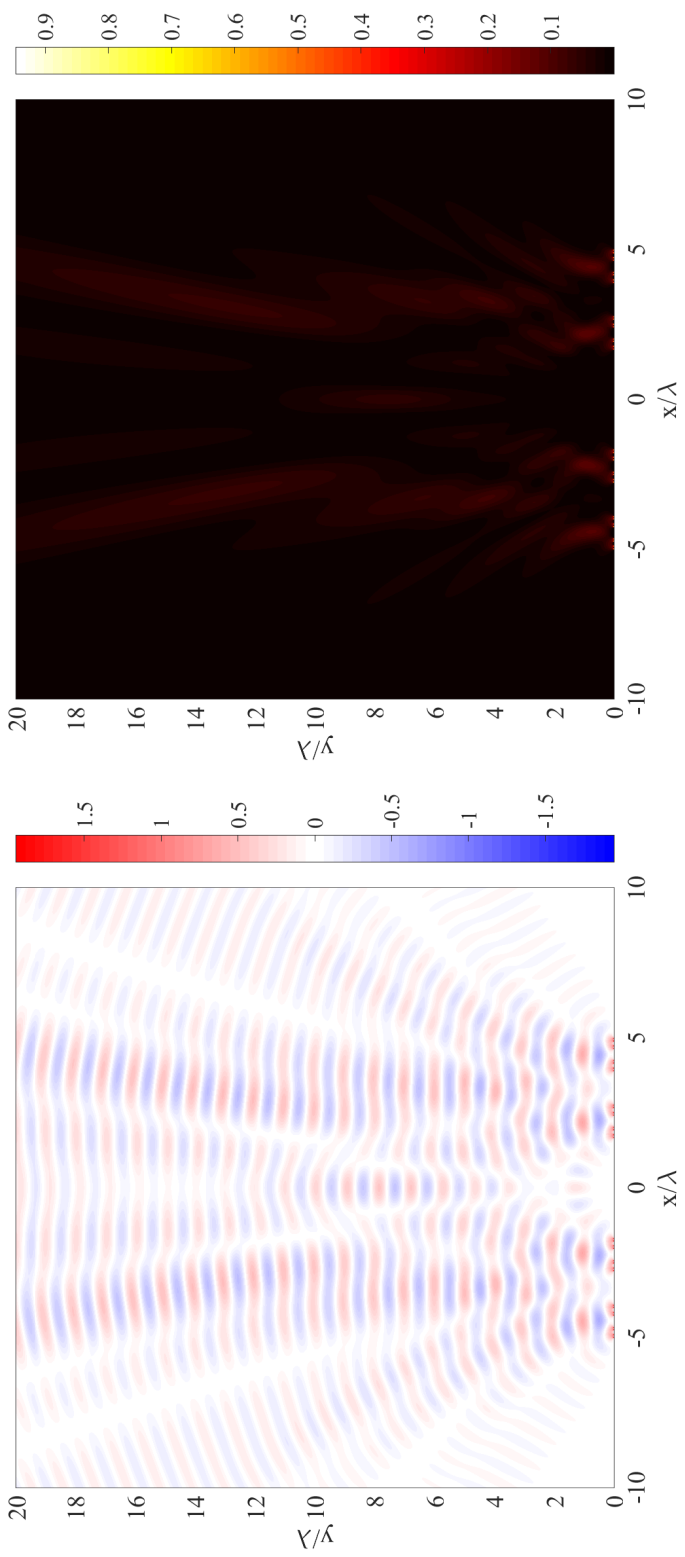

Figure C.21: Diffraction of a plane wave from the $n = 5$th pre-fractal level of the Cantor set with an $a_0 = 5\lambda$. Electric field, $2\Re e\left(\frac{E_z}{E_0}\right)$, *(left)* and intensity, $\left|\frac{E_z}{E_0}\right|^2$ *(right)*.

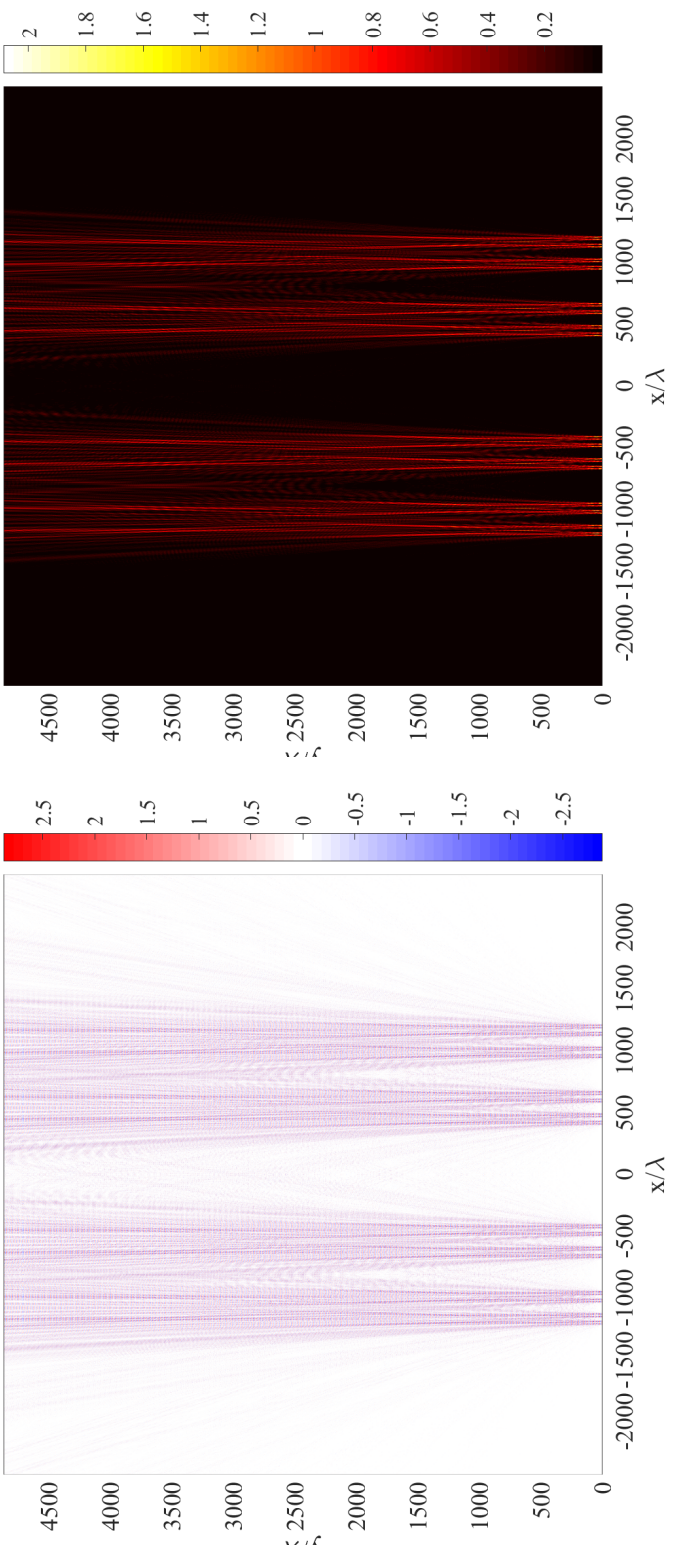

Figure C.22: Diffraction of a plane wave from the $n = 5$th pre-fractal level of the Cantor set with $a_n = 5\lambda$. Electric field, $2\Re e\left(\frac{E_z}{E_0}\right)$, *(left)* and intensity, $\left|\frac{E_z}{E_0}\right|^2$ *(right)*.

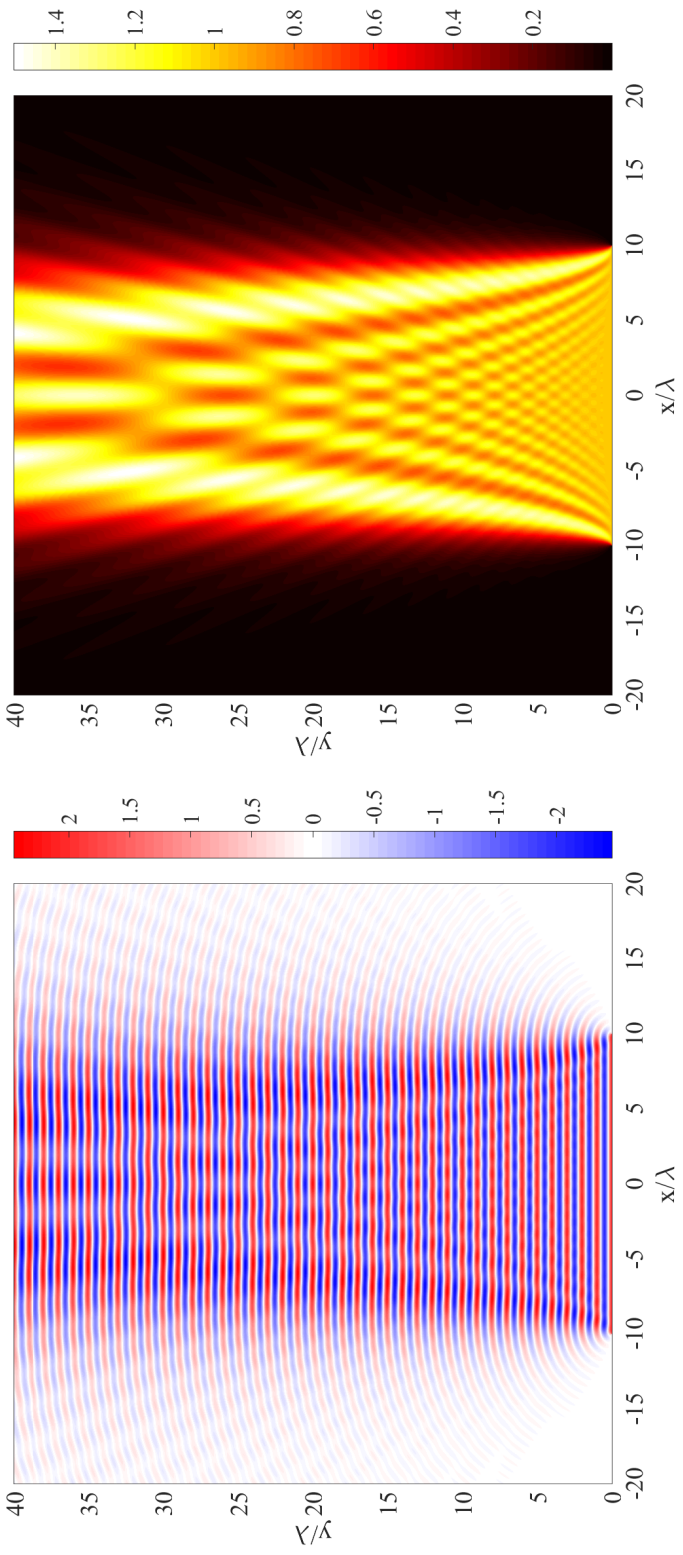

Figure C.23: Diffraction of a plane wave from the $n = 0$th pre-fractal level of the Cantor set with $a_0 = 10\lambda$. Electric field, $2\Re e\left(\frac{E_z}{E_0}\right)$, *(left)* and intensity, $\left|\frac{E_z}{E_0}\right|^2$ *(right)*.

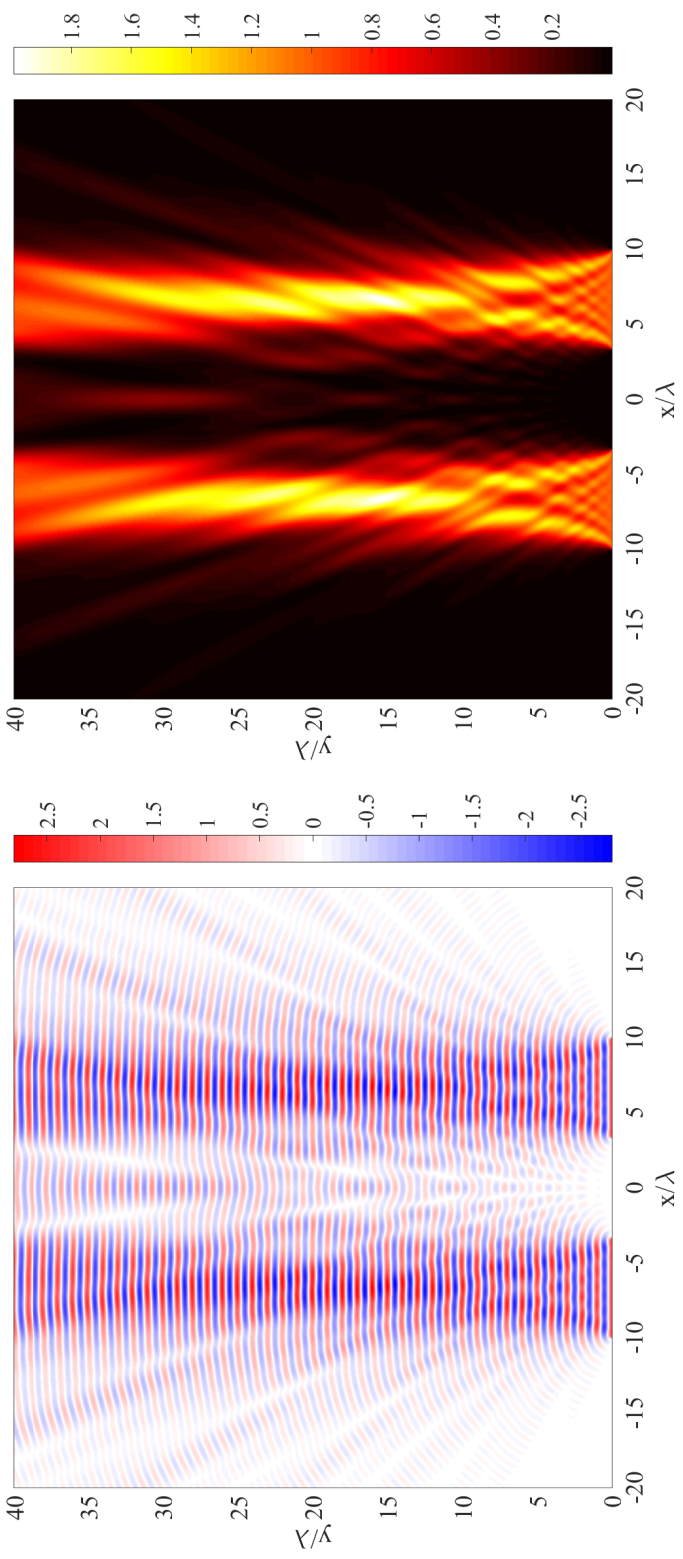

Figure C.24: Diffraction of a plane wave from the $n = 1$th pre-fractal level of the Cantor set with $a_0 = 10\lambda$. Electric field, $2\Re e\left(\frac{E_z}{E_0}\right)$, *(left)* and intensity, $\left|\frac{E_z}{E_0}\right|^2$ *(right)*.

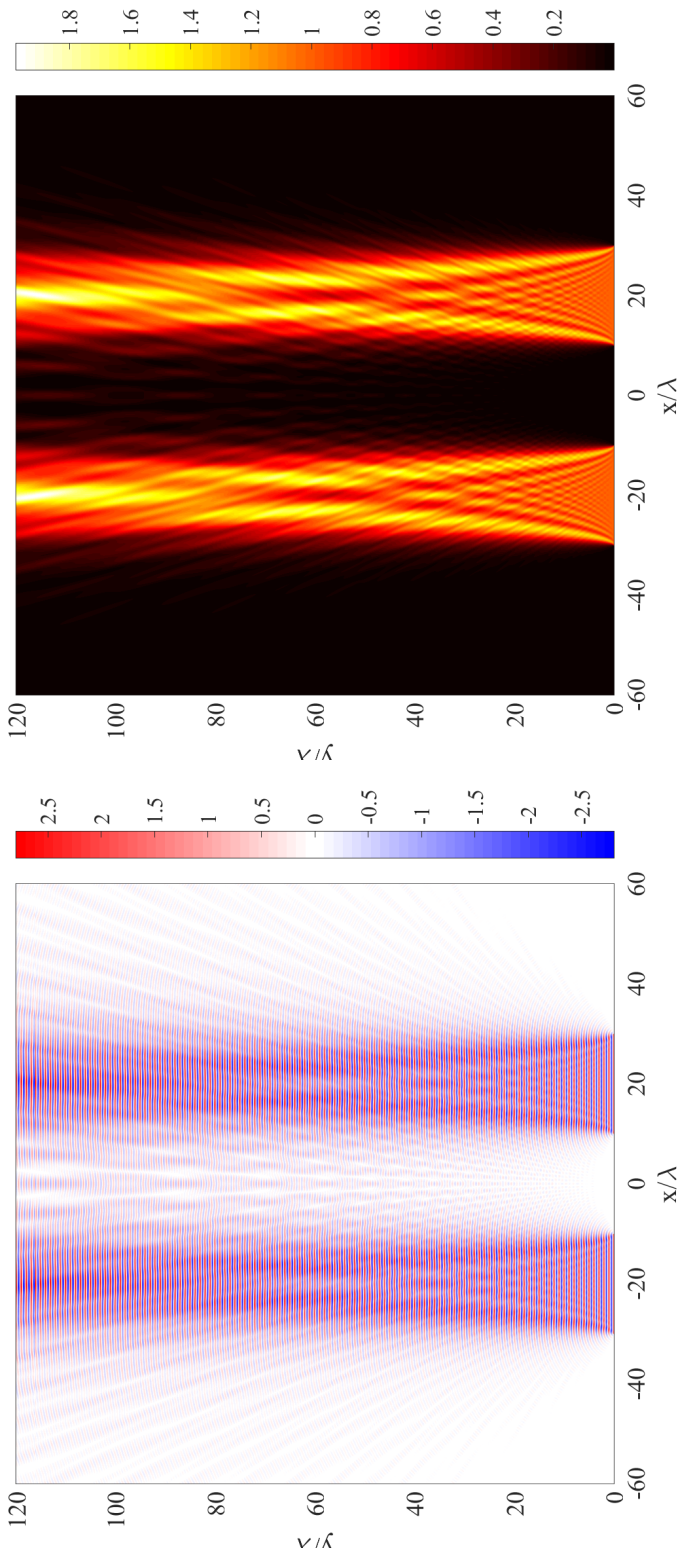

Figure C.25: Diffraction of a plane wave from the n = 1th pre-fractal level of the Cantor set with $a_n = 10\lambda$. Electric field, $2\Re e\left(\frac{E_z}{E_0}\right)$, *(left)* and intensity, $\left|\frac{E_z}{E_0}\right|^2$ *(right)*.

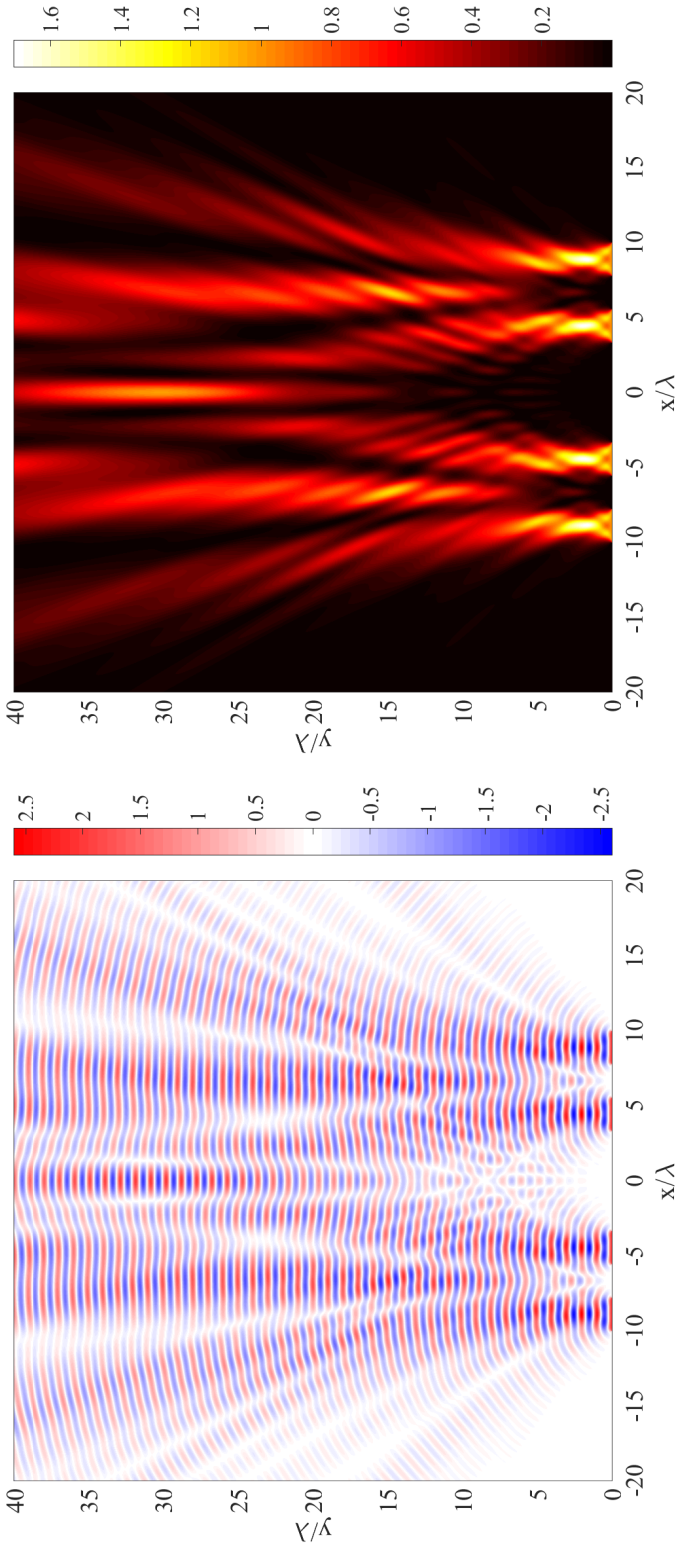

Figure C.26: Diffraction of a plane wave from the $n = 2$th pre-fractal level of the Cantor set with $a_0 = 10\lambda$. Electric field, $2\Re e\left(\frac{E_z}{E_0}\right)$, *(left)* and intensity, $\left|\frac{E_z}{E_0}\right|^2$ *(right)*.

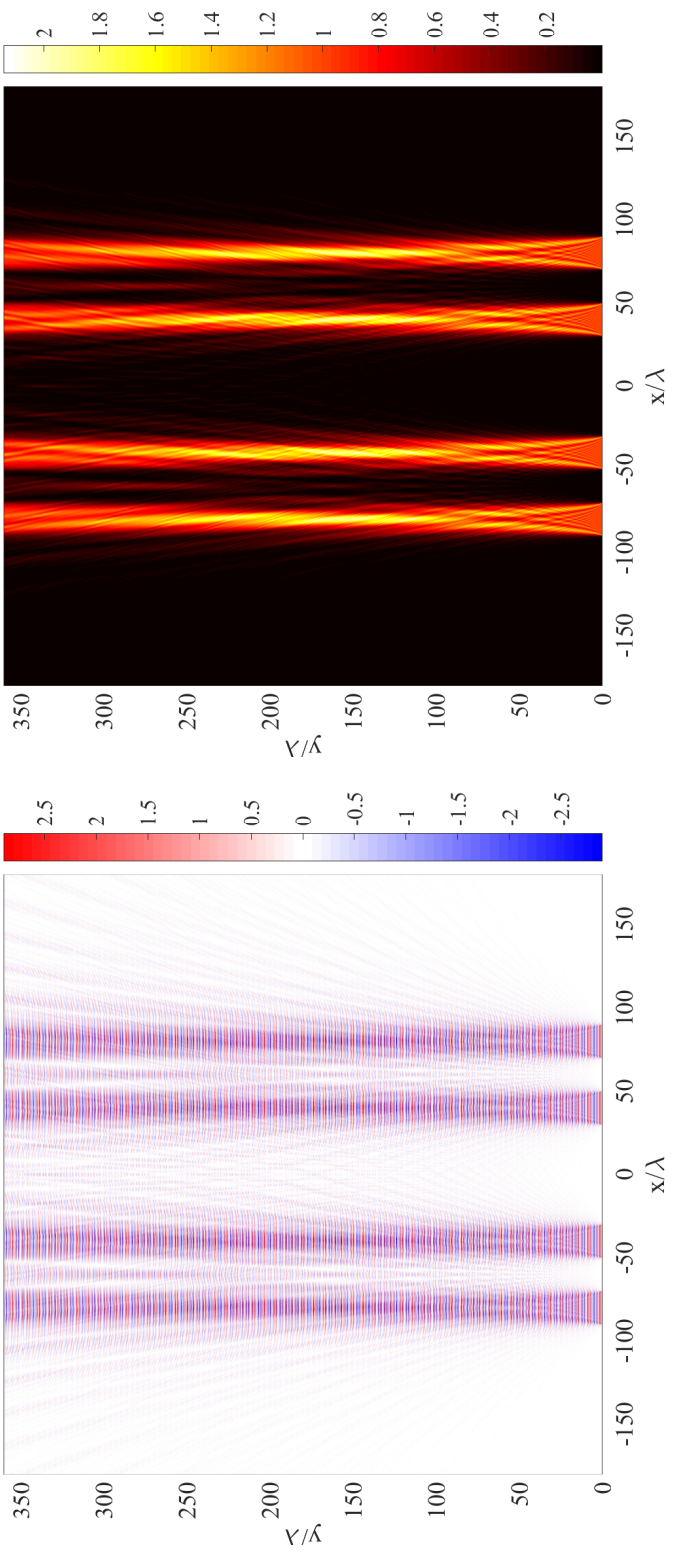

Figure C.27: Diffraction of a plane wave from the $n = 2$th pre-fractal level of the Cantor set with $a_n = 10\lambda$. Electric field, $2\Re e\left(\frac{E_z}{E_0}\right)$, *(left)* and intensity, $\left|\frac{E_z}{E_0}\right|^2$ *(right)*.

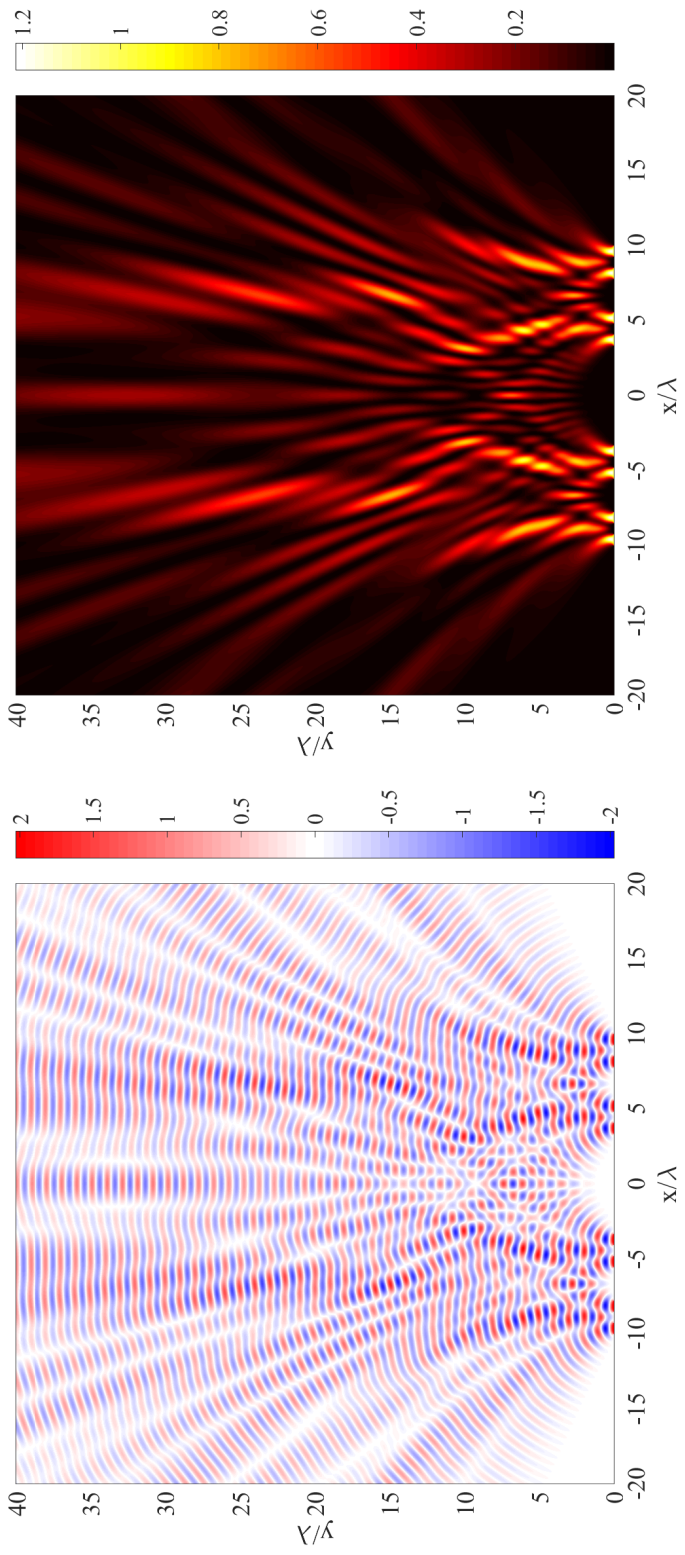

Figure C.28: Diffraction of a plane wave from the $n = 3$th pre-fractal level of the Cantor set with $a_0 = 10\lambda$. Electric field, $2\Re e\left(\frac{E_z}{E_0}\right)$, *(left)* and intensity, $\left|\frac{E_z}{E_0}\right|^2$ *(right)*.

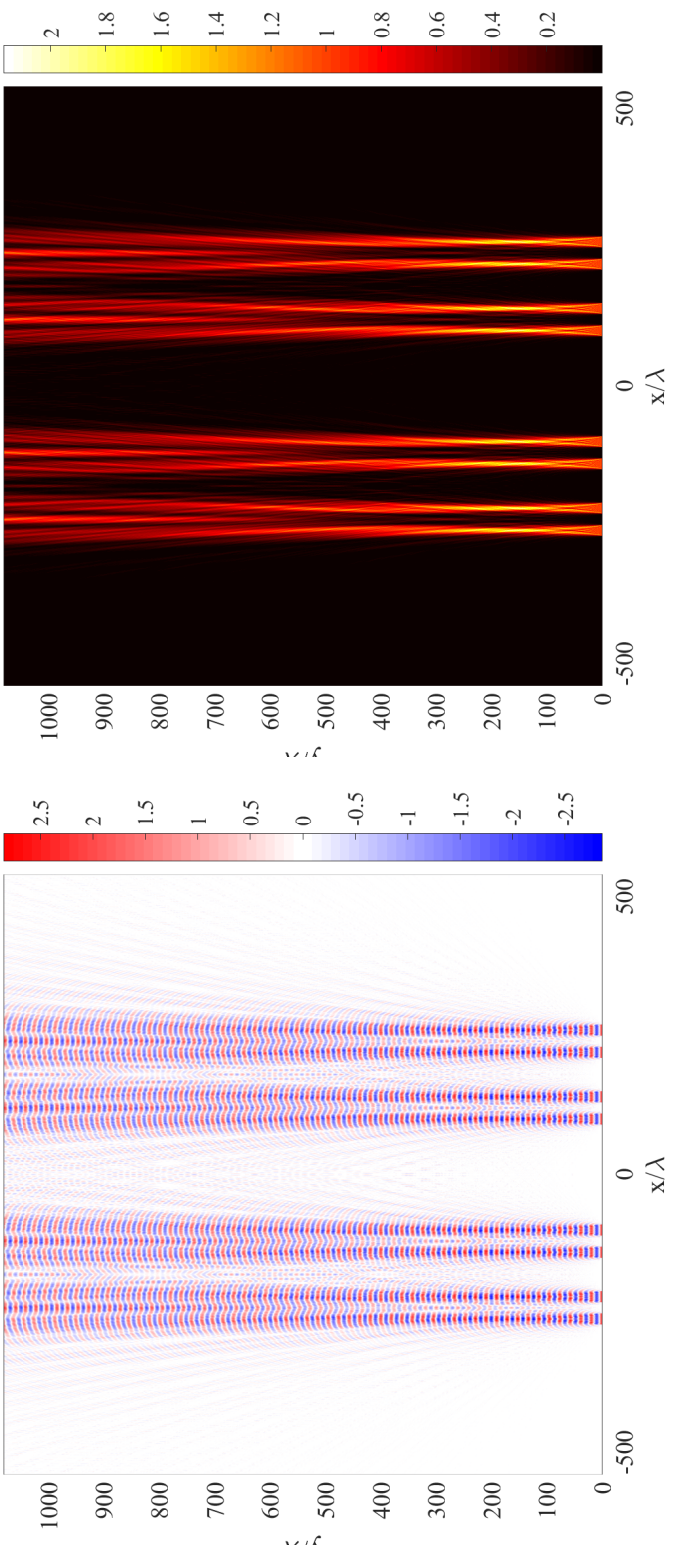

Figure C.29: Diffraction of a plane wave from the n = 3th pre-fractal level of the Cantor set with $a_n = 10\lambda$. Electric field, $2\Re e\left(\frac{E_z}{E_0}\right)$, *(left)* and intensity, $\left|\frac{E_z}{E_0}\right|^2$ *(right)*.

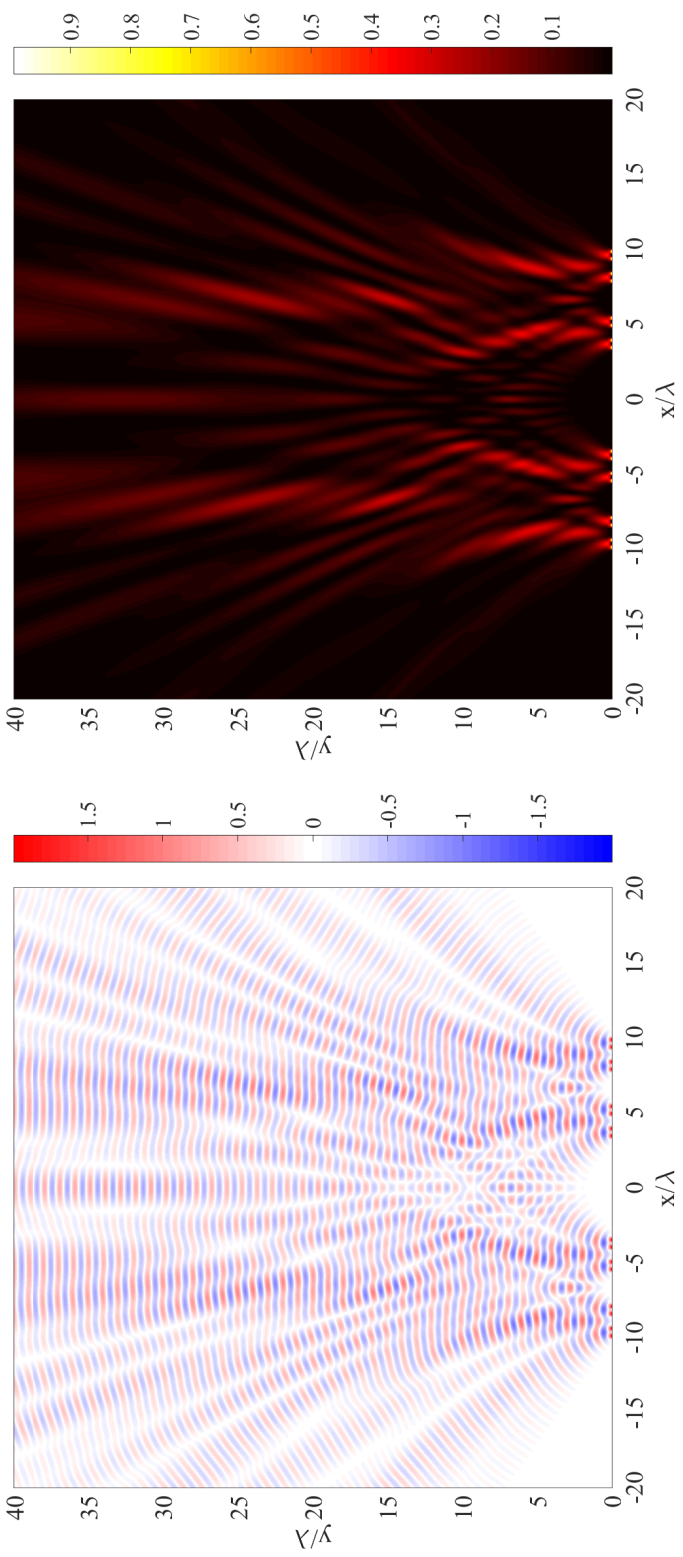

Figure C.30: Diffraction of a plane wave from the $n = 4$th pre-fractal level of the Cantor set with $a_0 = 10\lambda$. Electric field, $2\Re e\left(\frac{E_z}{E_0}\right)$, *(left)* and intensity, $\left|\frac{E_z}{E_0}\right|^2$ *(right)*.

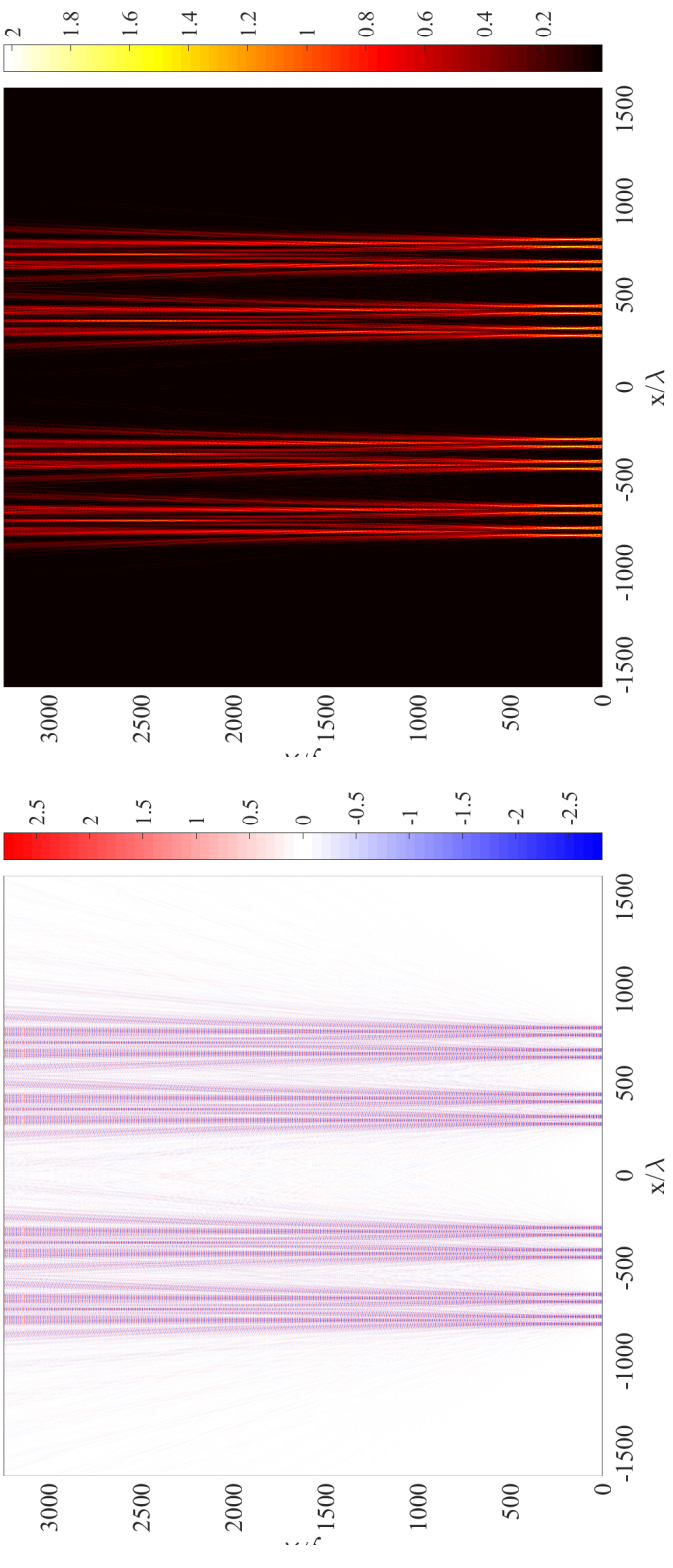

Figure C.31: Diffraction of a plane wave from the $n = 4$th pre-fractal level of the Cantor set with $a_n = 10\lambda$. Electric field, $2\Re e\left(\frac{E_z}{E_0}\right)$, *(left)* and intensity, $\left|\frac{E_z}{E_0}\right|^2$ *(right)*.

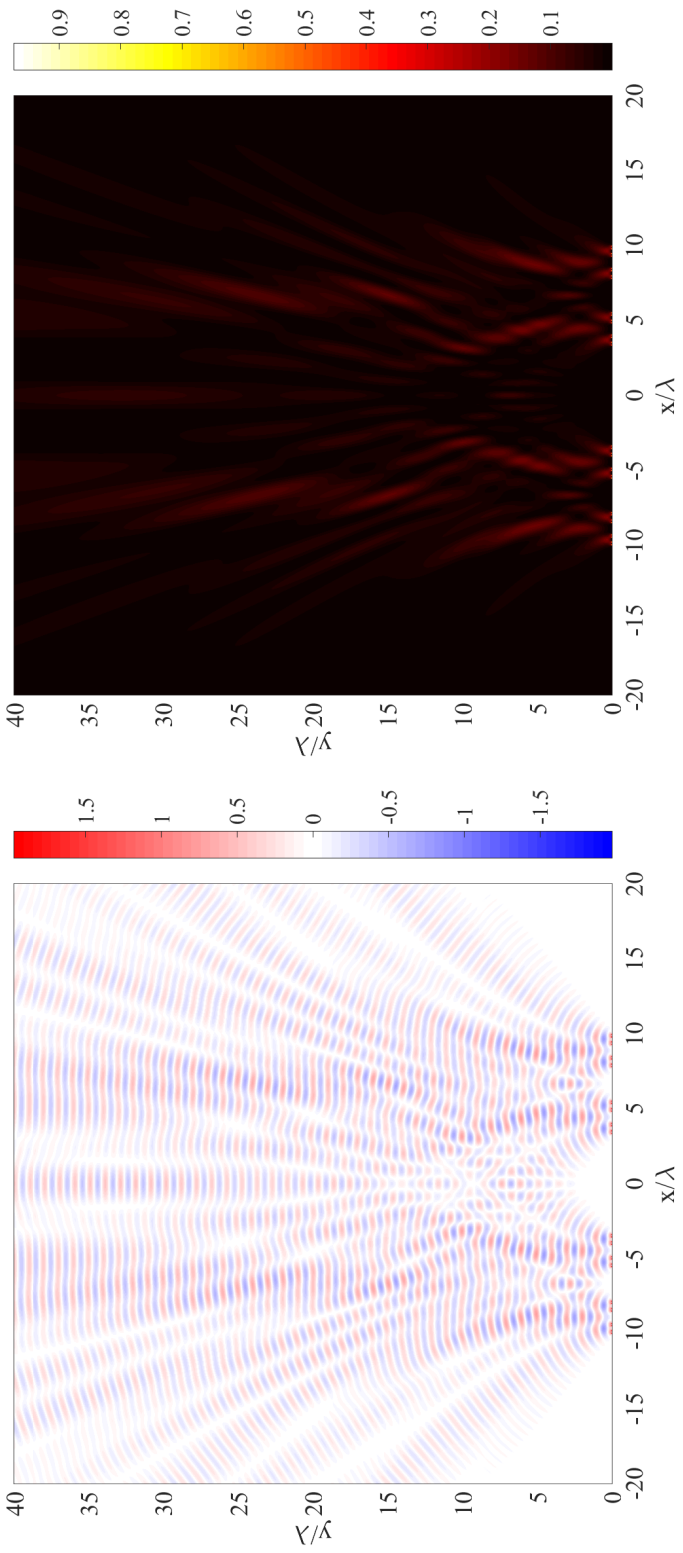

Figure C.32: Diffraction of a plane wave from the $n = 5$th pre-fractal level of the Cantor set with $a_0 = 10\lambda$. Electric field, $2\Re e\left(\frac{E_z}{E_0}\right)$, *(left)* and intensity, $\left|\frac{E_z}{E_0}\right|^2$ *(right)*.

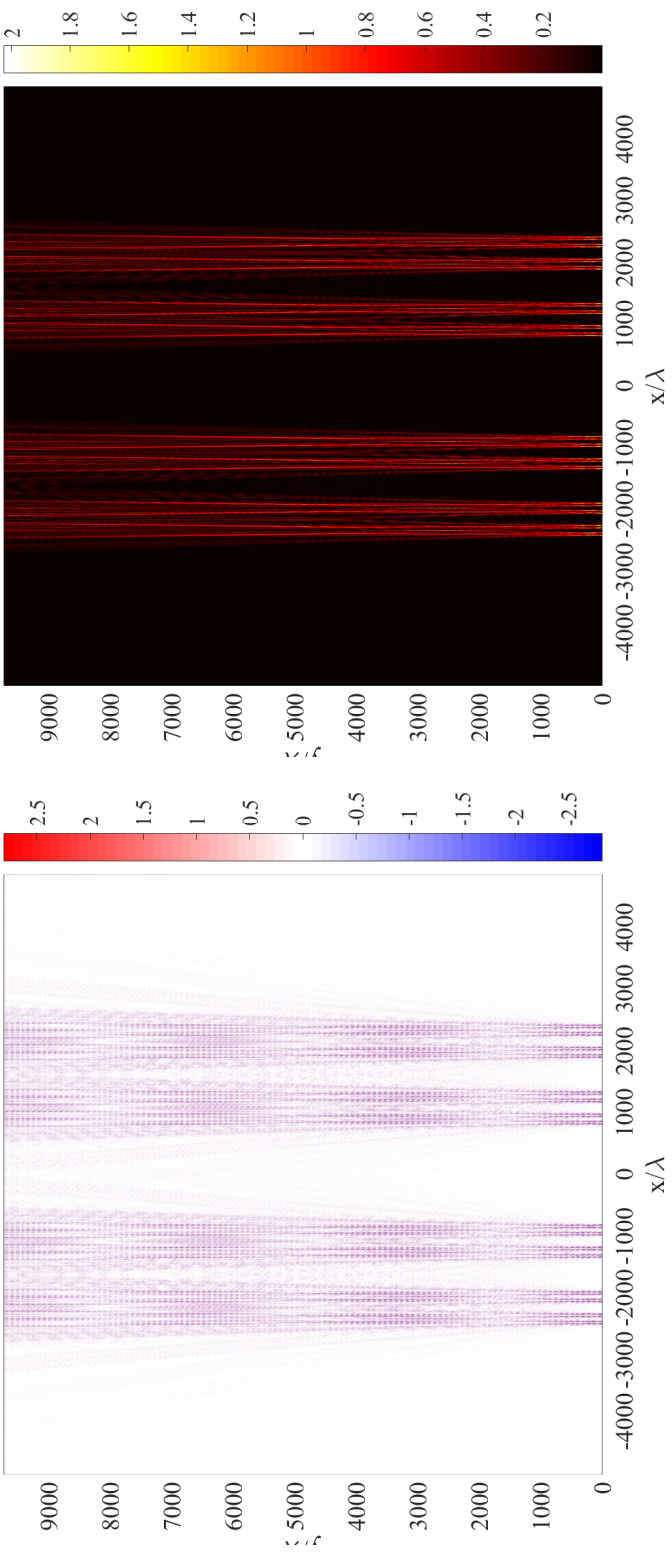

Figure C.33: Diffraction of a plane wave from the $n = 5$th pre-fractal level of the Cantor set with $a_n = 10\lambda$. Electric field, $2\Re e\left(\frac{E_z}{E_0}\right)$, *(left)* and intensity, $\left|\frac{E_z}{E_0}\right|^2$ *(right)*.

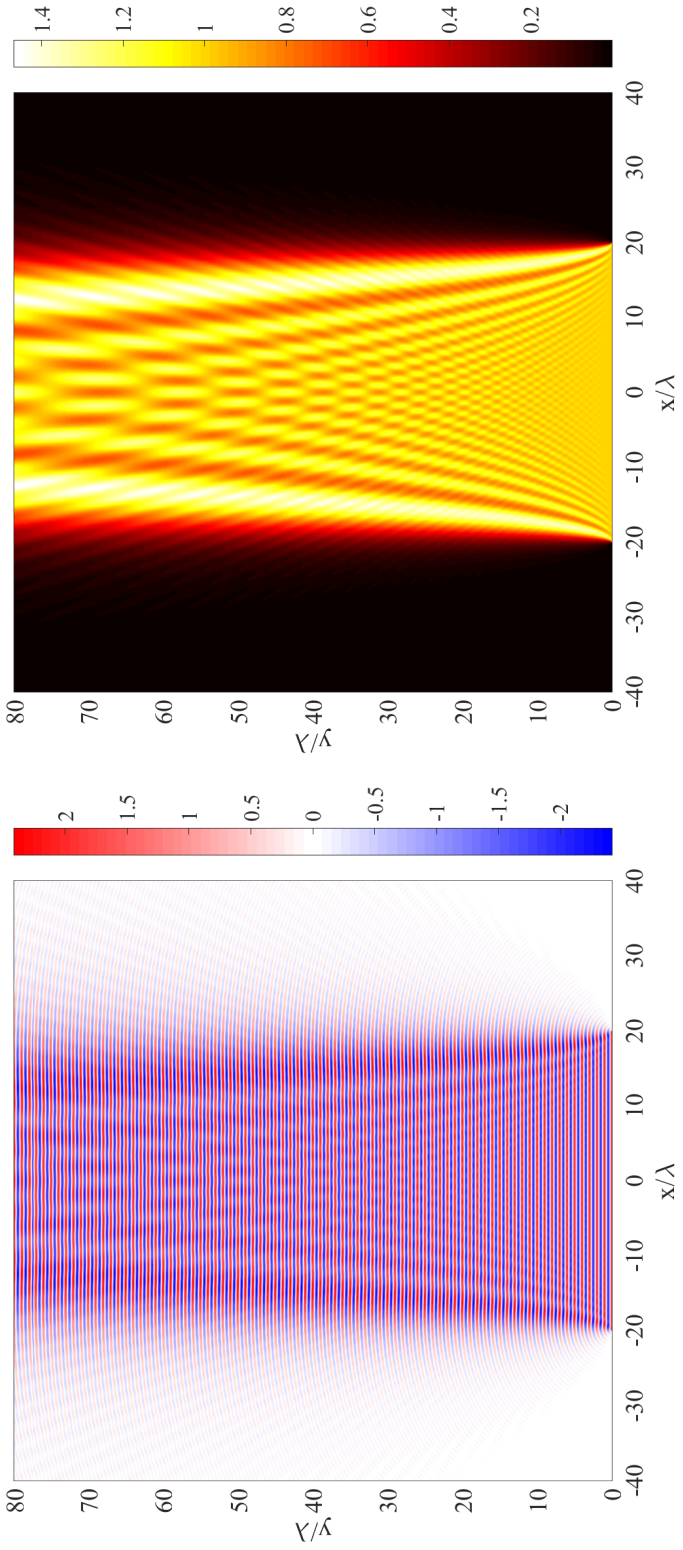

Figure C.34: Diffraction of a plane wave from the $n = 0$th pre-fractal level of the Cantor set with $a_0 = 20\lambda$. Electric field, $2\Re e\left(\frac{E_z}{E_0}\right)$, *(left)* and intensity, $\left|\frac{E_z}{E_0}\right|^2$ *(right)*.

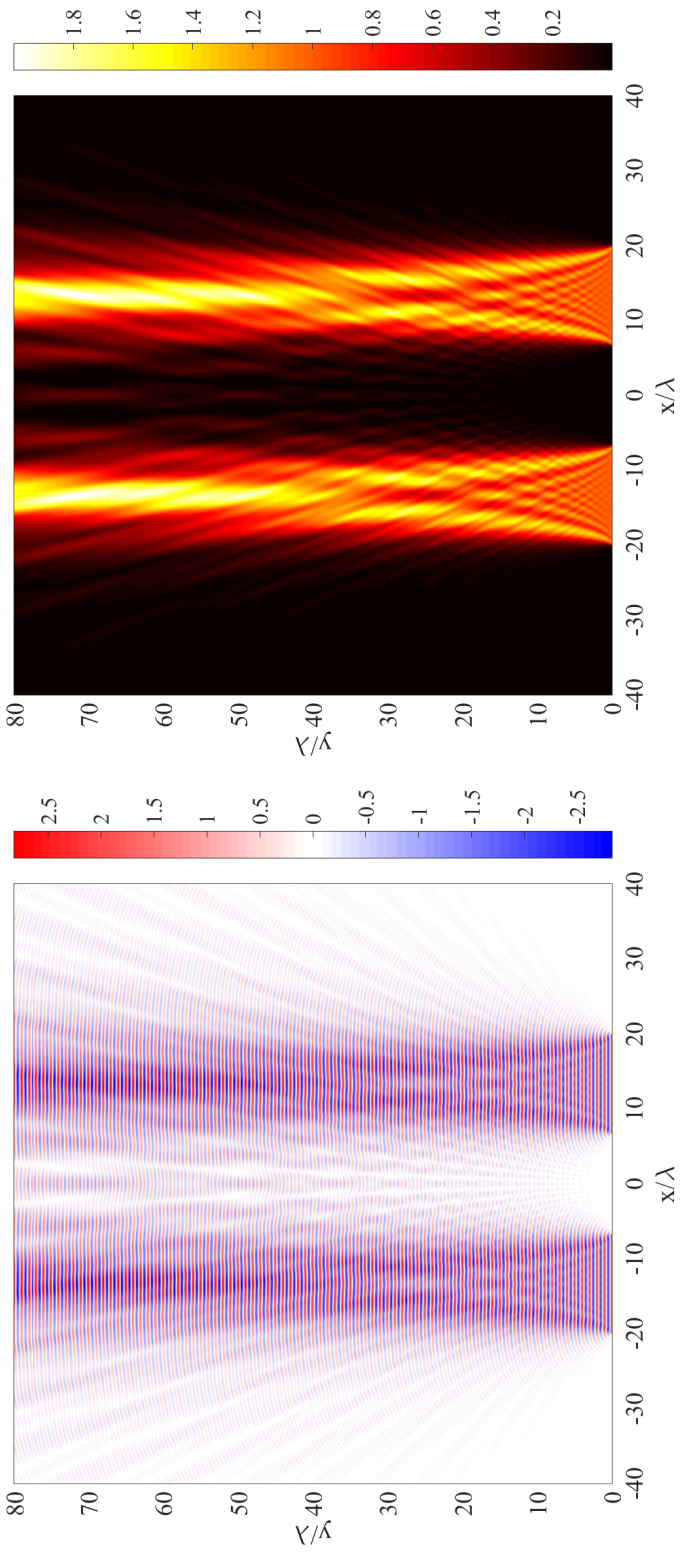

Figure C.35: Diffraction of a plane wave from the $n = 1$th pre-fractal level of the Cantor set with $a_0 = 20\lambda$. Electric field, $2\Re e\left(\frac{E_z}{E_0}\right)$, *(left)* and intensity, $\left|\frac{E_z}{E_0}\right|^2$ *(right)*.

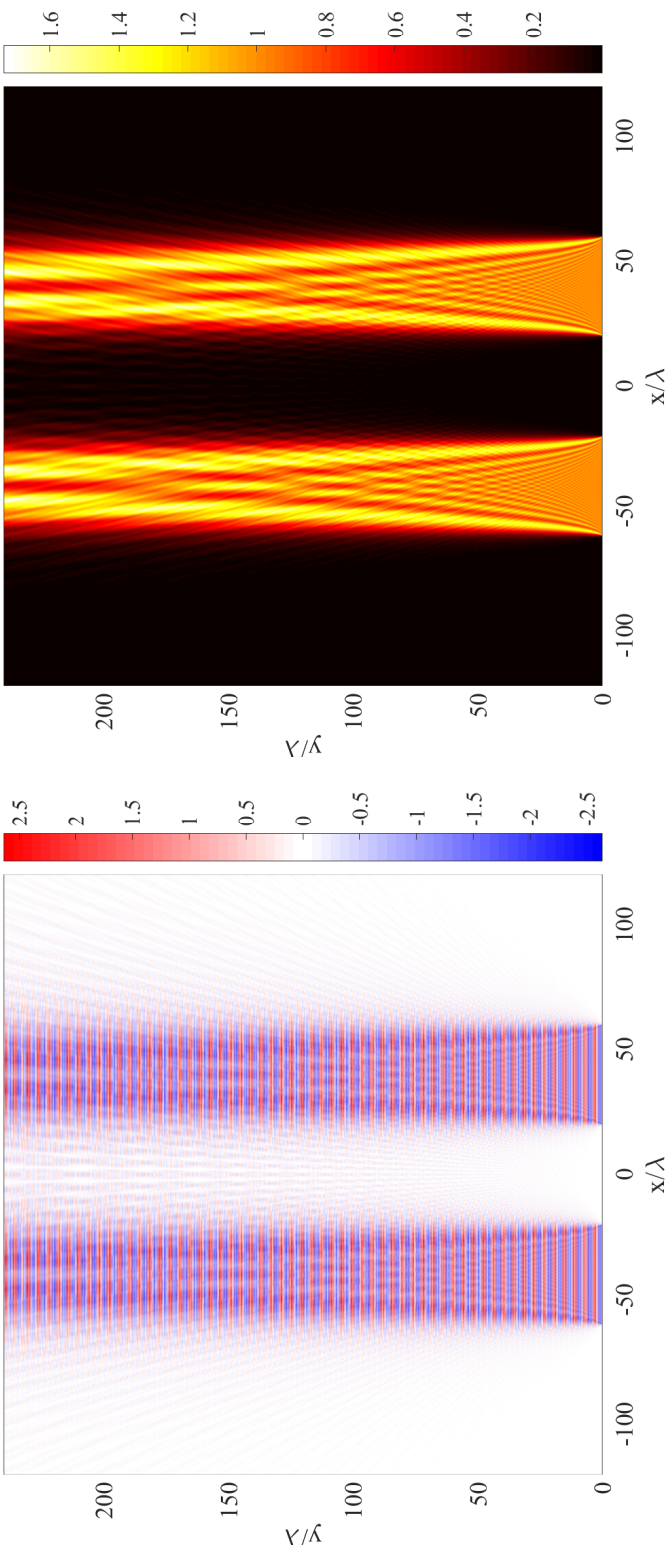

Figure C.36: Diffraction of a plane wave from the n = 1th pre-fractal level of the Cantor set with $a_n = 20\lambda$. Electric field, $2\Re e\left(\frac{E_z}{E_0}\right)$, *(left)* and intensity, $\left|\frac{E_z}{E_0}\right|^2$ *(right)*.

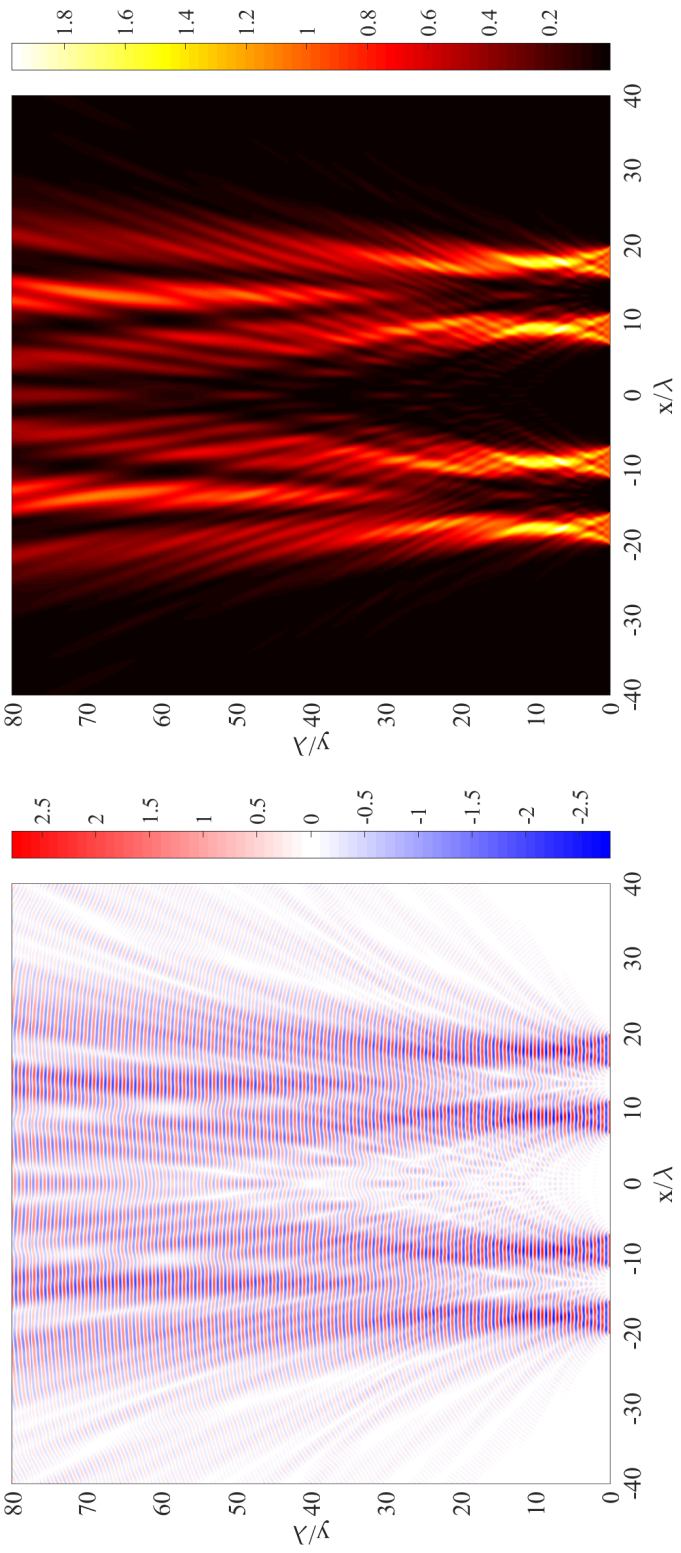

Figure C.37: Diffraction of a plane wave from the $n = 2$th pre-fractal level of the Cantor set with $a_0 = 20\lambda$. Electric field, $2\Re e\left(\frac{E_z}{E_0}\right)$, *(left)* and intensity, $\left|\frac{E_z}{E_0}\right|^2$ *(right)*.

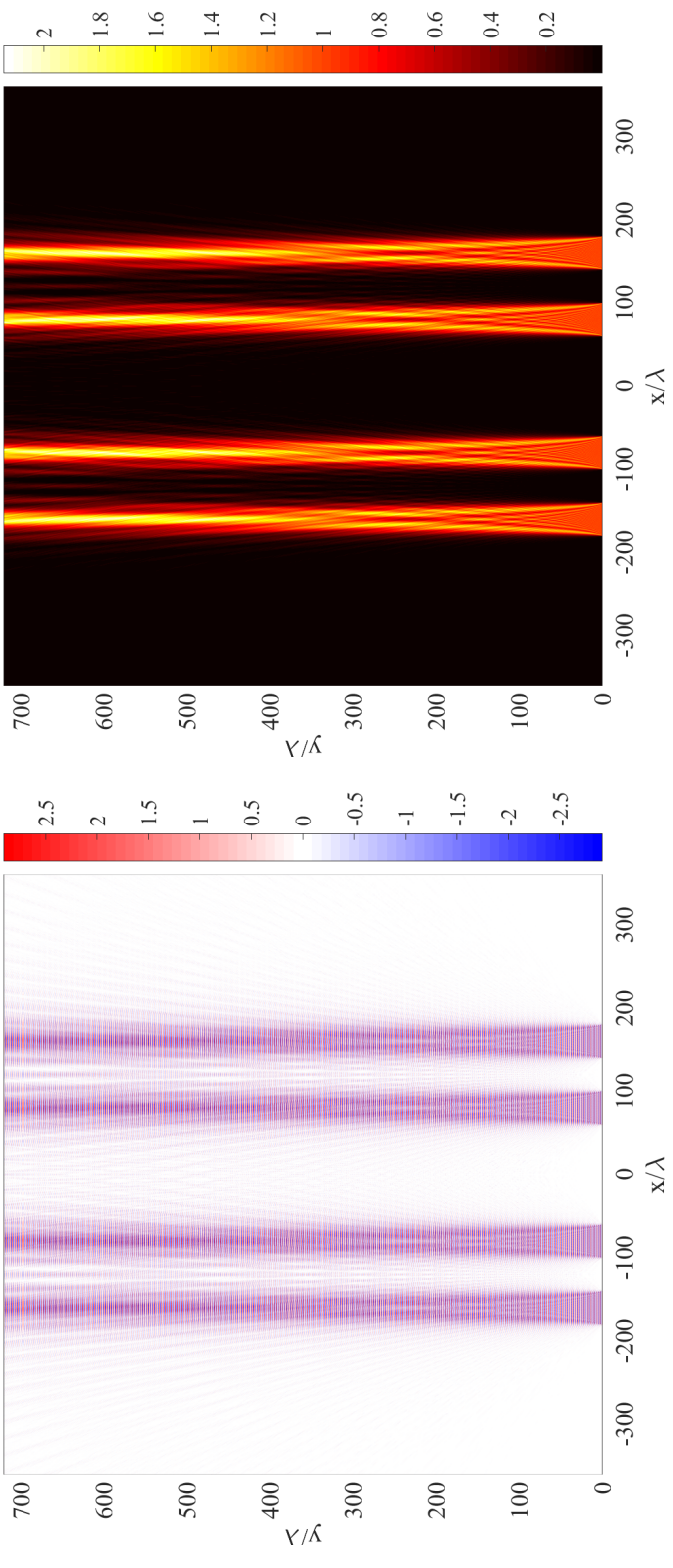

Figure C.38: Diffraction of a plane wave from the $n = 2$th pre-fractal level of the Cantor set with $a_n = 20\lambda$. Electric field, $2\Re e\left(\frac{E_z}{E_0}\right)$, *(left)* and intensity, $\left|\frac{E_z}{E_0}\right|^2$ *(right)*.

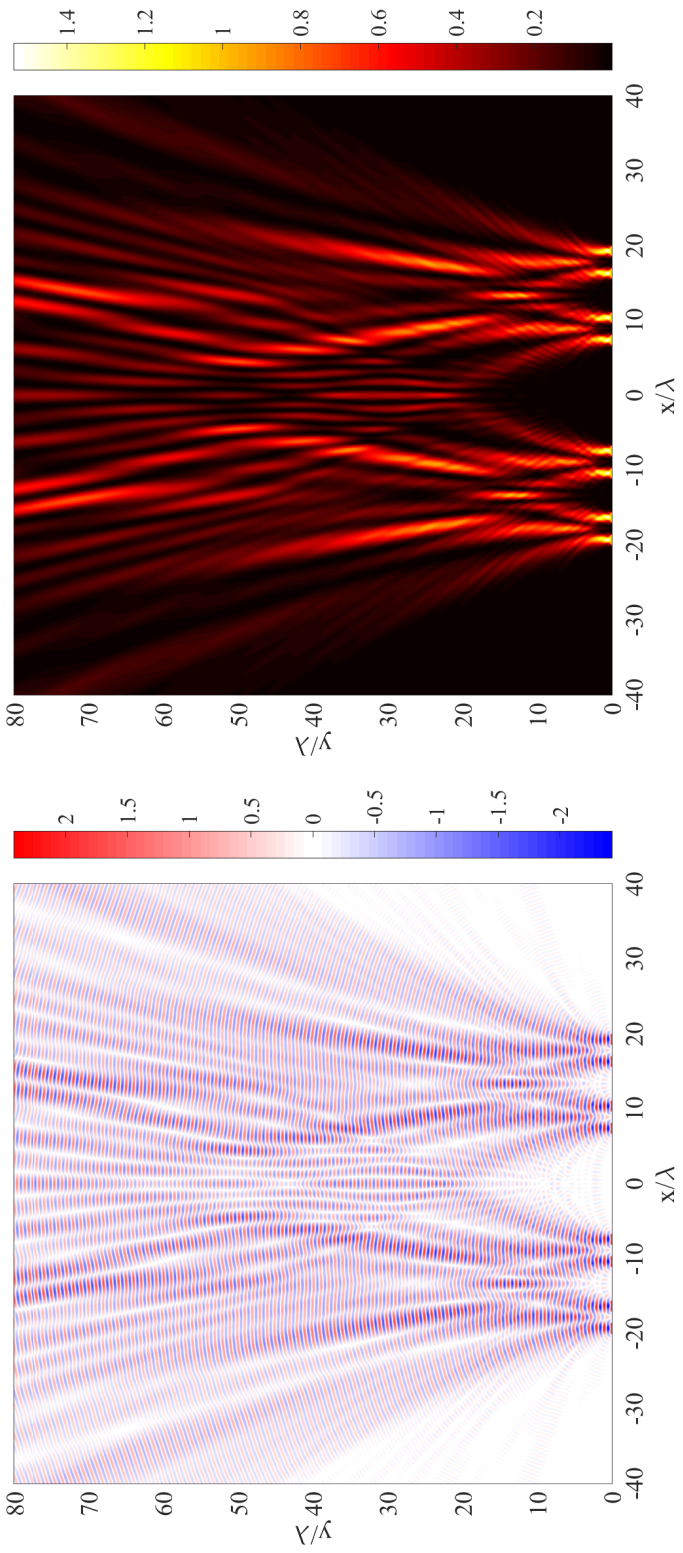

Figure C.39: Diffraction of a plane wave from the $n = 3$th pre-fractal level of the Cantor set with $a_0 = 20\lambda$. Electric field, $2\Re e\left(\frac{E_z}{E_0}\right)$, *(left)* and intensity, $\left|\frac{E_z}{E_0}\right|^2$ *(right)*.

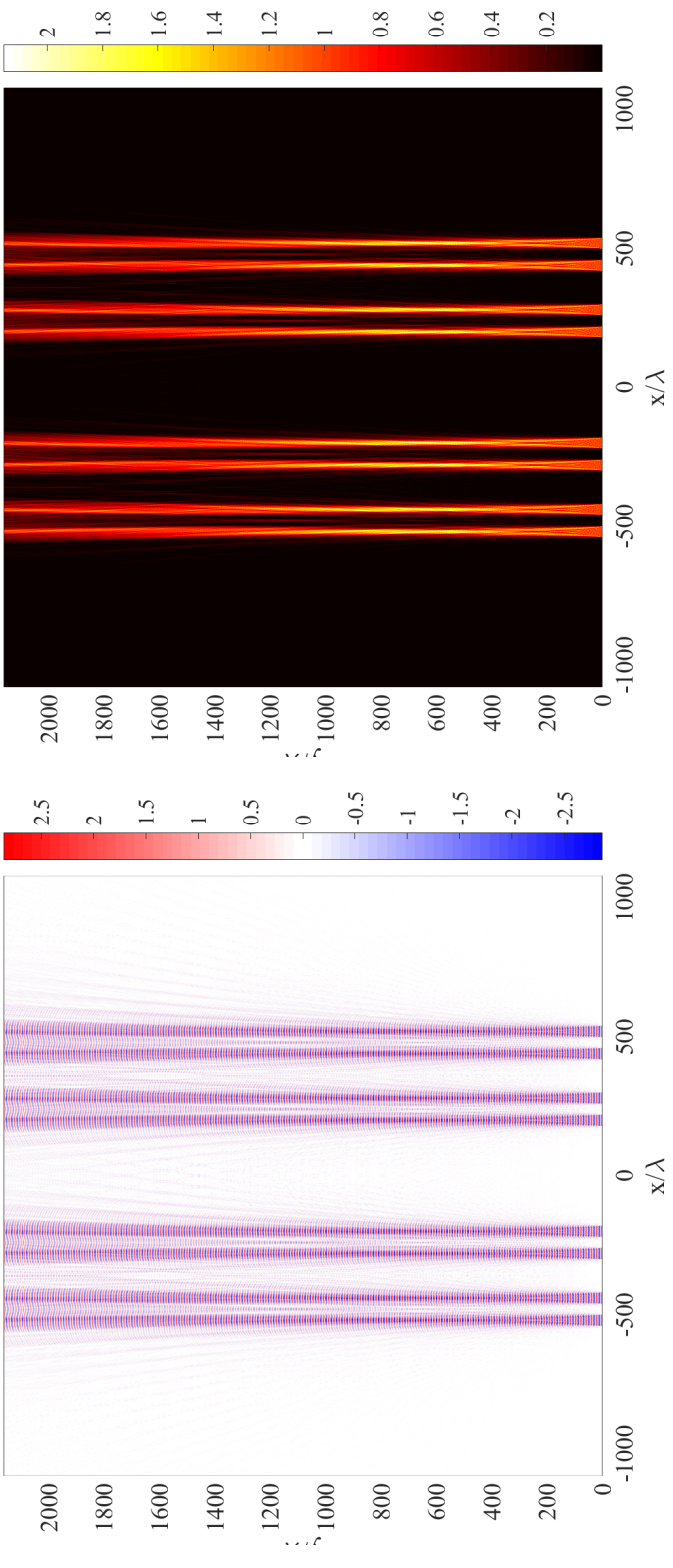

Figure C.40: Diffraction of a plane wave from the $n = 3$th pre-fractal level of the Cantor set with $a_n = 20\lambda$. Electric field, $2\Re e\left(\frac{E_z}{E_0}\right)$, *(left)* and intensity, $\left|\frac{E_z}{E_0}\right|^2$ *(right)*.

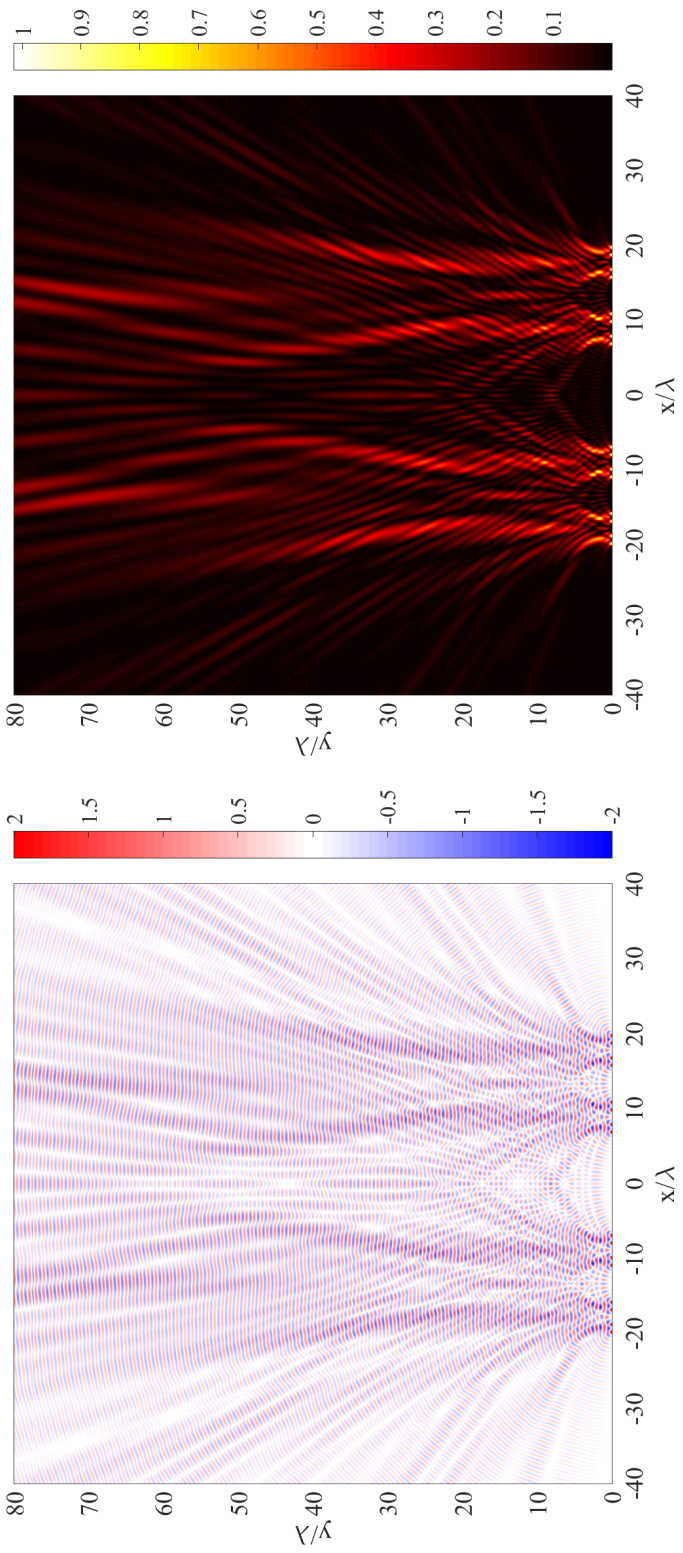

Figure C.41: Diffraction of a plane wave from the $n = 4$th pre-fractal level of the Cantor set with $a_0 = 20\lambda$. Electric field, $2\Re e\left(\frac{E_z}{E_0}\right)$, *(left)* and intensity, $\left|\frac{E_z}{E_0}\right|^2$ *(right)*.

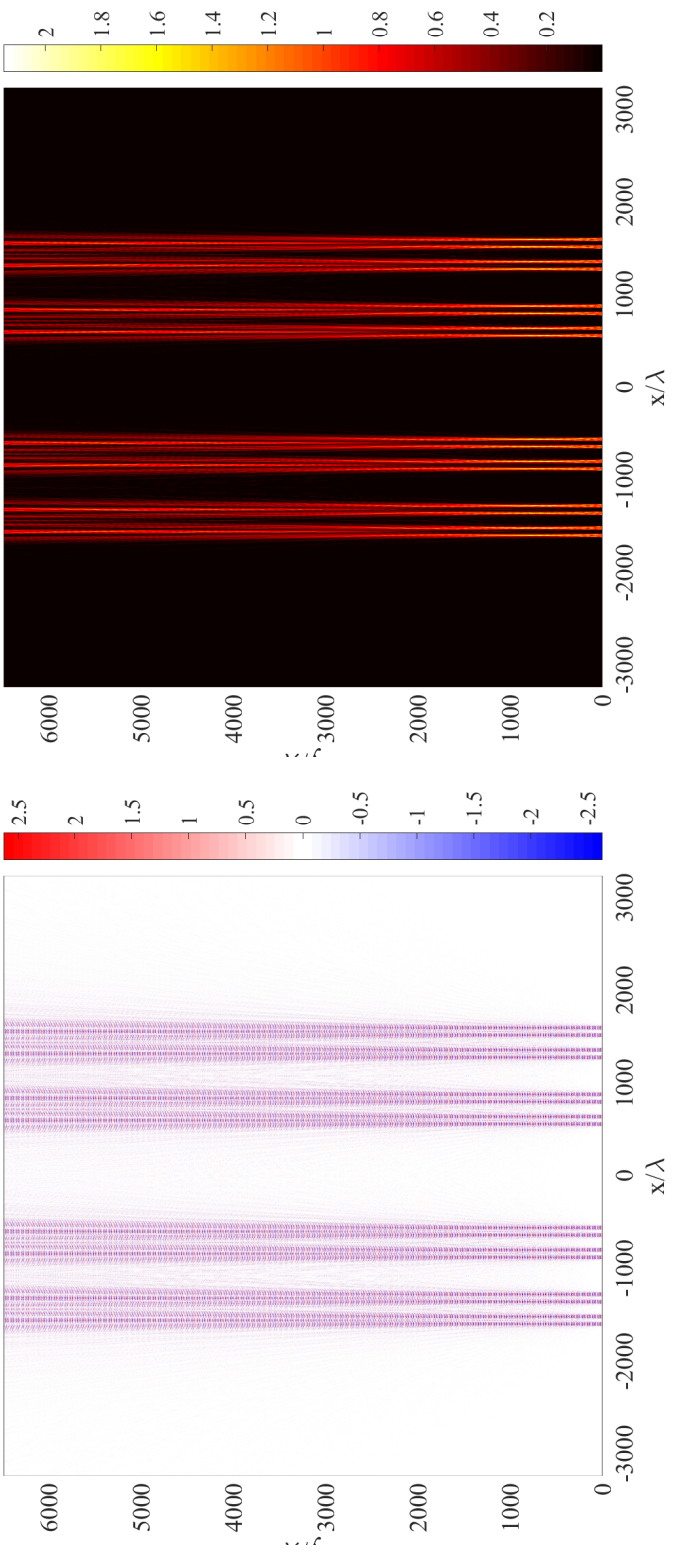

Figure C.42: Diffraction of a plane wave from the $n = 4$th pre-fractal level of the Cantor set with $a_n = 20\lambda$. Electric field, $2\Re e\left(\frac{E_z}{E_0}\right)$, *(left)* and intensity, $\left|\frac{E_z}{E_0}\right|^2$ *(right)*.

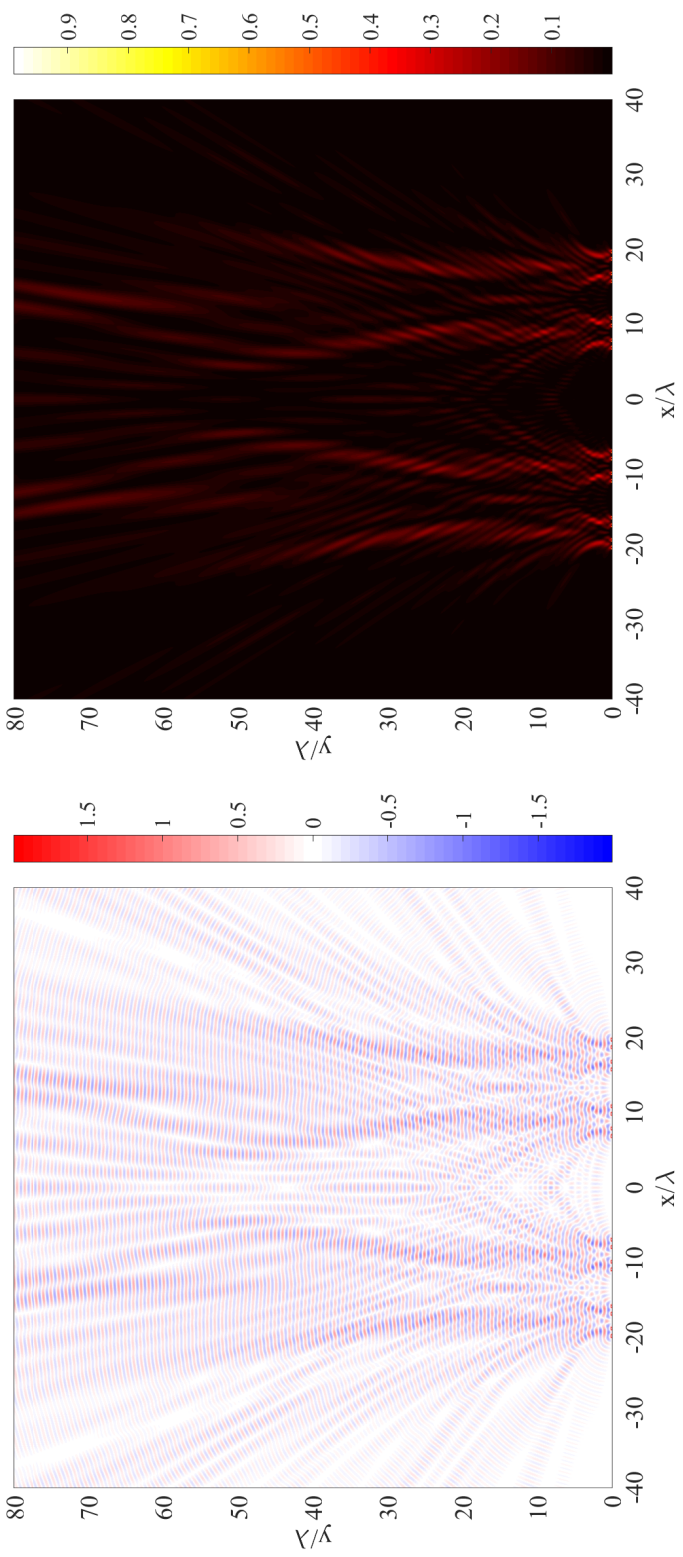

Figure C.43: Diffraction of a plane wave from the $n = 5$th pre-fractal level of the Cantor set with $a_0 = 20\lambda$. Electric field, $2\Re e\left(\frac{E_z}{E_0}\right)$, *(left)* and intensity, $\left|\frac{E_z}{E_0}\right|^2$ *(right)*.

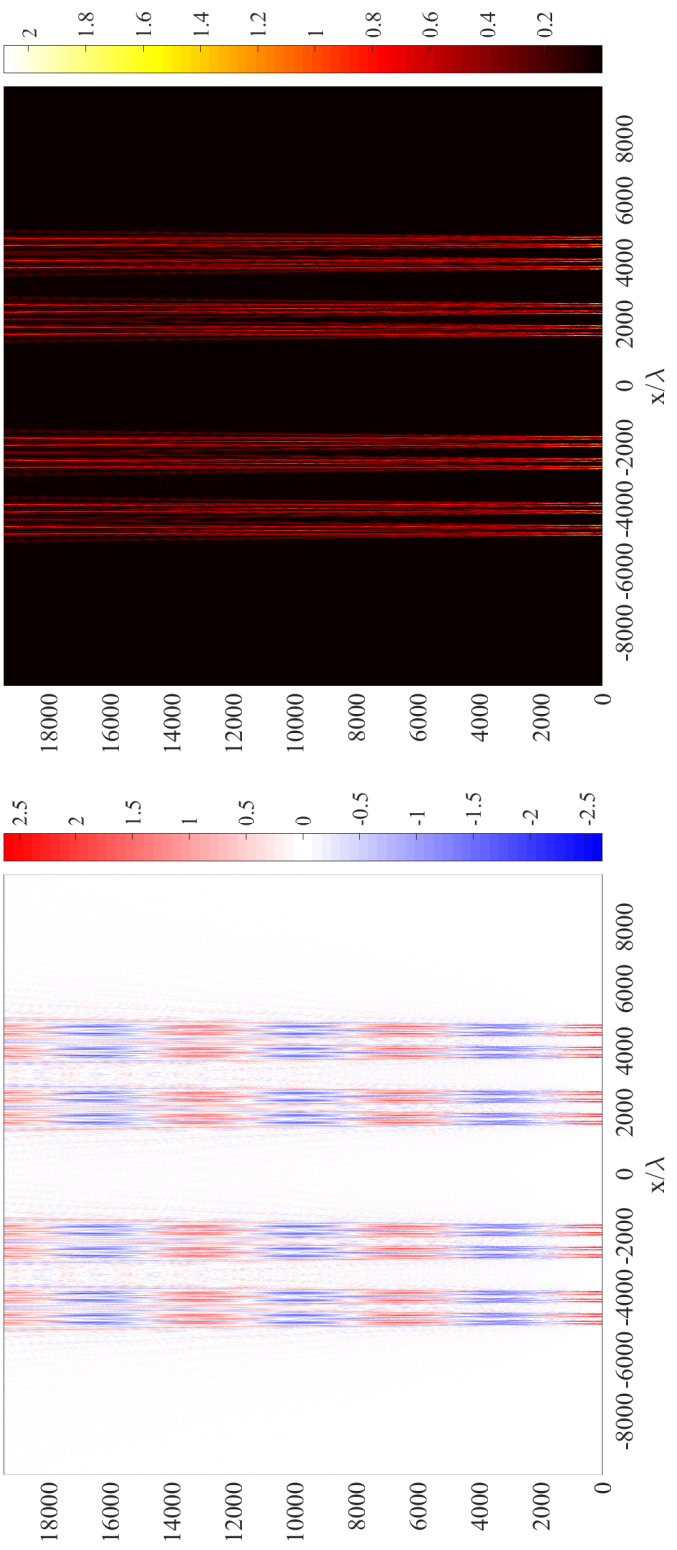

Figure C.44: Diffraction of a plane wave from the n = 5th pre-fractal level of the Cantor set with $a_n = 20\lambda$. Electric field, $2\Re e\left(\frac{E_z}{E_0}\right)$, *(left)* and intensity, $\left|\frac{E_z}{E_0}\right|^2$ *(right)*.

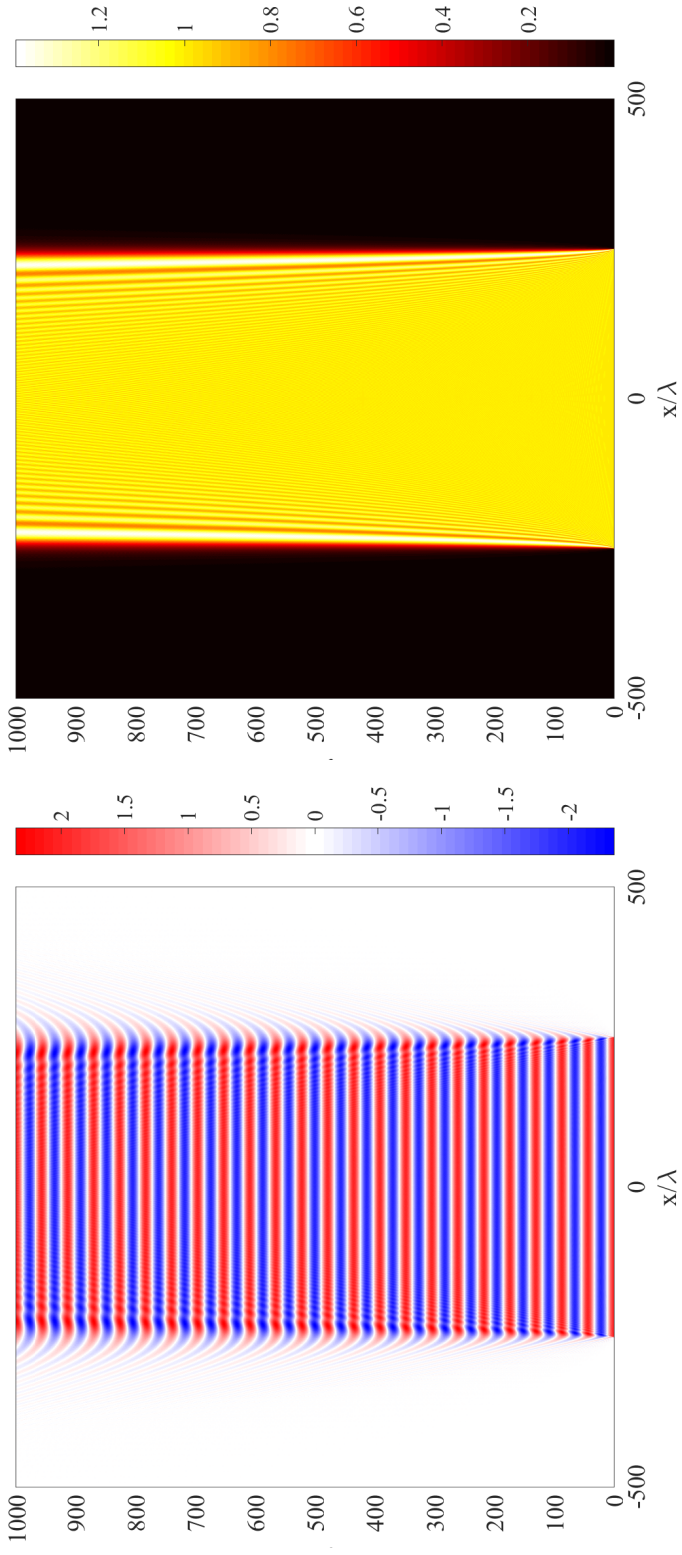

Figure C.45: Diffraction of a plane wave from the $n = 0$th pre-fractal level of the Cantor set with $a_0 = 250\lambda$. Electric field, $2\Re e\left(\frac{E_z}{E_0}\right)$, *(left)* and intensity, $\left|\frac{E_z}{E_0}\right|^2$ *(right)*.

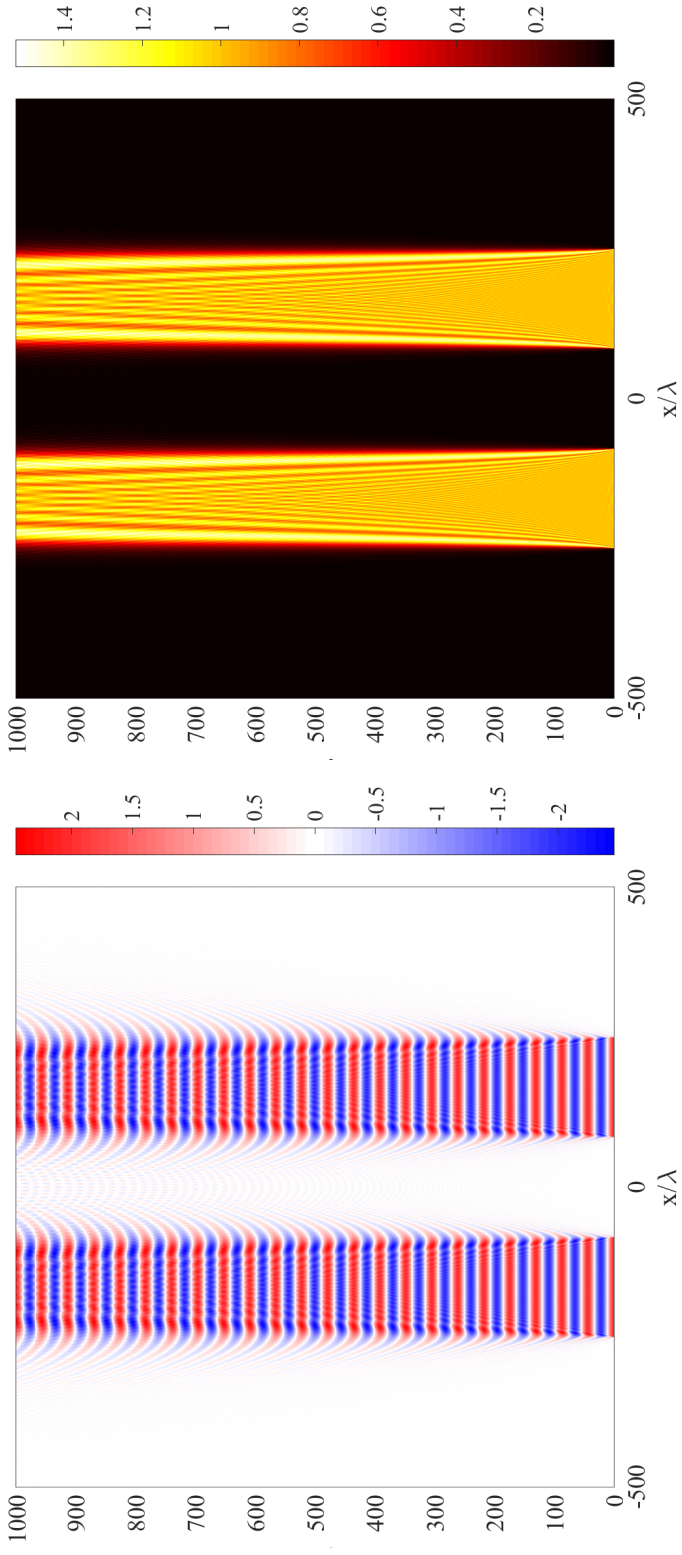

Figure C.46: Diffraction of a plane wave from the $n = 1$th pre-fractal level of the Cantor set with $a_0 = 250\lambda$. Electric field, $2\Re e\left(\frac{E_z}{E_0}\right)$, *(left)* and intensity, $\left|\frac{E_z}{E_0}\right|^2$ *(right)*.

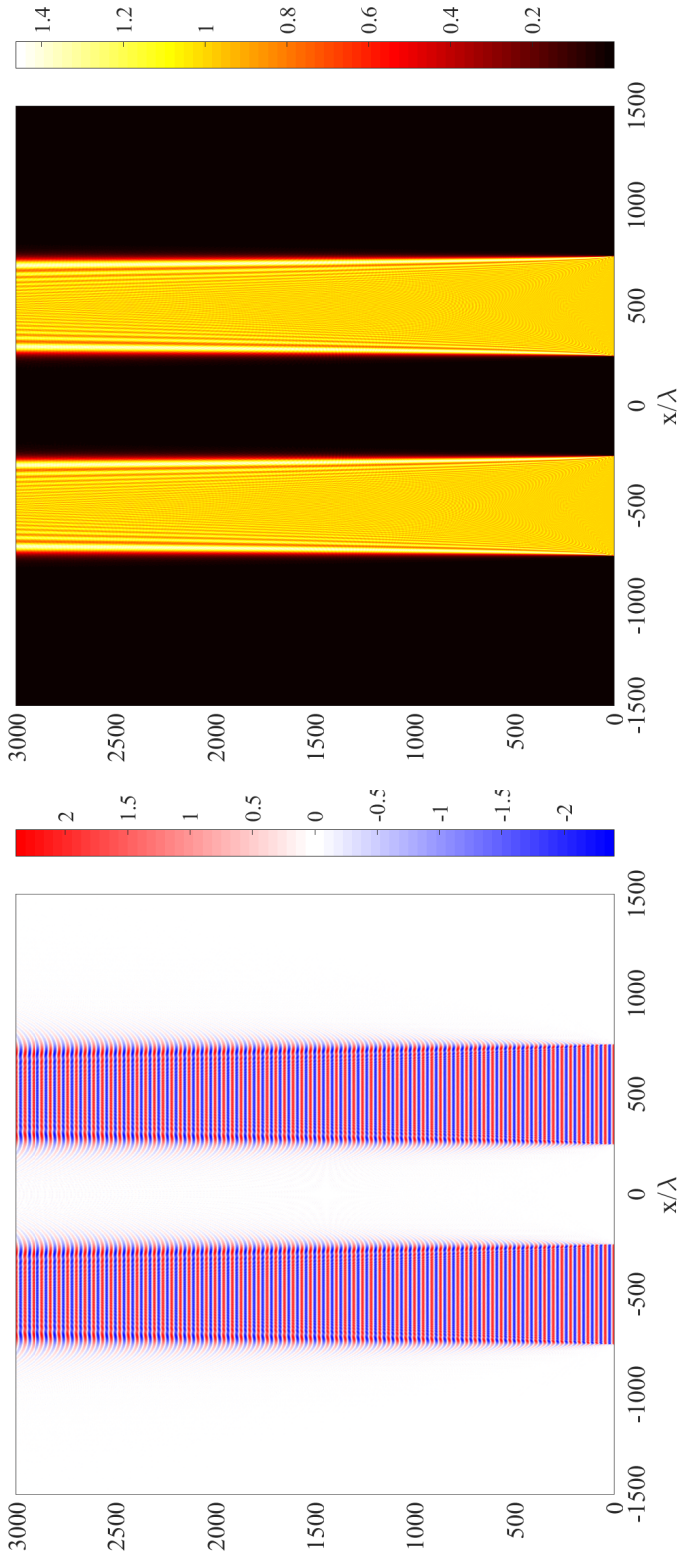

Figure C.47: Diffraction of a plane wave from the $n = 1$th pre-fractal level of the Cantor set with $a_n = 250\lambda$. Electric field, $2\Re e\left(\frac{E_z}{E_0}\right)$, *(left)* and intensity, $\left|\frac{E_z}{E_0}\right|^2$ *(right)*.

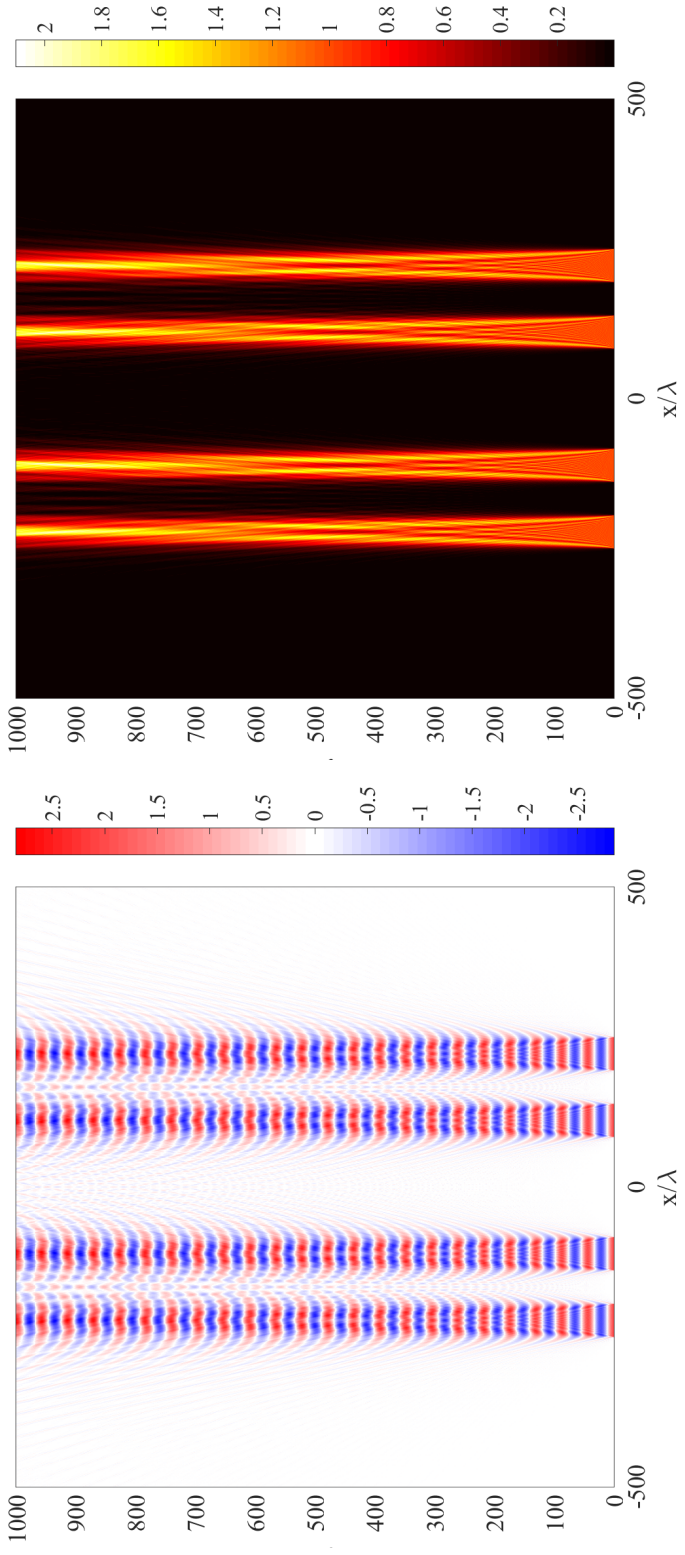

Figure C.48: Diffraction of a plane wave from the $n = 2$th pre-fractal level of the Cantor set with $a_0 = 250\lambda$. Electric field, $2\Re e\left(\frac{E_z}{E_0}\right)$, *(left)* and intensity, $\left|\frac{E_z}{E_0}\right|^2$ *(right)*.

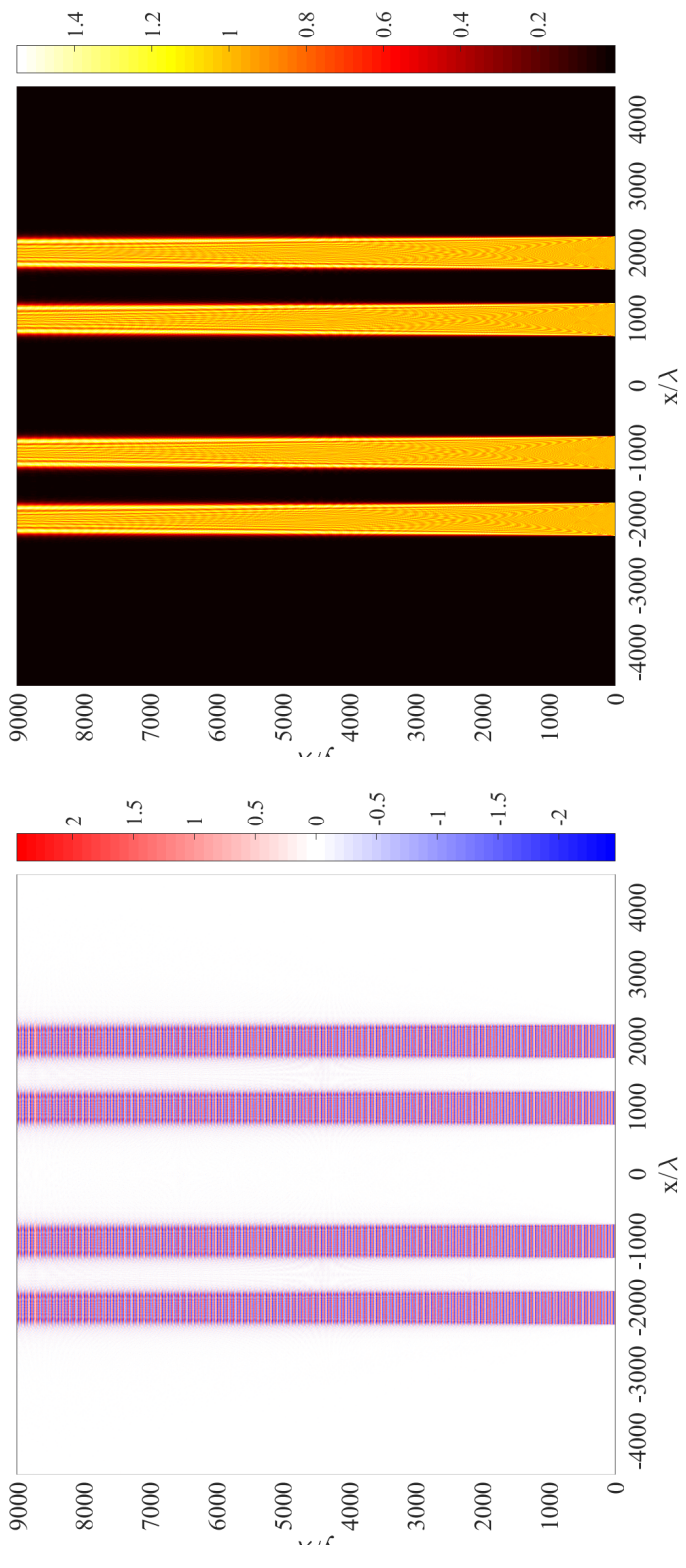

Figure C.49: Diffraction of a plane wave from the $n = 2$th pre-fractal level of the Cantor set with $a_n = 250\lambda$. Electric field, $2\Re e\left(\frac{E_z}{E_0}\right)$, *(left)* and intensity, $\left|\frac{E_z}{E_0}\right|^2$ *(right)*.

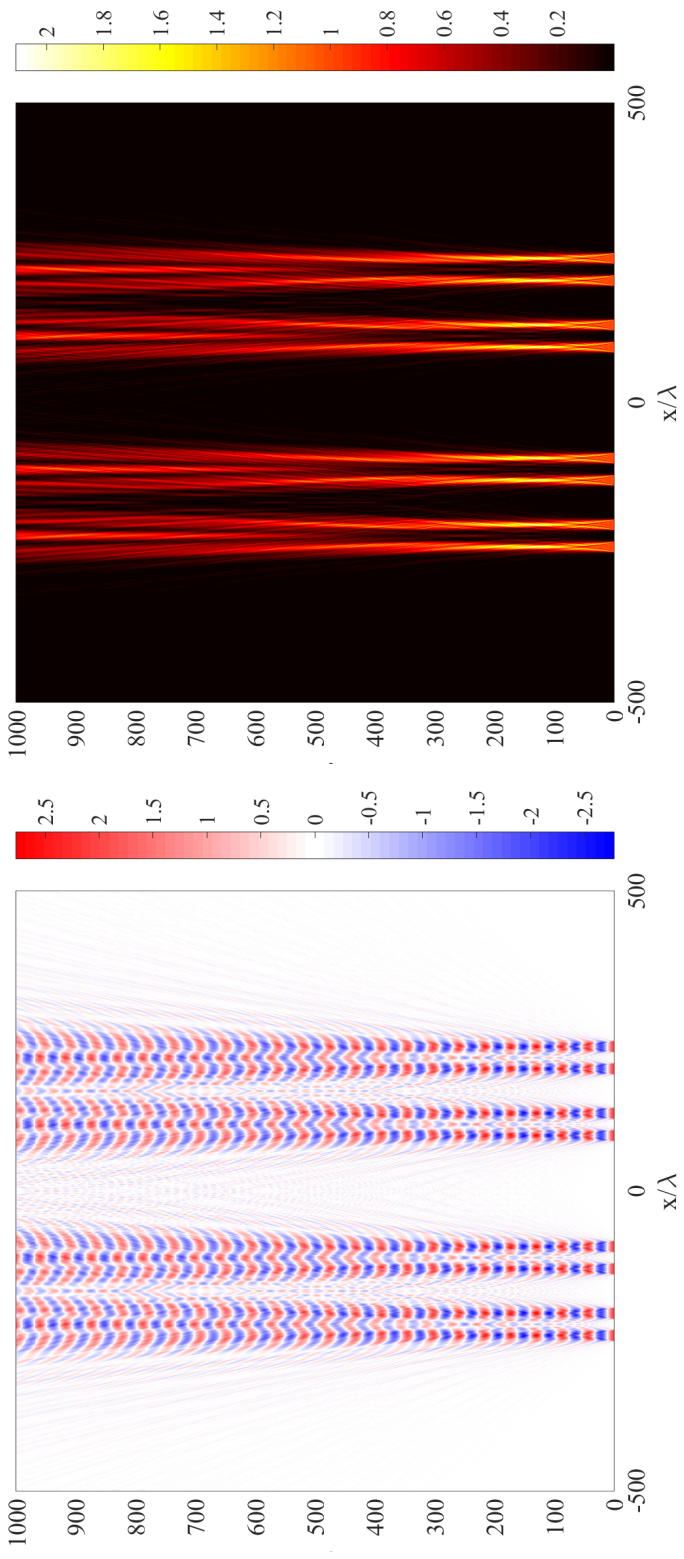

Figure C.50: Diffraction of a plane wave from the $n = 3$th pre-fractal level of the Cantor set with $a_0 = 250\lambda$. Electric field, $2\Re e\left(\frac{E_z}{E_0}\right)$, *(left)* and intensity, $\left|\frac{E_z}{E_0}\right|^2$ *(right)*.

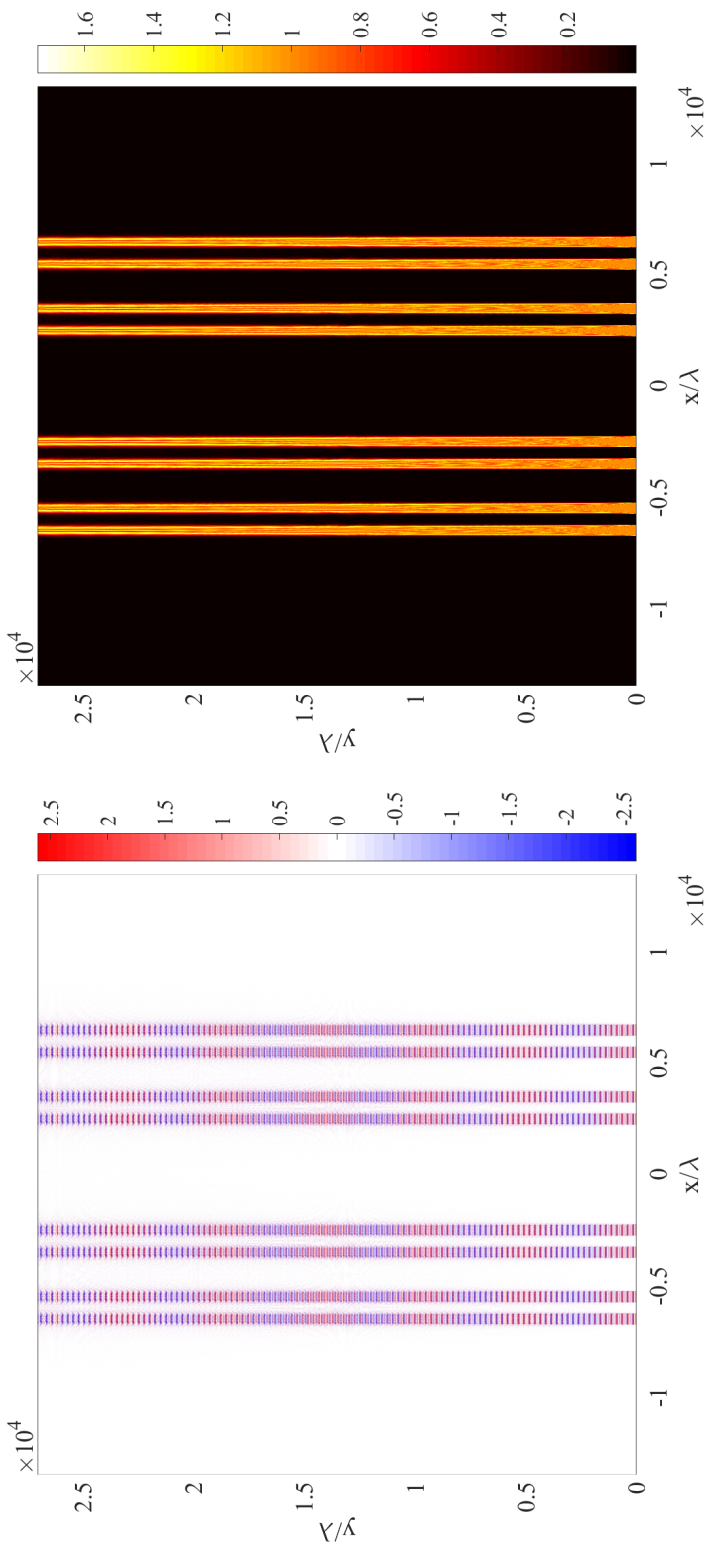

Figure C.51: Diffraction of a plane wave from the $n = 3$th pre-fractal level of the Cantor set with $a_n = 250\lambda$. Electric field, $2\Re e\left(\frac{E_z}{E_0}\right)$, *(left)* and intensity, $\left|\frac{E_z}{E_0}\right|^2$ *(right)*.

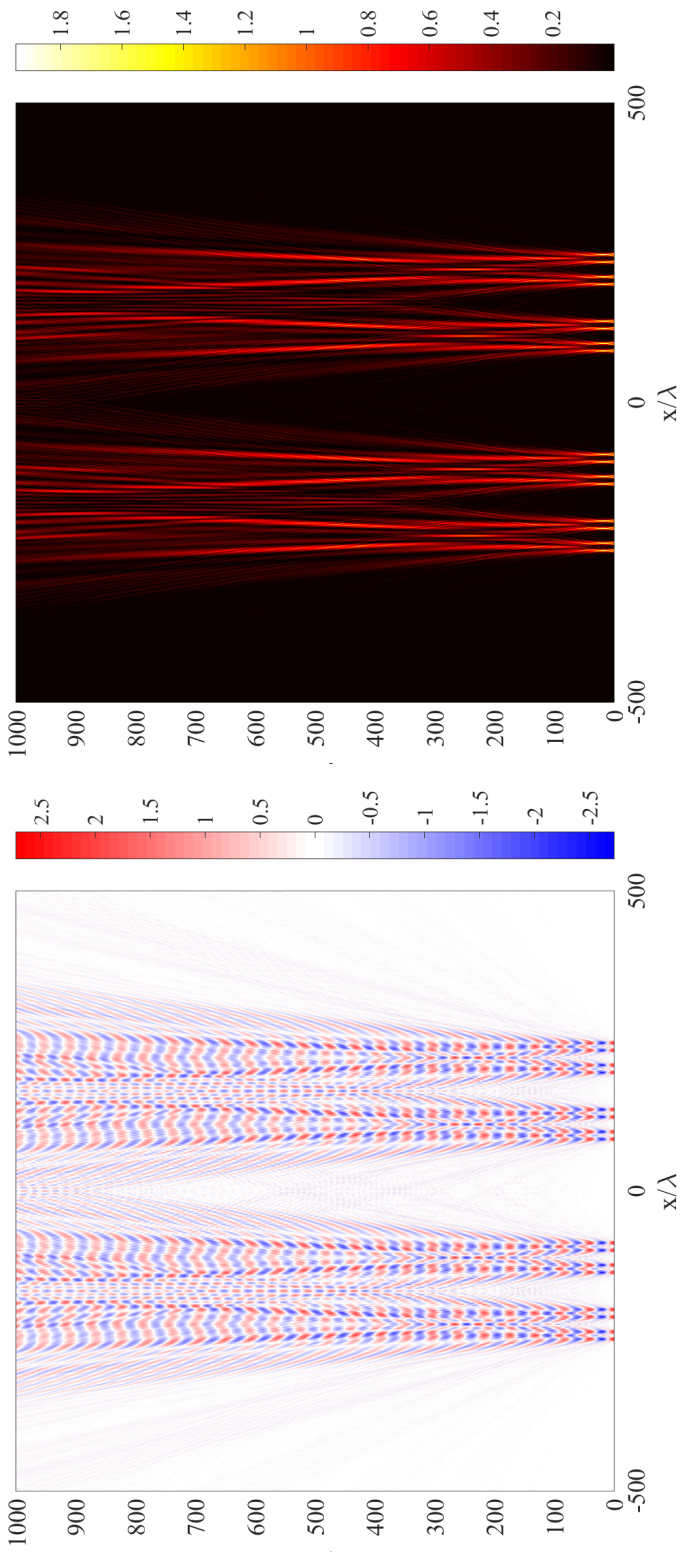

Figure C.52: Diffraction of a plane wave from the $n = 4$th pre-fractal level of the Cantor set with $a_0 = 250\lambda$. Electric field, $2\Re e\left(\frac{E_z}{E_0}\right)$, *(left)* and intensity, $\left|\frac{E_z}{E_0}\right|^2$ *(right)*.

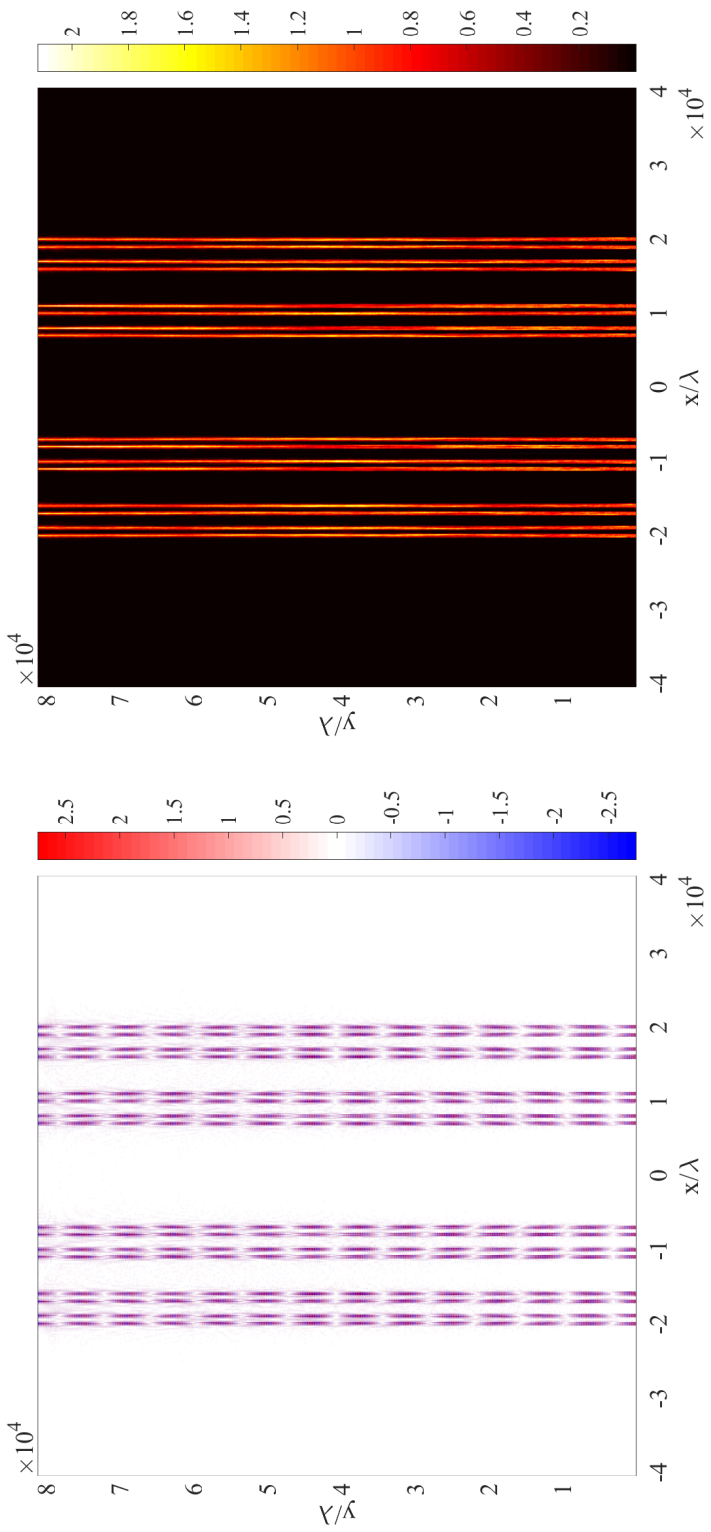

Figure C.53: Diffraction of a plane wave from the $n = 4$th pre-fractal level of the Cantor set with $a_n = 250\lambda$. Electric field, $2\Re e\left(\frac{E_z}{E_0}\right)$, *(left)* and intensity, $\left|\frac{E_z}{E_0}\right|^2$ *(right)*.

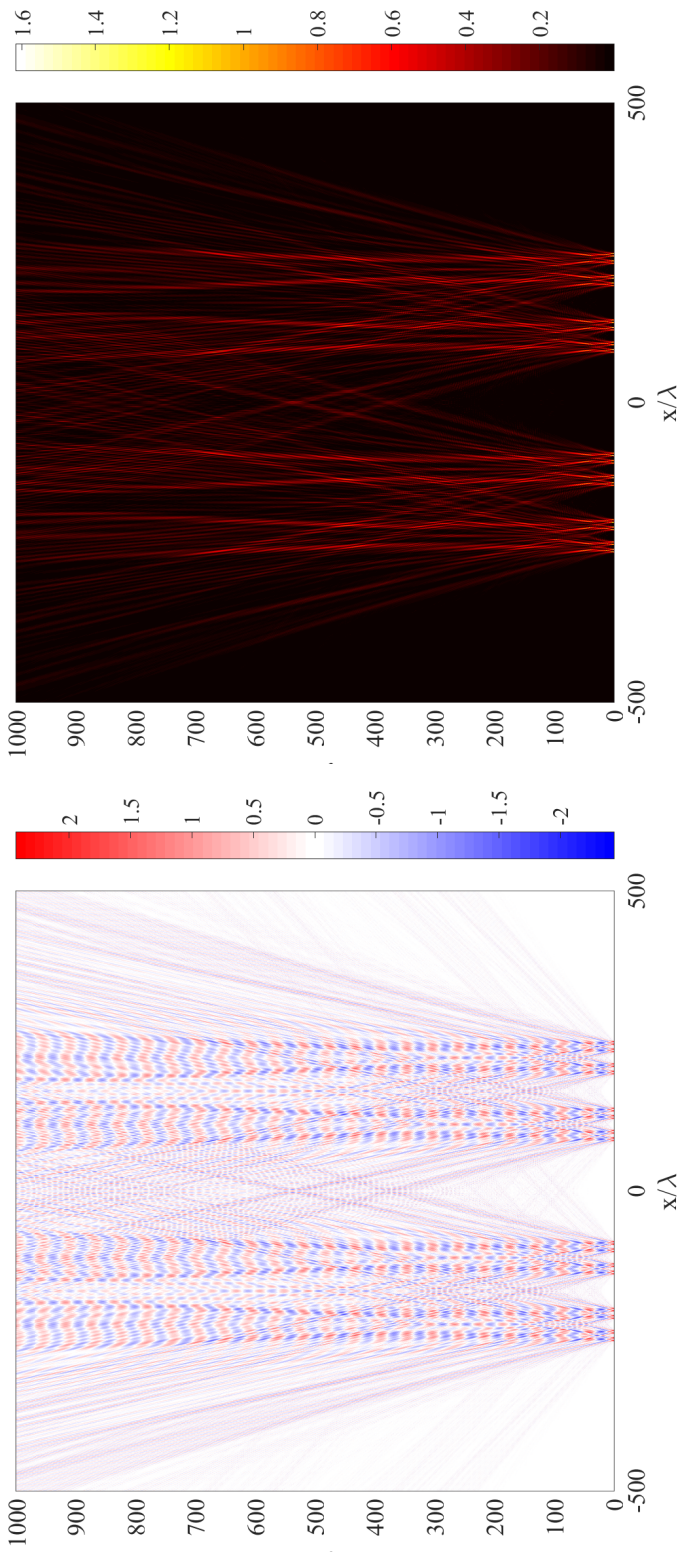

Figure C.54: Diffraction of a plane wave from the $n = 5$th pre-fractal level of the Cantor set with $a_0 = 250\lambda$. Electric field, $2\Re e\left(\frac{E_z}{E_0}\right)$, *(left)* and intensity, $\left|\frac{E_z}{E_0}\right|^2$ *(right)*.

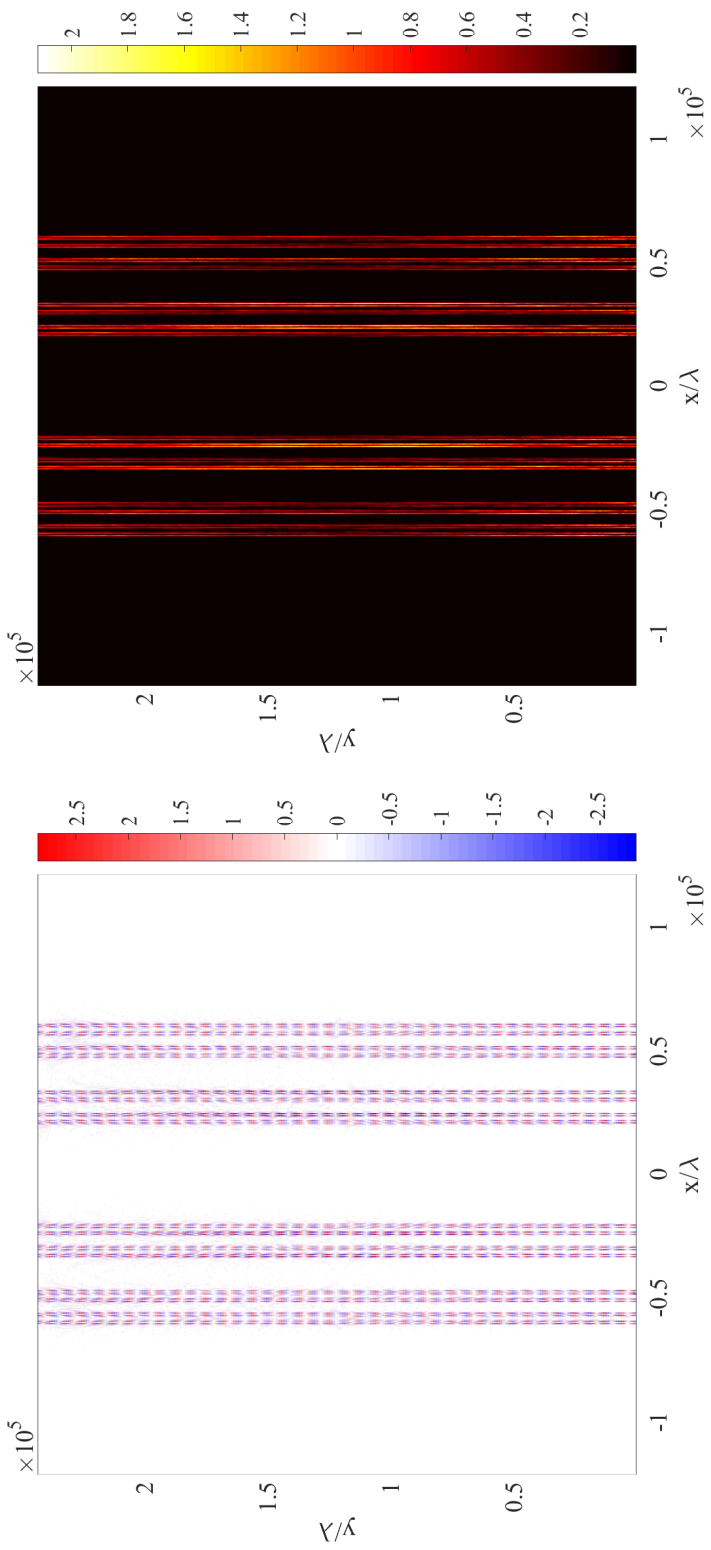

Figure C.55: Diffraction of a plane wave from the $n = 5$th pre-fractal level of the Cantor set with $a_n = 250\lambda$. Electric field, $2\Re e\left(\frac{E_z}{E_0}\right)$, *(left)* and intensity, $\left|\frac{E_z}{E_0}\right|^2$ *(right)*.

APPENDIX D

EXTRA RESULTS FROM CHAPTER 5

Due to the excessive computation times required to solve the 'pre-fractal on complex domains' class of problem, higher pre-fractal levels for the modified Cantor-set gratings (such as $n = 4$ and $n = 5$) became unattainable. Also, while running, it become apparent (as days turned into weeks and weeks turned into months) that generating 32 results for each D_0 value was an unrealistic goal. As a partial remedy, results for $D_0 = 1.3$ and 1.7 at $n = 2$ were allowed to finish but $n \geq 3$ had to be abandoned.

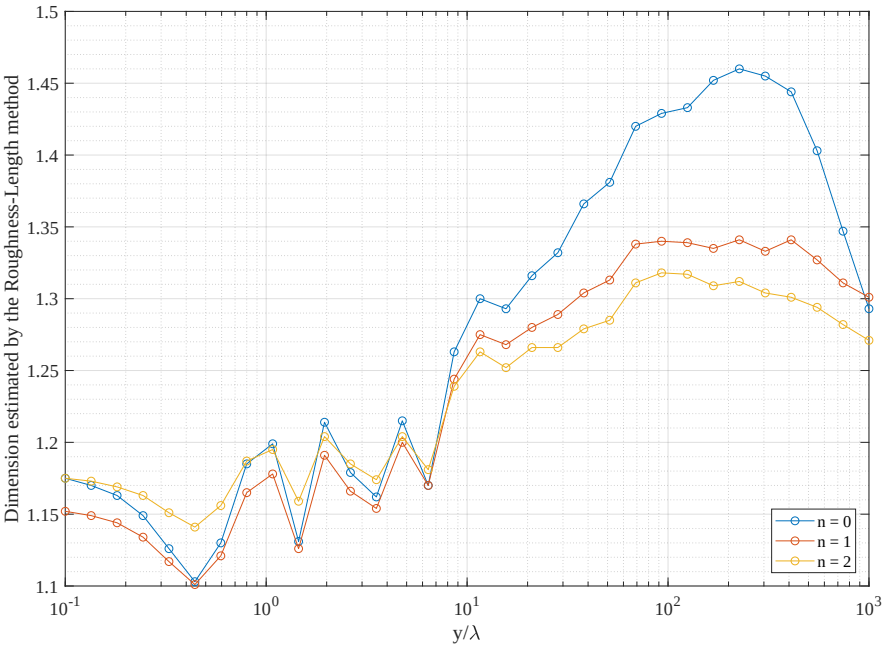

Figure D.1: Estimated roughness-length dimension for diffracted intensity, $\left|\frac{E_z}{E_0}\right|^2$, of a truncated-Weierstrass waveform with $D_0 = 1.3$ from a modified Cantor set with $a_n = 250\lambda$.

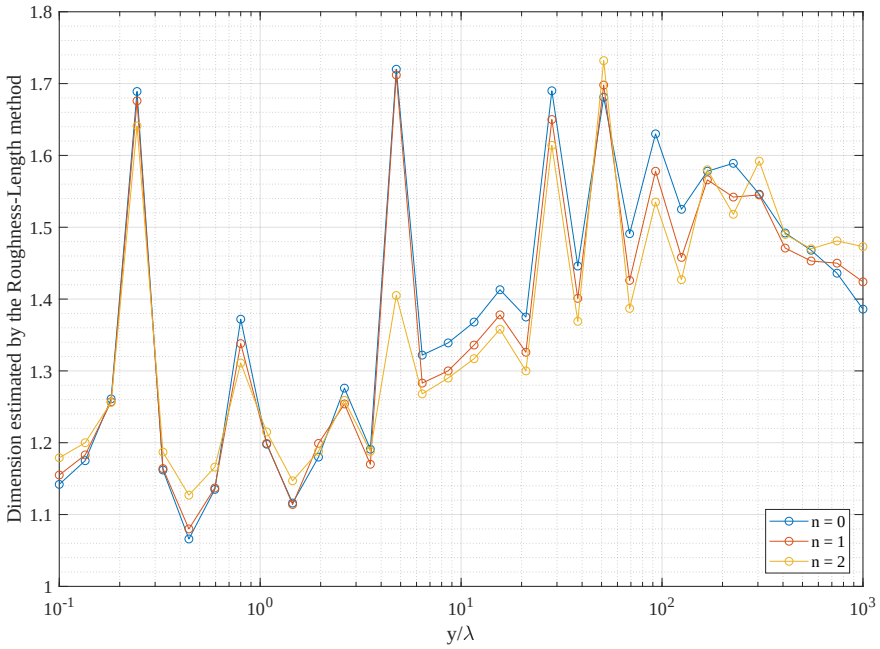

Figure D.2: Estimated roughness-length dimension for diffracted electric field, $2\Re e\left(\frac{E_z}{E_0}\right)$, of a truncated-Weierstrass waveform with $D_0 = 1.3$ from a modified Cantor set with $a_n = 250\lambda$.

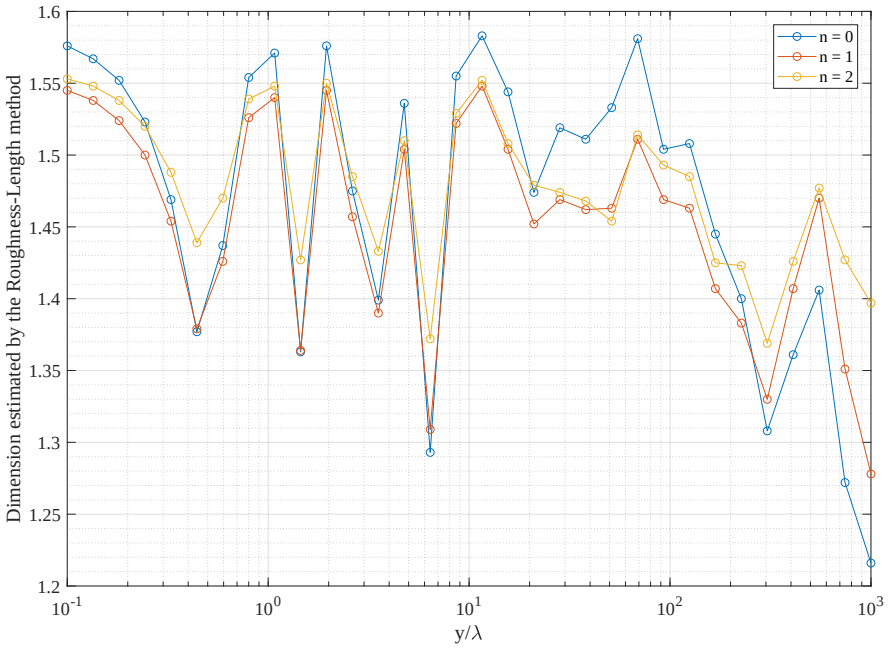

Figure D.3: Estimated roughness-length dimension for diffracted intensity, $\left|\frac{E_z}{E_0}\right|^2$, of a truncated-Weierstrass waveform with $D_0 = 1.7$ from a modified Cantor set with $a_n = 250\lambda$.

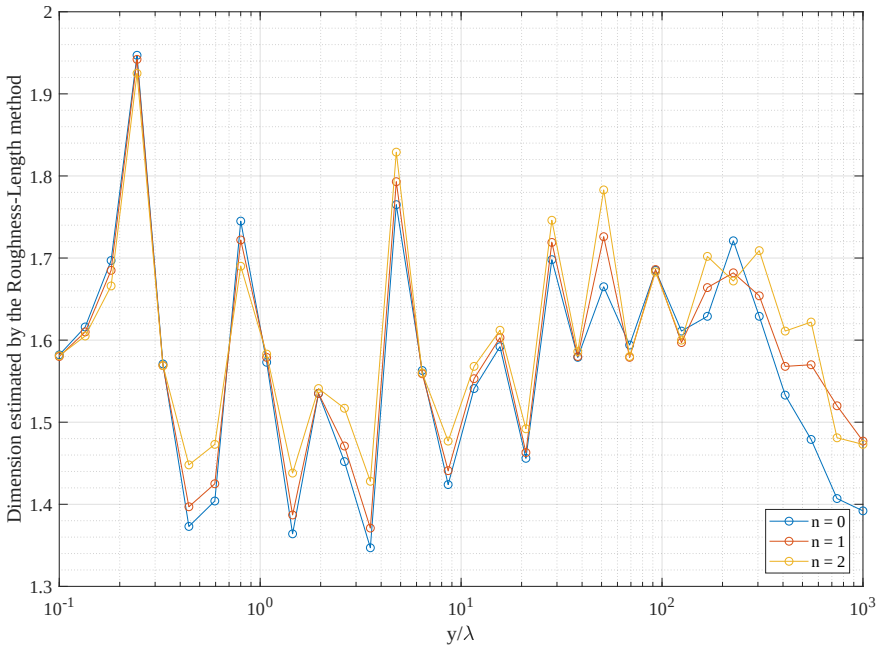

Figure D.4: Estimated roughness-length dimension for diffracted electric field, $2\Re e\left(\frac{E_z}{E_0}\right)$, of a truncated-Weierstrass waveform with $D_0 = 1.7$ from a modified Cantor set with $a_n = 250\lambda$.

APPENDIX E

2D DIFFRACTION - CANTOR DUST

After focusing on a 1D aperture in the main body of the thesis it is natural to be curious about how to develop the analysis for a 2D aperture. A few examples of 2D fractal apertures have been studied in the past, mostly focusing on the Sierpinki Triangle and Von Koch curve, however in this Appendix the 2D generalization of the Cantor set will be studied – the Cantor dust. Looking at these diffraction patterns is an attractive proposition and the results that come from studying the intensity can be visually appealing.

E.1 Mathematical background

The 2DRS formulation is [28]

$$E_z(x,y,z) = -\frac{1}{2\pi}\int_{-\infty}^{\infty}\int_{-\infty}^{\infty} dx'dz' E_z(x',0,z')\frac{\partial}{\partial y}\frac{\exp(ikR)}{R}\bigg|_{y=0}, \tag{E.1}$$

and therefore the 2DRS formulation for the Cantor dust is

$$E_z(x,y,z) = -\frac{1}{2\pi}\sum_{j=0}^{2^{2n}-1}\int_{b_-(\Xi_j)}^{b_+(\Xi_j)}\int_{a_-(\Xi_j)}^{a_+(\Xi_j)} dx'dz' E_z(x',0,z')\frac{\partial}{\partial y}\frac{\exp(ikR)}{R}\bigg|_{y=0}, \tag{E.2}$$

where $R = \sqrt{(x-x')^2+(z-z')^2+y^2}$, $a_\pm(\Xi_j)$ is the edge of the slit on the x axis and $b_\pm(\Xi_j)$ is the edge of the slit on the z axis.

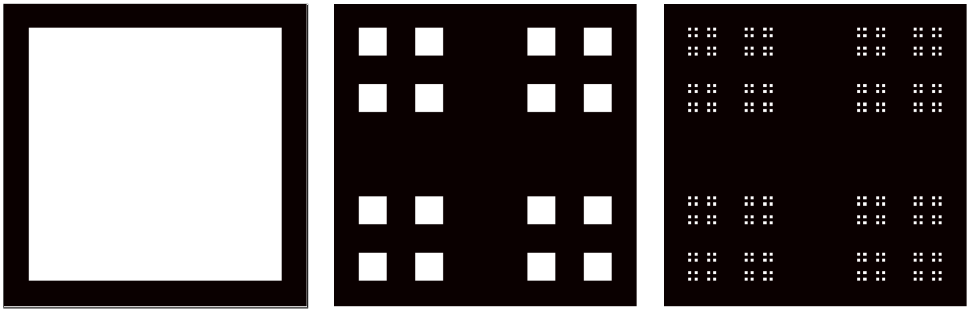

Figure E.1: The zeroth (*left*), second (*middle*) and fourth (*right*) pre-fractal level of the Cantor dust. The black is the screen (opaque region) and white is the aperture (transparent region)

For each iteration of the pre-fractal, the half width of the individual square apertures is kept at 250λ and the overall size of the total slit grows accordingly. There is an inherent four-fold symmetry in the Cantor-dust aperture which can hence be exploited – calculating merely the diffraction pattern from the top-right (or any) quarter of dust and mirroring the result saves a lot of computation time, which is wonderful. The distances are kept in terms of L_{char}, where $L_{char} = (\frac{k(2a_n)^4}{8})^{\frac{1}{3}}$ (from Eq. 1.39).

E.2 Results

This Appendix features many figures produced looking at the diffraction of a plane wave from a pre-fractal Cantor dust. The computations are for $n = 1, 2$ and 3, $y = 10L_{char}$, $15L_{char}$, $20L_{char}$, $25L_{char}$, $50L_{char}$, $75L_{char}$,$100L_{char}$ and $200L_{char}$. Numerical calculations are performed on a grid of 1024x1024 points, with the 2D integrals evaluated using the `integral2` routine in MATLAB.

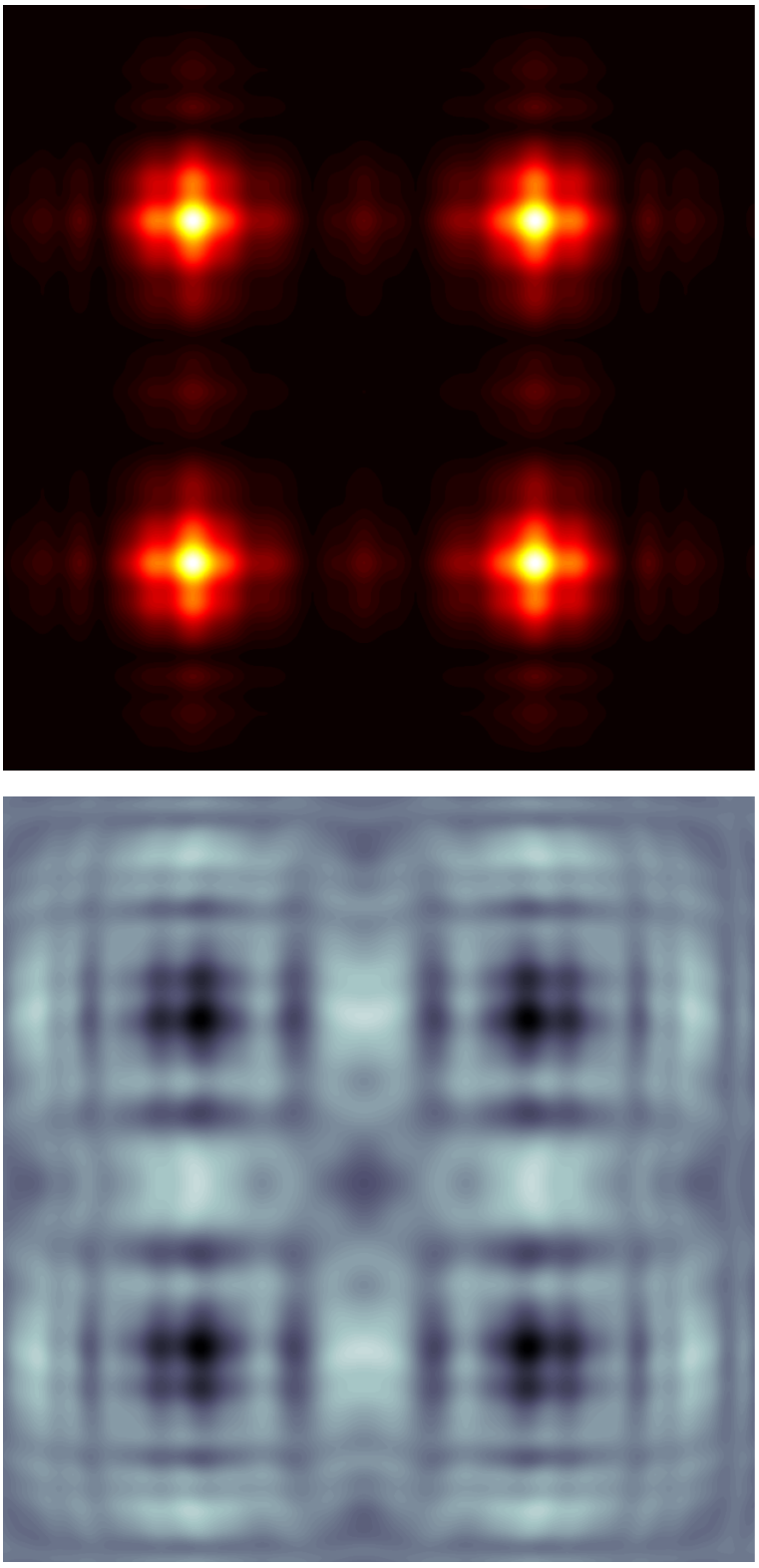

Figure E.2: Diffraction from pre-fractal level $n = 1$ of the Cantor dust with $y = 10L_{char}$. $2\Re e\left(\frac{E_z}{E_0}\right)$ *(left)* and $\left|\frac{E_z}{E_0}\right|^2$ *(right)*.

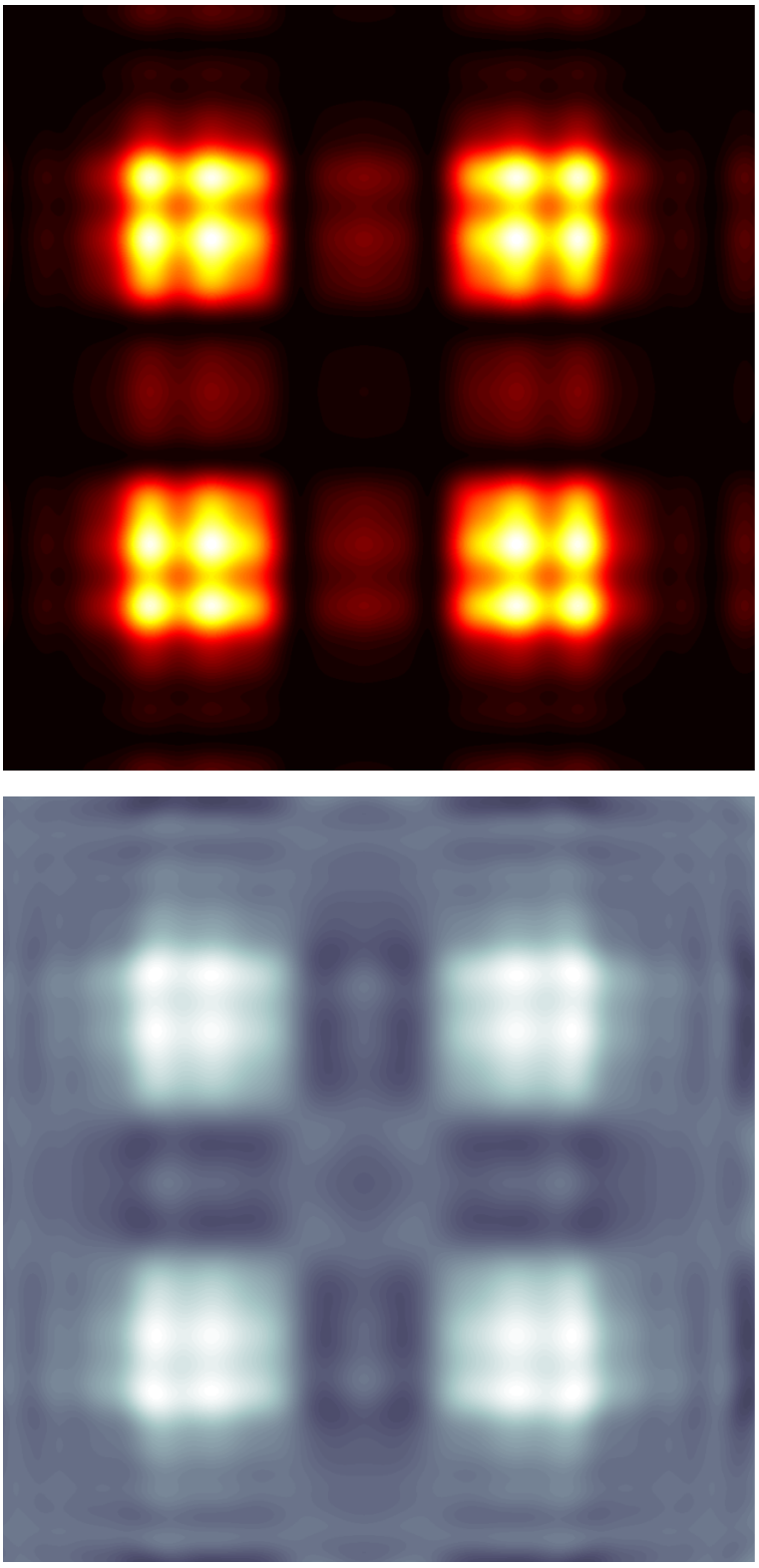

Figure E.3: Diffraction from pre-fractal level $n = 1$ of the Cantor dust with $y = 15L_{char}$. $2\Re e\left(\frac{E_z}{E_0}\right)$ *(left)* and $\left|\frac{E_z}{E_0}\right|^2$ *(right)*.

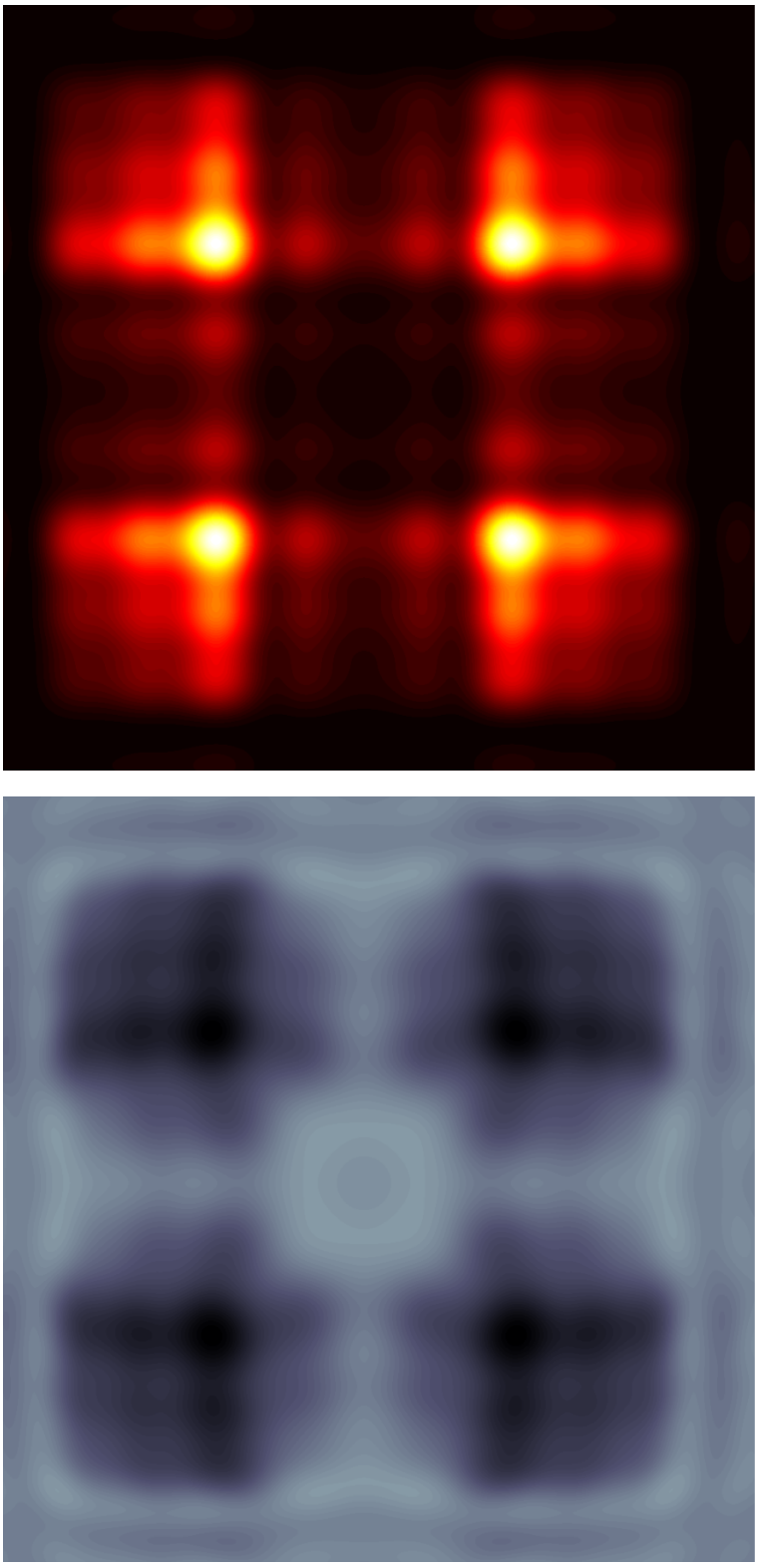

Figure E.4: Diffraction from pre-fractal level $n = 1$ of the Cantor dust with $y = 20L_{char}$. $2\Re e\left(\frac{E_z}{E_0}\right)$ *(left)* and $\left|\frac{E_z}{E_0}\right|^2$ *(right)*.

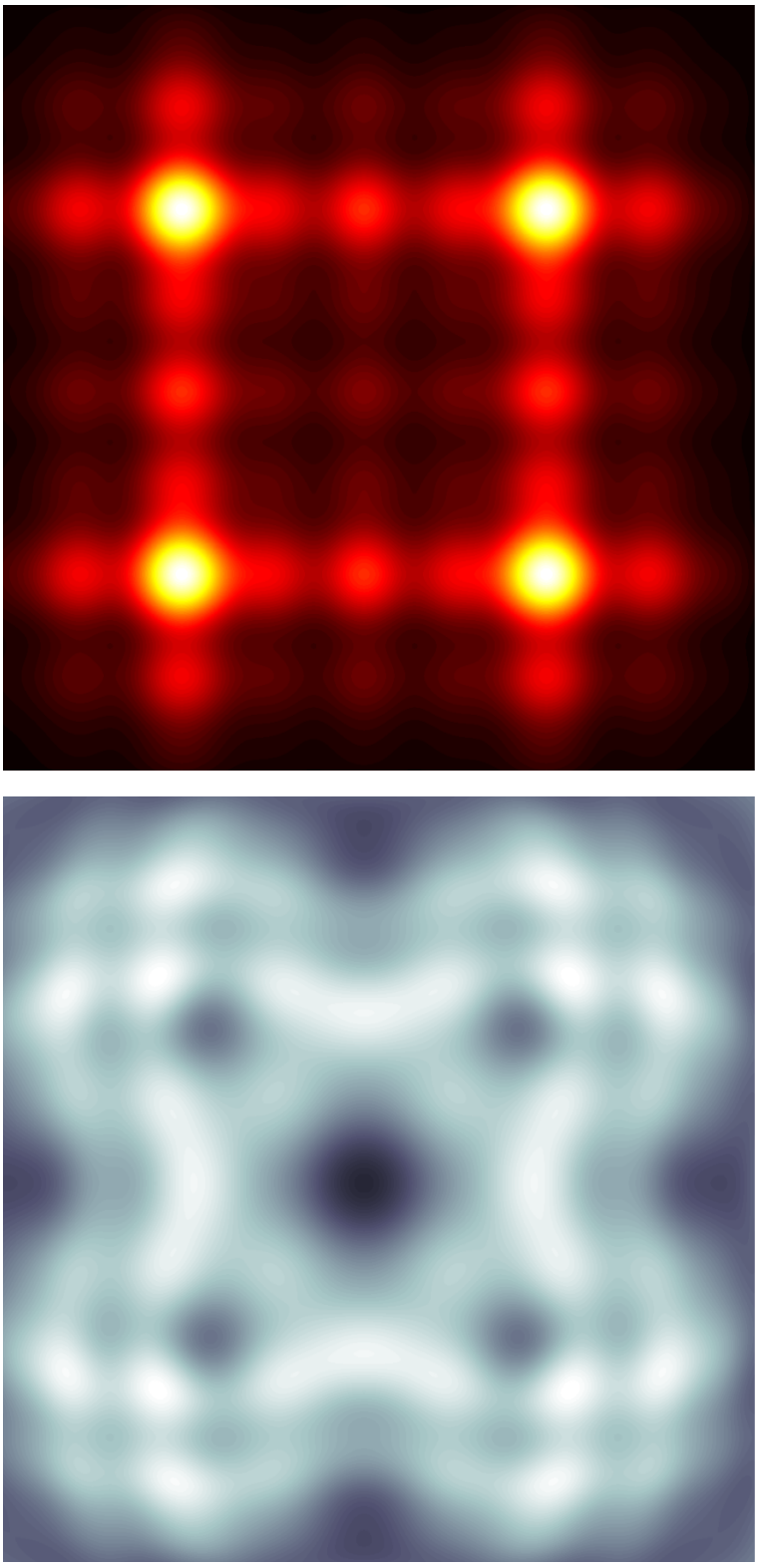

Figure E.5: Diffraction from pre-fractal level $n = 1$ of the Cantor dust with $y = 25L_{char}$. $2\Re e\left(\frac{E_z}{E_0}\right)$ *(left)* and $\left|\frac{E_z}{E_0}\right|^2$ *(right)*.

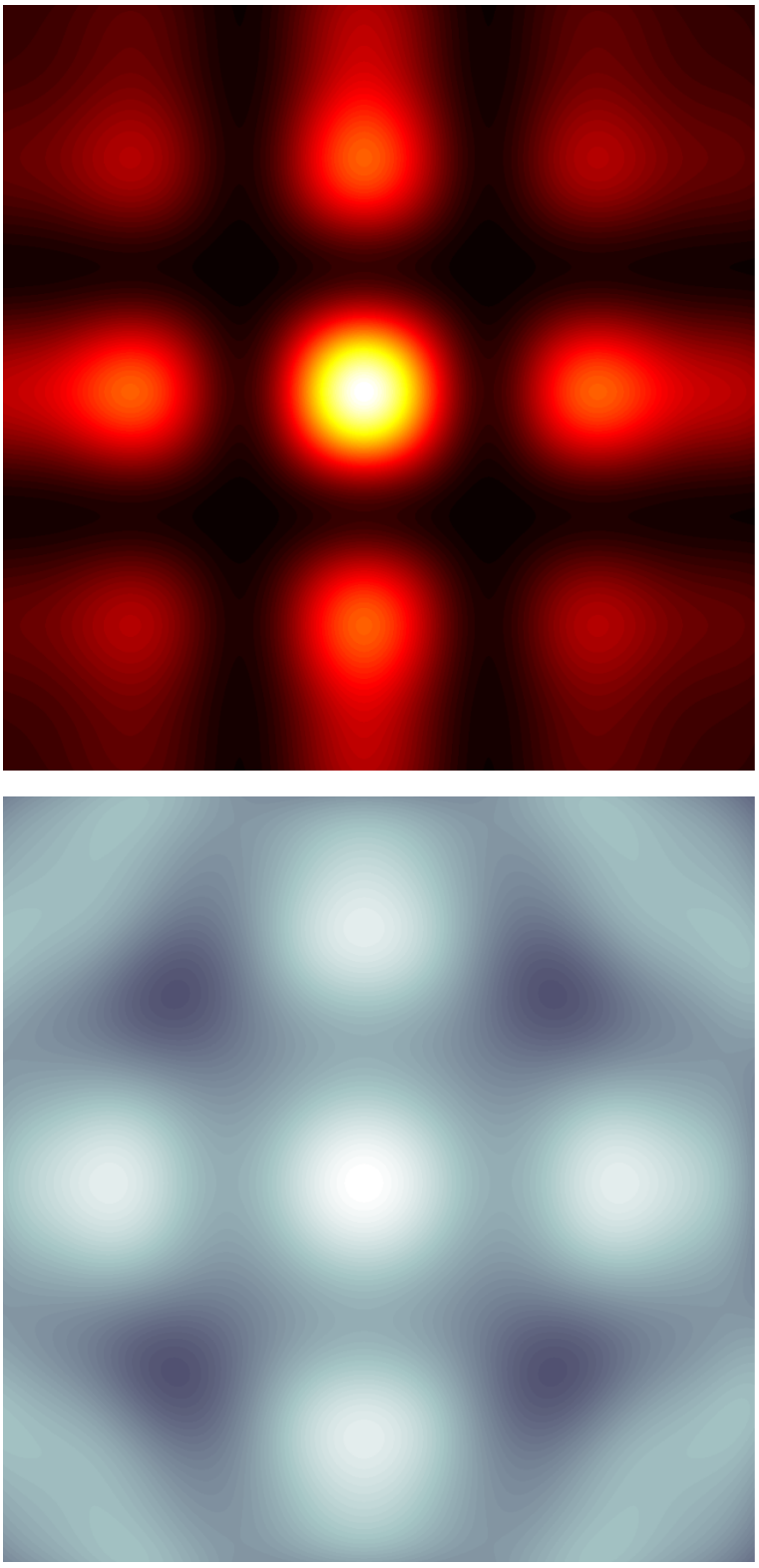

Figure E.6: Diffraction from pre-fractal level $n = 1$ of the Cantor dust with $y = 50L_{char}$. $2\Re e\left(\frac{E_z}{E_0}\right)$ *(left)* and $\left|\frac{E_z}{E_0}\right|^2$ *(right)*.

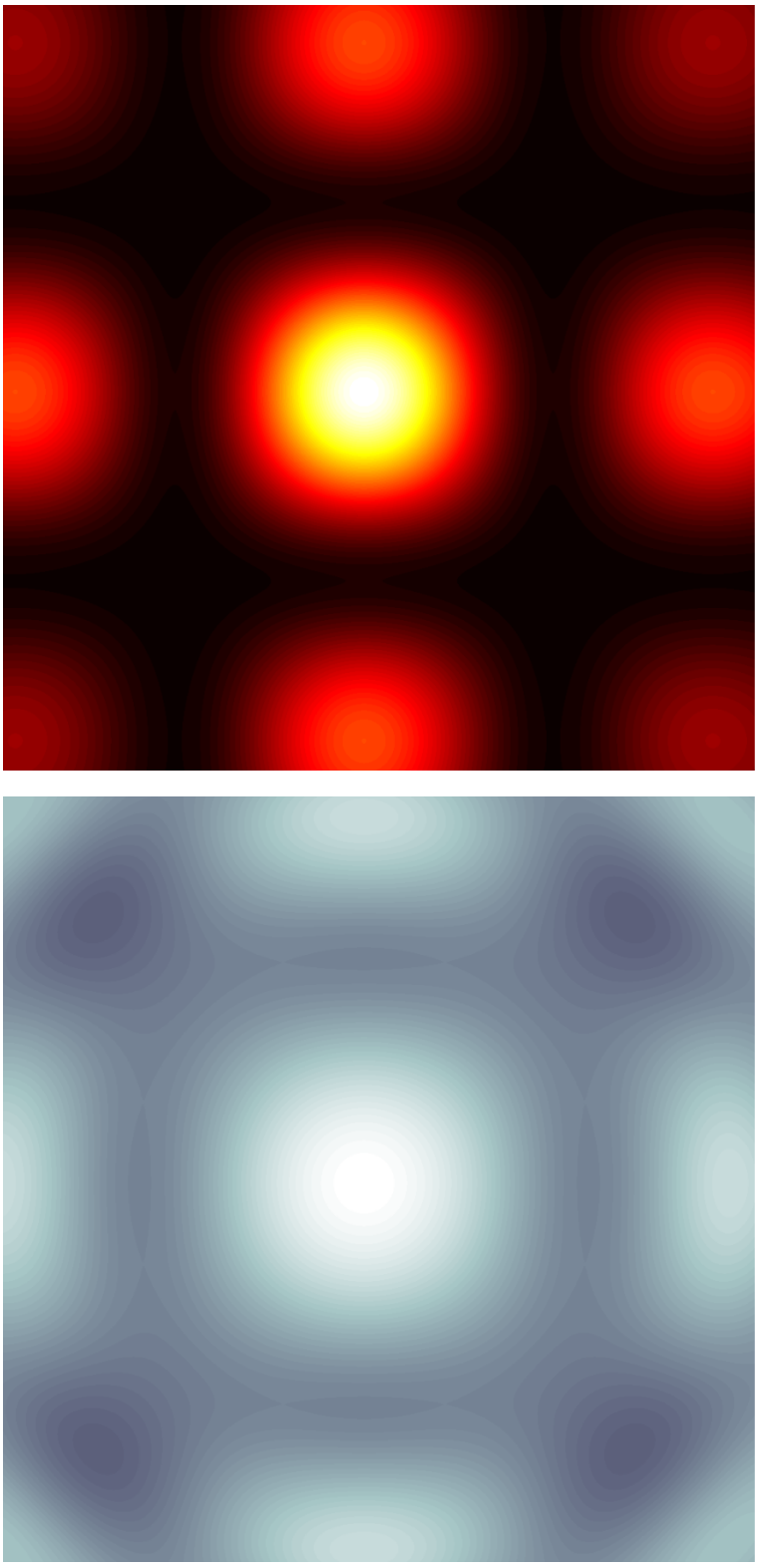

Figure E.7: Diffraction from pre-fractal level $n = 1$ of the Cantor dust with $y = 75L_{char}$. $2\Re e\left(\frac{E_z}{E_0}\right)$ *(left)* and $\left|\frac{E_z}{E_0}\right|^2$ *(right)*.

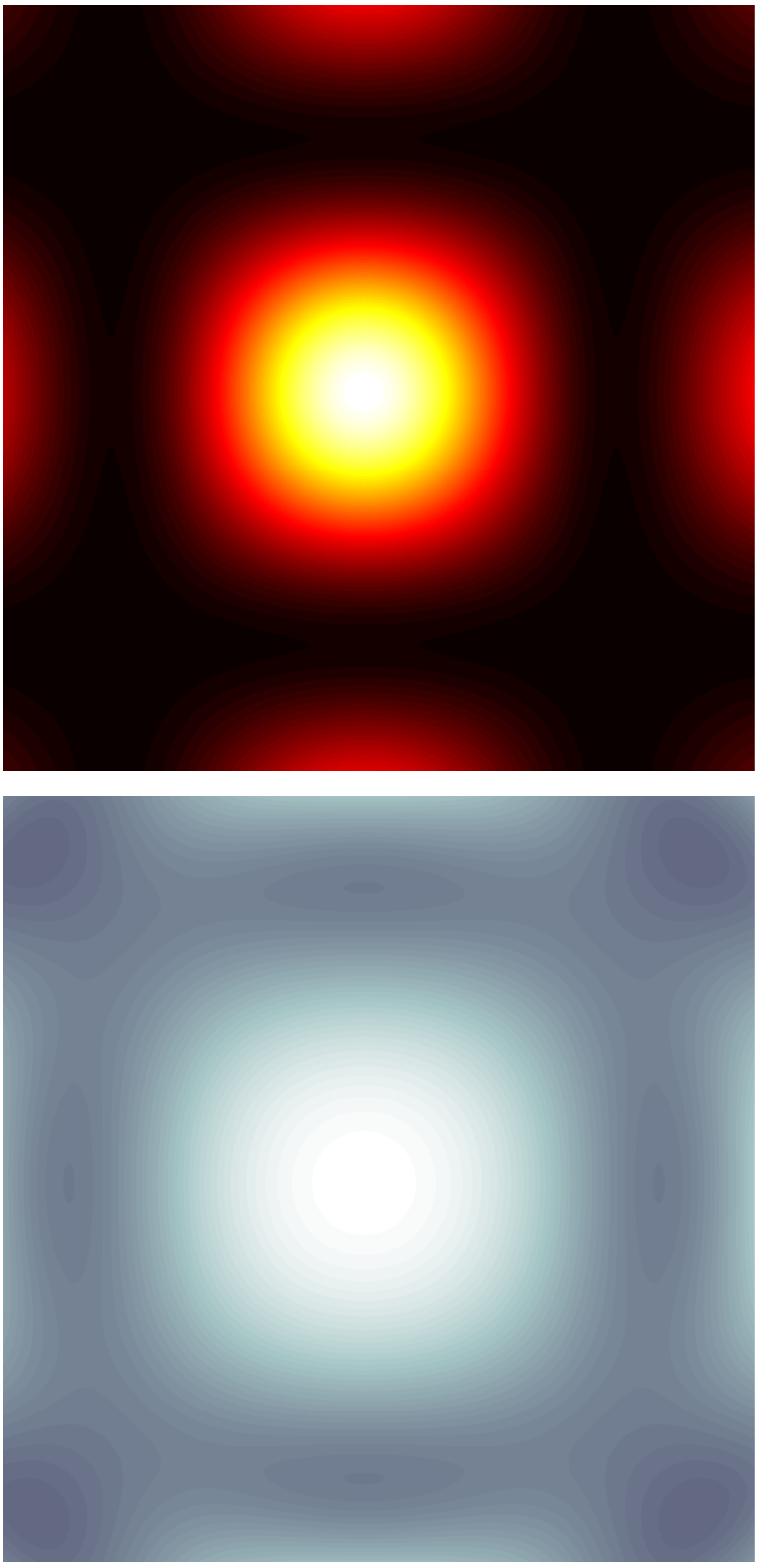

Figure E.8: Diffraction from pre-fractal level $n = 1$ of the Cantor dust with $y = 100L_{char}$. $2\Re e\left(\frac{E_z}{E_0}\right)$ *(left)* and $\left|\frac{E_z}{E_0}\right|^2$ *(right)*.

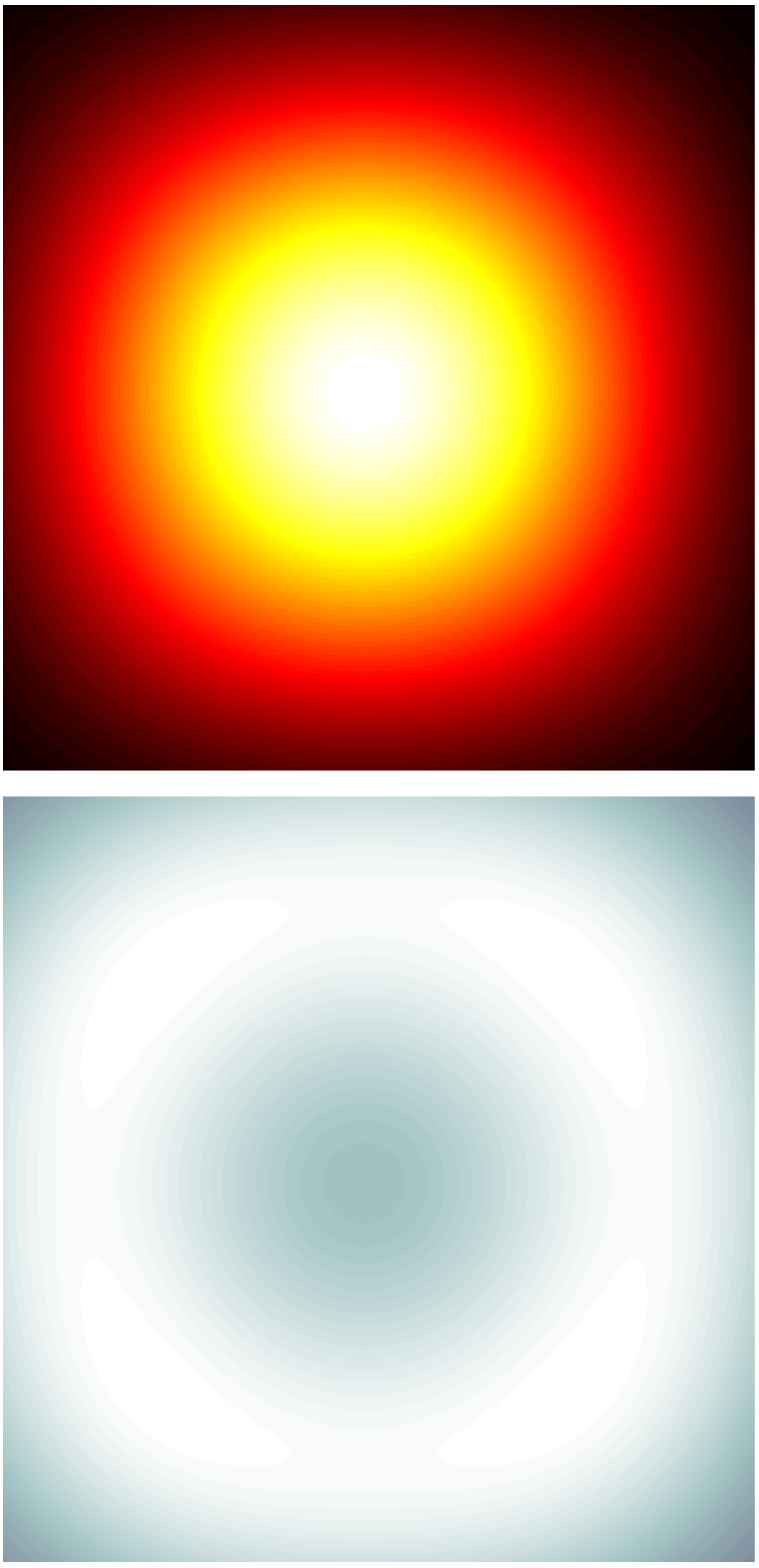

Figure E.9: Diffraction from pre-fractal level $n = 1$ of the Cantor dust with $y = 200L_{char}$. $2\Re e\left(\frac{E_z}{E_0}\right)$ *(left)* and $\left|\frac{E_z}{E_0}\right|^2$ *(right)*.

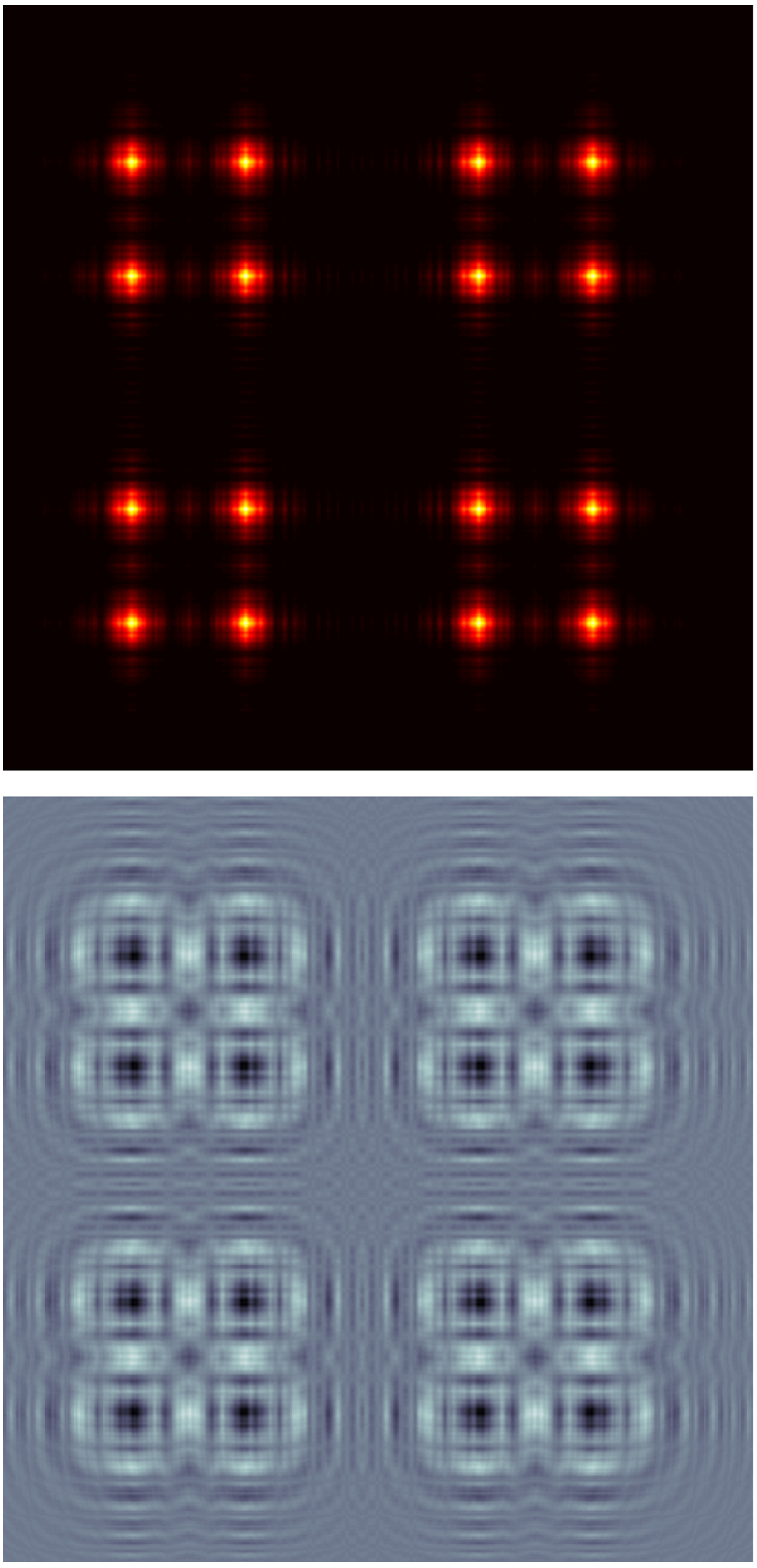

Figure E.10: Diffraction from pre-fractal level $n = 2$ of the Cantor dust with $y = 10L_{char}$. $2\Re e\left(\frac{E_z}{E_0}\right)$ *(left)* and $\left|\frac{E_z}{E_0}\right|^2$ *(right)*.

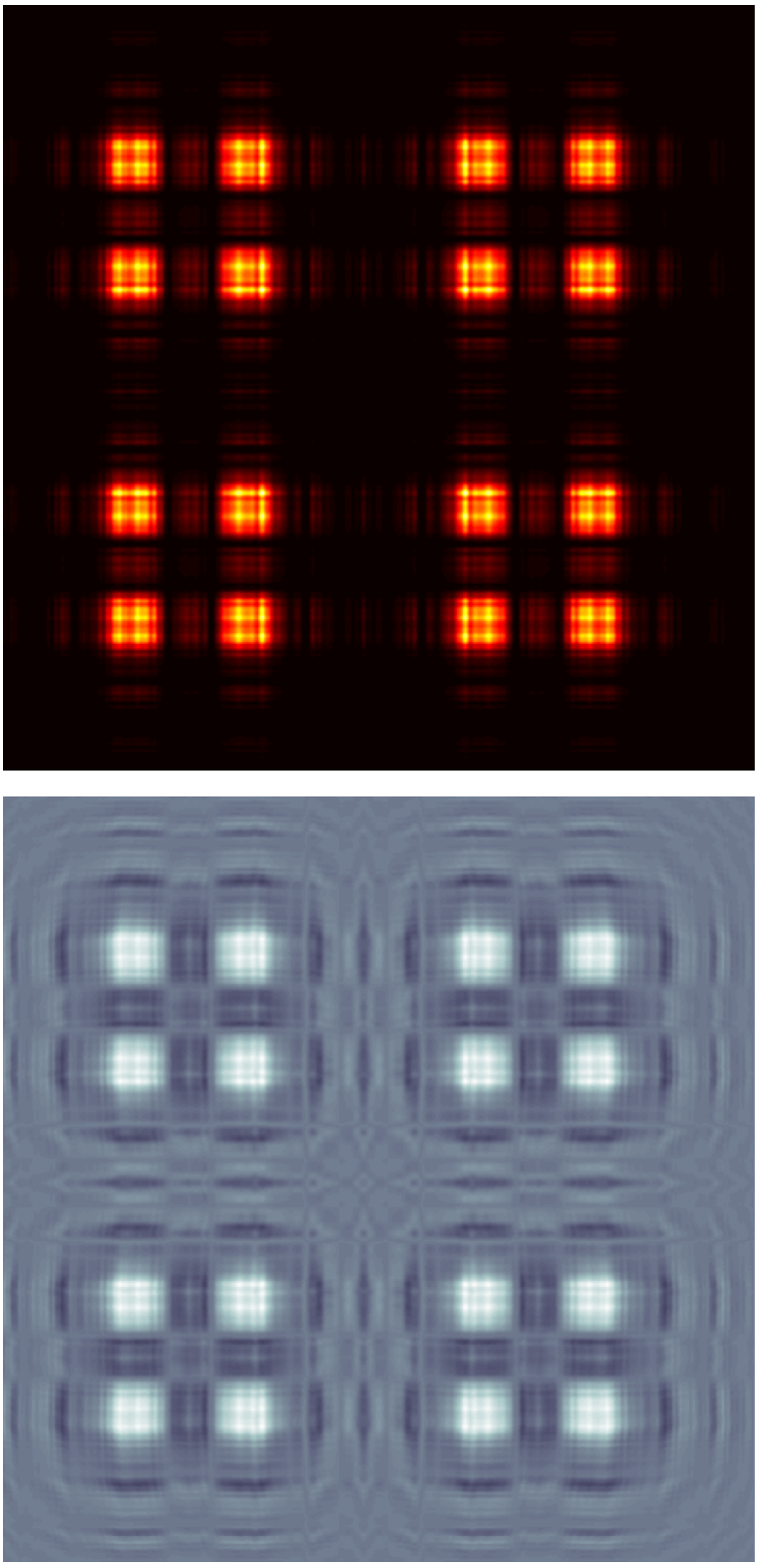

Figure E.11: Diffraction from pre-fractal level $n = 2$ of the Cantor dust with $y = 15L_{char}$. $2\Re e\left(\frac{E_z}{E_0}\right)$ *(left)* and $\left|\frac{E_z}{E_0}\right|^2$ *(right)*.

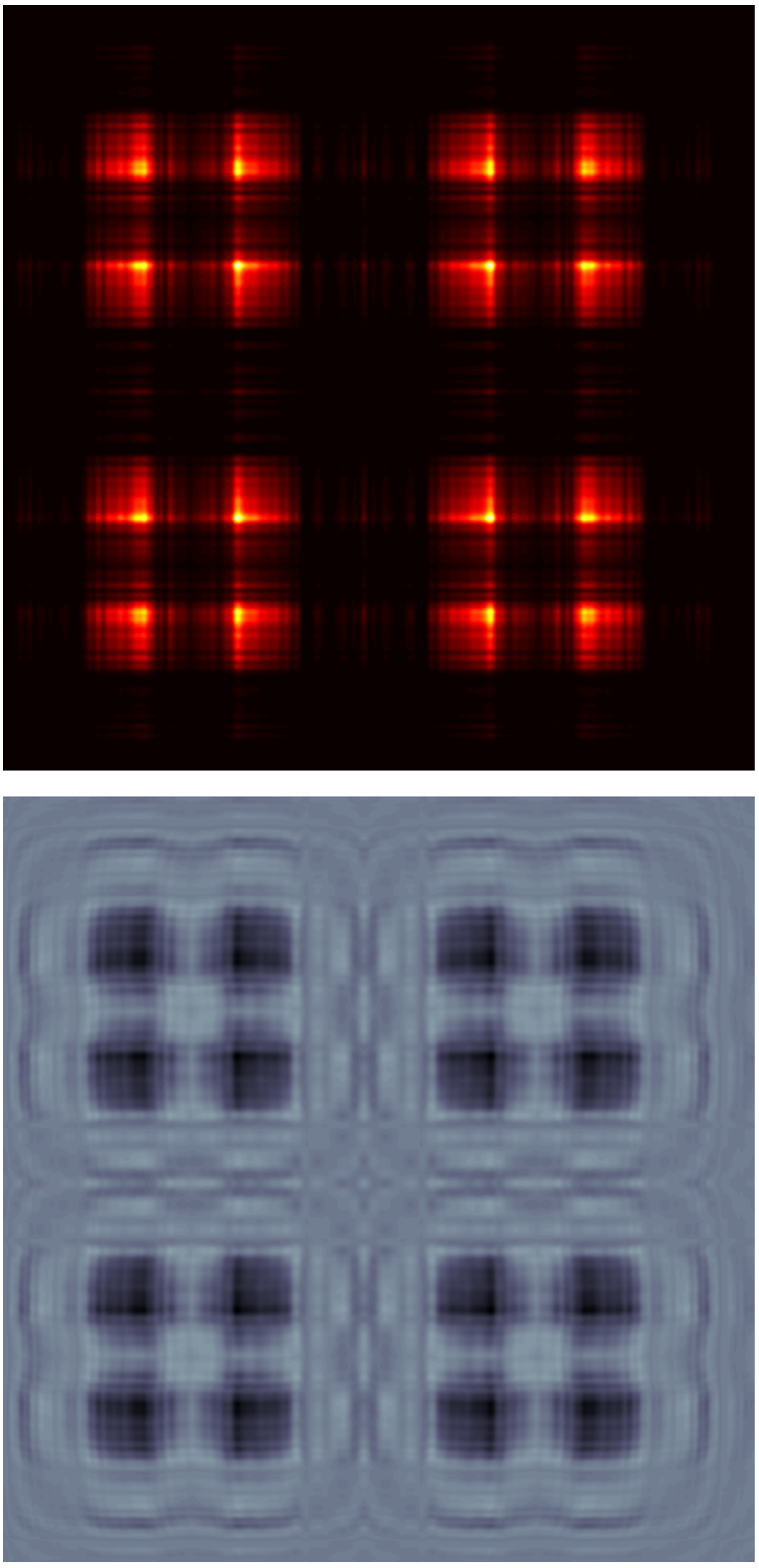

Figure E.12: Diffraction from pre-fractal level $n = 2$ of the Cantor dust with $y = 20L_{char}$. $2\Re e\left(\frac{E_z}{E_0}\right)$ *(left)* and $\left|\frac{E_z}{E_0}\right|^2$ *(right)*.

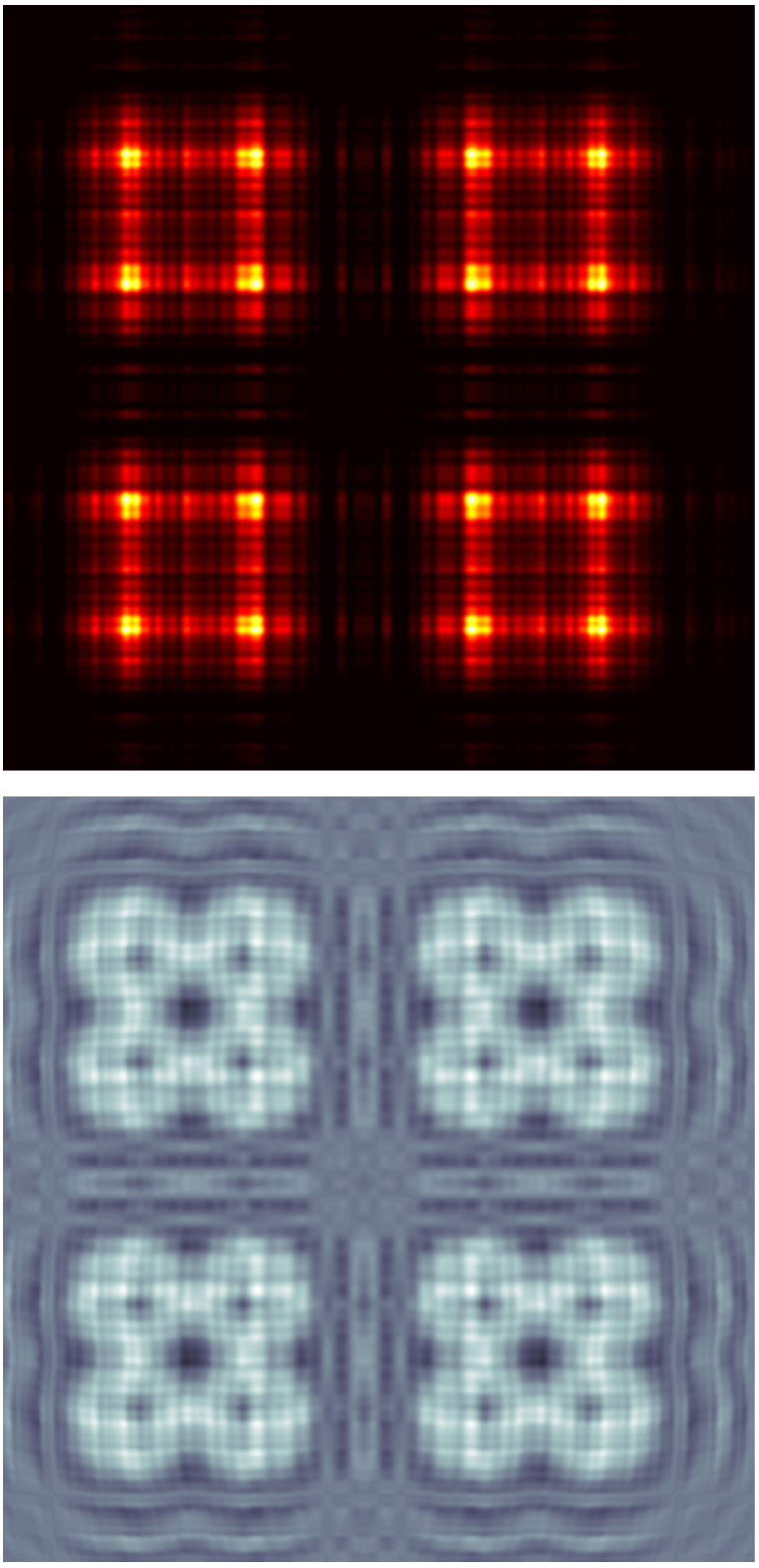

Figure E.13: Diffraction from pre-fractal level $n = 2$ of the Cantor dust with $y = 25L_{char}$. $2\Re e\left(\frac{E_z}{E_0}\right)$ *(left)* and $\left|\frac{E_z}{E_0}\right|^2$ *(right)*.

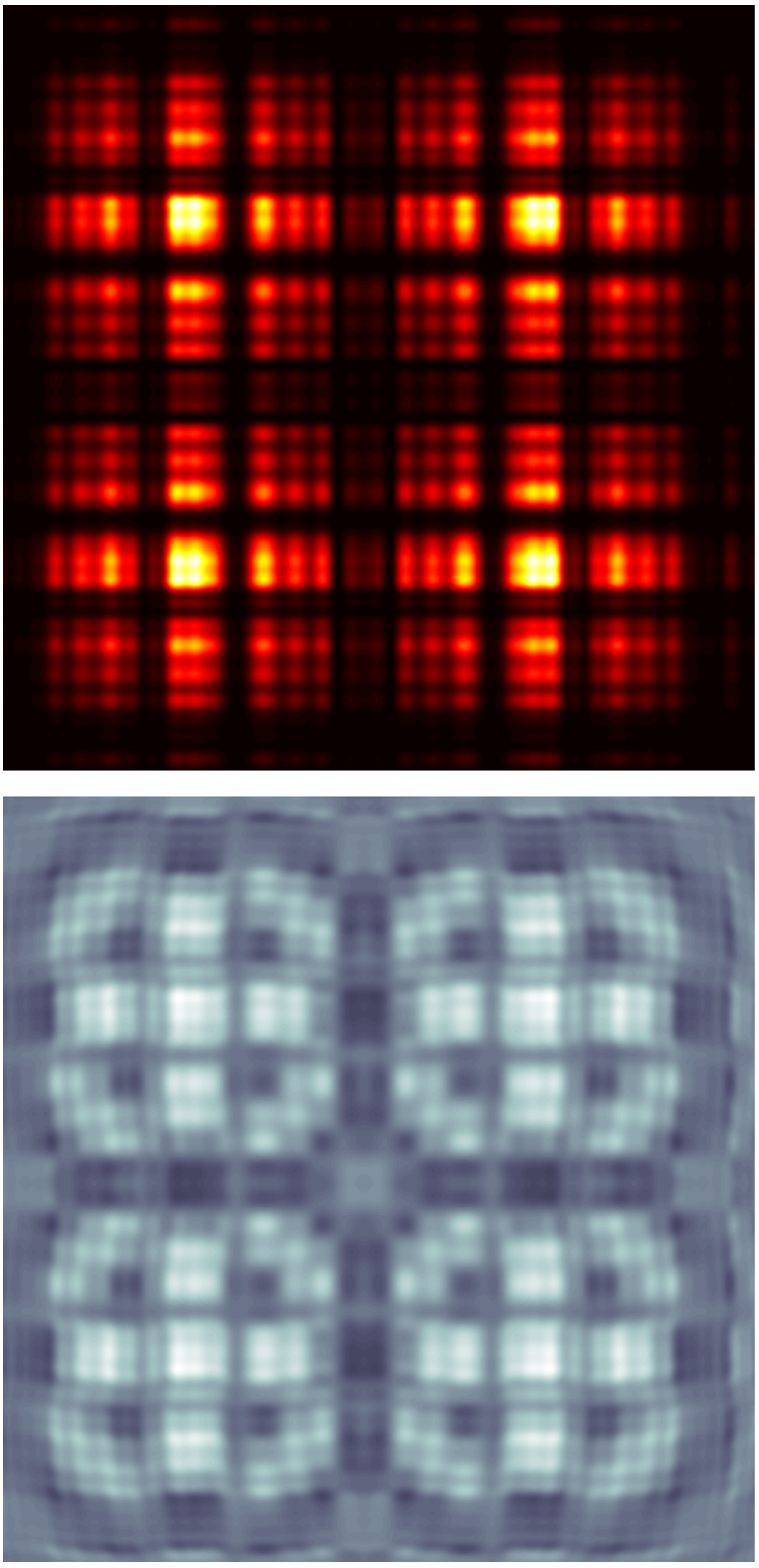

Figure E.14: Diffraction from pre-fractal level $n = 2$ of the Cantor dust with $y = 50L_{char}$. $2\Re e\left(\frac{E_z}{E_0}\right)$ *(left)* and $\left|\frac{E_z}{E_0}\right|^2$ *(right)*.

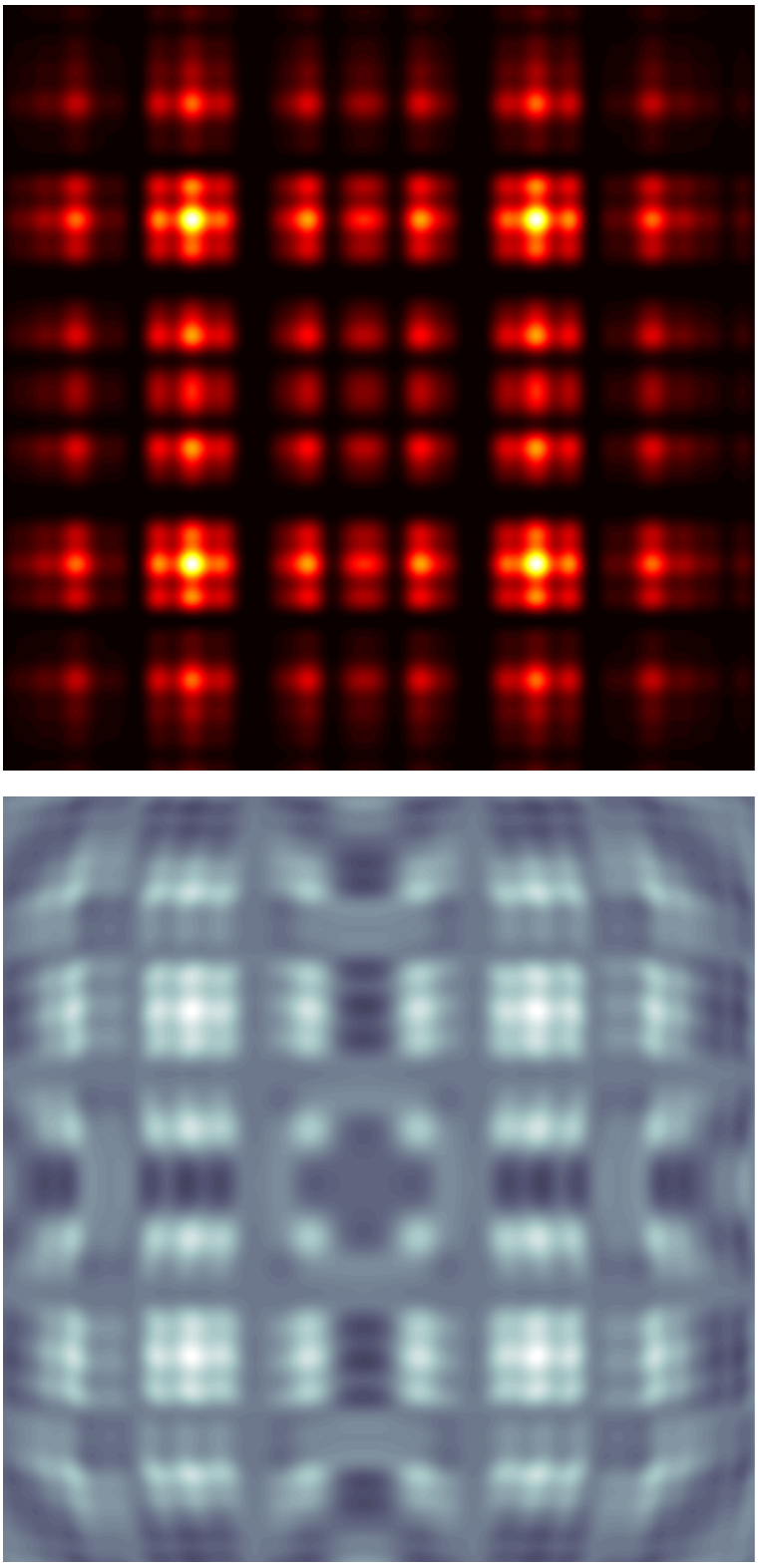

Figure E.15: Diffraction from pre-fractal level $n = 2$ of the Cantor dust with $y = 75L_{char}$. $2\Re e\left(\frac{E_z}{E_0}\right)$ *(left)* and $\left|\frac{E_z}{E_0}\right|^2$ *(right)*.

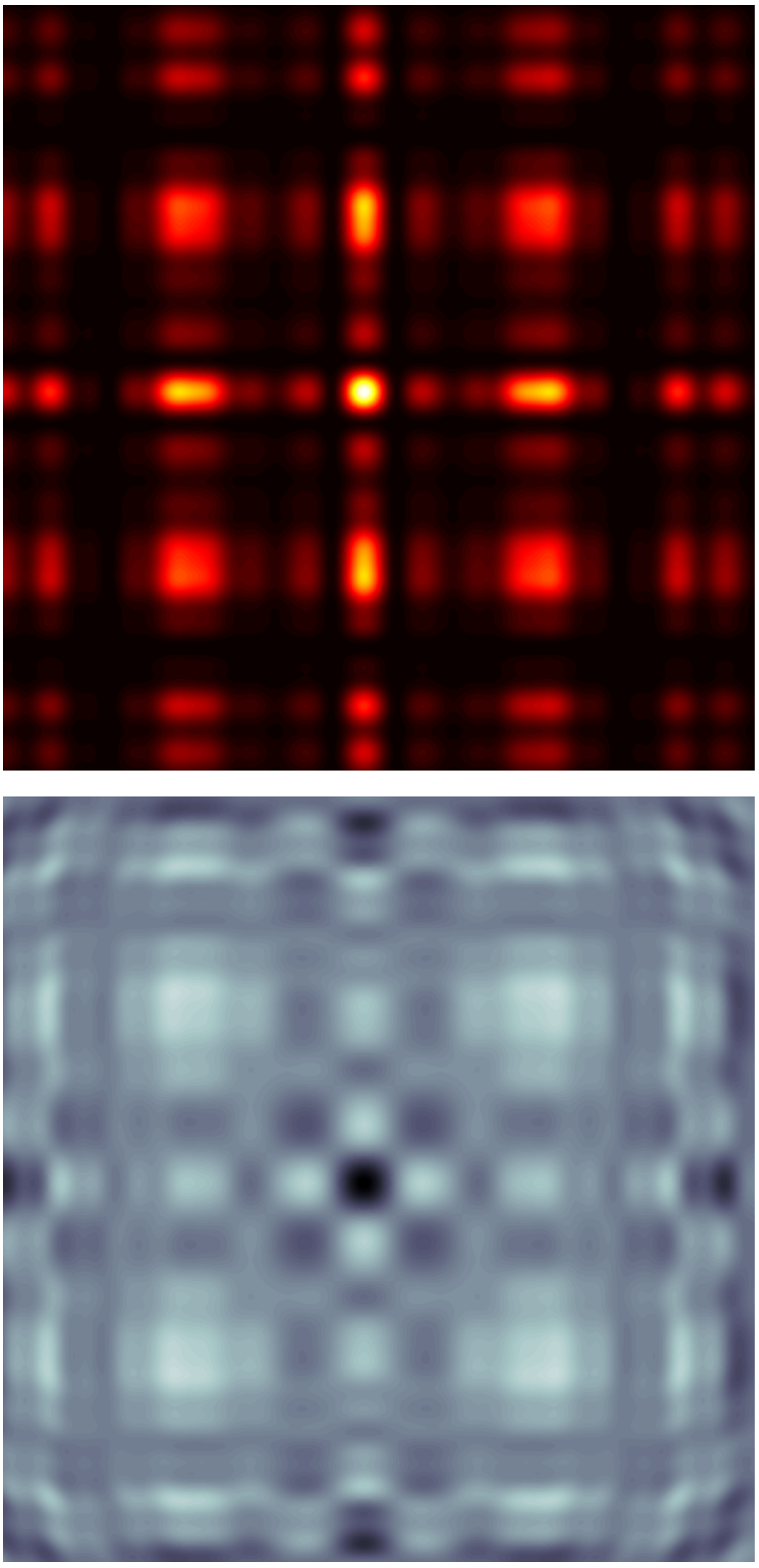

Figure E.16: Diffraction from pre-fractal level $n = 2$ of the Cantor dust with $y = 100L_{char}$. $2\Re e\left(\frac{E_z}{E_0}\right)$ *(left)* and $\left|\frac{E_z}{E_0}\right|^2$ *(right)*.

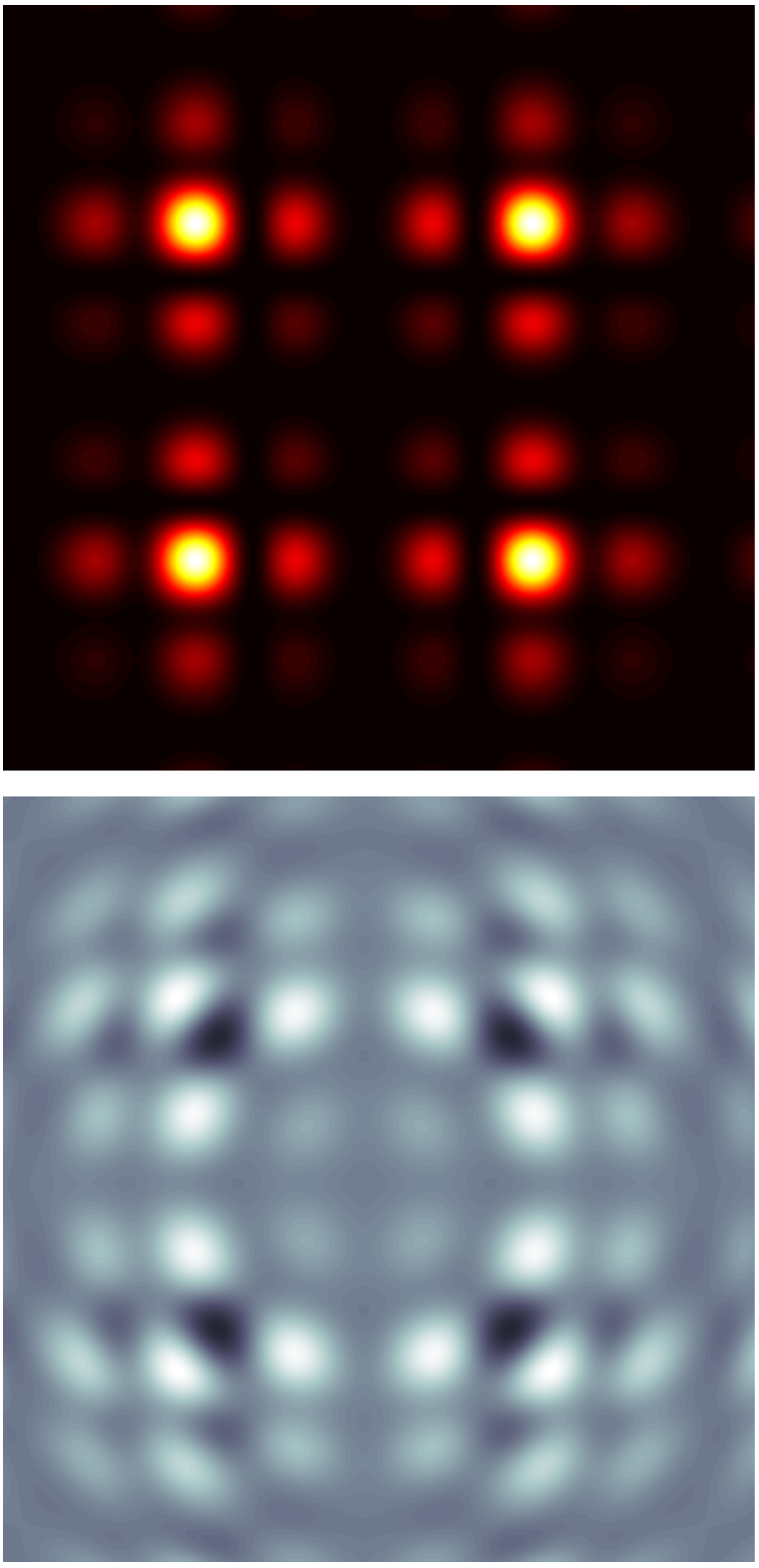

Figure E.17: Diffraction from pre-fractal level $n = 2$ of the Cantor dust with $y = 200L_{char}$. $2\Re e\left(\frac{E_z}{E_0}\right)$ *(left)* and $\left|\frac{E_z}{E_0}\right|^2$ *(right)*.

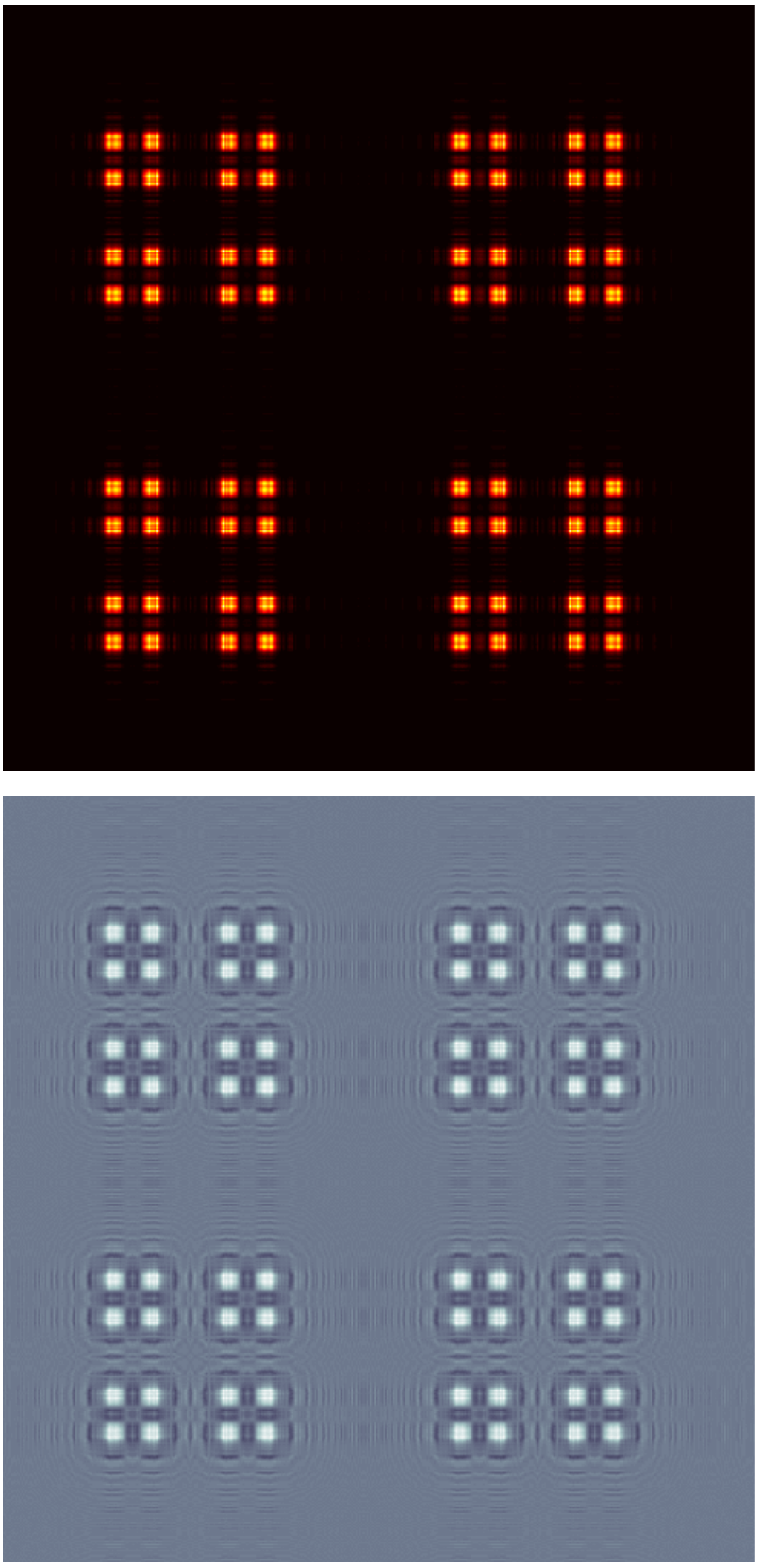

Figure E.18: Diffraction from pre-fractal level $n = 3$ of the Cantor dust with $y = 15L_{char}$. $2\Re e\left(\frac{E_z}{E_0}\right)$ *(left)* and $\left|\frac{E_z}{E_0}\right|^2$ *(right)*.

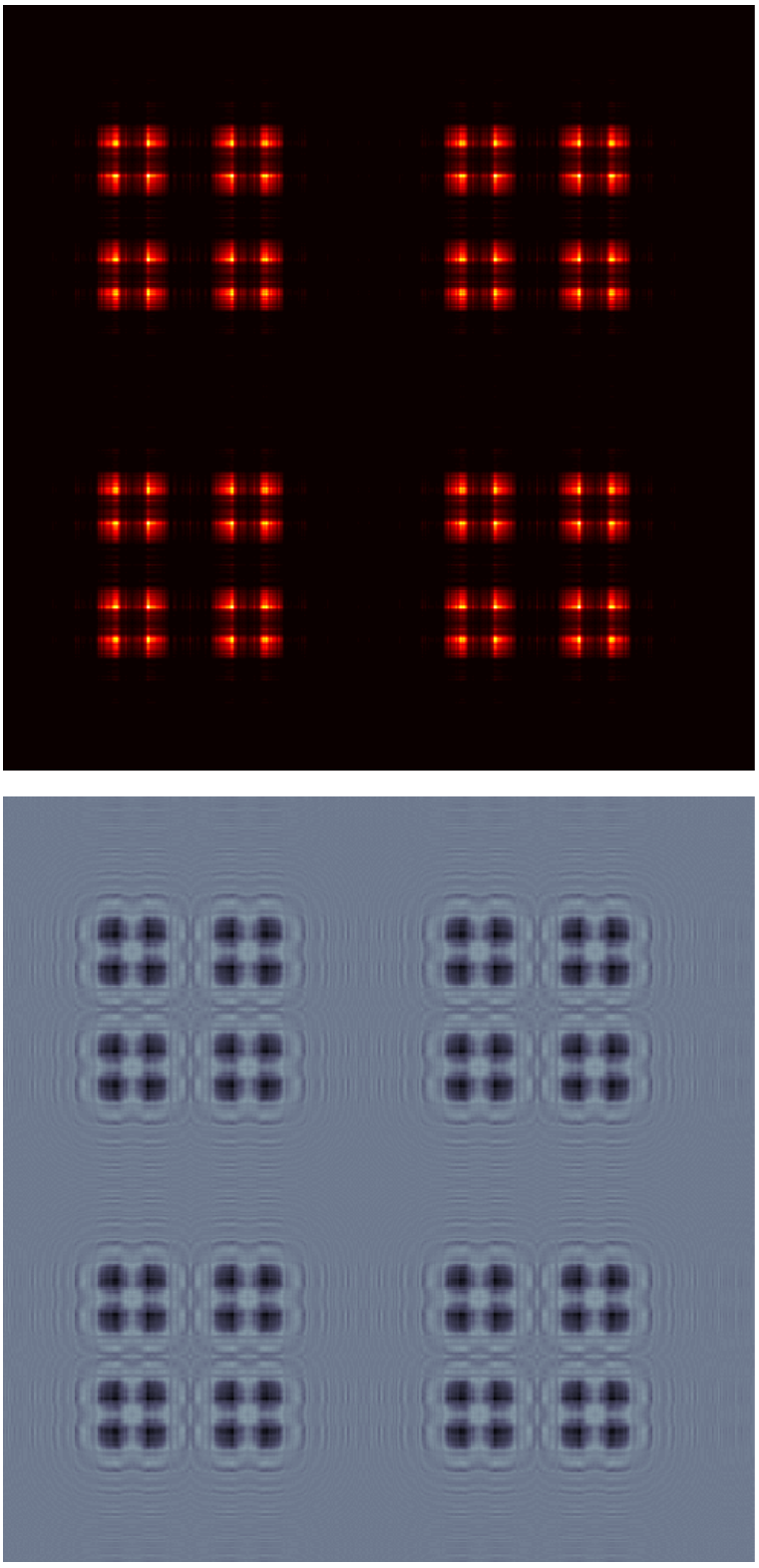

Figure E.19: Diffraction from pre-fractal level $n = 3$ of the Cantor dust with $y = 20L_{char}$. $2\Re e\left(\frac{E_z}{E_0}\right)$ *(left)* and $\left|\frac{E_z}{E_0}\right|^2$ *(right)*.

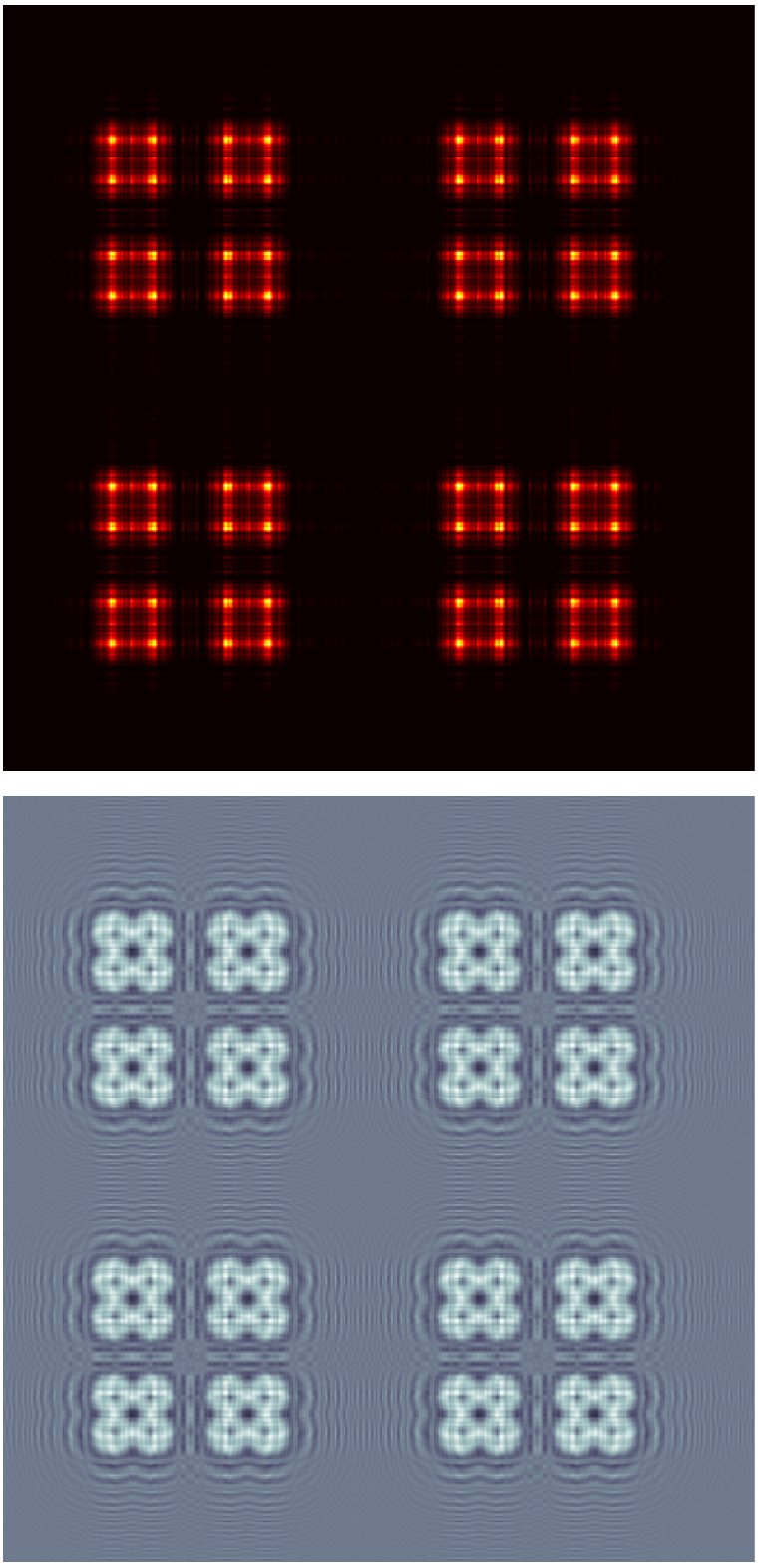

Figure E.20: Diffraction from pre-fractal level $n = 3$ of the Cantor dust with $y = 25L_{char}$. $2\Re e\left(\frac{E_z}{E_0}\right)$ *(left)* and $\left|\frac{E_z}{E_0}\right|^2$ *(right)*.

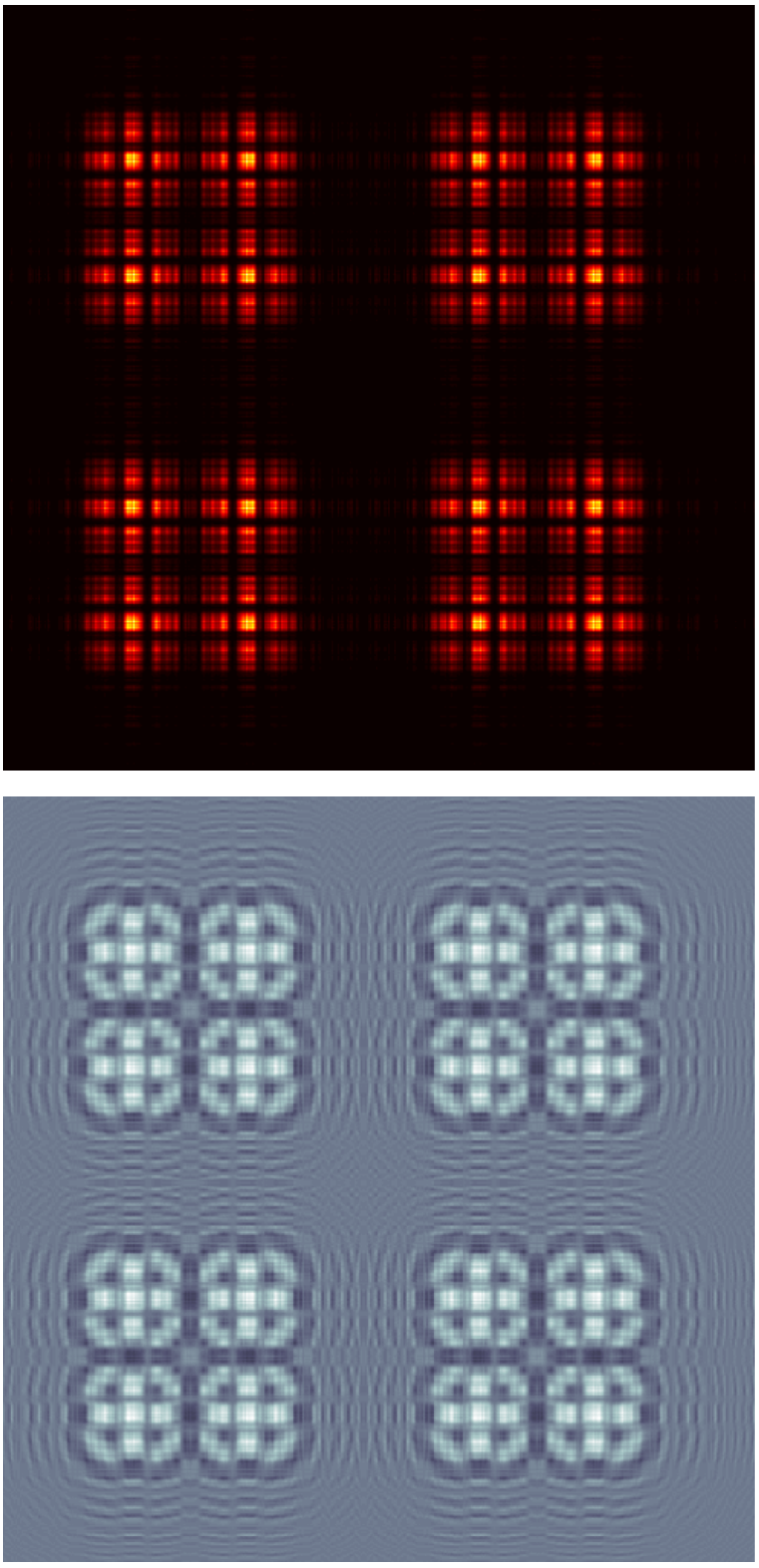

Figure E.21: Diffraction from pre-fractal level $n = 3$ of the Cantor dust with $y = 50L_{char}$. $2\Re e\left(\frac{E_z}{E_0}\right)$ *(left)* and $\left|\frac{E_z}{E_0}\right|^2$ *(right)*.

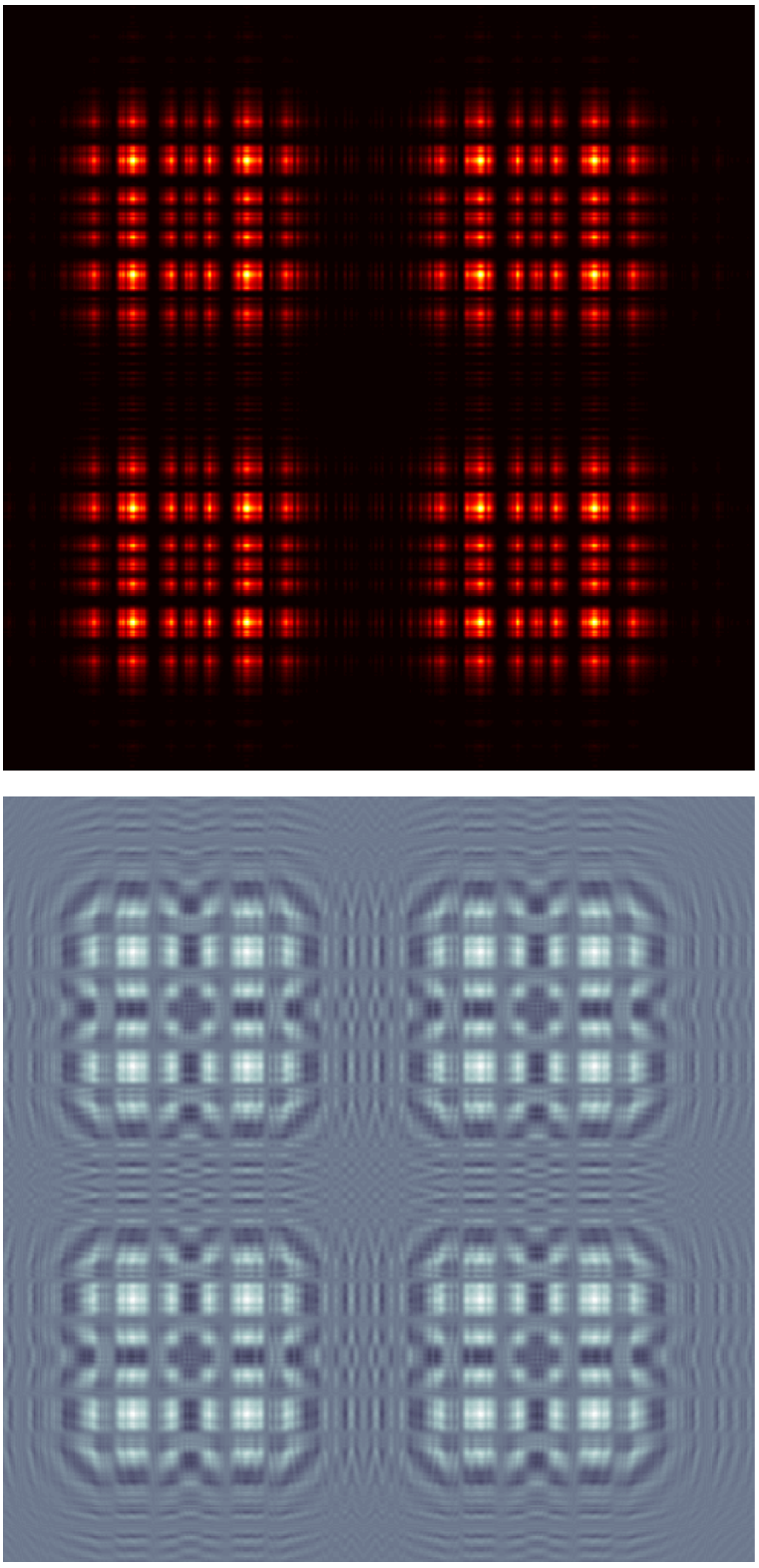

Figure E.22: Diffraction from pre-fractal level $n = 3$ of the Cantor dust with $y = 75L_{char}$. $2\Re e\left(\frac{E_z}{E_0}\right)$ *(left)* and $\left|\frac{E_z}{E_0}\right|^2$ *(right)*.

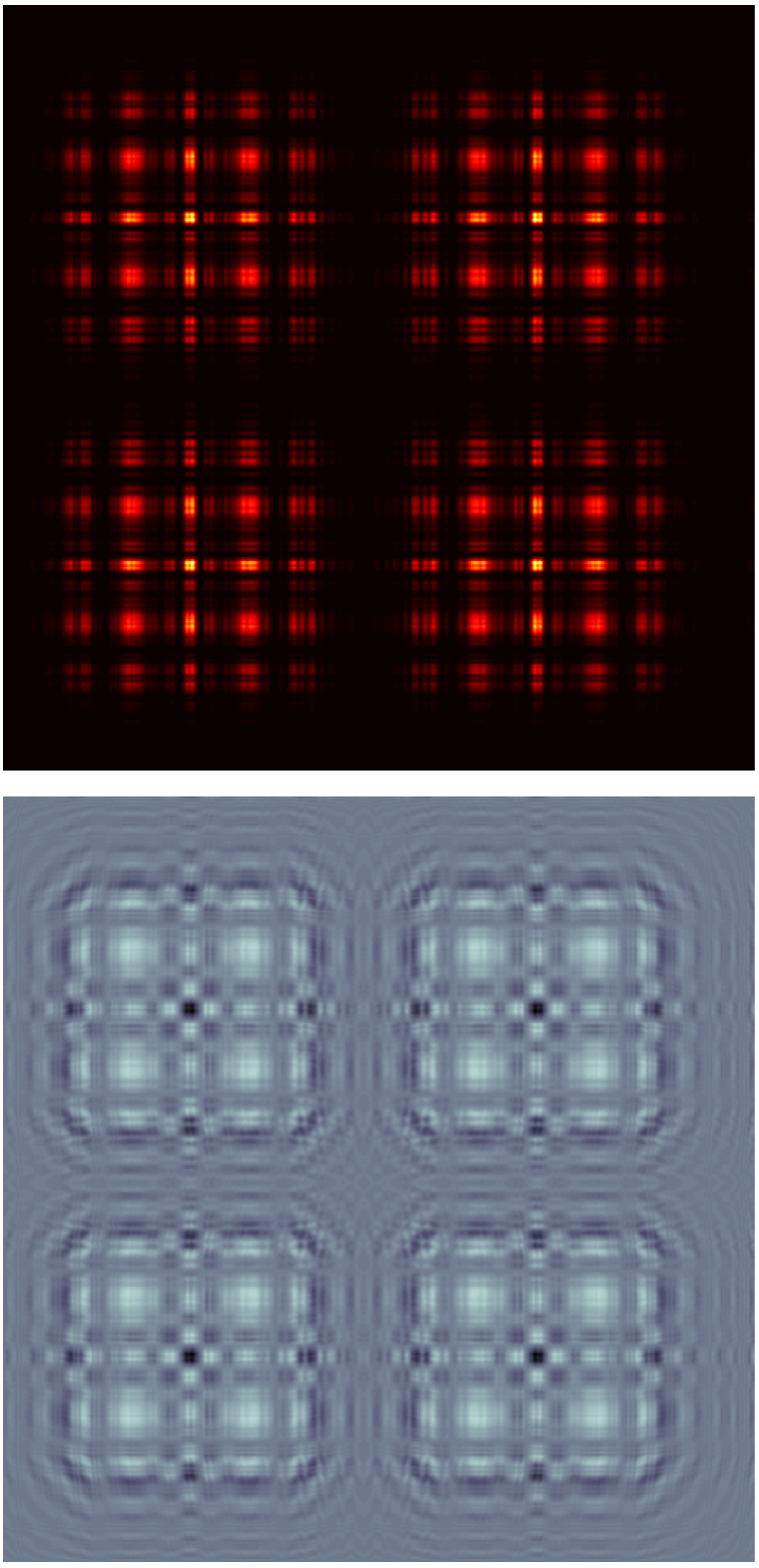

Figure E.23: Diffraction from pre-fractal level $n = 3$ of the Cantor dust with $y = 100L_{char}$. $2\Re e\left(\frac{E_z}{E_0}\right)$ *(left)* and $\left|\frac{E_z}{E_0}\right|^2$ *(right)*.

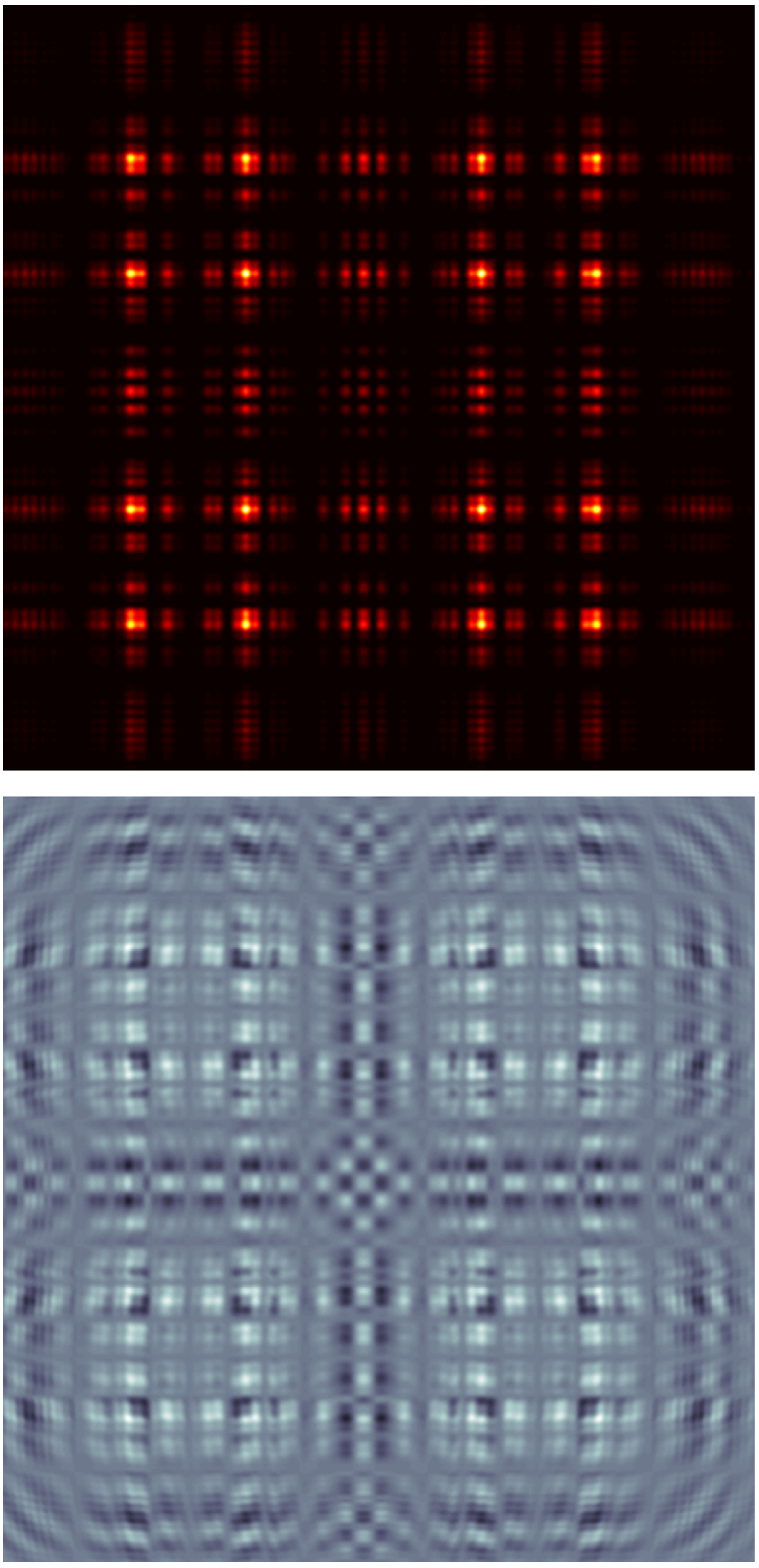

Figure E.24: Diffraction from pre-fractal level $n = 3$ of the Cantor dust with $y = 200L_{char}$. $2\Re e\left(\frac{E_z}{E_0}\right)$ *(left)* and $\left|\frac{E_z}{E_0}\right|^2$ *(right)*.

BIBLIOGRAPHY

[1] A. Malinverno, "A simple method to estimate the fractal dimension of a self affine series," *Geophysical Research Letters*, vol. 17, no. 11, pp. 1953–1956, 1990.

[2] G. New and T. Albaho, "Spatial spectrum of intensity profiles diffracted by a slit," *Journal of Modern Optics*, vol. 50, no. 2, pp. 155–160, 2003.

[3] J. M. Christian, "On fresnel optics problems with fractal boundaries: apertures, screens, and unstable resonators." Wave propagation in complex domains, 2017.

[4] J. M. Christian, E. P. Woodroofe, and G. McDonald, "Diffraction of weierstrass scalar fractal waves by circular apertures: symmetry and patterns, complexity and dimension." WAVES 2015 - 12th International Conference on the Mathematical and Numerical Aspects of Wave Propagation, 2015.

[5] J. M. Christian and G. McDonald, "On the diffraction of monsters: Weierstrass and young, analysis and edge waves." European Optical Society Bi-Annual Meeting, 2016.

[6] A. E. Siegman, *Lasers*.
University Science Books, 1986.

[7] S. N. Chandler-Wilde and D. P. Hewett, "Well-posed pde and integral equation formulations for scattering by fractal screens," *SIAM J. Math. Analysis*, vol. 50, pp. 677–717, 2018.

[8] S. N. Chandler-Wilde, D. P. Hewett, and A. Moiola, "Sobolev spaces on non-lipschitz subsets of $\mathbb{R}^n$ with application to boundary integral equations on fractal screens," *Integral Equations and Operator Theory*, vol. 87, pp. 179–224, Feb 2017.

[9] B. Mandelbrot, *The Fractal Geometry of Nature*.
Einaudi paperbacks, 1997, 1982.

[10] K. Falconer, *Fractal Geometry: Mathematical Foundations and Applications*.
John Wiley & Sons, 2004.

[11] K. Weierstraß, *Über Continuirliche Functionen eines Reellen Arguments, die für keinen Werth des Letzteren einen Bestimmten Differentialquotienten Besitzen*, pp. 190–193.
Vieweg+Teubner Verlag, 1988.

[12] M. V. Berry and Z. V. Lewis, "On the Weierstrass-Mandelbrot fractal function," *Proceedings of the Royal Society of London. Series A, Mathematical and Physical Sciences*, vol. 370, no. 1743, pp. 459–484, 1980.

[13] B. R. Hunt, "The Hausdorff dimension of graphs of Weierstrass functions," *Proceedings of the American Mathematical Society*, vol. 126, no. 3, pp. 791–800, 1998.

[14] J. L. Kaplan, J. Mallet-Paret, and J. A. Yorke, "The Lyapunov dimension of a nowhere differentiable attracting torus," *Ergodic Theory and Dynamical Systems*, vol. 4, no. 2, pp. 261–281, 1984.

[15] F. Rezakhanlou, "The packing measure of the graphs and level sets of certain continuous functions," *Mathematical Proceedings of the Cambridge Philosophical Society*, vol. 104, no. 2, pp. 347–360, 1988.

[16] TruSoft International Inc., "Benoit."

[17] W. Seffens, "Order from chaos," *Science*, vol. 285, p. 1228, August 1999.

[18] J. R. Carr, "Statistical self-affinity, fractal dimension, and geologic interpretation," *Engineering Geology*, vol. 48, no. 3, pp. 269 – 282, 1997.

[19] T. Babadagli and K. Develi, "Fractal characteristics of rocks fractured under tension," *Theoretical and Applied Fracture Mechanics*, vol. 39, no. 1, pp. 73 – 88, 2003.

[20] M. L. Boas, *Mathematical Methods in the Physical Sciences*.
Wiley, 1966.

[21] J. Brewer and L. D. Girolamo, "Limitations of fractal dimension estimation algorithms with implications for cloud studies," *Atmospheric Research*, vol. 82, no. 1, pp. 433 – 454, 2006.

[22] T. Higuchi, "Relationship between the fractal dimension and the power law index for a time series: A numerical investigation," *Physica D: Nonlinear Phenomena*, vol. 46, no. 2, pp. 254 – 264, 1990.

[23] N. R. Draper and H. Smith, *Applied Regression Analysis*.
New York : Wiley, 2d ed ed., 1981.

[24] P. Kulatilake and J. Um, "Requirements for accurate quantification of self affine roughness using the roughness-length method," *International Journal of Rock Mechanics and Mining Sciences*, vol. 34, no. 3, pp. 166.e1 – 166.e15, 1997.

[25] H. E. Hurst, "The problem of long-term storage in reservoirs," *International Association of Scientific Hydrology. Bulletin*, vol. 1, no. 3, pp. 13–27, 1956.

[26] F. C. D. la Torre, J. I. G. Trejo, C. A. R. Ramirez, and L. F. H. Reyes, "Fractal dimension algorithms and their application to time series associated with natural phenomena," *Journal of Physics: Conference Series*, vol. 475, no. 1, p. 012002, 2013.

[27] J. D. Jackson, *Classical electrodynamics*.
New York, NY: Wiley, 3rd ed. ed., 1999.

[28] J. J. Stamnes, *Waves in Focal Regions*.
CRC Press, 1986.

[29] G. N. Watson, *A Treatise on the Theory of Bessel Functions*.
Cambridge Mathematical Library, Cambridge University Press, 1995.

[30] M. Abramowitz and I. A. Stegun, *Handbook of Mathematical Functions with Formulas, Graphs, and Mathematical Tables*.
New York: Dover, 9th ed. ed., 1964.

[31] M. V. Berry and S. Klein, "Integer, fractional and fractal talbot effects," *Journal of Modern Optics*, vol. 43, no. 10, pp. 2139–2164, 1996.

[32] M. V. Berry, "Diffractals," *Journal of Physics A: Mathematical and General*, vol. 12, no. 6, p. 781, 1979.

[33] A. Sommerfeld, "Mathematische theorie der diffraction. (mit einer tafel)," *Mathematische Annalen*, vol. 47, pp. 317–374, 1896.

[34] M. Born and E. Wolf, *Principles of Optics : Electromagnetic Theory of Propagation, Interference and Diffraction of Light*.
Cambridge University Press, 7th ed. ed., 1999.

[35] G. D. Durgin, "The practical behavior of various edge-diffraction formulas," *IEEE Antennas and Propagation Magazine*, vol. 51, pp. 24–35, June 2009.

[36] D. L. Jaggard and Y. Kim, "Diffraction by band-limited fractal screens," *J. Opt. Soc. Am. A*, vol. 4, pp. 1055–1062, Jun 1987.

[37] H. Talbot, "Facts relating to optical science. no. iv," *The London, Edinburgh, and Dublin Philosophical Magazine and Journal of Science*, vol. 9, no. 56, pp. 401–407, 1836.

[38] J. Wen, Y. Zhang, and M. Xiao, "The Talbot effect: recent advances in classical optics, nonlinear optics, and quantum optics," *Advances in optics and photonics*, vol. 5, no. 1, pp. 83–130, 2013.

[39] A. K. Golmankhaneh and D. Baleanu, "Diffraction from fractal grating cantor sets," *Journal of Modern Optics*, vol. 63, no. 14, pp. 1364–1369, 2016.

[40] C. Allain and M. Cloitre, "Optical diffraction on fractals," *Phys. Rev. B*, vol. 33, pp. 3566–3569, Mar 1986.

[41] M. A. Yates, G. New, and T. Albaho, "Calculating higher-order modes of one-dimensional unstable laser resonators," *Journal of Modern Optics*, vol. 51, no. 5, pp. 657–667, 2004.

[42] M. Yates and G. New, "Fractal dimension of unstable resonator modes," *Optics Communications*, vol. 208, no. 4, pp. 377 – 380, 2002.

[43] J. Uozumi, H. Kimura, and T. Asakura, "Laser diffraction by randomized koch fractals," *Waves in Random Media*, vol. 1, no. 1, pp. 73–80, 1991.

[44] J. Uozumi, H. Kimura, and T. Asakura, "Fraunhofer diffraction by koch fractals: The dimensionality," *Journal of Modern Optics*, vol. 38, no. 7, pp. 1335–1347, 1991.

[45] Wave propagation in complex domains workshop, University College London, 30 March 2017.

[46] D. P. Hewett, S. Langdon, and S. N. Chandler-Wilde, "A frequency-independent boundary element method for scattering by two-dimensional screens and apertures," *IMA Journal of Numerical Analysis*, vol. 35, no. 4, pp. 1698–1728, 2015.